

HARVARD  
Kenneth C. Griffin



GRADUATE SCHOOL  
OF ARTS AND SCIENCES

DISSERTATION ACCEPTANCE CERTIFICATE

The undersigned, appointed by the  
Department of Physics  
have examined a dissertation entitled

Ultracold molecules in an optical tweezer array: From dipolar interaction to ground state cooling

presented by Yicheng Bao

candidate for the degree of Doctor of Philosophy and hereby  
certify that it is worthy of acceptance.

Signature John Doyle

Typed name: Prof. John Doyle

Signature Mikhail Lukin

Typed name: Prof. Mikhail Lukin

Signature Matteo Mitrano

Typed name: Prof. Matteo Mitrano

Date: May 6, 2024



# Ultracold molecules in an optical tweezer array: From dipolar interaction to ground state cooling

A DISSERTATION PRESENTED  
BY  
YICHENG BAO  
TO  
THE DEPARTMENT OF PHYSICS

IN PARTIAL FULFILLMENT OF THE REQUIREMENTS  
FOR THE DEGREE OF  
DOCTOR OF PHILOSOPHY  
IN THE SUBJECT OF  
PHYSICS

HARVARD UNIVERSITY  
CAMBRIDGE, MASSACHUSETTS  
MAY 2024

©2024 – YICHENG BAO  
ALL RIGHTS RESERVED.

# Ultracold molecules in an optical tweezer array: From dipolar interaction to ground state cooling

## ABSTRACT

Ultracold molecules are attractive candidates for various applications including ultracold chemistry, quantum information processing, quantum simulation and searches for physics beyond the standard model. Combined with optical tweezer techniques, an optical tweezer array of ultracold polar molecules holds promise for versatile quantum applications. Their long-lived molecular rotational states form robust qubits, while the long-range dipolar interaction between molecules provides quantum entanglement.

In this thesis, we build a new generation experiment of optical tweezer array of ultracold CaF molecules. We optically transport the laser cooled and optically trapped molecules into a science glass cell using a hybrid method, where high numerical aperture optical access allows for tighter optical tweezers. In an array of these tight optical tweezers, we demonstrate dipolar spin-exchange interactions between single CaF molecules for the first time. We realize the spin- $\frac{1}{2}$  quantum XY model by encoding an effective spin- $\frac{1}{2}$  system into the rotational states of the molecules, and use it to generate a Bell state through an iSWAP operation. Conditioned on the verified existence of molecules in both tweezers at the end of the measurement, we obtain a Bell state fidelity of 0.89(6). Employing interleaved tweezer arrays, we demonstrate single site molecular addressability. To further improve the platform, cooling of the molecules to near

Thesis advisor: Professor John M. Doyle

Yicheng Bao

the motional ground state is crucial for reducing various dephasings. We demonstrate Raman sideband cooling (RSC) of CaF molecules in optical tweezers to near their 3-D motional ground state, with a 3-D motional ground state probability of  $54 \pm 18\%$  of the molecules that survive the RSC. This paves the way to increase molecular coherence times in optical tweezers for robust quantum information processing and simulation applications in the near future.

# Contents

TITLE	i
COPYRIGHT	ii
ABSTRACT	iii
TABLE OF CONTENTS	ix
LISTING OF FIGURES	xxv
LISTING OF TABLES	xxvi
CITATIONS TO PREVIOUS WORK	xxvii
DEDICATION	xxviii
ACKNOWLEDGMENTS	xxix
0 INTRODUCTION	1

0.1	Why molecules? . . . . .	1
0.2	How to create them? . . . . .	5
0.3	This Thesis . . . . .	6
<b>1</b>	<b>MOLECULAR STRUCTURE</b>	<b>8</b>
1.1	Diatomic Molecules . . . . .	9
1.2	Our Choice of Molecule : CaF . . . . .	15
<b>2</b>	<b>MAGNETO-OPTICAL TRAPPING OF CaF MOLECULES</b>	<b>22</b>
2.1	Cryogenic Buffer Gas Beam Source . . . . .	23
2.2	Ultra-high Vacuum System . . . . .	27
2.3	Laser Systems for MOT . . . . .	32
2.4	Laser Slowing of CaF . . . . .	43
2.5	3D RF MOT of CaF . . . . .	43
2.6	$\Lambda$ -enhanced Gray Molasses of CaF . . . . .	46
2.7	Conveyor Belt MOT of CaF . . . . .	47
2.8	Summary . . . . .	48
<b>3</b>	<b>OPTICAL TRAPPING AND TRANSPORT OF MOLECULES</b>	<b>49</b>
3.1	Optical Dipole Trap of CaF . . . . .	50
3.2	Optical Transport Setup . . . . .	53
3.3	Optical Transport Performance . . . . .	79
3.4	Outlook . . . . .	83
<b>4</b>	<b>AN OPTICAL TWEEZER ARRAY OF MOLECULES</b>	<b>84</b>
4.1	Microscope Objective . . . . .	85
4.2	Interferometric Test of Objective and Glass Cell . . . . .	90



4.3	Alignment Procedure . . . . .	98
4.4	Tweezer Imaging . . . . .	106
4.5	Making it an Array . . . . .	107
4.6	Properties of Optical Tweezers . . . . .	110
<b>5</b>	<b>DIPOLAR INTERACTION BETWEEN MOLECULES IN OPTICAL TWEEZERS</b>	<b>114</b>
5.1	Dipolar Interaction . . . . .	115
5.2	Initial State Preparation . . . . .	117
5.3	Rotational Coherence and Microwave Setup . . . . .	118
5.4	Coherent Dipolar Spin-exchange Interaction . . . . .	128
5.5	Anisotropy of the Dipolar Interaction . . . . .	133
5.6	Fidelity of Created Bell States . . . . .	135
5.7	Towards Arbitrary Initial State Preparation . . . . .	140
5.8	Summary . . . . .	143
<b>6</b>	<b>RAMAN SIDEBAND COOLING OF MOLECULES</b>	<b>145</b>
6.1	Introduction to Raman Sideband Cooling . . . . .	146
6.2	Initial State Preparation . . . . .	149
6.3	Resolving Motional Sidebands using Raman Transitions . . . . .	153
6.4	Optical Pumping . . . . .	161
6.5	Raman Sideband Thermometry . . . . .	165
6.6	RSC Results . . . . .	169
6.7	Conclusion and Outlook . . . . .	174
<b>7</b>	<b>NEXT GENERATION BEAM BOX</b>	<b>176</b>
7.1	Potential Improvements . . . . .	177

7.2	Consideration of the New Design . . . . .	183
8	CONCLUSION AND OUTLOOKS	185
APPENDIX A HIGH MAGNETIC FIELD COIL		188
A.1	Design . . . . .	189
A.2	Construction of the coil . . . . .	190
A.3	Coil mounting . . . . .	192
A.4	Blackening the coil . . . . .	195
A.5	Coil testing . . . . .	196
APPENDIX B TRIPLE SEEDED SFG		199
B.1	Lithium Niobate and Quasi-Phase Matching . . . . .	200
B.2	Tips . . . . .	202
B.3	Alignment Procedure . . . . .	204
APPENDIX C WHITE-LIGHT EOM		207
C.1	RLC resonant circuit . . . . .	207
C.2	Design . . . . .	209
C.3	Performance . . . . .	211
APPENDIX D CRYOGENIC BEAM BOX DETAILS		213
D.1	1K Pulse tube cryocooler . . . . .	213
D.2	Gold plated 40K shields . . . . .	217
D.3	Pulse tube leaks . . . . .	218
D.4	Heater aided warm up . . . . .	218

APPENDIX E	CONTROL SYSTEM	220
E.1	Save scanning variables with Cicero . . . . .	221
E.2	Imaging software . . . . .	222
E.3	Spectrum Instrumentation AWG card sequence generator . . . . .	223
E.4	Tweezer AOD waveform generator . . . . .	224
E.5	LabVIEW control . . . . .	226
APPENDIX F	RF MOT COIL AND AMPLIFIER	227
F.1	Resonant tank circuit and impedance matching . . . . .	227
F.2	Issues with MOT coil . . . . .	229
F.3	1kW RF amplifier . . . . .	231
APPENDIX G	MAGNETIC FIELD COMPENSATION	234
G.1	Magnetic field compensation coils . . . . .	234
G.2	Magnetic field compensation controller . . . . .	235
APPENDIX H	WAVEMETER AND LITHIUM LASER LOCK	238
H.1	Wavemeter and Galvanometer switcher . . . . .	238
H.2	Lithium laser lock . . . . .	239
APPENDIX I	COLLECTION OF OPTO-MECHANICAL IDEAS	242
I.1	Fiber-optics vacuum feedthrough . . . . .	242
I.2	“Eye safe” optical isolator . . . . .	243
I.3	Compact programmable waveplate . . . . .	244
I.4	Minilite YAG button pusher . . . . .	245
REFERENCES		258

# Listing of figures

1	Various applications of cold molecules. The arrow represents the typical temperature required to enable such application. . . . .	2
2	3D rendering of the full vacuum system for CaF Gen2. . . . .	7
1.1	Examples of wavefunctions for vibrational eigenstates of two Morse potentials. . . . .	10
1.2	(a) Hund's case (a). (b) Hund's case (b). Reproduced from 16 . . . . .	12
1.3	CaF X-state Zeeman shifts. . . . .	19
2.1	3D model of the cryogenic buffer gas beam box. . . . .	25
2.2	(a) Cross section view of the buffer gas cell 3D model. (b) Zoom in for details. . . . .	26
2.3	3D rendering of the UHV system viewed from the top. . . . .	28
2.4	Assembled in-vacuum RF MOT coils. Coils are upside-down in this photo, since the supporting feedthroughs are supporting the coils from the top once installed into the MOT chamber. . . . .	30

2.5	Nano-textured coated 3-inch octagonal glass cell. . . . .	31
2.6	“Hyperfine board” setup . . . . .	34
2.7	Beat note lock (OPLL) setup. . . . .	36
2.8	Slowing optical beam path. The Pockels cell here is a Conoptics 350-80 electro-optic phase modulator angled at 45° to scramble the polarization. . . . .	38
2.9	(a) Optical spectrum of the output of the C-band PM-EDFA (EAR-10-C-LP, IPG Photonics) with three seeded input. (b) Four wave mixing peaks can be seen when vertical sensitivity is increased, but they are small and will not affect the SFG. . . . .	40
2.10	Triple seeded SFG setup . . . . .	41
2.11	(a) CaF RF MOT picture taken with EMCCD camera. (b) CaF RF MOT picture taken with a Google Pixel phone camera. . . . .	45
2.12	(a) CaF (2+1) frequency conveyor belt MOT compression. (b) Relative molecule numbers at different stages of the experiment. . . . .	47
3.1	Sloshing of the molecules in the ODT when molecules are not loaded at the center of the ODT in the axial direction. The oscillation disappears when the ODT focus is moved to the center of the molasses in the axial direction. . . . .	53
3.2	Double-pass AOM setup for initial transport tests. . . . .	57
3.3	(a) Lifetime of molecules held in the lattice. A Siglent signal generator is used here with external frequency modulation turned on (blue) and off (red). (b) Initial observation of transport using the Siglent signal generator. . . . .	58

3.4	RF output spectrum. (a) Siglent SDG2122X with its internal reference clock. (b) Siglent SDG2122X with external 10 MHz reference clock provided by a Rohde&Schwarz FSW signal analyzer. (c) RIGOL DG4102 with its internal reference clock. (d) RIGOL DG4102 with external 10 MHz reference clock provided by a Rohde&Schwarz FSW signal analyzer. (e) Tektronix AWG70001A with its internal reference clock. (f) Tektronix AWG70001A with external 10 MHz reference clock provided by a Rohde&Schwarz FSW signal analyzer. Note that spectrum (a)-(e) are all taken with 3 Hz resolution bandwidth, while (f) is taken with 10 Hz resolution bandwidth. . . . .	60
3.5	(a) and (b) A soft membrane deforms under the force exerted by a voice coil motor, changing the focal length of the lens. Reproduced from Optotune website. (c) A “tombstone” mount used to mount the ETL for better wave front error. . . . .	61
3.6	(a) Acoustic beam steering AOD using a stepped crystal. (b) Bragg angle of the AOD. Red curve shows the steered acoustic beam angle, and the blue curve shows the optimal Bragg angle. (c) Acoustic wave vector steered at varying RF drive frequency. . . . .	66
3.7	Final transport lattice setup view from the top. The tunable lens mount section inside the dashed box is vertically mounted on the optical table.	67
3.8	(a) Medium distance transport with new ETL. (b) Loss of molecules is observed when transporting too close to the viewport. . . . .	72
3.9	Typical frequency response of the EL-16-40-TC. The driving amplitude is $-50$ mA to $50$ mA. Reproduced from EL-16-40-TC datasheet by Optotune. . . . .	73

3.10	(a) Impulse response measurement setup (b) Measured step response and impulse response functions of the 20D and 5D lenses. (c) Optimized driving waveform for a simple linear ramp as a target trajectory. . . . .	76
3.11	Lens response driven with a simple linear ramp (red) versus an optimized waveform (green). The gray area is the Rayleigh range of the ODT along the target trajectory. Key moments during lattice acceleration and deceleration are zoomed in for clarity. . . . .	78
3.12	(a) Transport efficiency versus the furthest distance reached by the focus of the ODT beam, taken with different round-trip transport distances (indicated in the legend) defined by the lattice motion. Data points on each trace are obtained by scanning the amplitude of the tunable lens driving waveform. The left vertical axis shows the normalized fluorescence signal after transport referenced to the fluorescence signal before the transport. The right vertical axis shows the transport efficiency calculated by dividing the signal by the peak value of the static hold condition. The error bars are all referenced to the left vertical axis. All transports shown in this figure are round-trip, with the longest distance being 45.7 cm to the science cell and then back to MOT chamber. The acceleration is $6.3 \text{ km/s}^2$ and the round-trip transport time is 100 ms. (b) Relative transport efficiency versus the lattice depth with different acceleration during acceleration phases. Relative transport efficiency is all normalized relative to the peak efficiency in this data set. . . . .	80
3.13	Heated molecules failed to decelerate at the end of transport and fly away.	81

4.1	(a) RMS TWE of the default objective setup at different wavelengths. Blue, green, red, yellow curves are center, 50 $\mu\text{m}$ , 100 $\mu\text{m}$ and 150 $\mu\text{m}$ distance from the center of field of view. Black curve is the indication of diffraction limit. (b) FFT diffraction encircled energy of the default objective setup. . . . .	86
4.2	(a) Rainbow colored Newton rings are observed when fused silica plate is mounted on the objective flat front element. (b) Interferometric test of the surface flatness of the 1 mm fused silica plate. . . . .	88
4.3	(a) RMS TWE of the objective setup at different wavelengths after replacing 1 mm thick sapphire with 1 mm thick fused silica, with (solid lines) and without (dashed lines) the effect of bowed fused silica plate. (b) FFT diffraction encircled energy of the objective setup described in (a).	89
4.4	(a) RMS TWE of the objective setup at different wavelengths with (solid lines) and without (dashed lines) the effect of glass cell viewport bent inwards under vacuum. (b) FFT diffraction encircled energy of the objective setup described in (a). . . . .	91
4.5	(a)-(b) Incoherent light source based on TA and SLD. (c) Optical delay line with coarse and fine scan capability. (d) Fizeau interferometer used in this work. . . . .	93
4.6	(a) The measured glass cell primary viewport deformation under vacuum. (b) Compare measurement to COMSOL simulation, measurement is shown in color dots. . . . .	94
4.7	Interferometer raw image acquired during a glass cell vacuum vent. . .	95

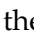


4.8	The setup of the objective transmitted wavefront error test using a bearing ball. (b) The transmitted wavefront error measured using a bearing ball and Fizeau interferometer. . . . .	96
4.9	(a) Absorption and emission spectrum of the Fluorescence nanospheres. “Pink” nanospheres are used in this test. Reproduced from datasheet of SPHERO™ fluorescent particles. (b) Setup of the objective PSF test. . . . .	97
4.10	(a) The PSF of the objective measured at 610 nm using fluorescence nanospheres and an imaging lens with 750 mm long focal length. (b) 1D fit of the cross section of the measured PSF to an Airy model. . . . .	98
4.11	(a)-(b) Microscope objective mounted on a five-axis translation stage. . . . .	99
4.12	Align objective to glass cell center using a long focal length camera lens. . . . .	101
4.13	Objective alignment beam path. . . . .	102
4.14	Tweezer imaging beam path. . . . .	105
4.15	Tweezer ROI histogram of the first image shot and second image shot, plotted in linear scale (a) and logarithmic scale (b). Imaging exposure time is 15 ms. . . . .	107
4.16	Dual AOD tweezer beam path. . . . .	109
4.17	(a) Survival fraction versus number of tweezer spacing distance moved during rearranging in a 10-site tweezer array with incorrect phase. (b) Survival fraction versus number of tweezer spacing distance moved during rearranging in a 40-site tweezer array with correct phase. . . . .	111
4.18	1-D tweezer array rearrange. Top image is the first image of randomly loaded tweezers, and is used for identification. Second image is confirmation of rearranging towards left side of the array. . . . .	111

4.19	(a) Trap depth modulation spectroscopy showing two parametric heating loss features. The lower frequency feature is parametric heating on the axial direction. The higher frequency feature is parametric heating on the radial direction. (b) An example of release and recapture measurement of the temperature of the molecule in the optical tweezer trap. Data is fitted to a Monte-Carlo simulation. . . . .	113
5.1	Relevant rotational ( $N$ ) and hyperfine ( $F$ ) states in the ground electronic state of CaF. Figure (a)-(d) show steps of state preparation using optical pumping, microwave transfer and resonant blow out. . . . .	118
5.2	Cartoon of optical tweezers and the coordinate system used in this work. For visual clarity, only four sites of the realized twenty-site array are depicted. Between a pair of tweezers, we define $\theta$ as the relative angle between the applied bias magnetic field $\vec{B}$ (in the $XY$ plane) and the inter-molecular vector $\vec{r}$ . The tweezer light propagates along $Z$ . . . . .	119
5.3	The diagram of the simple microwave setup. . . . .	119
5.4	(a) Coherent Rabi oscillation averaged over 10 sites in an optical tweezer array. (b) Rabi oscillation frequency per tweezer site. . . . .	120
5.5	(a) Magnetic field noise in the lab measured by a fluxgate magnetometer. Y-axis is vertical direction. (b) Same measurement, but taken at another day. The time axis value should be multiplied by 1.2 to obtain the time in the unit of second. . . . .	122

5.6	(a) Repeated phase scans of Ramsey sequence. Each scan take about 2 min, with the black flocked paper in place. (b) Same phase scans with the black flocked paper replaced by a piece of Acktar Metal Velvet black sheet. . . . .	122
5.7	Repeated phase scans of Ramsey sequence. Each scan take about 2 min. Ion gauge is turned off after finishing scan 1. . . . .	124
5.8	(a) Ionizer bar with 4 pairs of electrodes. (b) Ion sweeper installed in the beam box. . . . .	124
5.9	(a) Ramsey, single $\pi$ -pulse spin-echo and XY8 dynamical decoupling pulse sequences used in the experiment. $\frac{\pi_x}{2}$ denotes a $\frac{\pi}{2}$ -pulse, which rotates the quantum state around x-axis of the Bloch sphere by $90^\circ$ . Similarly, $\pi_x$ ( $\pi_y$ ) denotes a $180^\circ$ rotation around x-axis (y-axis) on the Bloch sphere. $\frac{\pi_\theta}{2}$ denotes a $\frac{\pi}{2}$ -pulse around an axis that has $\theta$ angle relative to the x-axis on the X-Y plane. “ $\times N$ ” means the block of XY8 pulses is repeated multiple times during the evolution time. $T$ is the total time between the two $\frac{\pi}{2}$ -pulses for all the sequences. (b) Measured single molecule rotational coherence time between $ \uparrow\rangle$ ( $N=1$ ) and $ \downarrow\rangle$ ( $N=0$ ) using Ramsey, single $\pi$ -pulse spin-echo, and the XY8 dynamical decoupling sequences. The coherence time is fitted as a Gaussian $1/e$ decay time constant. . . . .	126
5.10	(a) Oscillating XY8 phase scan contrast due to X and Y rotation axis deviation from $90^\circ$ angle between X and Y rotation. (b) Oscillating phase in the XY8 phase scan due to X and Y rotation axis deviation from $90^\circ$ .	127

5.11	The diagram of the new microwave setup using I/Q modulator inside SR392. An additional microwave switch is added to increase isolation. Both microwave switches are controlled by the AWG synchronized digital output. . . . .	128
5.12	(a) Dipolar spin-exchange oscillation at various tweezer spacings, with fitted decay time constant and oscillation period shown in the legends. (b) Dipolar spin-exchange interaction strength $J$ versus the tweezer spacing $ \vec{R} $ . Orange line (dashed) is the theoretical prediction of $J$ at zero temperature. Blue line (solid) is the simulated result of $J$ with the thermal motion of the molecules taken into account. . . . .	130
5.13	(a) Simulated $1/e$ dipolar coherence times at different tweezer spacings are shown in the red. $1/e$ dipolar coherence times fitted from the measured data are shown in blue. (b) Simulated number of dipolar oscillation cycles (contrast decayed to $1/e$ ) at different tweezer spacings are shown in the red. Fitted data from measured oscillations are shown in blue. . . . .	132
5.14	(a) Dipolar spin-exchange interaction at different angles $\theta = 0^\circ, 54.7^\circ$ and $90^\circ$ . The $\theta = 0^\circ$ and $90^\circ$ data is fitted to an exponentially decaying sinusoidal model with decay time constant $\tau_D$ and oscillation cycle time $T$ , shown in solid lines. (b) Simulated $P_{\uparrow\uparrow}$ at different $\theta$ angle and a tweezer spacing $ \vec{R}  = 2 \mu\text{m}$ . Solid lines are the simulation results while the data is the same as (a). . . . .	134

5.15 (a) Microwave pulse and detection sequence used in the parity oscillation measurement.  $\frac{\pi_\varphi}{2}$  denotes a  $\frac{\pi}{2}$ -pulse with a microwave phase shifted by  $\varphi$  relative to the first  $\frac{\pi_x}{2}$  pulse in the sequence, effectively rotating the quantum state around an axis that is angled  $\varphi$  relative to the x-axis on the Bloch sphere. The pulse (, in yellow) represents imaging of the molecules. Note that the first imaging pulse for tweezer loading identification, as well as the microwave pulses for initial state preparation, are applied before this sequence and not shown in this figure. (b) Parity oscillation at  $\theta = 0^\circ$  and  $\theta = 90^\circ$ .  $A$  is the fitted parity oscillation amplitude. (c) With the addition of a  $\pi$ -pulse and a third imaging step to the sequence in (a), molecules are verified to be present throughout the entanglement and readout process. (d) Parity oscillation for  $\theta = 90^\circ$  with empty traps excluded and corrected for measurement error, using the sequence depicted in (c). . . . . 136

5.16 (a) The measured probability of the four outcomes after the creation of Bell state. (b) The measured probability of the four outcomes with an additional  $\pi$ -pulse added after the creation of Bell state. (c) The full distribution of all the probable events. . . . . 141

5.17 **Optical setup for generating the optical tweezer array.** A cartoon of the optical setup around the glass cell is shown on the left. A zoomed in sketch of the dual AOD setup is shown on the right. The typical AOD setups are used to create separate array for the odd and even sites. The purple and pink beams denote the laser beams generated by AOD setup 1 and 2. . . . . 143

5.18	<p>(a) Rabi oscillation after preparation of the molecular pair in <math> \downarrow\uparrow\rangle</math>. (b) Dipolar spin-exchange oscillation with a initial <math> \uparrow\downarrow\rangle</math> state at <math>\theta = 90^\circ</math>. Shown here is the outcome of <math> \downarrow\uparrow\rangle</math> and <math> \uparrow\downarrow\rangle</math>. . . . . 144</p>	144
6.1	<p>(a) Zeeman energy levels of the <math> X^2\Sigma, N = 1\rangle</math> manifold. The <math>(m_S = -1/2, m_I = -1/2)</math> subspace used for RSC in this work is highlighted in the blue inset. (b) Motional eigenstates <math> n\rangle</math> in a harmonic trap. Red arrows labeled RB1 and RBx (<math>x = 2, 3</math> or <math>4</math>) represent the Raman transition driven to lower the motional quantum number <math>n</math> by 1 for a specific trap axis. The green arrows represent the <math>\sigma+</math> and the <math>\pi</math> optical pumping transitions. The dashed green arrow indicates spontaneous emission. The <math>\pi</math>-polarized transition is driven to prevent accumulation of population in <math> X^2\Sigma, N = 1, m_N = 0\rangle</math> state during OP. Note the negative sign in front of the Raman two-photon detuning <math>\delta</math>, indicating cooling sidebands have a negative <math>\delta</math> value. The <math>m_N = +1</math> state is the final state to which the molecules are cooled by RSC. . . . . 148</p>	148
6.2	<p>Relevant rotational (<math>N</math>) and hyperfine (<math>F</math>) states in the ground electronic state of CaF. Figure (a)~(c) show steps of state preparation using optical pumping, microwave Landau-Zener transfer and resonant blow out. Figure (d) shows the final step of preparing molecules in <math> N = 1, F = 2, m_F = -2\rangle</math>. Figure (e) shows the final step of preparing molecules in <math> N = 1, F = 0, m_F = 0\rangle</math>. 151</p>	151
6.3	<p>(a) Loss from <math> F = 2, m_F = -1\rangle</math> is observed as the amplitude of the magnetic field ramp is scanned. (b) No loss is observed from <math> F = 2, m_F = -1\rangle</math> as the amplitude of the magnetic field ramp is scanned. . . . . 152</p>	152

6.4	(a) Avoided crossing between $ F = 2, m_F = -2\rangle$ state and $ F = 1+, m_F = 0\rangle$ state around magnetic field $B_{\text{cross}} \approx 14.5$ G. (b) Loss is much reduced after tweezer trap depth is reduced to $1/5$ . . . . .	153
6.5	Raman laser optical setup . . . . .	154
6.6	(a) Motion sensitive Raman transition driven with B-field aligned with tweezer $k$ -vector (configuration A). (b) Scanning frequency difference between Raman beams at different Raman beam power. (c) Scanning frequency difference between Raman beams at different tweezer trap depth. . . . .	156
6.7	(a) Motion insensitive Raman transition driven with B-field aligned with tweezer polarization (configuration B). (b) Scanning frequency difference between Raman beams at different Raman beam power. (c) Scanning frequency difference between Raman beams at different tweezer trap depth. . . . .	157
6.8	(a) Motion insensitive Raman transition driven with B-field aligned with tweezer $k$ -vector (configuration A). (b) Scanning frequency difference between Raman beams at different Raman beam power. (c) Coherent Rabi oscillation observed. . . . .	159
6.9	Configuration of Raman beams and optical pumping beams used in RSC. RB1 and RB2 address the radial motion in $x$ -direction, RB1 and RB3 address the radial motion in $y$ -direction, and RB1 and RB4 mainly address the axial motion in $z$ -direction. The RB1 path is also be employed to drive a motion-insensitive Raman $\pi$ pulse for population swapping between $ m_N = \pm 1\rangle$ states. . . . .	161
6.10	Optical pumping frequency scan. . . . .	162

6.11	(a) Bad $\sigma$ optical pumping data, showing polarization is not pure enough. (b) $\pi$ optical pumping is working properly. . . . .	163
6.12	(a) The reflection from the 808 nm waveplate causing OP issues with the $\sigma$ -OP beam. (b) $\sigma$ -OP purity recovers after moving the 808 nm waveplate (red arrow in (a)). . . . .	165
6.13	Experimental sequence of tweezer array preparation, state initialization, RSC, RST, and state-sensitive detection. $B_y$ and $B_z$ are the applied magnetic field along $y$ direction and $z$ direction. $U_{trap}$ is the trap depth of the optical tweezer trap. $\pi$ denotes the motion-insensitive Raman $\pi$ -pulse used to transfer the population from $ m_N = -1\rangle$ to $ m_N = +1\rangle$ . .	169
6.14	Raman sideband cooling pulse sequences used in this work. . . . .	171
6.15	Raman sideband thermometry spectra: (a) radial $x$ direction; (b) radial $y$ direction; and (c) axial $z$ direction. Blue curves are the spectra obtained after RSC, orange curves are the spectra obtained before RSC. For the axial $z$ direction, an additional purple curve represents the spectrum obtained without the last step of RSC applied (partial cooling). The Raman pulse durations used for these RST spectra are $t_x = 75 \mu s$ , $t_y = 110 \mu s$ and $t_z = 350 \mu s$ . Green dashed line indicates the carrier frequency for each spectrum. Gray bands indicate the baseline for the spectra measured at the far detuned limit. . . . .	172



6.16	Rabi oscillations of the carrier transition: (a) radial $x$ direction; (b) radial $y$ direction; and (c) axial $z$ direction. Rabi oscillations of the first heating sideband: (d) radial $x$ direction; (e) radial $y$ direction; and (f) axial $z$ direction. In each figure, the data showing rapid dephasing before the application of RSC are plotted as orange squares, fitted to an exponential decaying model. Coherent Rabi oscillations after the application of RSC are plotted as blue circles, fitted to a numerically simulated model. . . .	173
7.1	Molecule numbers in CaF MOT versus cell temperature. Laser ablation energy and slowing time are optimized slightly for different temperatures.	178
7.2	Double density sorb plate module . . . . .	179
7.3	COMSOL simulation of the temperature of 40 K shield. (a) and (b) shows the design where window is mounted outside. (c) and (d) shows the design where window is mounted inside. . . . .	180
7.4	(a) "Donut" on the 40 K shield highlighted in blue. (b) A design that extends the 40 K panel to cover the "Donut" and brass screws. . . . .	181
A.1	Delamination of a 1/4 inch thick G-10 sheet that was pierced and cut using water jet machining. . . . .	192
A.2	The coil winding setup on the lathe. . . . .	193

A.3	(a) The zoomed in photo of the coil winding setup on the lathe. Teflon wire tensioner can be seen in this photo, installed on the cutting tool clamp. Low-profile thermocouples are inserted from the back of the winding adapter disk, through pre-cut slots on G-10 bobbin and clamped inside the coil windings. (b) Teflon tensioner designed to clamp on the wire with rectangular cross section. Tension can be tuned by adjusting the clamping screws on the lathe tool holder. . . . .	194
A.4	Three pairs of high magnetic field coils mounted on titanium mounts .	195
A.5	(a) Homemade high pressure water cooling system. (b) Brazed copper lug with a high current lead attached. . . . .	197
A.6	Magnetic field measurement of coils built. . . . .	198
B.1	Refractive index of lithium niobate versus wavelength at different temperature. . . . .	201
B.2	Transmission and reflectance of Thorlabs DMSP950. Reproduced from Thorlabs Inc. . . . .	203
C.1	White-light EOM 3D rendering, front view (a) and rear view (b). . . . .	210
C.2	White-light EOM as constructed, front view (a) and details of the crystal mount (b). . . . .	212
C.3	White-light EOM performance. (a) Beat note measurement of the broadened laser. (b) Spectrum bandwidth versus driving power into the ZHL-5W-1+ amplifier, gain is about 44 dB. . . . .	212
D.1	Diagram of the gas handling system for the 1K circulation system. . . . .	214
E.1	Imaging software based on PyQt. . . . .	223

E.2	(a) Microwave I/Q modulator software based on the Spectrum Instrumentation AWG card sequence generator code. (b) Raman beam pulse sequence generator based on the Spectrum Instrumentation AWG card sequence generator code. . . . .	224
E.3	1-D Tweezer AWG controller . . . . .	225
F.1	Circuit diagram of the RF MOT coil tank circuit. . . . .	228
F.2	(a) Tank circuit box used for each coil. Note the balancing variable capacitor is not shown in this photo. (b) 1kW RF amplifiers used for driving the RF MOT coils. . . . .	230
F.3	Arcing on the RF MOT coil electrical feedthrough. . . . .	231
H.1	(a) Wavemeter and galvanometer scanner setup. (b) A closer look at the 16-channel galvanometer switcher. . . . .	240
H.2	(a) Lithium laser lock setup. (b) Lithium laser lock frequency noise read by wavemeter. Gray area indicates standard deviation of the noise. . .	241
I.1	Fiber-optics vacuum feedthrough . . . . .	244
I.2	Compact programmable waveplate. . . . .	245
I.3	Minilite button pusher. . . . .	246

# Listing of tables

1.1	Useful molecular structure constants for CaF molecule. . . . .	17
-----	--	----

# Citations to Previous Work

Portions of this thesis or results described herein have previously been published in the references below.

- [1] Yicheng Bao, Scarlett S Yu, Loïc Anderegg, Sean Burchesky, Derick Gonzalez-Acevedo, Eunmi Chae, Wolfgang Ketterle, Kang-Kuen Ni, and John M Doyle. Fast optical transport of ultracold molecules over long distances. *New Journal of Physics*, 24(9):093028, 2022.
- [2] Yicheng Bao, Scarlett S Yu, Loïc Anderegg, Eunmi Chae, Wolfgang Ketterle, Kang-Kuen Ni, and John M Doyle. Dipolar spin-exchange and entanglement between molecules in an optical tweezer array. *Science*, 382(6675):1138–1143, 2023.
- [3] Yicheng Bao, Scarlett S Yu, Jiaqi You, Loïc Anderegg, Eunmi Chae, Wolfgang Ketterle, Kang-Kuen Ni, and John M Doyle. Raman sideband cooling of molecules in an optical tweezer array to the 3-d motional ground state. *arXiv preprint arXiv:2309.08706 (Accepted by Physical Review X)*, 2023.

TO MY FAMILY.

# Acknowledgments

First and foremost, I would like to thank my advisor, John Doyle, for his guidance, mentorship, unequivocal support and trust. John's outstanding leadership, vision and scientific expertise are crucial for the success of the group. He is also an excellent educator and considerate group manager, making the Doyle group a pleasant place to work. His optimism and courage for taking the risk on trying new ideas has a strong influence on me. John is a nice PhD advisor both inside and outside the lab, his kind advice covers almost anything graduate students might ever need in their life, from leak checking a cryostat, to choices of ham and cheese for CUA retreat. John also demonstrate to us, how to apply our scientific expertise to areas outside AMO physics. We have worked together many days and nights on the mask reuse project and aerosol mitigation prototypes during the hard times of COVID-19.

I would like to thank Wolfgang Ketterle, Kang-Kuen Ni and Eunmi Chae for the wonderful collaboration on the CaF experiment. Wolfgang always comes up with intuitive physical insights into a problem that seems complicate at first glance, which inspires everyone in the CaF weekly meeting. Kang-Kuen brings a lot of valuable ex-

periences on optical tweezer arrays and Raman sideband cooling into the experiment. I am also grateful for the scientific instruments that Kang-Kuen's group generously lend to us. Eunmi is the Doyle group alumni who built the first generation CaF experiment. I learned a lot about molecular structure of diatomic molecules from her thesis.

I appreciate Matteo Mitrano, Mikhail Lukin and Roxanne Guenette for being on my committee. It is always a nice learning experience talking to an expert from another field. Special thanks goes to Misha and his group, for valuable comments on our manuscripts and inspiring discussions when we are still new to optical tweezer arrays.

To the CaF team, it is a great experience working with all of you during my PhD time. The initial laser cooling team when I joined the group is Loic Anderegg, Ben Augenbraun, Sean Burchesky and Lawrence Cheuk. Loic, thanks for teaching me everything from scratch. Loic always has new technical and design ideas, as well as brilliant fixes to many problems on the experiment. We have many good discussions about new engineering ideas and simulation. Sean is a graduate student of my year. The moment he sits next to me in the bat cave, I start to learn a wide range of knowledge from him, including but not limited to, curling, mountain biking and car maintenance. It is always a lot of fun exploring New England with Sean, where he always saves me a seat on the way to CUA retreat. I am grateful for his invitation to the Thanksgiving dinner with his family (including showing me his scientific instrument collection). Ben is the ultimate molecular structure and spectroscopy guru, where I learned a lot about CaF molecule (and also polyatomic molecules) from him. Lawrence is the postdoc on CaF team, he brings so many valuable knowledge into the group from his experiences with quantum gas microscope and is a good teacher. Later, I moved on to build the CaF Gen2 experiment in the other corner of the room. Scarlett Yu is the initial member of the new CaF Gen2 experiment, and helps through the entire construction of the experiment. We



have witnessed many "first" on this experiment together. Jiaqi You joined the group in 2022. I believe the CaF Gen2 experiment will keep flourishing in their hands and wish them a fruitful journey with their academic career.

I would like to show my gratitude to the entire Doyle group for their support in the past 8 years. I arrive in the group during the summer of 2016 as a visiting student, and was helping around with SrOH bichromatic force experiment, mentored by Ivan Kozyryev, Louis Baum, Ben Augenbraun and Loic Anderegg. I thank all of you for teaching me the ABCs of molecular physics and welcoming me into the big family of Doyle group. Christian Hallas is my go-to for discussing about random physics ideas. Grace Li is the talented young student on CaOH, and we have many good discussions on conveyor belt MOT, together with Christian. Nathaniel has helped me a lot with paper editing and is always considerate sharing the lab resource with us. Debayan Mitra is always helpful with experiment and always optimistic. I spend many good time having dinners and lunches with Hiro, talking about anything, from Japanese anime to capturing a molecular MOT. Alex Frett, thanks for being my office mate and sharing all your knowledge about mushrooms. Abdullah, Paige and Annika, thank you for organizing birthday and outing events for the whole group. It is always a pleasure chatting with Zack Lasner, where my questions about precision measurement can be instantly answered. Xing Wu, Zhen Han, Peiran Hu are the electron EDM masters on the ACME experiment, where we borrowed many instruments and learned valuable knowledge from them.

My PhD time could not be that joyful without my friends. I would like to thank all of them for the companionship and support, including but not limited to, Zeyu Hao, Ruihua Fan, Muqing Xu, Lingyang Wu, Lin Su, Yiqin Cai, Yu Wang, Bingtian Ye, Weijie Wu, Chang Liu, Yimu Bao, Lingbang Zhu, Qianshu Lu, Tianning Zhao, Timothy Guo,

Allen Chiu, Yi Zhu, Yichao Yu, Haoning Tang, Xueyang Song, Sepehr Ebadi, Nicolò Foppiani, Ian Davenport, Cari Cesarotti, Brendon Bullard, Zoe Zhu, Iris Cong, Grace Zhang, Henry Zhou, Yuiki Takahashi, Zeyang Li, Jिंगgang Xiang, Li Du, Pai Peng, Guoqing Wang. Special thanks goes to Zeyu, Ruihua, Muqing, Lin, Yu and Kenneth, who I always go for a casual chat or ask for advice. I would not be able to survive the graduate school without you.

I want to thank Jim MacArthur for allowing me to dig through his stock electric components, as well as discussing random electronics with me. I would like to thank Stan, Steve, Andy and Alejandro for teaching me everything I need to know about machining and keeping the machine shop running in the most difficult times during COVID-19. Thank you Lisa Cacciabaudo and Jacob Barandes for keeping track of everything for the graduate student program. I want to thank Silke Exner and Adam Ackerman for navigating me through all the financial paperworks. Thanks Erica Mantone, Erica Colwell, Paola Martinez for making everything on the right track for the group. Our experiment cannot move forward without the support from all of you.

I would like to thank my undergraduate advisor Prof. Meng-Khoon Tey and Prof. Li You in Tsinghua University. They are my first mentors taking me into the world of experimental AMO physics. I still remember the afternoon when Prof. Li You handed me a new issue of Physics Today, with the page turned to the article "Diatomic molecules, a window onto fundamental physics" by Prof. Dave Demille. This leads to my interests towards ultracold molecules, and later my summer internship in Doyle group, thanks to his recommendation.

Finally, I would like thank my family for their support, encouragement and love.

# 0

## Introduction

### 0.1 WHY MOLECULES?

One might ask the question, why do we need to go for molecules? Compared to an atom, while it is more complicated to control all the degrees of freedom in a molecule, they promise more features that are not available in atoms, which in turn enable more possibilities. The rotational states and vibrational states in molecules are long lived,

and can be easily addressed using microwave and optical fields. The use of these states may allow promising schemes for storage, manipulation and high fidelity readout of quantum states. The permanent electric dipole moment in polar molecules offers an additional handle for a controlled interaction between the molecules and could be used for studying dipolar gas<sup>133</sup> and creating entanglement. The applications of molecules span widely from precision measurement, ultracold chemistry to quantum information processing and simulation, while many of these advantages can only be exploited when the motional and rotational temperature of the molecule is sufficiently low (Figure 1).

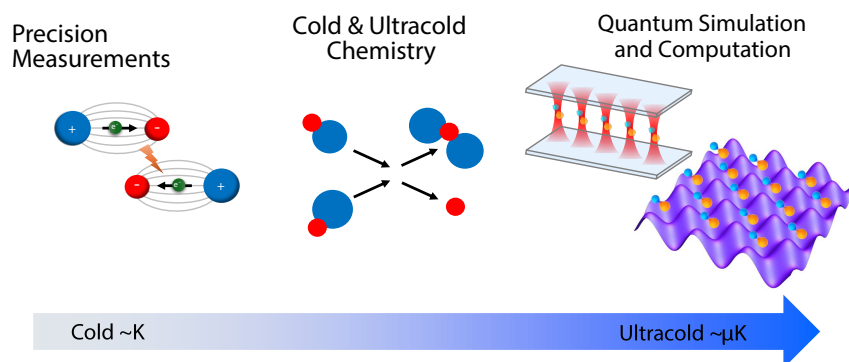


**Figure 1:** Various applications of cold molecules. The arrow represents the typical temperature required to enable such application.

### 0.1.1 PRECISION MEASUREMENT

Molecules are useful in precision measurements due to rich internal structures accommodating near degenerate energy states, which could be sensitive to fundamental physics. One successful example is search for the electron electric dipole moment (eEDM) using molecules<sup>31,30</sup> or molecular ions<sup>20,104</sup>, where a non-zero eEDM indicates evidence of CP-violation physics beyond Standard Model<sup>70</sup>. Molecules are also proposed to be sensitive to other variations of fundamental constants. For example, SrOH has been

proposed as a candidate that is sensitive to the proton-to-electron mass ratio, which can be used to detect ultralight dark matter<sup>73</sup>. Most of these measurements can be built as a relatively small table-top scale experiment, which is advantageous compared to many modern high energy physics experiments relying on particle accelerators. Precision measurements using cold molecules are currently limited to molecular beam experiments, which limits the interrogation time and complicates the process of understanding systematic errors. Trapping large quantities of molecules in a controlled environment with a long coherence time would greatly increase the sensitivity of these measurements, and is a goal currently pursued by the scientific community.

#### 0.1.2 ULTRACOLD CHEMISTRY

One unsolved question is what happens when two ultracold molecules meet with each other at short distance. There are predictions of so called "sticky collisions", where the molecules goes into a region with a very high density of states, forming a long lifetime complex<sup>83</sup>. Theoretical predictions of these collisions require precise determination of the potential energy surface of the interaction between molecules. State-of-art experiments have observed collisions between ultracold molecules and are able to gain control over them<sup>92,96,61,72</sup>. These types of "sticky collisions" are also observed in experiments<sup>116,97</sup>. Detection of the chemical reaction products is also made possible utilizing ion mass spectrometry<sup>60</sup>. It is also crucial to understand and control collisional properties between molecules, in order to create high density sample of ultracold molecules for other applications. Efforts have been focused on realization of shielding of molecules, reducing loss by preventing molecules from reaching short distance<sup>82,5</sup>, and increasing elastic collisional cross section for efficient thermalization<sup>108</sup>.

### 0.1.3 QUANTUM PHYSICS

Ultracold polar molecules possess permanent, long-range, and spatially anisotropic electric dipoles whose interaction could be harnessed for high fidelity entanglement generation. Thus, molecules have also been proposed as a powerful platform for realizing quantum simulations of strongly interacting many-body dynamics<sup>84,43,8,125</sup> and for scalable quantum computing<sup>35,132,67,107,93</sup>. Towards these goals, molecules have been demonstrated to have long qubit (rotational and hyperfine state) coherence times, significantly longer than the predicted molecule-molecule dipolar gate times<sup>98,110,127,19,48,21,79,49</sup>. Generation of coherent dipole-dipole couplings between molecules is the key milestone towards using ultracold polar molecules for quantum simulations and multi-particle quantum gates<sup>45,93</sup>, which has been shown in sparsely filled 3D lattices<sup>130</sup>, 2D layers<sup>118</sup>, and in a molecular quantum gas microscope<sup>29</sup>. Recently, rearrangeable tweezer arrays offer an attractive quantum platform due to their scalability and potential for single site addressability<sup>42,9,13,81,6,137</sup>. Combining this technique with dipolar interaction between ultracold polar molecules allows for generation of high fidelity entanglement, which is one of the topics that we will discuss in this thesis.

I would also like to note that dipolar interaction is not the only feature that molecules can contribute to quantum physics. The rich internal states in molecules, once fully controlled, can enable many desired features for quantum computing applications. For example, the rotational states in molecules can be used to shelve the molecules from the cooling and imaging light, allowing the realization of continuous loading of optical tweezers and mid-circuit readout of ancilla qubits for quantum error correction.

## 0.2 HOW TO CREATE THEM?

Ultracold molecules can be created either by an “in-direct” way (assembly of individual ultracold atoms), or by direct cooling of molecules to ultracold temperature.

The first pathway is pioneered by the KRb team in JILA, where Feshbach resonance is used to associate ultracold potassium and rubidium atoms into weakly bounded molecules<sup>91</sup>. The molecules are then transferred into its vibrational and rotational ground state using stimulated Raman adiabatic passage (STIRAP). This revolutionary way creates ultracold molecules at a temperature that no other methods can compete with, at that time. Similar method has been employed in many other ultracold atom species<sup>87,116,97,54,105</sup>. Recent developments of this method lead to several major advances, including the use of direct photo-association instead of Feshbach resonance to assemble NaCs molecules<sup>81</sup>, and creation of ultracold triatomic molecules<sup>131</sup>. However, these methods can only be applied to species of atoms that are already cooled to ultracold temperature.

To directly cool molecules to ultracold temperature, several methods are explored by the community, including supersonic expansion cooling or cryogenic buffer gas cooling. Supersonic expansion cooling relies on collision of the molecules with the buffer gas cooled during the rapid expansion. This has been a workhorse for molecular spectroscopy, due to its high yield and simplicity. However, the molecular beams extracted from supersonic expansion sources usually feature a very high forward velocity. Cryogenic buffer gas cooling works by thermalizing the molecules with cold buffer gas cooled by the wall of the buffer gas cell. This method allows creation of bright molecular beams with a slow forward velocity.

To reach ultracold temperature ( $T < 1\text{K}$ ), one method is optoelectrical Sisyphus

cooling in an electro-static trap. Submillikelvin temperatures of polyatomic organic molecules have been achieved with this method<sup>135,101</sup>. The other method is laser cooling, which is first demonstrated using atoms. Laser cooling has enabled atoms to be cooled to microkelvin temperature, and even temperatures low enough to realize Bose-Einstein condensates. In the past decade, ultracold molecules have been successfully achieved through a combination of cryogenic buffer gas cooling and laser cooling<sup>11,4,119,32,123</sup>. To reach even colder temperature with the “direct” method, laser cooling is the obvious choice. This is the method that this thesis is based on, and will be discussed in detail in the following chapters.

### 0.3 THIS THESIS

In this thesis, we will introduce the design and construction of a second generation experiment of the laser cooling of CaF molecules (CaF Gen2). A 3D rendering of the full vacuum system for this new apparatus is shown in Figure 2. The new experiment is focused on using CaF molecules in tightly confined optical tweezer arrays as candidate qubits, in pursue of quantum information processing and quantum simulation applications. We will introduce basic properties of diatomic molecules and the underlying principles for laser cooling of molecules in chapter 1. Buffer gas cooling, magneto optical trapping (MOT) and sub-Doppler cooling of CaF molecules will be discussed in chapter 2. Chapter 3 focuses on a new optical transport scheme that is crucial for shuttling molecules from MOT chamber to science glass cell. Chapter 4 will discuss the creation of high numerical aperture optical tweezer array. Chapter 5 will cover dipolar interaction between individual molecules in tweezers and generation of entanglement with such interaction. In chapter 6, we will talk about our work of Raman



sideband cooling of molecules in a tweezer array to the motional ground state. Finally, in chapter 7, we will discuss several improvements for the next generation buffer gas beam source, as well as outlooks of optical tweezer arrays of molecules as a versatile platform for various applications.

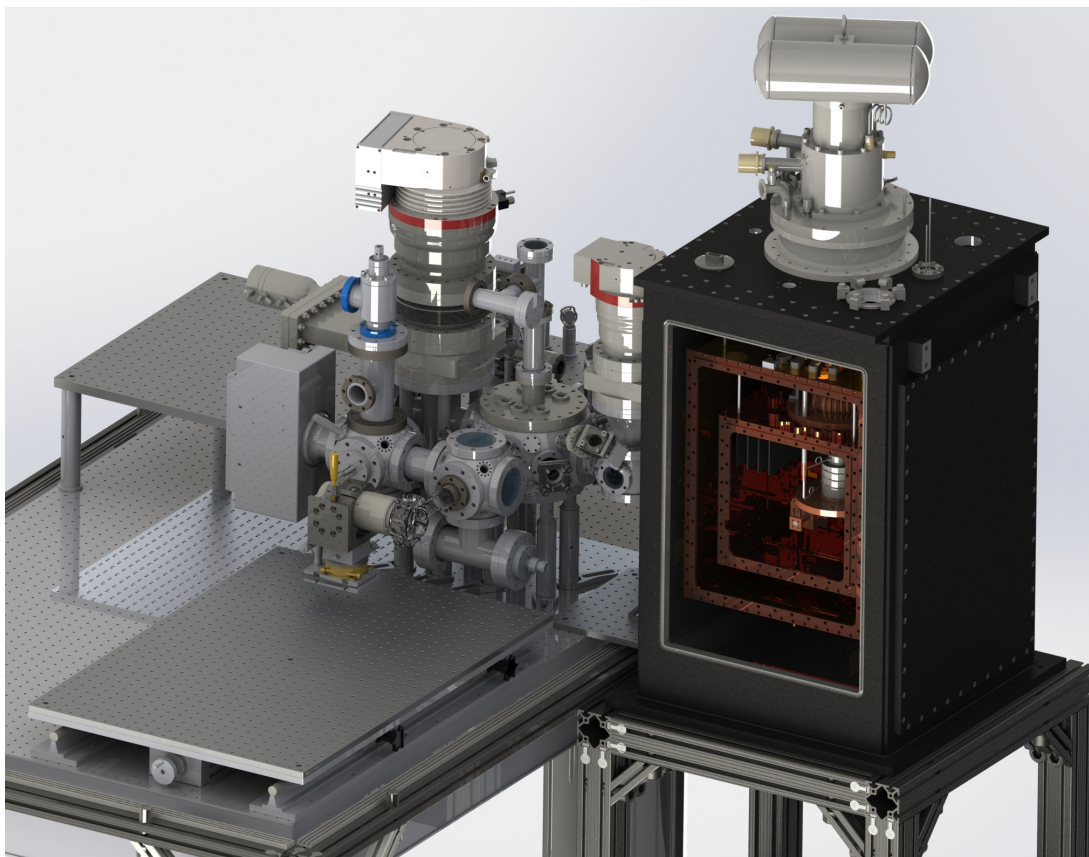


**Figure 2:** 3D rendering of the full vacuum system for CaF Gen2.

*A diatomic molecule is one atom too many.*

Arthur Schawlow

# 1

## Molecular Structure

To understand the structure of atoms and molecules, it is important to keep track of the energy scale of different interactions and always start from the largest energy scale. We will introduce the structure of diatomic molecules following the order of electronic, vibrational, rotational, and hyperfine levels.

## 1.1 DIATOMIC MOLECULES

### 1.1.1 BORN-OPPENHEIMER APPROXIMATION

The quantum state of the molecule should include states of all the nucleus and electrons. To further simplify this problem, the Born-Oppenheimer approximation can be applied, where the state can be separated into the motion of the nuclei and electrons<sup>16</sup>. This is due to the large mass difference between nucleus and electrons, where the nuclei coordinates can be approximated as fixed when treating the motion of electrons.

$$|\psi_{\text{mol}}\rangle = |\psi_{\text{nuclear}}\rangle |\psi_{\text{elec}}\rangle \quad (1.1)$$

The nuclear motion can be further separated into pure vibrational motion and rotational motion, if the rovibrational interaction is neglected.

### 1.1.2 VIBRATIONAL STATES

The vibrational motion of the nucleus is defined by the potential between two nuclei. For a perfect harmonic oscillator potential, the vibrational energy levels have even spacing. However, in a real molecule, the potential deviates from a quadratic form when the wavefunction extends away from the bottom of the potential, making it an anharmonic oscillator. The potential energy surfaces of a real molecules are complicated, but good analytical models exist that can well approximate these potentials. An example of a simple analytical form of molecular potential is the Morse potential<sup>16</sup>.

$$V_{\text{Morse}}(r) = D_e(1 - e^{-a(r-r_0)})^2 \quad (1.2)$$

One can analytically solve the Schrödinger equation for this specific potential to obtain the vibrational wavefunction (Figure 1.1), but numerical integration is required for more complicated potentials.

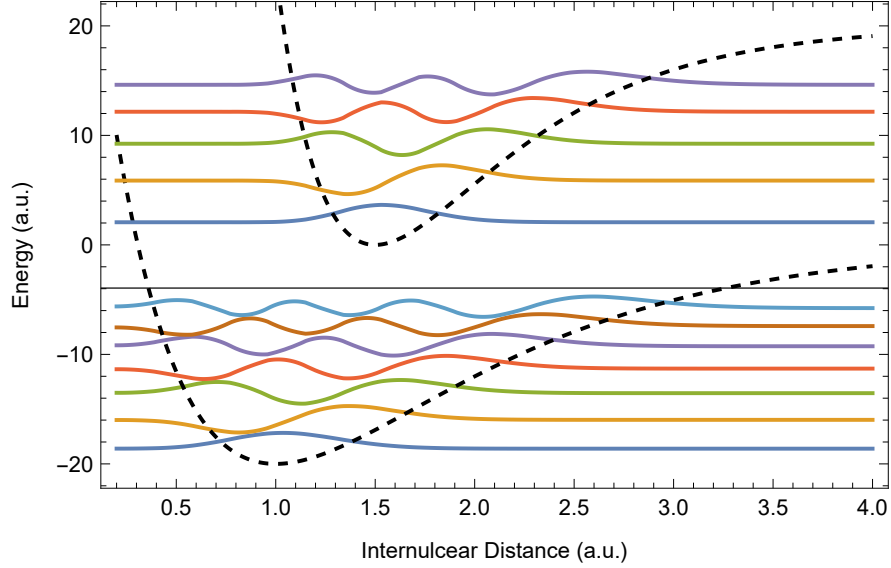


**Figure 1.1:** Examples of wavefunctions for vibrational eigenstates of two Morse potentials.

Nevertheless, it is still intuitive to approximate the potential as a harmonic oscillator, with the equilibrium distance and vibrational frequency as free parameters. The strength of rovibronic transitions can be calculated by evaluating the expectation value of the electric dipole operator  $\mu = er$ . Using the Born-Oppenheimer approximation and noticing that the nuclear wavefunction does not depend on electronic configuration.

$$\langle \psi'_{\text{mol}} | \mu | \psi''_{\text{mol}} \rangle = \langle \psi'_{\text{nuclear}} | \langle \psi'_{\text{elec}} | \mu | \psi''_{\text{elec}} \rangle | \psi''_{\text{nuclear}} \rangle \quad (1.3)$$

$$= \langle \psi'_{\text{nuclear}} | \psi''_{\text{nuclear}} \rangle \langle \psi'_{\text{elec}} | \mu | \psi''_{\text{elec}} \rangle \quad (1.4)$$

The term  $\langle \psi'_{\text{elec}} | \mu | \psi''_{\text{elec}} \rangle$  is the same for the electric dipole moment of a transition in

atomic physics. The other term  $\langle \psi'_{\text{nuclear}} | \psi''_{\text{nuclear}} \rangle$  includes both vibrational and rotational motion of the molecules. The vibrational part of this term is the overlap of the vibrational wavefunctions of the two states  $|\psi'\rangle$  and  $|\psi''\rangle$ . This term is named Franck-Condon factor (FCF). The Franck-Condon principle tells us that a vibronic transition strength is determined by the FCF and the electronic transition strength.

### 1.1.3 ROTATIONAL STATES

The rotational state for a rigid rotor can be written as  $H = \frac{\mathbf{R}^2}{2I}$ , where  $\mathbf{R}$  is the rotational angular momentum operator and  $I$  is the moment of inertia around the axis that is perpendicular to the internuclear axis of a diatomic molecule. By solving the Schrödinger equation, we find that the energy of the eigenstates can be expressed as  $E_{rot} = BR(R+1)$ , where  $B = \frac{\hbar^2}{2I}$ . In reality, molecules are rigid rotors, the moment of inertia  $I$  is not constant due to the centrifugal distortion. This can be approximated with the expansion

$$E_{rovib} = \sum_{k,l} Y_{kl} (v + \frac{1}{2})^k (R(R+1))^l \quad (1.5)$$

where  $Y_{kl}$  are the Dunham coefficients.

### 1.1.4 HUND'S CASE

Hund's cases are different ways of coupling various angular momenta in a molecule. These cases are decided by the order of strengths for coupling between angular momenta in a molecule. Among the electronic states that we are interested in for CaF molecules, the  $X$  state and  $B$  state are best described by Hund's case (b) and the  $A$  state and  $C$  state are best described by Hund's case (a). In Hund's case (a) (Figure 1.2 (a)), electrostatic coupling of  $L$  to the internuclear axis is strong, making the projection of  $L$

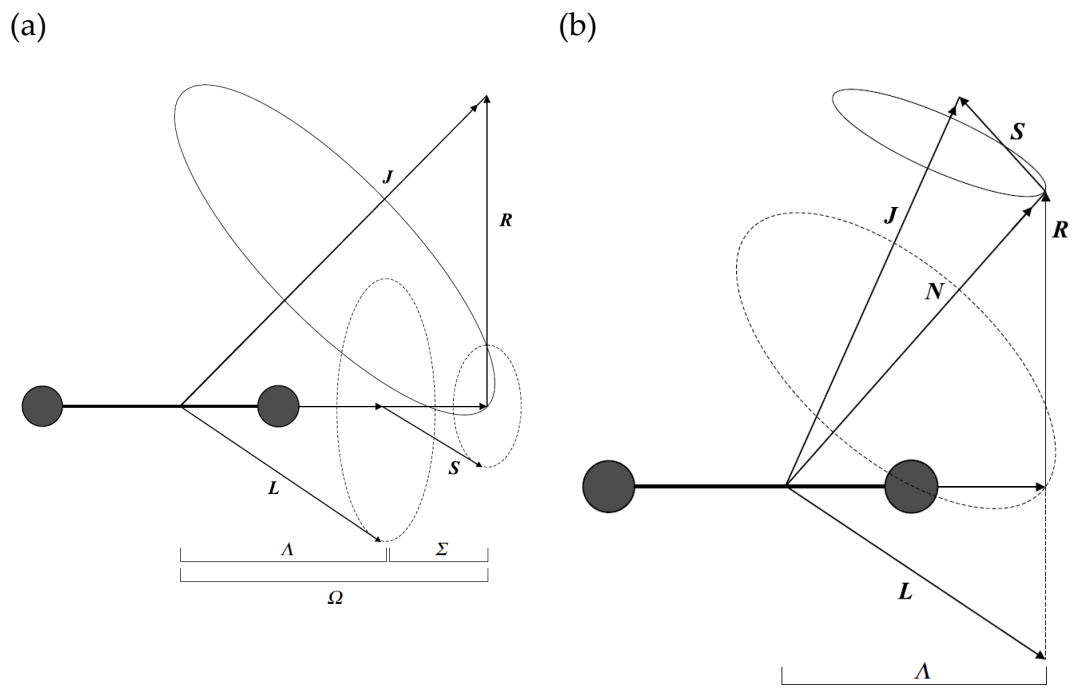


**Figure 1.2:** (a) Hund's case (a). (b) Hund's case (b). Reproduced from 16

onto the internuclear axis  $\Lambda$  a good quantum number. The next strongest coupling is spin-orbit coupling, which causes coupling of  $S$  onto  $L$ , making the projection of  $S$  onto the internuclear axis  $\Sigma$  also a good quantum number\*. Finally, we couple the rotational angular momentum  $R$  to get the total angular momentum  $J$ . For diatomic molecules, rotation is around the axis that is perpendicular to the internuclear axis. The total angular momentum projection onto the internuclear axis is named  $\Omega$ , where  $\Omega = \Sigma + \Lambda$ .

Due to mixing coming from nearby  $\Sigma$  states, the alignment of  $|\Lambda| = 1$  on the internuclear axis is no longer degenerate in the  $A$  state of CaF molecule. The energy splitting between these two states is known as  $\Lambda$ -doubling. Due to the opposite parity of these two states and the relatively small energy spacing, it is easy to be mixed by external electric fields. When the molecule is excited to  $A$  state, mixing with the opposite parity state in the  $A$  state would cause loss of population to the wrong parity state in the ground state, breaking the photon cycling that laser cooling relies on.

In Hund's case (b) (Figure 1.2 (b)),  $L$  is still strongly coupled to the internuclear axis, so the projection  $\Lambda$  is still a good quantum number. However, the next strongest coupling is rotation  $R$ , making the sum of rotational angular momentum  $R$  and  $L$  a good quantum number. This quantity is denoted as  $N = R + L$ . Finally, adding spin-orbit coupling gives the total angular momentum  $J = N + S$ .

---

\*Note "abuse of notation" here.  $\Sigma$  as a quantum number has nothing to do with the molecular term symbol  $\Sigma$  for zero projection of total angular momentum on the internuclear axis ( $\Lambda = 0$ ).

### 1.1.5 SPIN-ROTATIONAL COUPLING

The coupling between the electron spin and the rotation of the nuclei requires including the following spin-rotational coupling term in the Hamiltonian.

$$H_{SR} = \gamma_{vN} \mathbf{S} \cdot \mathbf{N} \quad (1.6)$$

where the coefficient  $\gamma_{vN}$  depends on the specific rotational and vibrational state and can be expanded similarly to the Dunham coefficient.

$$\gamma_{vN} = \sum_{l,m} \gamma^{lm} \left(v + \frac{1}{2}\right)^l (N(N+1))^m \quad (1.7)$$

### 1.1.6 HYPERFINE STRUCTURE

When the nuclei has nuclear spin  $\mathbf{I}$ , it can couple to the electron spin  $\mathbf{S}$  and rotation of the nuclei  $\mathbf{N}$ , giving rise to the hyperfine structure of the molecules, with the Hamiltonian in the following form. In this Hamiltonian, the first term is the isotropic interaction between the electron spin and nuclear spin. The second term is the anisotropic interaction between the electron spin and nuclear spin. The last term is the interaction between the rotation of the nuclei and the nuclear spin. This term is usually very small and can be neglected.

$$H_{HF} = b_{vN} \mathbf{S} \cdot \mathbf{I} + c_{vN} S_z I_z + C_{vN} \mathbf{N} \cdot \mathbf{I} \quad (1.8)$$

Similar to the spin-rotation coefficient, the hyperfine coefficients in the form  $X_{vN}$  can



also be expanded similarly to the Dunham coefficient, described by a set of  $X^{lm}$  values.

## 1.2 OUR CHOICE OF MOLECULE : CaF

To achieve laser cooling of molecules, photons need to be absorbed and spontaneously emitted from the molecules. The key to successful laser cooling is repeating this scattering process many times, which requires returning the molecule back to the same internal state after a spontaneous emission event. This is known as photon cycling. It is easy to locate a photon cycling transition in alkaline or alkali earth atoms, but harder for diatomic molecules. Due to the rotational and vibrational degrees of freedom that are present in the diatomic molecules, one must suppress spontaneous emission into unwanted electronic ground states to achieve photon cycling.

For vibrational degrees of freedom, we care about the branching ratio from the electronic excited state to the different vibrational states in the electronic ground state, which is governed by the FCFs. When an electronic excited state has close to unity probability for returning to the electronic ground state without changing its vibrational quantum number, that is  $\langle \psi'_v | \psi''_v \rangle \approx 1$ , we call that a diagonal FCF. Since there are no selection rules for vibrational branching, to reduce loss from the photon cycling transition during the laser cooling of molecules, a diagonal FCF is desired. To obtain a diagonal FCF, two requirements must be met, the equilibrium distance of two the molecular potential must be similar, and the vibrational frequency of the vibrational states must be similar. If we take the two potentials in Figure 1.1 as an example, the FCFs of these two potentials are not diagonal at all, due to mismatch of both requirements. It would not be a good idea to choose these two vibrational states as a laser cooling transition. In special cases of some molecules, for example CaF, one electron of the calcium atom

forms the bond with fluorine atom, and the other electron is the dominant electron that interacts with external electromagnetic field. This unpaired electron stays close to the end of calcium and far away from the fluorine atom, for both the electronic ground state  $X$  and the excited states  $A$  and  $B$ , and hence has little effect on the bond length and vibration frequency. This results in a fairly diagonal Franck-Condon factor and opens the possibility of applying laser cooling to the molecule world<sup>36</sup>.

For rotational degrees of freedom, fortunately, branching between different rotational states obeys the angular momentum selection rules. By choosing an appropriate transition in the P-branch that connects  $J = 1$  and  $J' = 0$  in a simple diatomic molecule (rigid-rotor), the molecule always returns to the same initial rotational state (rotational closure).

CaF molecules are one of the choice of molecules that meet these requirements for laser cooling. Its properties are well studied in previous works. The full Hamiltonian of the  $X$  state of the molecule is

$$H_X = BN^2 + \gamma \mathbf{S} \cdot \mathbf{N} + b\mathbf{I} \cdot \mathbf{S} + cI_z S_z + C\mathbf{I} \cdot \mathbf{N} \quad (1.9)$$

Several important parameters of the molecule is described in the Table 1.1, compiled from 25, 27.

There are three electronic states that were used in our laser cooling scheme. In our experiment, the electronic ground state is  $X, ^2\Sigma$ . The first electronic excited state  $A, ^2\Pi_{1/2}$  state is used for magneto optical trapping and sub-Doppler cooling. The next higher electronic excited state  $B, ^2\Sigma$ , is used for slowing.

As we can see, the Franck-Condon factor between the  $X$  state and  $B$  state is highly diagonal. This is chosen for slowing due to higher photon momentum and lower re-

Constant	Value	Comments
$Y_{10}$ ( $\approx \omega_e$ )	17.647137THz	Vibrational
$Y_{01}$ ( $\approx B_e$ )	10 304.1447MHz	Rotational
$Y_{02}$ ( $\approx D_e$ )	0.014 060 MHz	
$\gamma_X^{00}$	39.6589 MHz	Spin Rotation
$b_X^{00}$	109.1840 MHz	Hyperfine
$c_X^{00}$	40.6471 MHz	
$C_X^{00}$	$2.907 \times 10^{-2}$ MHz	

**Table 1.1:** Useful molecular structure constants for CaF molecule.

quirement of repump lasers. To make it easier to repump vibrational states, it is desirable to find a slightly less diagonal transition. We choose to repump through the  $A$  state. The 3D magneto-optical trap (MOT) is realized on the  $X - A$  transition. We will show that the  $C$  state is used for background-free velocity sensitive detection during the chirp slowing.

In CaF molecules, due to the  $I = \frac{1}{2}$  nuclear spin on the fluorine atom, hyperfine structure is observed on CaF molecules. Since the wavefunction of the unpaired electron is closer to the calcium atom in the  $X$ ,  $A$  and  $B$  states, these hyperfine splittings are relatively small (on the order of  $\sim 10$  MHz) compared to many alkali atoms. This further complicates the energy level structures of CaF molecules due to the energy splitting between nearby states, which is close to the excited state linewidth  $\Gamma$ . The hyperfine splitting in the  $A$  state is below the natural linewidth of the  $X - A$  transition and thus not resolved. To drive a photon cycling transition between the  $X$  and  $A$  state, all the hyperfine levels must be addressed in the main cycling laser and the vibrational repump lasers.

### 1.2.1 CAF ZEEMAN STRUCTURE

The Zeeman shift is the energy shift of states due to an external magnetic field  $\mathbf{B}$ . Zeeman shifts can be written as  $H_{\text{Zeeman}} = (-g_S\mu_B\mathbf{S} - g_L\mu_B\mathbf{L} + g_I\mu_N\mathbf{I}) \cdot \mathbf{B}$ . Note that the external magnetic field  $\mathbf{B}$  is referenced to the lab frame, so one has to change into the molecular frame in order to evaluate this Hamiltonian. For the CaF X-state, since it is a  $\Sigma$  state,  $\mathbf{L} = 0$ , so the second term vanishes. The third term is small enough and can be ignored in most of the situations, due to the suppression of the coefficient  $\mu_N = \frac{\mu_B}{1836}$ . The first term can be further expanded in the expression below.

$$\begin{aligned}
 H_{\text{Zeeman}} &= (-1)^p (-1)^{F'-M'} \begin{pmatrix} F' & 1 & F \\ -M' & -p & M \end{pmatrix} \\
 & \quad (-1)^{J'+I+F+1} \sqrt{(2F+1)(2F'+1)} \begin{Bmatrix} J' & F' & I \\ F & J & 1 \end{Bmatrix} \\
 & \quad (-1)^{N+S+J'+1} \sqrt{(2J+1)(2J'+1)} \sqrt{S(S+1)(2S+1)} \begin{Bmatrix} S & J' & N \\ J & S & 1 \end{Bmatrix}
 \end{aligned}$$

Adding this to the molecular Hamiltonian, one can then diagonalize it to obtain the Zeeman energy levels and eigenstates. The Zeeman shifted energy levels are plotted in Figure 1.3.

### 1.2.2 CAF AC STARK SHIFT

The AC Stark shift is a frequency shift of internal states of an atom or molecule driven by an oscillating external electric field, e.g. a laser field  $\mathbf{E} = \frac{1}{2}E_0(\varepsilon e^{-i\omega t} + \varepsilon^* e^{i\omega t})$ . The

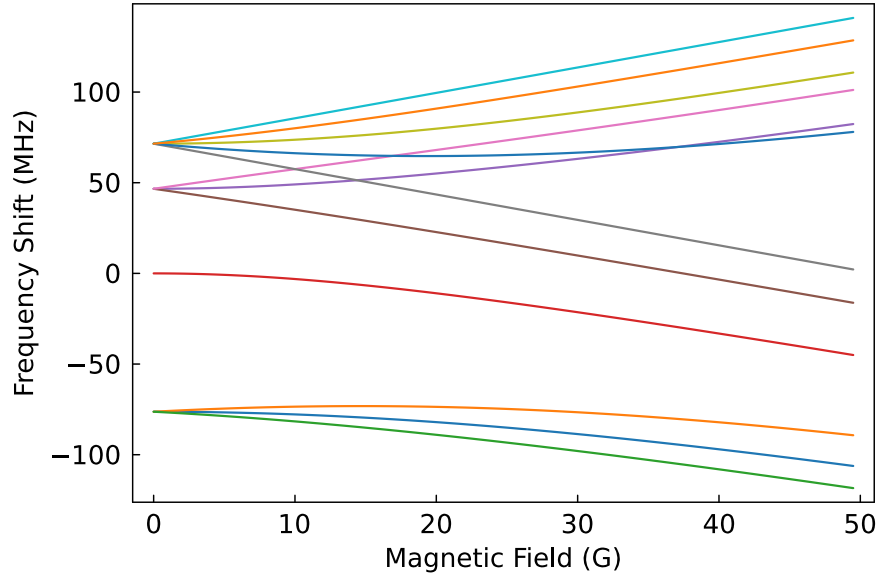


**Figure 1.3:** CaF X-state Zeeman shifts.

oscillating electric field polarizes the molecule, generating an induced oscillating dipole moment. The interaction between this induced dipole moment and the external field causes an energy shift. For the CaF X-state, when the energy shift is relative small compared to other energy scales, we can derive the Hamiltonian of the AC Stark shift using second-order perturbation theory<sup>22</sup>.

$$H_{\text{AC Stark}} = -\frac{E^2}{4} \sum_{K=0}^2 \sum_{P=-K}^K -(-1)^P \mathcal{A}_P^K \mathcal{P}_{-P}^K$$

In this expression,  $\mathcal{A}_p^K$  is the polarizability tensor and  $\mathcal{P}_{-p}^K$  is the polarization tensor.

$$\mathcal{P}_0^0 = \varepsilon \cdot \varepsilon^* = 1 \quad (1.10)$$

$$\mathcal{P}_0^1 = \varepsilon_1 \varepsilon_1^* - \varepsilon_{-1} \varepsilon_{-1}^* \quad (1.11)$$

$$\mathcal{P}_{\pm 1}^1 = \mp(\varepsilon_0 \varepsilon_{\mp 1}^* + \varepsilon_0^* \varepsilon_{\pm 1}) \quad (1.12)$$

$$\mathcal{P}_0^2 = -\frac{1}{2}(1 - 3\varepsilon_0 \varepsilon_0^*) \quad (1.13)$$

$$\mathcal{P}_{\pm 1}^2 = \frac{\sqrt{3}}{2}(-\varepsilon_0 \varepsilon_{\mp 1}^* + \varepsilon_0^* \varepsilon_{\pm 1}) \quad (1.14)$$

$$\mathcal{P}_{\pm 2}^2 = -\sqrt{\frac{3}{2}} \varepsilon_{\mp 1}^* \varepsilon_{\pm 1} \quad (1.15)$$

In the above expression,  $\varepsilon$  is the unit polarization vector of the light field and  $\varepsilon_{0,\pm 1}$  is its components in a spherical basis.

This can be further expanded and converted into the molecular frame following the angular momentum coupling scheme of Hund's case (b). The result is shown below.

$$H_{\text{AC Stark}} = -\frac{E_0^2}{4} \sum_{K=0}^2 \sum_{P=-K}^K \left[ -(-1)^P (-1)^{F-M} \begin{pmatrix} F & K & F' \\ -M & P & M' \end{pmatrix} \right. \\
(-1)^{J+I+K+F'} \sqrt{(2F+1)(2F'+1)} \begin{Bmatrix} J & F & I \\ F' & J' & K \end{Bmatrix} \\
(-1)^{N+S+J'+K} \sqrt{(2J+1)(2J'+1)} \begin{Bmatrix} N & J & S \\ J' & N' & K \end{Bmatrix} \\
(-1)^{N-\Lambda} \sqrt{(2N+1)(2N'+1)} \begin{pmatrix} N & K & N' \\ -\Lambda & 0 & \Lambda' \end{pmatrix} \\
\left. \alpha_K \mathcal{P}_{-P}^K \right]$$

In the above expression,  $\alpha_K$  is the polarizability in the molecule frame, where  $\alpha_0$ ,  $\alpha_1$  and  $\alpha_2$  are scalar, vector and tensor polarizabilities. For calculating AC Stark shifts in the  $X$  state in a near infrared (NIR) light field, it is usually sufficient to include the  $A$  state and the  $B$  state. Similar to the Zeeman Hamiltonian, by adding the above term and diagonalizing the Hamiltonian, we can include the effect of AC Stark shift in CaF molecules.

*The Doyle group's pathway to laser cooling...*

Doyle Group Gurus

# 2

## Magneto-optical Trapping of CaF Molecules

When you search "CaF" in your favorite chemical catalog, you will quickly realize there is only CaF<sub>2</sub> available and you cannot buy CaF off the shelf. The unpaired electron in CaF molecules makes it a radical. And many radicals are highly reactive and cannot quietly stay in your test tubes. To create CaF molecules, we utilize a chemical reac-



tion between laser ablated atomic calcium and sulfur hexafluoride ( $\text{SF}_6$ ) gas. The CaF molecules generated in this way have a very high rotational temperature and translational temperature. Since the laser cooling of molecules requires population in the  $N = 1$  rotational manifold, we have to cool the rotational degree of freedom. We would also like to have a low velocity molecular beam to start with, as this relieves the number of photons required during the laser slowing step. In this experiment, we start with a cryogenic buffer gas beam (CBGB) source. Specifically, we flow  $\text{SF}_6$  into the CBGB cell and laser ablate a solid calcium target, creating CaF molecules. These hot molecules are then cooled by collision with cold helium buffer gas and hydro-dynamically extracted from the cell, forming a slow and bright molecular beam of CaF with high population in the  $N = 1$  rotational manifold.

## 2.1 CRYOGENIC BUFFER GAS BEAM SOURCE

### 2.1.1 THE "BEAM BOX"

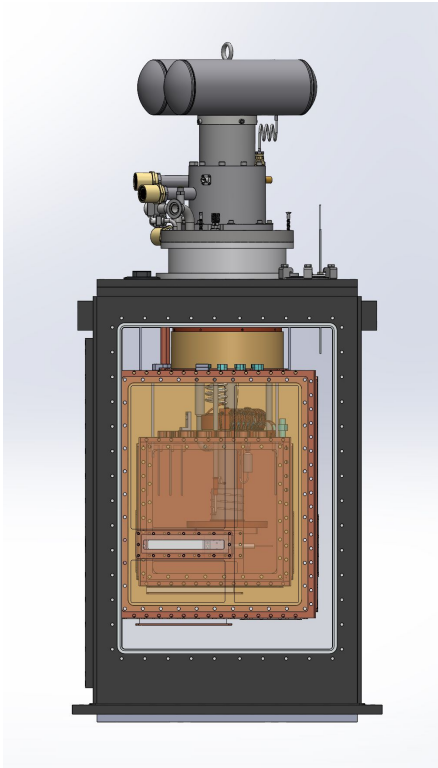
The CBGB source is kept inside a cryostat that we call it "beam box" for short. The cryostat is built around a Cryomech 1K cryocooler (Figure 2.1 (a)). This cryocooler is equipped with a standard Cryomech PT415 pulse tube cryocooler that is able to provide 45 W@40 K cooling power on its first stage and 1.5 W@4.2 K cooling power on its second stage. To reach a temperature closer to 1 K, a liquid helium pot is installed below the second stage of the pulse tube cryocooler. Helium gas from room temperature is flowed into a stainless tube which gradually cools the gas as the tube winds around the first stage regenerator, first stage heat exchanger, second stage regenerator and finally the second stage head exchanger of the pulse tube cryocooler. After the helium goes through the last counter-flow heat exchanger in the 1 K pot, the helium gas is then

throttled by a needle valve. The helium gas undergoes a Joules-Thompson (J-T) expansion process, where temperature is lowered further and helium gas is liquefied and collected in the 1 K pot. A circulation pump is pumping on the 1 K pot to maintain a low vapor pressure in the 1 K pot and cool the copper plate below the pot to a temperature  $< 2$  K when no heat load is presented. Note that the J-T expansion plays a crucial role in the operation of this system. When we monitor the pressure of the inlet and the temperature of second stage heat exchanger, we usually operate the system with a second stage heat exchanger temperature around  $\sim 4.5$  K and  $\sim 300$  Torr inlet pressure. Liquid helium boiling point at 300 Torr is  $\sim 3.37$  K, much lower than the 4.5 K provided by the pulse tube cryocooler, indicating no liquefaction could occur in the first place without additional cooling mechanism.

Based on this 1K cryocooler, we built a black-body radiation shield cooled to 40 K by the first stage of pulse tube, and another smaller black-body radiation shield cooled 4 K by the second stage of the pulse tube (Figure 2.1 (b)). The buffer gas cell is directly mounted below the 1 K stage of the cryocooler. The internal surface of the 4 K shield is covered by active coconut charcoal for adsorption of helium at a cryogenic temperature between 3 K and 10 K<sup>63</sup>. Additional charcoal sorb plates are installed in an arrangement resembling heat sink fins, hanging above the 1 K stage inside 4 K shield. Note that charcoal sorbs should only be installed on the 4 K shield, not on the 1 K stage. At a temperature below  $2 \sim 3$  K, the diffusion speed of helium from surface to bulk drops and the charcoal sorb becomes less effective<sup>76,23</sup>.

The buffer gas cell is shown in Figure 2.2. The buffer gas cell is made of Cu-101. It has a 1 in diameter bore that is 1.5 in long. The front aperture has a 6 mm aperture for beam extraction. The distance from the cell aperture to the 4 K front aperture is  $\sim 7$  in to avoid helium build up in the region of the molecular beam. A long snorkel is

(a)



(b)

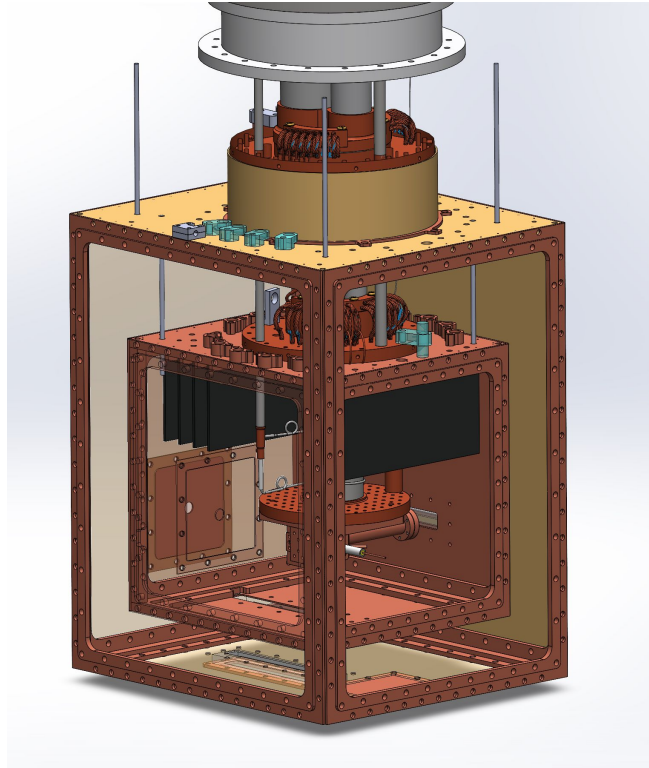


**Figure 2.1:** 3D model of the cryogenic buffer gas beam box.

used to move the ablation window far away from the calcium target. Our new design features a larger clear aperture ablation window and doubles the length of snorkel. The new design further reduces coating of ablated calcium on the window and ensures long term stability of the ablation. Larger clear aperture allows raster scanning of the ablation spot over a large  $1\text{ cm} \times 1\text{ cm}$  calcium target. The helium buffer gas is flowed into the cell through the copper tube located on the center of the back plate. A diffuser is used to better thermalize the helium gas and reduce turbulence of the flow. The  $\text{SF}_6$  gas is flowed through the heated nozzle that is thermally insulated from the buffer gas cell through a long Teflon tube. The Teflon tube is rigid enough to snugly fit onto the copper tube on the back plate and automatically align the nozzle to the center of the copper tube.

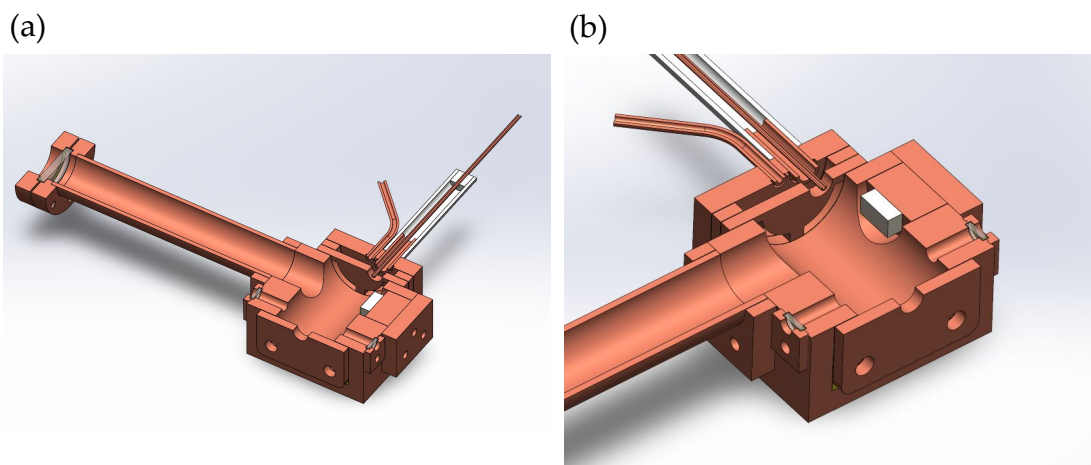


**Figure 2.2:** (a) Cross section view of the buffer gas cell 3D model. (b) Zoom in for details.

A UHV shutter is mounted on the front panel of the beam box and is used to prevent helium buffer gas from leaking outside of the beam box, which will degrade the vacuum in the UHV section of the experiment. This is not a very reliable mechanical device,

and the quality varies a lot from batch to batch. The common failure mode is one of the blades becoming open or stuck close. It would be an improvement of the apparatus if a new UHV shutter based on closed loop motion control is developed.

## 2.2 ULTRA-HIGH VACUUM SYSTEM

The ultra-high vacuum (UHV) system for the CaF Gen2 experiment is quite similar to a standard ultracold atom experiment, except for some challenges due to the CBGB source. The UHV section is divided in three sections by the stainless steel differential pumping apertures. These apertures have a hole diameter of 1/2-inch, and are mounted using groove grabbers onto the ConFlat flanges. This gives three stages of attenuation of residual helium buffer gas into the science glass cell. The 3D rendering of the setup viewed from the top is shown in Figure 2.3.

### 2.2.1 INTERMEDIATE PUMPING CHAMBER

The first section is an intermediate pumping chamber (MCF450-SphSq-E2C3r1A4, Kimball Physics), which is pumped by a turbomolecular pump with 350 L/s nitrogen pump speed (HiPace 350, Pfeiffer). The intermediate pumping chamber is connected to the beam box through a flexible edge-welded bellow, since the beam box is referenced to the floor but the chamber is referenced to the optical table.

### 2.2.2 MOT CHAMBER

The second section is the main MOT chamber (MCF800-SphSq-G2E4C4A16, Kimball Physics), hosting the in-vacuum RF MOT coil. The chamber is pumped by a titanium sublimation pump (TSP, Gamma Vacuum) and a turbomolecular pump with 550 L/s

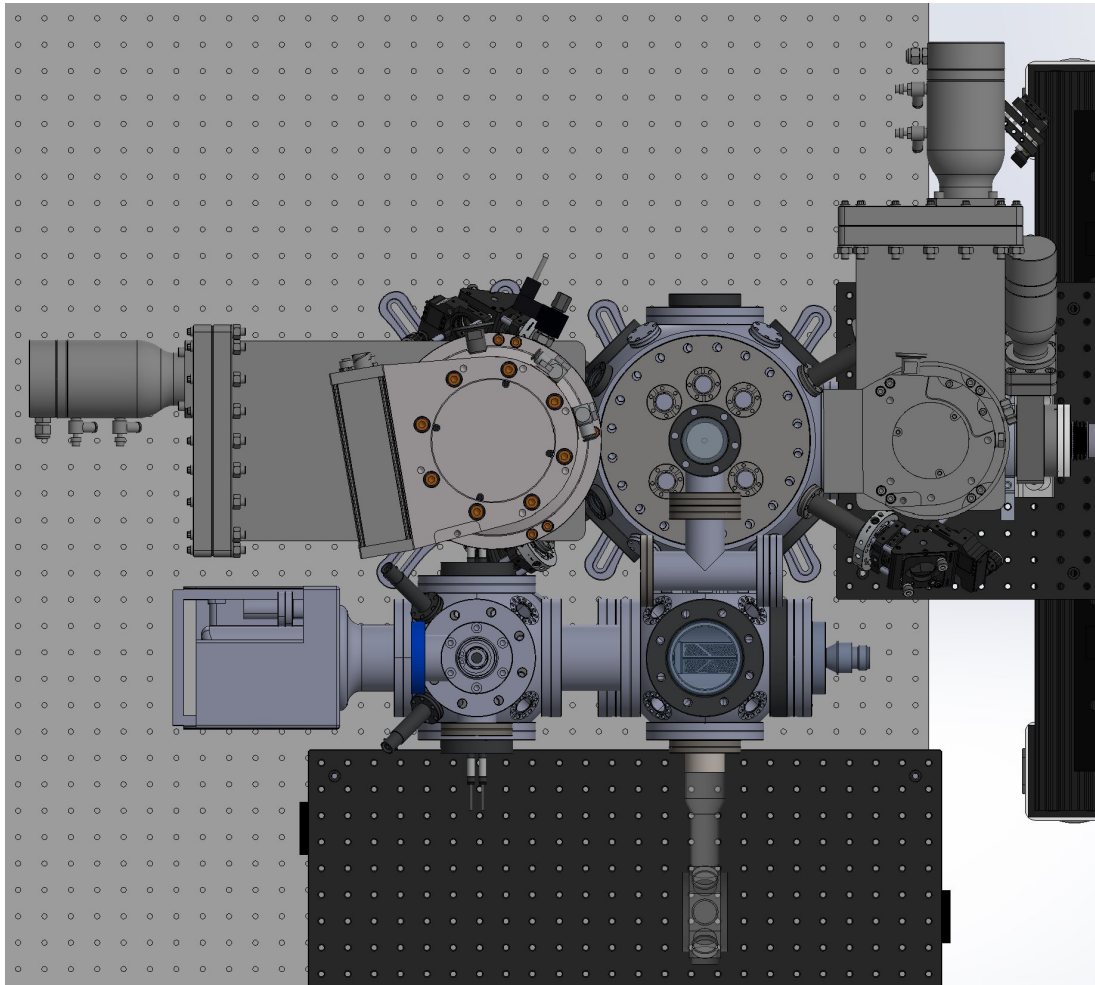


Figure 2.3: 3D rendering of the UHV system viewed from the top.

nitrogen pump speed (Turbo-V 551 Navigator, Agilent). Both turbomolecular pumps are installed to the chamber through vibration dampers and pneumatically controlled gate valves. They are then backed by another turbomolecular pump station (HiPace 80 Eco, Pfeiffer) at a vacuum pressure around  $1 \times 10^{-7}$  Torr. By connecting turbomolecular pumps in series, we can get a very high compression ratio for the helium gas. This also allows us to use a quiet and long lifetime diaphragm pump in the pump station for backing the whole system. All turbomolecular pumps and roughing pumps are powered by uninterruptible power supply (UPS).

The RF MOT coil is constructed by direct bonding copper onto AlN ceramic. The conductors are then gold plated for preventing oxidation and better electrical contact. This design is UHV compatible, allows for high temperature baking, and provides good cooling to the coil (Figure 2.4). Coils are mounted on electrical feedthroughs that were used for both mechanical support and thermal management. Both top and bottom coils are paired with a resonant tank circuit and are impedance matched to a 1 kW homemade RF amplifier at 1 MHz. The top and bottom coils are spaced by  $\sim 20$  mm, with elliptical holes cut to allow up to 2 mm diameter laser beams reaching the MOT region through small angled mini-CF viewports on our vacuum chamber. We are able to reach a maximum of 60 G/cm RMS magnetic field gradient on the vertical direction with 12 A RMS current in the coil. Details of the construction of this setup can be found in Appendix F.

### 2.2.3 GLASS CELL SECTION

The third section is the glass cell section, where the glass cell and a port expander chamber is connected to an interconnect chamber (MCF450-SphCube-E6A8, Kimball Physics). Custom length nipples and close couplers are used to assembly this section for maximum conductance and minimum distance between glass cell and MOT cham-

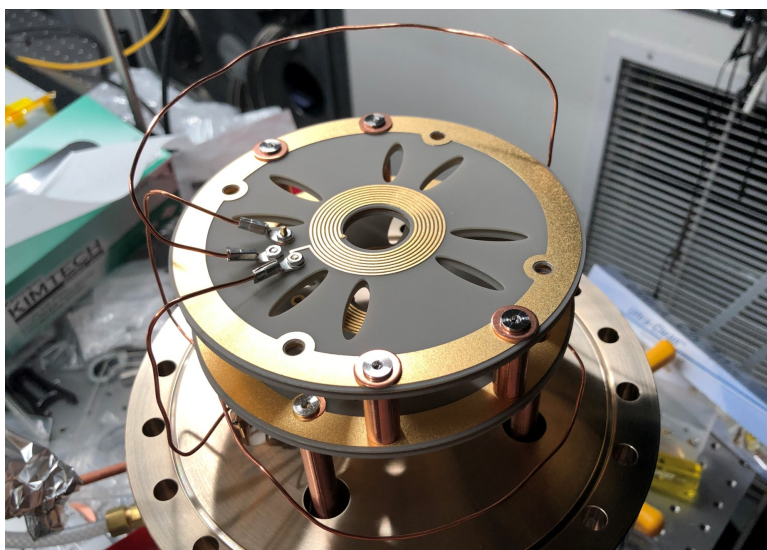


**Figure 2.4:** Assembled in-vacuum RF MOT coils. Coils are upside-down in this photo, since the supporting feedthroughs are supporting the coils from the top once installed into the MOT chamber.

ber. Their large sizes make it possible to upgrade the experiment in the future by inserting electrodes and cryogenic shields into the glass cell. There is a non-evaporable getter (NEG) pump (CapaciTorr Z400, SAES) installed below the interconnect chamber for pumping all the residual gases except noble gases. A second chamber of the same model is used as a port expander to accommodate an ion gauge (UHV-24p, Agilent), an ion pump (VacIon Plus 55 StarCell, Agilent), and future electrical feedthroughs for the electrodes. Initial pumping down is through an all-metal angle valve installed on this chamber.

The whole chamber is assembled in stages. At the beginning, we only have the intermediate pumping chamber and MOT chamber installed. The whole UHV section is baked to  $150^{\circ}\text{C}$ . We then extended the MOT chamber to a temporary chamber after successful demonstration of short distance round trip transport. Finally, the glass cell section is installed, and the newly added sections are baked to  $150^{\circ}\text{C}$ .



The glass cell is constructed by mounting high quality fused silica windows onto a precisely machined fused silica octagonal frame (Precision Glass Blowing of Colorado). The pieces are attached to each other using glass frit bonding technique, where the glass cell has to be heated up to 900 °C. Since the frame and windows are made from the same material, the stress on the window is minimized and the surface flatness of the windows is maintained. The glass cell frame is then adapted to a fused silica tubing, which is then enlarged and transitioned into Pyrex, and finally to a 316L stainless steel ConFlat flange using a non-magnetic glass to metal transition. The primary window has a 3-inch diameter and 1/4-inch thickness. The fused silica tubing is designed as large as possible to accommodate a structure with 24 mm diameter to be inserted into the glass cell. The glass cell received is shown in Figure 2.5.

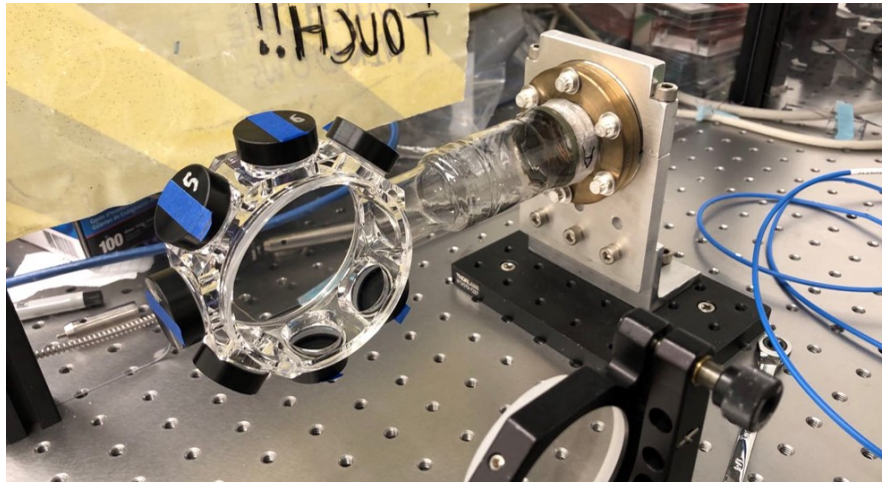


**Figure 2.5:** Nano-textured coated 3-inch octagonal glass cell.

Many dielectric anti-reflection (AR) coatings cannot withstand the high temperature required to assemble this glass cell. Due to various laser wavelengths that we might use in the future, it is also hard to predict which AR coating to apply where on the glass cell during the design stage. We chose to apply nano-textured AR coating to our

glass cell. This coating works by etching nanometer scale pyramid-like structures on a fused silica substrate, which effectively modulate the refractive index of the material. These structures make an adiabatic transition of the effective refractive index from bulk fused silica to air, eliminating reflections. However, by just arranging these structures in an array, diffraction of light would occur at specific angles. This technology solves this issue by randomizing the structure pattern (making the surface look like mountains in Guilin, Guangxi, China), giving the name "RAR" (Random AR) of the coating. We would like to note that this technology does not come without a cost, as the nano-textured surface does increase the scattering when a laser beam is transmitted through the surface. Due to the nano-textured structure, any contamination would degrade the AR performance and would be hard to clean. Because of this, it is strictly forbidden to touch the surface with bare hands.

To bake the glass cell section, special care must be taken not to crack the glass cell or contaminate the nano-textured coating. We made a stainless steel cage around the glass cell, wrapped with aluminum foil and heating tape. This ensures that the glass cell is heated by radiation and convection. The temperature of the glass cell is measured by attaching thermocouples along the glass tubing from the glass cell to the vacuum flange. We closely monitor the temperature gradient across the glass to metal transition as the temperature is ramping up and down.

### 2.3 LASER SYSTEMS FOR MOT

As a major advancement of the Gen 2 experiment, we transition our laser system to all solid-state based lasers. All the lasers on the experiment are locked to wavelength meter (wavemeter, for short) and operate  $24 \times 7$  without any human intervention (Ap-

pendix H). This makes it possible to run the experiment unattended in the future and greatly increase the data collection efficiency. As you will see in this section, thanks to the development of high power single frequency polarization-maintaining fiber amplifiers, only four amplifiers are required to create all the required lasers for realizing a MOT of CaF molecules.

### 2.3.1 X-A LASER (606 NM)

A Raman fiber amplifier (RFA) is used to generate up to 4 W at 606 nm for driving the X-A  $v = 0$  to  $v' = 0$  transition. The amplifier is seeded by an external cavity diode laser (ECDL) (DL pro, Toptica) tuned to 1212 nm. Dual MgO:PPLN crystals are used after the RFA to convert the high power 1212 nm laser light into 606 nm. The RFA and frequency doubling module is provided by Precilasers as a system.

We have tried to lock the beat note frequency between the 606 nm output of the RFA and our single frequency OPO used in the first generation of the experiment, in the hope that it will enable fast and precise frequency hopping and eliminate the need of a double pass AOD. Unfortunately, due to the delay time introduced by the very long passive Raman fiber used in this specific RFA, a phase lock cannot be obtained and only frequency stabilization is possible. We later switched back to the double pass AOD setup for fast frequency hopping. This scheme could be realized nicely if beat note frequency lock on the 1212 nm seed laser is possible (with a frequency stabilized 1212 nm laser or a frequency comb). As we will see in the next subsection, this fast beat note frequency hopping scheme is successfully realized in our 531 nm laser system.

The 606 nm laser after the double pass AOD is then fiber coupled and delivered to a board ("Hyperfine Board"). Here, 606 nm is combined with  $v = 1$  repump lasers and polarization switched by a Pockels Cell (Conoptics 350-160 with 25D driver). The

combined light is then split and goes through various AOMs to create sidebands for CaF hyperfine levels, finally combined using a 4x4 PM fiber combiner (Evanescent Optics). Three of the output ports of the fiber combiner are used for three MOT beams, and the last port is connected to a small free space splitter board to generate four fiber coupled outputs, with three being used as imaging beams for the glass cell side, and one left for future use. The hyperfine board layout are shown in Figure 2.6.

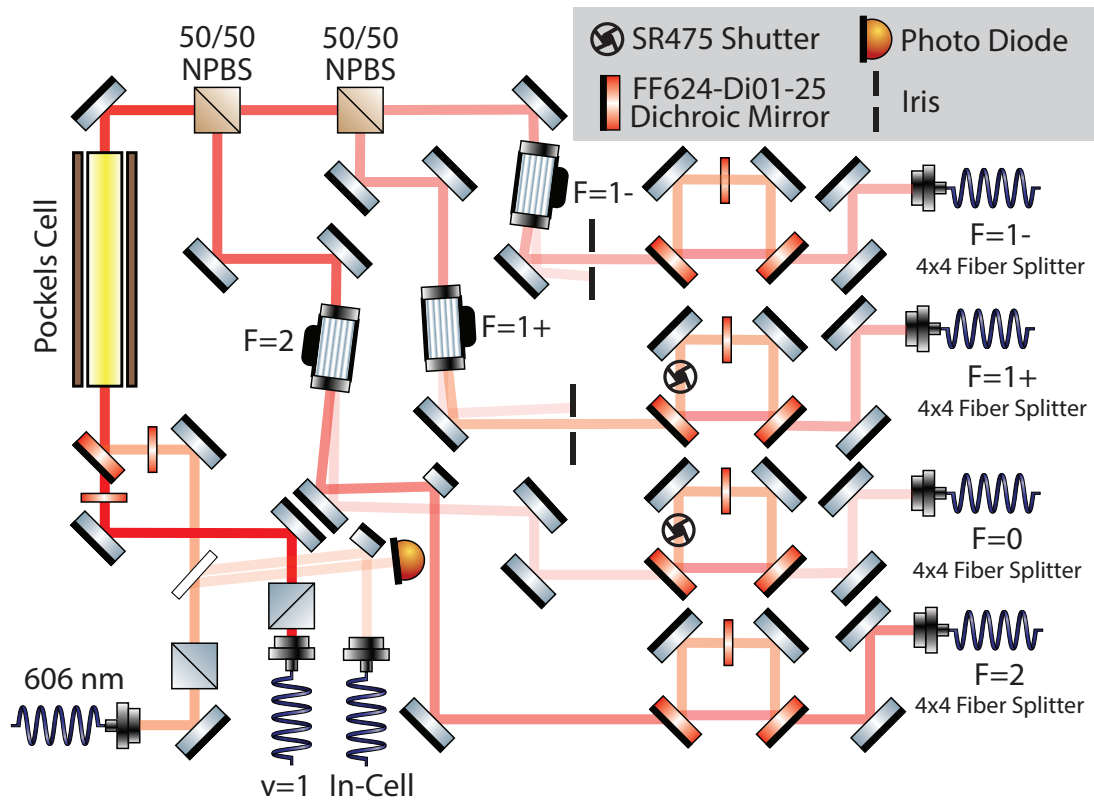


Figure 2.6: "Hyperfine board" setup

### 2.3.2 X-B LASER (531 NM)

We use a high power polarization-maintaining ytterbium doped fiber amplifier (PM-YDFA) seeded by a 1062 nm single frequency seed laser. The amplified light is then passed through a MgO:PPLT crystal to generate up to 10 W of 531 nm light. The PM-YDFA and frequency doubling module is provided by Precilers as a system.

This laser system is also used for the optical pumping step in the Raman sideband cooling. To achieve fast and precise frequency sweeping and frequency hopping between slowing detuning and OP detuning for RSC, a beat note frequency locking (also known as optical phase lock loop, OPLL) scheme is implemented, as shown in Figure 2.7. We use a 1062 nm NKT Photonics fiber DFB seed laser as our reference laser. This laser is amplified to the  $\sim 100$  mW level and then frequency doubled using a waveguide PPKTP doubler (AdvR). The resulting 531 nm output is delivered to our wavemeter locking system to stabilize the frequency of the 1062 nm reference laser at 282.288 750 THz (reading on our uncalibrated wavemeter). The reference laser is power split using PM fiber splitters and a small portion of the power is combined with a 1062 nm DBR diode laser (PH1062DBR080BF-ISO, Photodigm) using PM fiber combiners to create a beat note signal  $\sim 2.57$  GHz. This beat note signal is detected using a fast photodiode (DETo8CFC, Thorlabs), frequency divided by 8 times by an RF pre-scaler, and 5 times by the internal divider of the phase lock loop (PLL) chip (ADF4002, Analog Devices). This signal is then compared with an external reference clock in the frequency range of  $\sim 65$  MHz by the PLL to feedback on the DBR diode driving current. The DBR diode is used as a seed for the YDFA to generate high power 531 nm laser. By tuning or switching the frequency of the external reference clock, one can hop the laser frequency quickly and precisely in less than 1 ms. We use a voltage-controlled oscillator (ZOS-100,

Mini-Circuits) to control the laser frequency during slowing, and switch to a Siglent signal generator for Raman sideband cooling optical pumping.

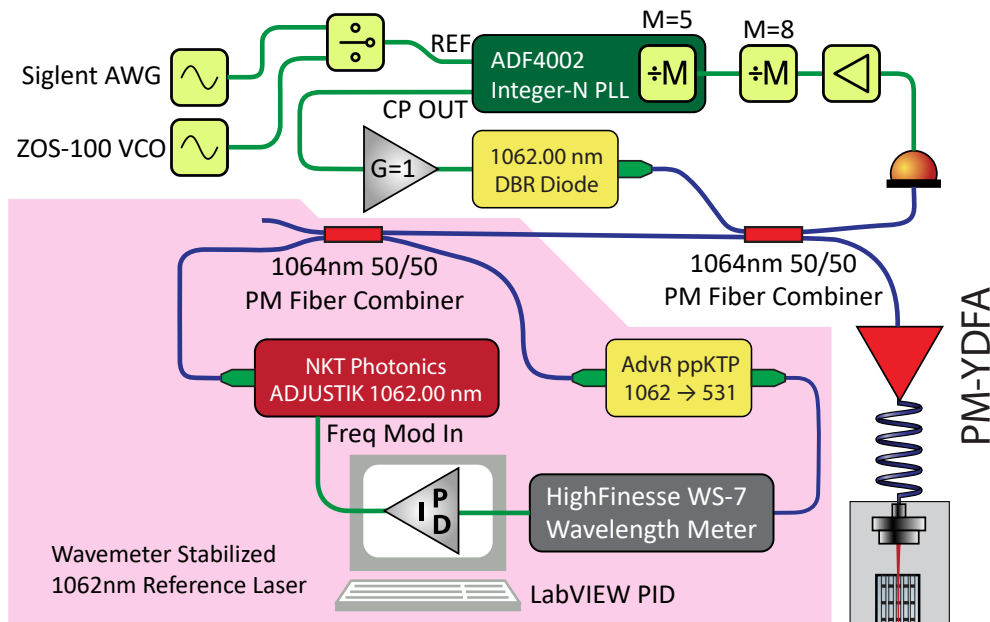


**Figure 2.7:** Beat note lock (OPLL) setup.

High power 531 nm brings issues with many optics, where special precautions must be taken. The beam out of this laser has a diameter of 0.5 mm, which is relatively small (due to the limited space inside the frequency doubling head; long focal length lenses are hard to be fitted in). Sending this beam directly into an AOM made of flint glass gives us very pronounced thermal lensing at a power just above 2W. Going to full power will create a focus roughly 20 cm away from the AOM, which can be easily observed by eye, and is not acceptable at all. A normal half inch polarization beam splitter (PBS) cube also shows thermal lensing, and the optical cement used to glue the two prisms might be damaged. We solve this issue by placing a 2x telescope close to the laser aperture, switching to a quarter inch optically contacted fused silica PBS cube and a high

power quartz AOM (Gooch&Housego AOMO 3080-394). Note that quartz AOMs usually require higher RF driving power than a flint glass or TeO<sub>2</sub> AOM. The RF driving power required for an AOM follows a quadratic relation to the wavelength of the laser. The quartz AOM we used requires about 5 W of RF driving power at 532 nm, which would scale up to 20 W when designed for 1064 nm (water cooling of the AOM would then be mandatory). 5 W of heat dissipation on the AOM is still manageable by conductive cooling through the base plate and air convection, especially since this AOM is only turned on for less than 10 ms in a single experimental run. Care should still be taken when turning on this AOM continuously for laser beam alignment. Another note is that a quartz AOM only meets its high diffraction efficiency specification when input light is linearly polarized in the correct direction according to the data sheet (in our case, 90° relative to the mounting plate). The perpendicular direction will still provide diffraction, but first order diffraction efficiency will be very low.

The slowing beam path is shown in Figure 2.8. To provide some confinement on the radial direction during slowing, the slowing beam is slightly focused to cover a diameter  $\sim 18$  mm at the MOT coil center and  $\sim 6$  mm at the CBGB cell aperture.

### 2.3.3 VIBRATIONAL REPUMP LASERS (628 NM)

In the first generation of CaF experiment, two dye lasers are used to provide the  $v = 1$  repumps, where one is for MOT repumping and one for slowing repumping. Two injection locked diode lasers seeded by two homemade ECDLs are used for  $v = 2$  repump and  $v = 3$  repump. It is challenging to maintain the operation of a single frequency 628 nm diode laser, since this wavelength is hard to reach for semiconductor gain mediums. The closest laser diode available (HL63163DG, Ushio) is specified at 633 nm 100 mW at room temperature. Pulling the peak of the gain profile towards

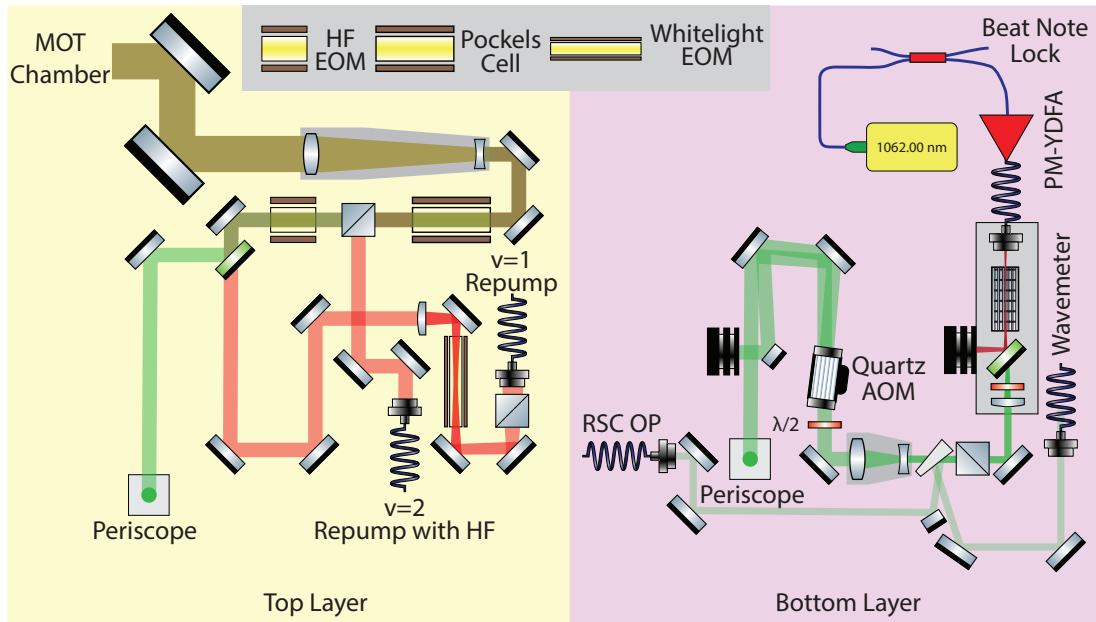


**Figure 2.8:** Slowing optical beam path. The Pockels cell here is a Conoptics 350-80 electro-optic phase modulator angled at  $45^\circ$  to scramble the polarization.

shorter wavelength requires cooling close to the dew point, which complicates the laser setup and risks damaging the laser diode or shortening its lifetime. The injection lock system also suffers from frequent unlocking due to low gain from the diodes and insufficient seed power.

Because of these bad experiences, we decided to switch to a complete solid state system that is based on state-of-art single frequency fiber lasers and sum frequency generation (SFG) using nonlinear optical crystals. 628 nm sits just around the sweet point that it is the sum frequency of 1540 nm and 1053 nm. These wavelengths are close to the peak of the gain curve of erbium and ytterbium doped active fibers, where high power single frequency fiber amplifiers are available. The sum frequency generation process can then be efficiently realized in a bulk MgO:PPLN crystal under a quasi-phase matching (QPM) condition.



We first built one SFG system to replace the two dye lasers used for the  $v = 1$  vibrational repumps. Over 7.5 W power is obtained without much optimization effort. The setup consists of two 10 W fiber amplifiers and a 40 mm long MgO:PPLN crystal from Covision. This power is more than enough to support both generations of CaF experiments at that time.

However, this does not solve the instability problem of the  $v = 2$  and  $v = 3$  injection locked diode lasers. The need for power of the  $v = 2$  and  $v = 3$  vibrational repump is not that high compared to  $v = 1$ . From our experiences learned in the first generation of the experiment, power on the order of 20 mW is enough for the  $v = 2$  repump and 5 mW is enough for the  $v = 3$  repump in a typical CaF MOT setup. Ordering additional fiber amplifiers just for these low power repumps is not an economical option. Instead, we try to see if it is possible to seed a single fiber amplifier with multiple frequency lasers. It is expected that there are gain competition and four-wave mixing between the seed frequencies, but we still have to test our own amplifiers. We measured the amplifier output with an optical spectrum analyzer and confirmed that these issues will not affect our application. The test result is shown in Figure 2.9. As we can see, four-wave mixing is clearly visible after the amplifier, but kept at a relatively low level. We also see that for the two frequency seed input, the output power ratio between the seed is not proportional to the input power ratio, presumably due to gain competition. For example, to reach an output power ratio of 2:1, an input power ratio of 1.5:1 is needed.

We use several PM fiber combiners to combine three DFB diode seeds (QDFBLD-1550-50N or QDFBLD-1550-10, Q-Photonics). These DFB diodes are relatively cheap because their wavelengths lie in the popular telecommunication band. On the SFG breadboard, we add a second and a third MgO:PPLN crystal after the first one. Sum

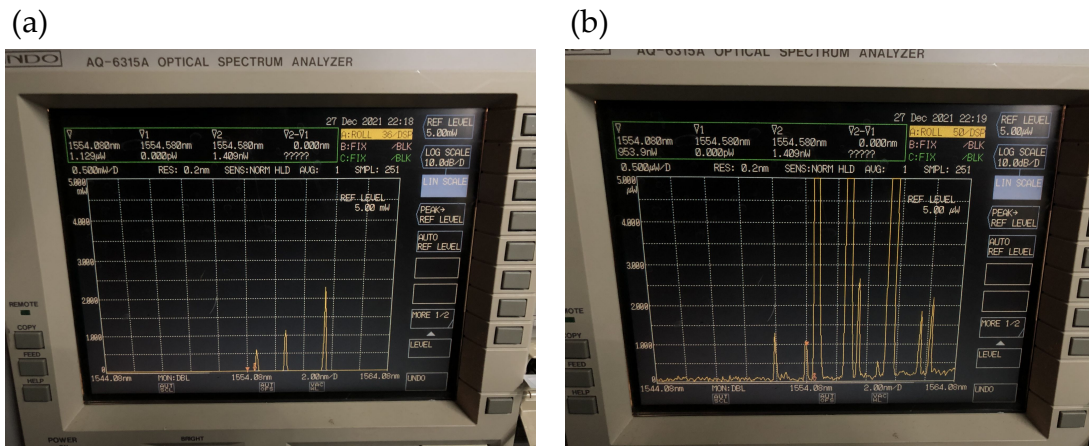


**Figure 2.9:** (a) Optical spectrum of the output of the C-band PM-EDFA (EAR-10-C-LP, IPG Photonics) with three seeded input. (b) Four wave mixing peaks can be seen when vertical sensitivity is increased, but they are small and will not affect the SFG.

frequency converted visible light is separated out using a dichroic mirror, before the residual infrared pump power is sent into the next crystal. The picture of the full setup as well as the schematic of the optical layout are shown in Figure 2.10.

This system successfully produces  $> 3$  W power of  $v = 1$  repump,  $> 250$  mW of  $v = 2$  repump and  $> 50$  mW of  $v = 3$  repump with 7W of total 1053 nm and 7W of 1550 nm amplifier. The slightly lower overall efficiency is due to beam quality degradation after the IR beams pass through several MgO:PPLN crystals (mostly astigmatism and focal shift between 1.5  $\mu$ m and 1  $\mu$ m laser beams). We deliberately arrange the crystals so the IR are going through the  $v = 1$  crystal first,  $v = 2$  second and  $v = 3$  at the end, since  $v = 1$  demands the highest power and high conversion efficiency is beneficial. Nevertheless, this is more than enough to run a single CaF laser cooling experiment, and will be more than enough to support two experiments if both amplifiers are turned up to full power. In the past 4 years of continuous running of this system, no major issue has

been observed from the SFG system \*. The triple seeded SFG system maintains good output power without any realignment after being put into service.

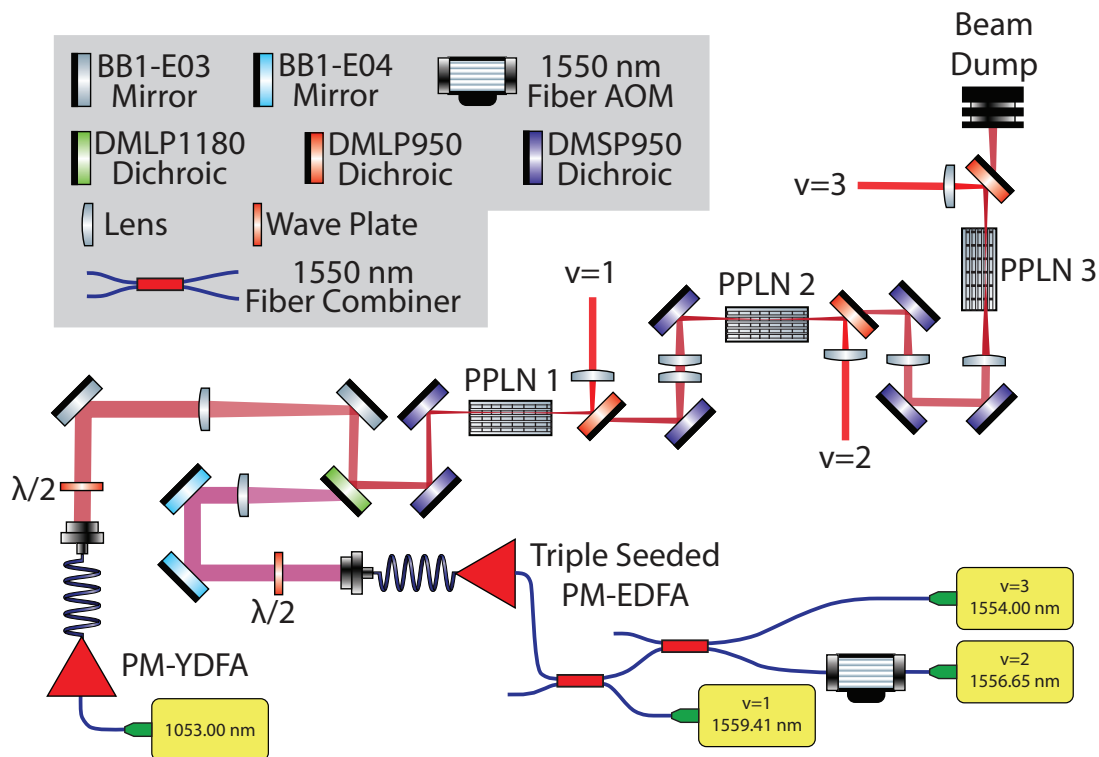


**Figure 2.10:** Triple seeded SFG setup

The  $v = 1$  repump is crucial to the slowing step. It is estimated that scattering more than  $1 \times 10^4$  photons are needed to slow CaF molecules from  $\sim 160\text{m/s}$  to zero velocity. On the  $X - B$  transition that we used for slowing, and with the  $v = 1$  repump, an average of  $2 \times 10^4$  photons can be scattered per molecule. The  $v = 1$  repump is split into two paths. Light in one path is frequency shifted down by 110 MHz and frequency broadened by a “white light EOM” and hyperfine EOM to  $\sim 500$  MHz bandwidth. The

\*other than a NP Photonics 1053 nm fiber amplifier suddenly deciding to kill its output fiber facet. This amplifier is later replaced by a new 15 W Precilasers fiber amplifier. Details of our “adventure” with NP Photonics lasers can be found in Loïc Anderegg’s thesis.

$v = 2$  repump is simply sent through a hyperfine EOM and illuminate the MOT region along the slowing beam path. The  $v = 3$  repump is also sent through a hyperfine EOM and shot into the MOT chamber through one of the mini-CF ports.

The “white light EOM” is a resonant EOM at  $\sim 5$  MHz with a very large modulation index, creating a comb like series of sidebands on the laser. Since the spacing between comb teeth is smaller than the linewidth of the transition, this light effectively looks like a broadband white light to the molecules. The use of white light broadening to cover a range of frequencies is more efficient than relying on power broadening. This can be easily seen by comparing the scaling. The same principle can be applied to the process of spectroscopy, where one is trying to locate a relatively narrow transition in a large range of frequencies.

The hyperfine EOM is a resonant EOM at 25 MHz with a modulation index  $\beta \approx 3.83$  to add sidebands to the laser, so it can efficiently address all required hyperfine levels for CaF molecules. Details of the design and construction of the “white light EOM” and “hyperfine EOM” can be found in Appendix C.

#### 2.3.4 SEQUENCE CONTROL SYSTEM

The experiment is controlled by several pieces of software. The sequence of the experimental run is controlled by Cicero Word Generator<sup>69</sup>. The housekeeping of the beam box and analog signal acquisition is controlled by a custom LabVIEW program. The camera images are acquired by a custom Python program based on PyQt. Details of the experimental control software can be found in Appendix E.

## 2.4 LASER SLOWING OF CaF

CaF molecules from the CBGB move at a high initial forward velocity  $\sim 160$  m/s. Shooting a laser beam counter-propagating against the molecular beam provides momentum kicks to the molecules when a photon is scattered. Due to the Doppler shift, a single frequency laser can only address a small portion of the velocity class in the molecular beam. In this experiment, we use frequency chirped slowing to track the Doppler shift and slow the molecular beam to less than the MOT capture velocity (estimated to be  $\sim 10$  m/s).

There are five parameters that have to be optimized: start frequency of the chirp, end frequency of the chirp, chirp duration, start time of the chirp and the shape of the chirp. The chirp start frequency determines the highest velocity class of molecules that we can slow. The chirp end frequency should be chosen so molecules do not get slowed beyond zero velocity and pushed back towards the beam box. The chirp duration should be optimized by matching the maximum scattering rate. The start time of the chirp is optimized so the peak of the pulse of molecules are slowed to zero velocity right at the moment of reaching the MOT capture volume. The frequency chirp is linear, since our goal is saturating the scattering rate, which should result in a constant acceleration.

## 2.5 3D RF MOT OF CaF

Rotational closure in laser cooling of molecules requires one to work with optical transitions in an inverted angular momentum structure, where the number of excited states is smaller than or equal to number of ground states. This is also known as type-II transitions, for example,  $J \rightarrow J' = J - 1$  or  $J \rightarrow J' = J$ . Dark states exist in this type of transitions. One of the challenges for laser cooling of molecules is destabilization of

these dark states. There are two well established methods to realize this. One is using a dual frequency effect to create a DC MOT<sup>11</sup>. The other is switching the magnetic field gradient and laser polarization at the same time to actively destabilize the dark states, which is called an RF MOT<sup>62,94,4</sup>. RF MOT is chosen for this experiment due to our experience that the RF MOT captures more molecules than DC MOT and allows reaching lower temperature and higher density.

To efficiently destabilize the dark states, the RF MOT magnetic field must be switched at a frequency that is on the scale of the scattering rate ( $\sim$  MHz). To achieve this high frequency, the in-vacuum RF MOT coil forms a LC tank circuit with a variable capacitor that tunes to be resonant at 1MHz. The tank circuit is then impedance matched to  $50\ \Omega$  and then driven by a homemade 1kW RF power amplifier. There are two pairs of the RF MOT coils, forming an anti-Helmholtz configuration to create the magnetic field gradient required by the MOT. The polarization of the MOT beams is switched by the Pockels cell at the same frequency, with an adjustable phase shift from the MOT coil driving signal to compensate cable and driver delays. By scanning this phase shift, one can switch between MOT and anti-MOT configurations.

We observed up to  $\sim 10^6$  molecules captured in the RF MOT on the CaF Gen2 experiment. The picture for the CaF RF MOT is shown in Figure 2.11, where (a) is taken with an EMCCD camera and (b) is taken with a Google Pixel (photo credit goes to Loïc Anderegg). This is almost an order of magnitude higher than the first generation of the experiment, making it visible to the human eye. We attribute the improvement to higher slowing beam power which minimizes the slowing distance and larger diameter MOT beams which increase the capture volume and capture velocity.

The CaF RF MOT is relatively hot when it is initially loaded. We measure the temperature using the time-of-flight method, where the trap is turned off for a variable time

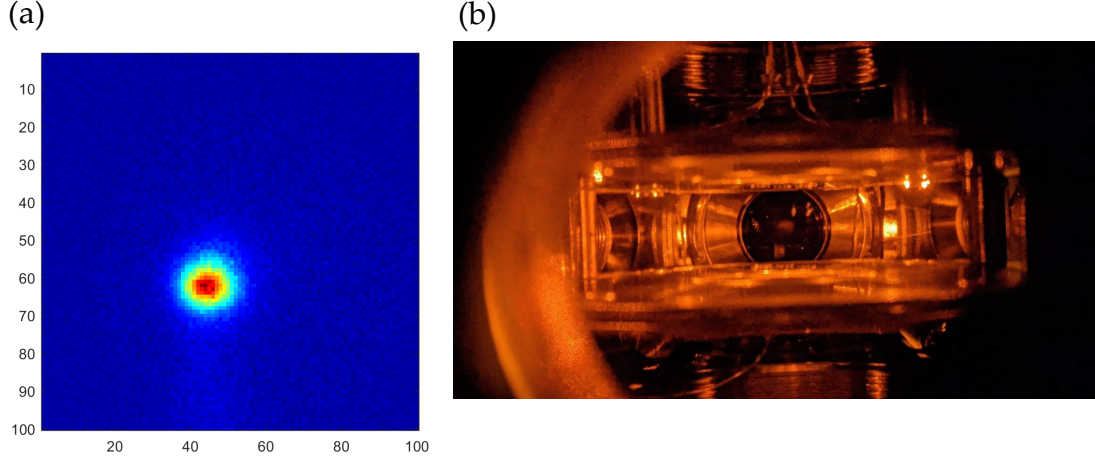


**Figure 2.11:** (a) CaF RF MOT picture taken with EMCCD camera. (b) CaF RF MOT picture taken with a Google Pixel phone camera.

$t$ , and a short resonant imaging pulse is used to take a snapshot of the density distribution of the expanding molecular cloud. One would find that at the expansion time  $t$ , the fitted cloud width  $\sigma_t$  follows the relation  $\sigma_t^2 = \frac{k_B T}{m} t^2 + \sigma_0^2$ , where  $m$  is the mass of the molecule,  $k_B$  is the Boltzmann constant, and  $\sigma_0$  is the cloud width at  $t = 0$ .

In a red detuned RF MOT using a Type-II transition, the counter-propagating laser beams creates a spatially varying potential for the molecules stays in bright states due to AC Stark shift, while the molecules in dark states are not affected. The molecules in bright states are accelerating down the potential hill while approaching the peak intensity. They are then preferentially optical pumped into the dark state near the peak intensity area. These molecules in dark states then move across the zero intensity area and non-adiabatically return to bright states. This process causes Sisyphus heating in the CaF RF MOT, where a higher MOT beam intensity results in a higher temperature<sup>94</sup>. This effect can be exploited as Sisyphus cooling by flipping the detuning, as we will see

in the next section<sup>119</sup>. For the red detuned RF MOT, by ramping down the intensity after initial loading, the temperature greatly reduces to below 500  $\mu\text{K}$ . Further ramping up the magnetic field gradient helps compressing the RF MOT to a smaller size of  $\sim 600 \mu\text{m}$ . This becomes a good starting point of sub-Doppler cooling of the molecules detailed in the next section.

## 2.6 $\Lambda$ -ENHANCED GRAY MOLASSES OF CaF

As we have discussed in the last section, by switching the laser to be blue detuned, Sisyphus heating effect turns into Sisyphus cooling and shows the capability of cooling the molecules below Doppler limit<sup>119</sup>. We further improve this method by leaving only  $F = 2$  and  $F = 1-$  components in the cooling beam. This forms a coherent dark state through two-photon a  $\Lambda$  system at zero velocity. The velocity sensitive coherent population trapping (VSCPT) effect then rapidly cools the molecules down to 10  $\mu\text{K}$  in free space. We called this cooling configuration  $\Lambda$  cooling for short. This is similar to previously reported performance of  $\Lambda$ -cooling on CaF molecules<sup>26</sup>. The scattered spontaneously emitted photons can be collected by imaging optics on a camera ( $\Lambda$ -imaging).

For most of sub-Doppler cooling schemes, a dark state is present, and it is important to stabilize the coherent dark state. This also applies to  $\Lambda$ -cooling, where we have to cancel the magnetic field at the MOT chamber center. This is realized using magnetic coils around the experimental table. The ideal cancellation is realized by monitoring the size of the  $\Lambda$ -cooled cloud after a fixed time-of-flight duration and iteratively scanning the magnetic field on all three axes.



## 2.7 CONVEYOR BELT MOT OF CaF

We recently implemented a blue-detuned MOT on the CaF Gen2 experiment and see good performance. I leave the details of our adventure with the blue-detuned MOT to the work from the CaOH team<sup>56</sup> and Christian Hallas's dissertation. I will only briefly discuss the performance of the CaF blue-detuned MOT in this thesis.

We use a three frequency (2+1) scheme of the blue-detuned MOT (referred to as a conveyor belt MOT). Preliminary results shows that we are able to transfer  $> 50\%$  of the molecules in our RF MOT into the conveyor belt MOT in less than 30 ms. The compressed conveyor belt MOT has a Gaussian width of  $63 \mu\text{m}$  and a temperature of  $\sim 130 \mu\text{K}$ . The image sequence of the (2+1) conveyor belt MOT of CaF during compression is shown in Figure 2.12 (a). The molecule numbers (in arbitrary units) at different stages of the experiment is shown in Figure 2.12 (b).

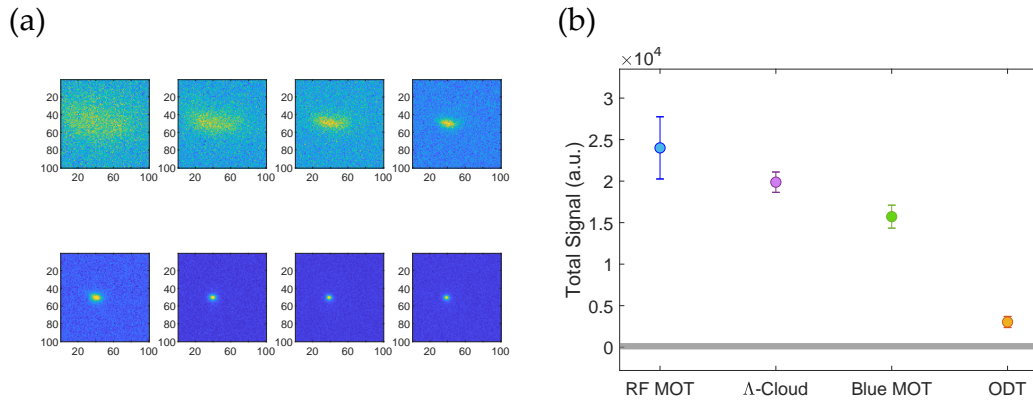


**Figure 2.12:** (a) CaF (2+1) frequency conveyor belt MOT compression. (b) Relative molecule numbers at different stages of the experiment.

## 2.8 SUMMARY

We created a high density 3D RF MOT of CaF molecules, loaded using a state-of-art CBGB source. The molecules are further compressed using a conveyor belt MOT and sub-Doppler cooled, ready to be transferred into a conservative trap, which will be the topic of the next section.

*If you already trapped your molecules, don't let them go.*

Wolfgang Ketterle, private communication

# 3

## Optical Trapping and Transport of Molecules

The MOT is a workhorse technology for almost all the modern ultracold atom and molecule experiments. However, continuous scattering of photons are required to maintain the trapping potential in a MOT, making it a non-conservative trap. This might be fine for an atomic MOT with continuous loading from a Zeeman slower,

2D MOT or even background gas, but not great for a molecular MOT that is loaded with a pulsed CBGB source with a limited photon budget. To preserve the lifetime of laser cooled and trapped molecules, we would like to transfer them into a conservative trap that minimizes photon scattering as much as possible. There are two common choices, both very successful with ultracold atoms: magnetic traps and optical dipole traps (ODT). We mainly use ODTs here in our lab, due to higher density and easier manipulation.

### 3.1 OPTICAL DIPOLE TRAP OF CAF

In an ODT, a strongly focused laser beam causes an AC Stark shift on the energy levels of molecules and the gradient of the spatially dependent potential leads to trapping. For a simple two-level system, the trap depth and the trap scattering rate can be derived from the real and imaginary parts of the polarizability and further simplified with second-order perturbation theory and the rotating-wave approximation.

$$U_{\text{trap}}(\mathbf{r}) = -\frac{\text{Re}(\alpha)I(\mathbf{r})}{2\varepsilon_0c} = -\frac{3\pi c^2}{2\omega_0^3} \frac{\Gamma}{\Delta} I(\mathbf{r}) \quad (3.1)$$

$$\Gamma_{\text{trap}}(\mathbf{r}) = \frac{\text{Im}(\alpha)I(\mathbf{r})}{2\hbar\varepsilon_0c} = \frac{3\pi c^2}{2\hbar\omega_0^3} \left(\frac{\Gamma}{\Delta}\right)^2 I(\mathbf{r}) \quad (3.2)$$

The trap depth of an optical dipole trap scales as  $\frac{1}{\Delta}$ , while the off-resonant scattering from the trap light scales as  $\frac{1}{\Delta^2}$ , where  $\Delta$  is the detuning of the trap light. One could easily see that it is advantageous to use a far detuned light field for ODT, since that provides lower scattering rate, scaling as  $\frac{1}{\Delta}$  for the same trap depth. From a technical point of view, it is desirable to choose a wavelength where high power laser is available at a reasonable cost. Here, we choose 1064 nm, where tens of watts of single frequency

laser light can be easily generated by a ytterbium doped fiber amplifier.

A simple ODT can be formed using a strongly focused Gaussian beam, with an intensity distribution in the form of  $I(r, z)$  expressed below.

$$\begin{aligned}
 I(r, z) &= \frac{2P_0}{\pi w_0^2} \left( \frac{w_0}{w(z)} \right)^2 e^{-\frac{2r^2}{w(z)^2}} \\
 w(z) &= w_0 \sqrt{1 + \left( \frac{z}{z_R} \right)^2} \\
 z_R &= \frac{\pi w_0^2}{\lambda}
 \end{aligned} \tag{3.3}$$

In this expression,  $w_0$  is the waist ( $1/e^2$  radius) at the focus of the Gaussian beam, and  $w(z)$  is the waist of the beam at a distance  $z$  from the focus along the  $k$ -vector of the laser beam.  $z_R$  is the Rayleigh range of the Gaussian beam, defined as the distance from the focus along the  $k$ -vector of the laser beam where the intensity of the beam drops to half.  $z_R$  only depends on the waist size at the focus and the wavelength of the Gaussian beam.

The ODT formed by a Gaussian beam can be further approximated by a harmonic oscillator potential close to the center of the trap. The oscillation frequency can be expressed using the trap depth at the center of the ODT  $U_{\text{trap}}$ , mass of the molecule  $m$ , and the Gaussian beam waist  $w_0$ .

$$\begin{aligned}
 \omega_{\text{radial}} &= \sqrt{\frac{4\text{Re}(\alpha)P\lambda^2}{2\pi^3\epsilon_0cmw_0^6}} = \sqrt{\frac{2U_{\text{trap}}\lambda^2}{m\pi^2w_0^4}} \\
 \omega_{\text{axial}} &= \sqrt{\frac{8\text{Re}(\alpha)P}{2\pi\epsilon_0cmw_0^4}} = \sqrt{\frac{4U_{\text{trap}}}{m\pi^2w_0^2}}
 \end{aligned} \tag{3.4}$$

The ODT laser is a 50 W single frequency polarization-maintaining ytterbium doped fiber amplifier (YFA-1055-SF, Precilasers) seeded by a single frequency 1064 nm seed

laser (ORION 1064 nm, RIO). The laser is optically isolated, passed through an AOM (AOMO 3080-1913, Gooch&Housego) and fiber coupled. The laser beam is delivered to the MOT chamber through a high power fiber patch cord based on LMA-PM-15 photonic crystal fiber (PCF)\*. The output polarization is cleaned by a high power plate polarizer (PBSW-1064, Thorlabs) and then expanded by a telescope and focused down to the required beam waist in the chamber. Some power after the polarizer is picked off by a UV fused silica plate, angled around Brewster's angle, and measured by a photodiode. An analog PID controller (SIM960, Stanford Research Systems) monitors the photodiode output and controls the AOM driving amplitude to regulate the power of the ODT beam into the MOT chamber. The power stabilized beam is then focused into the chamber through a lens to form the ODT. This setup is shown as the red colored beam path in Figure 3.7, but without the electrically focus-tunable lens.

To initially align ODT beam onto the  $\Lambda$ -enhanced gray molasses, we couple resonant light (606 nm) through the PCF. Although there would certainly be large focal shift between 1064 nm and 606 nm, as well as loss of power due to NIR coatings on all the mirrors, hundreds of  $\mu\text{W}$  of resonant light centered on the molasses is already sufficient to cause significant loss of molecules in the molasses. By steering the ODT beam while monitoring the molasses brightness on the camera, we can easily overlap the ODT beam path with the molasses. After turning on the high power 1064 nm ODT laser, an ODT signal is immediately observed. The next step is to move the focus of the ODT so it overlaps the center of the molasses. To achieve that, we lower the ODT trap depth, and then look for the focus that gives the highest molecule number in the ODT. We noticed that the ODT will still be loaded even the focus is not at the center of the molasses, but it will undergo a "sloshing" motion after the molasses light is turned off and molecules

---

\*SMA-6 with 8° angled 250  $\mu\text{m}$  long end caps on both ends, 2 m long. Made by ALPhANOV.

are supported only by the ODT. Once the ODT axial focus is moved to be centered on the molasses, this phenomenon disappears. This can be seen from the oscillating molecule signal versus ODT hold time curve shown in Figure 3.1.

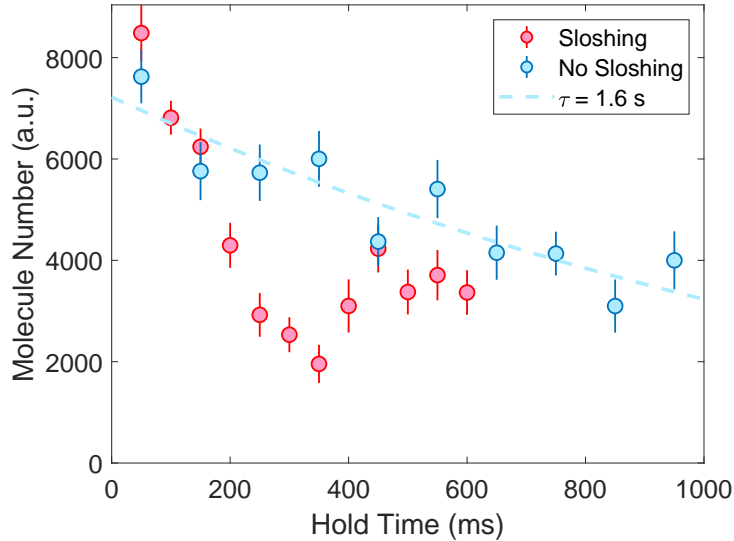


**Figure 3.1:** Sloshing of the molecules in the ODT when molecules are not loaded at the center of the ODT in the axial direction. The oscillation disappears when the ODT focus is moved to the center of the molasses in the axial direction.

### 3.2 OPTICAL TRANSPORT SETUP

The Gen1 experiment transfers CaF molecules into an 1064 nm ODT and then loaded them into an optical tweezer array, all in the same MOT chamber. This limits the available numerical aperture and optical access due to the presence of the in-vacuum RF MOT coils. We would like to push the Gen2 experiment further by optically transporting the molecular cloud over a macroscopic distance into a separate vacuum chamber for science applications.

There are several limitations posed for laser-cooled molecules that make the transport more challenging. Due to the black-body radiation exciting molecules into higher vibrational states<sup>17,127</sup>, CaF molecules have a  $\sim 5$  s lifetime in the  $v = 0$  vibrational state of the electronic ground state. As an optical tweezer experiment, good experimental data statistics require a lot of experimental runs. A short cycle time is beneficial. All these requirements indicate a very fast optical transport needs to be implemented for this experiment. Furthermore, the temperature in our optical dipole trap is around 20  $\mu$ K, and we are not aware of a straightforward way to reach even lower temperature at the time of building the experiment. This limits the minimum trap depth that must be provided during the transport.

Although there are various transport schemes for cold atoms, most of these methods are not suitable for molecules, as they cannot provide both high trap depths and rapid transport speeds. The two main methods for atoms are magnetic and optical moving trap transport. Magnetic transport can be realized by mechanically translating a magnetic coil<sup>78</sup> or controlling the sequence of currents into a set of coils placed along the transport path<sup>50,86</sup>. Magnetic transport typically produces a low density sample in a large volume trap, and can conflict with optimal optical access, while optical transport can be implemented with minimum obstruction of optical access. There are many different optical transport schemes based on moving the focus of an optical dipole trap (ODT), including using an electrically focus-tunable lens (ETL)<sup>74</sup>, rotating a Moiré pattern lens<sup>122</sup>, or, even simpler, mechanically moving a fixed lens on a translation stage<sup>55,51,89</sup>. These methods are often speed limited ultimately by the low axial trap frequency of the ODT. There are also demonstrations of using moving 1D optical lattices to shuttle atoms<sup>109,85,71</sup>, where one beam is a zero-order Bessel beam to maintain constant waist size over a long distance.



We first looked at the possibility of transporting the molecules using a moving ODT. At our choice of ODT wavelength of 1064 nm, in order to obtain a reasonable trap depth of 200  $\mu$ K with a 30 W laser beam, the waist of the beam cannot be larger than 60  $\mu$ m. In such a trap geometry, the radial trap frequency is 630 Hz and the axial trap frequency is 3.6 Hz. To reduce heating and spilling of the molecules during translation of the trap center along the axial direction, an adiabatic condition must be met where the speed of the transport is limited to a time scale much slower than  $1/\omega_{\text{axial}} = 0.28$  s. This matches the transport time that people usually expect for a direct moving ODT transport scheme along the z-direction. There is the option of reducing the size of the ODT waist, which could increase the axial trapping frequency, but at the cost of reduced the loading efficiency from the  $\Lambda$ -cooled cloud. On the other hand, the moving 1D optical lattice is a very attractive scheme for high speed transport. If we can combine the moving lattice transport with the tunable focus ODT, we might be able to get the best of both worlds. I will discuss how we turned this idea into a working setup in the following sections.

### 3.2.1 FIRST ATTEMPT: JUST A LATTICE

Based on the ODT, by sending a counter-propagating laser beam with the same frequency, an optical standing wave is created. This standing wave imposes a periodic AC Stark shift potential on the atoms or molecules and is known as an optical lattice. One would easily see that by perfectly overlapping the two equal power counter-propagating beams, the peak trap depth is increased by a factor of four due to constructive interference. When there is a frequency offset between the two beams, the lattice starts moving. The velocity of the moving lattice sites is proportional to the laser frequency difference between the two beams, expressed as  $v = \frac{\lambda}{2}\Delta f$ . For our choice of

lattice wavelength  $\lambda = 1064 \text{ nm}$ , a 1 MHz frequency difference corresponds to a moving velocity of 0.532 m/s. The final position of the transported molecules is controlled by the motion of the lattice sites, which is defined by the total phase difference accumulated during the frequency sweep, rather than the final focus position of the ODT. This greatly improves the stability of the final position against various drifts in the focus tunable devices (such as an electrically tunable lens, ETL)<sup>74</sup>. As we will see in the following sections, the ETL used in our setup is not temperature controlled nor is feedback used, and stable transport is still achieved.

To see if the idea would work at all, we first test the idea without using an ETL and limit the maximum distance of the transport to the scale of the Rayleigh range of the ODT ( $\sim 10 \text{ mm}$ ). At this stage of testing, our setup is built on a single 50 W fiber amplifier and the relative frequencies between the two beams are shifted by two double-pass AOM setups, based on Gooch&Housego AOMO 3080-1913. Since they are all simple AOMs that do not have wide tuning bandwidth<sup>†</sup>. This is not a big issue for now, since we can transport slowly for short distances in this preliminary test. Due to the double pass setup, changing the frequency of one double-pass AOM driver by 1 MHz, the lattice moving velocity changes by 1.064 m/s. The setup is shown in Figure 3.2.

Due to the finite polarization extinction ratio of the polarizer and alignment precision of the quarter waveplate, there are back reflections from the output of double-pass AOM back into the fiber amplifier. This is obviously an undesired condition even though the fiber amplifier has a built-in single stage isolator, as we have seen the fiber

---

<sup>†</sup>This should not be confused with the RF bandwidth of an AOM. A typical AOM (especially those with a higher center frequency) can accept a quite large range of RF frequencies. However, the diffraction efficiency can only be optimized for a single frequency once the AOM is fixed, and the diffraction efficiency drops quickly when the frequency is tuned away, due to change of optimal Bragg angle. To regain high diffraction efficiency at a different frequency, one must mechanically turn the AOM to match the new Bragg angle

amplifier reporting more reflection from its internal monitoring photodiode compared to just dumping the power on a beam dump. However, this reflection power is still within the laser's protection threshold so the laser is still safe to operate, but precaution should be taken and monitoring of this reflection power is recommended.

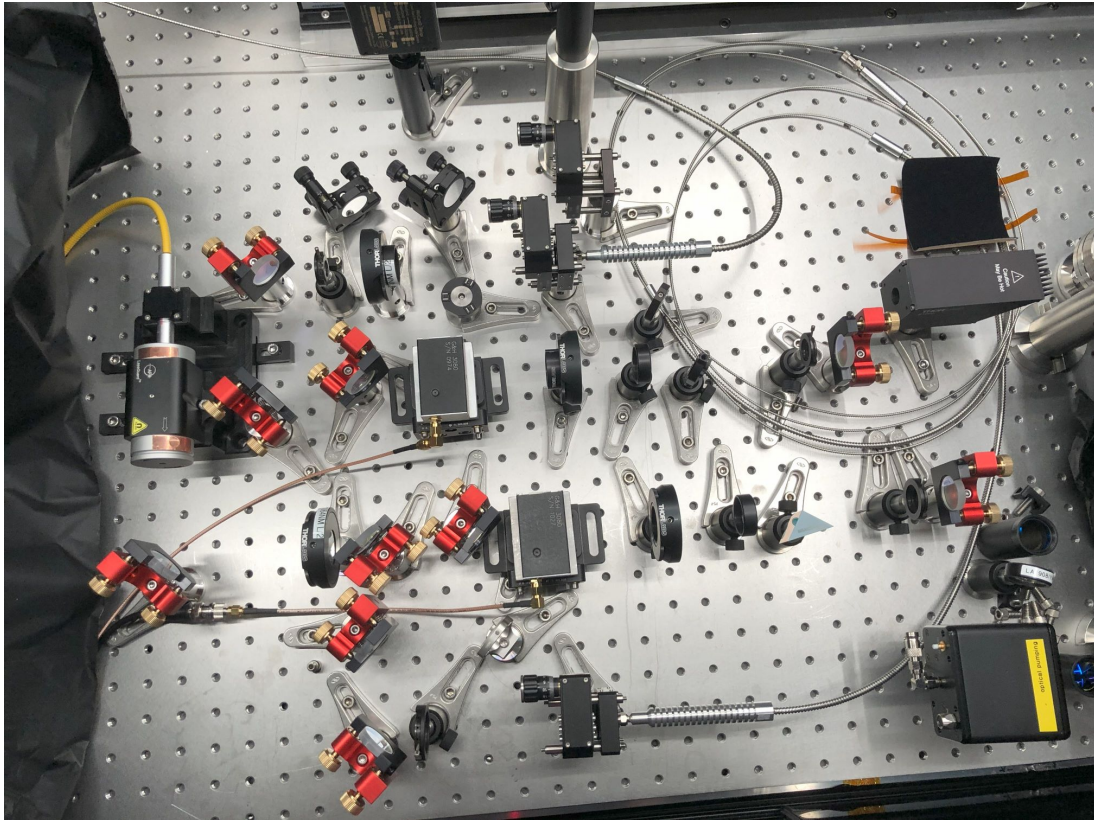


**Figure 3.2:** Double-pass AOM setup for initial transport tests.

The first trial of the transport was done with a “static” lattice generated by driving two AOMs with a dual-channel signal generator (Siglent SDG2122X). The frequency sweep is realized by using the frequency modulation function of the generator. An analog voltage signal from the Cicero NI card is fed into the modulation input port of the generator. We found this method is not reliable due to the way the frequency

modulation function is implemented in the generator. The generator reads the analog voltage using an ADC, and the digitized modulation signal is then fed into a DDS to control the frequency word. Any noise in the analog domain or digitizing error from the ADC would translate to frequency noise at the output, finally causing shaking in the lattice. We checked the lifetime of the molecules in this “static” lattice and find a shorter lifetime due to this fluctuation, shown in Figure 3.3 (a). If the external modulation is turned off on the Siglent generator, the lifetime is back to normal for such a deep lattice. Nevertheless, this is enough to observe evidence of a shortened transport distance. As we can see in Figure 3.3, we can test the transport by performing either a round trip transport or only moving molecules out but not back. There is a much smaller molecule number signal for the moving out only case compared to the round trip transport case.

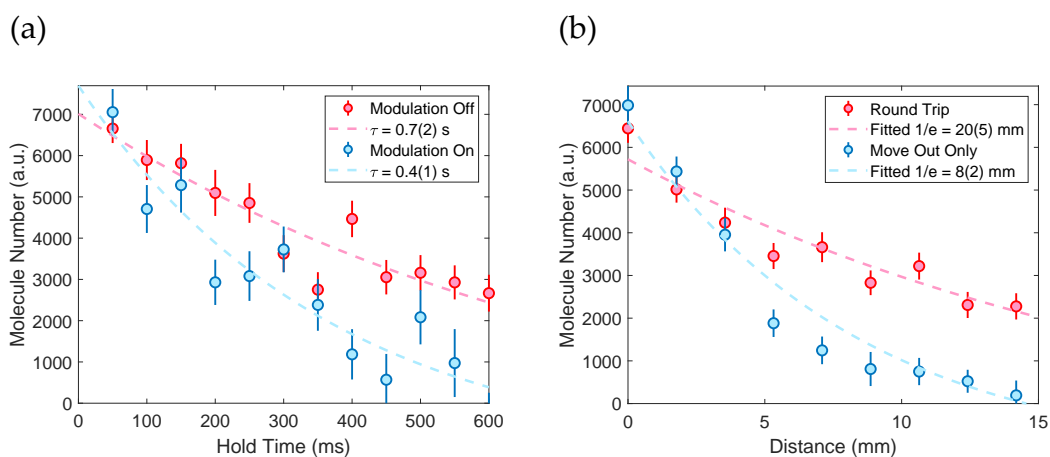


**Figure 3.3:** (a) Lifetime of molecules held in the lattice. A Siglent signal generator is used here with external frequency modulation turned on (blue) and off (red). (b) Initial observation of transport using the Siglent signal generator.

The best way to synthesize these kind of highly coherent low phase noise signals is to digitally program two DDS generators with a shared reference clock. However,

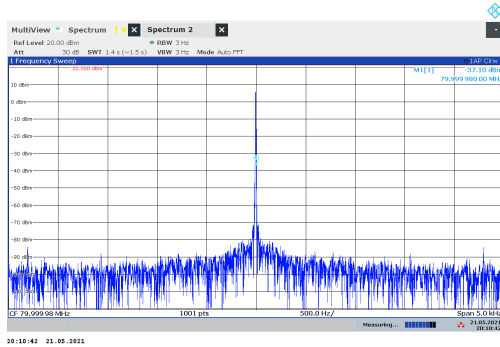
this option is not readily available in the lab at that time. We decided to use a very overkill solution. We borrowed an expensive AWG (AWG70001, Tektronix) to synthesize the frequency sweep. The full waveform is calculated using a MATLAB script and uploaded to the AWG through an Ethernet connection. The AWG is sharing a reference clock with a Siglent generator that drives the fixed frequency AOM. We use the internal sequencer of the AWG to loop through a static frequency waveform, generating a fixed frequency sine wave for lattice loading. Then, the AWG will jump to the transport waveform once triggered by Cicero. After installing the AWG, we found that there are some issues with the Siglent SDG2122X generator using an external reference from the Tektronix AWG. The output is measured on an RF spectrum analyzer (Figure 3.4). We switched the fixed frequency generator to a RIGOL DG4102 generator to solve this problem.

We see much less loss due to the frequency fluctuation after switching to the AWG. To see the effect of transport, we have to move the cloud out of the field of view of the imaging system. We apply an AWG waveform to transfer the cloud away and back from the MOT center for various distances, and compare that to transporting molecules away only. We observed more loss of the molecule signal as the cloud is moved out only compared to round trip transport (Figure 3.3), indicating the molecules are moved by the lattice. This gives us initial confirmation that the lattice transport scheme works at a short distance.

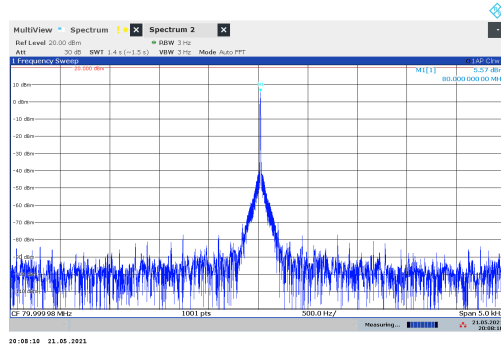
### 3.2.2 BEYOND RAYLEIGH RANGE

To move the molecules further than the Rayleigh range of the ODT, the ETL is added. It seems a formidable challenge to maintain overlapping of two dynamically focused laser beam. So we choose to only sweep the focus of one of the beams. This focus-tunable

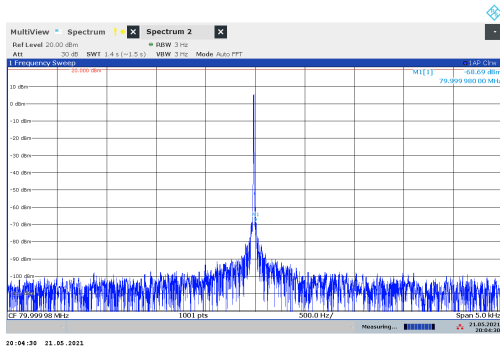
(a)



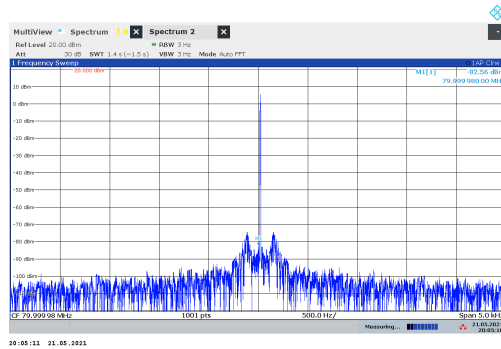
(b)



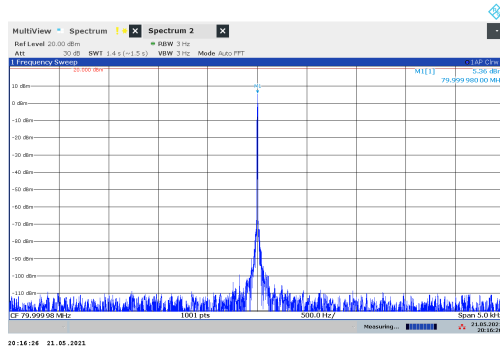
(c)



(d)



(e)



(f)

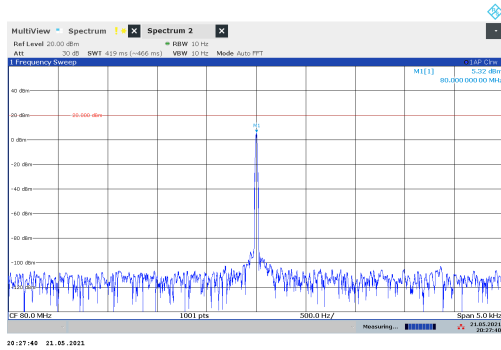


**Figure 3.4: RF output spectrum.** (a) Siglent SDG2122X with its internal reference clock. (b) Siglent SDG2122X with external 10 MHz reference clock provided by a Rohde&Schwarz FSW signal analyzer. (c) RIGOL DG4102 with its internal reference clock. (d) RIGOL DG4102 with external 10 MHz reference clock provided by a Rohde&Schwarz FSW signal analyzer. (e) Tektronix AWG70001A with its internal reference clock. (f) Tektronix AWG70001A with external 10 MHz reference clock provided by a Rohde&Schwarz FSW signal analyzer. Note that spectrum (a)-(e) are all taken with 3 Hz resolution bandwidth, while (f) is taken with 10 Hz resolution bandwidth.

beam is a small-waist ( $w = 57 \mu\text{m}$ ) Gaussian beam. This tight ODT beam itself allows for a deep trap (typically  $k_B \times 157 \mu\text{K}$ ), which facilitates simple and efficient loading of CaF molecules from the  $\Lambda$ -enhanced gray molasses<sup>26</sup>. By tuning the ETL, the focus of this beam can be moved for tens of centimeters along the optical axis, without changing its Gaussian waist. We call this beam the “ODT beam.”

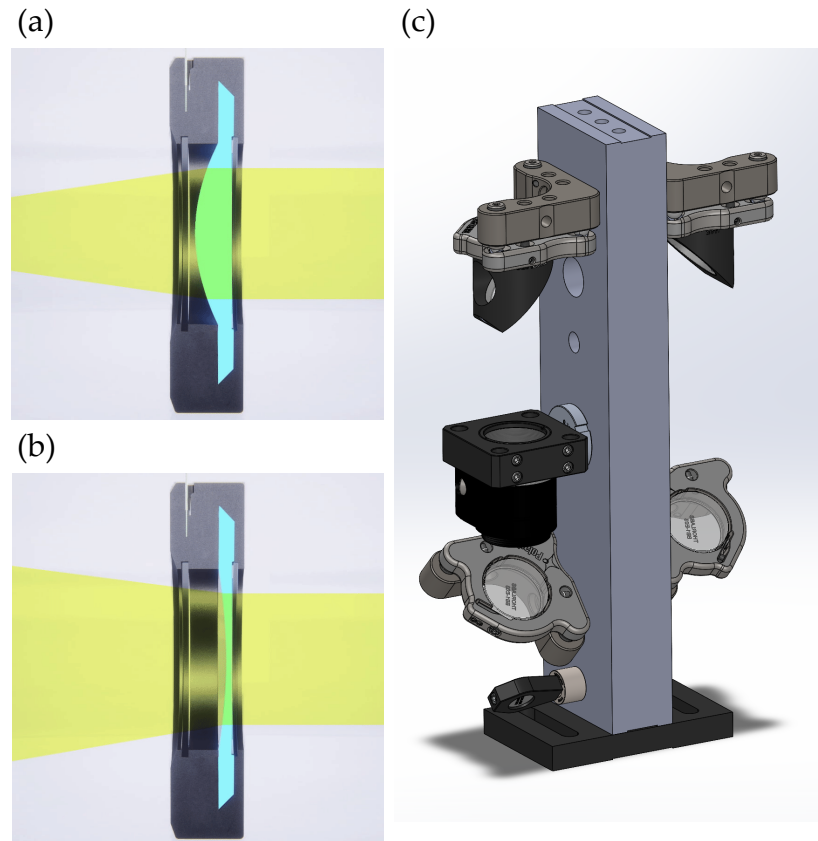


**Figure 3.5:** (a) and (b) A soft membrane deforms under the force exerted by a voice coil motor, changing the focal length of the lens. Reproduced from Optotune website. (c) A “tombstone” mount used to mount the ETL for better wave front error.

To solve the limited Rayleigh range problem for the other beam, we simply choose

to use a large-waist Gaussian beam ( $w = 320 \mu\text{m}$ ) with a long Rayleigh range ( $z_R = 302 \text{ mm}$ ), with its focus fixed at the center of the transport path. The trap depth provided solely by this beam is less than  $k_B \times 7 \mu\text{K}$ , too shallow to hold molecules on its own. The ODT also holds molecules against gravity during the transport. In the presence of both beams ( $\lambda = 1064 \text{ nm}$ ), the interference between them creates a 1D lattice with  $532 \text{ nm}$  spacing between lattice sites. This 1D lattice has a peak-to-trough potential of  $\sim k_B \times 100 \mu\text{K}$  at the center position of the MOT chamber, sufficient to trap molecules at  $32 \mu\text{K}$ . The axial trap frequency in the 1D lattice at the typical  $k_B \times 100 \mu\text{K}$  trap depth is estimated to be  $157 \text{ kHz}$ . Without the large-waist focus-fixed beam, the axial trap frequency in the ODT would be only  $\sim 3.5 \text{ Hz}$ , much lower than that of the 1D lattice and not sufficient for the acceleration needed for fast transport.

To avoid coma aberration originating from gravitational sag of the soft membrane in tunable lenses, the lens is installed with its optical axis aligned to gravity. A custom mount is made to achieve this (the “tombstone”), as shown in Figure 3.5. To maintain a constant trap depth at the focus during the transport, the tunable lens is placed at the focal plane of the main focusing lens  $L_1$ . With a collimated laser beam incident on the tunable lens, the trap focus after  $L_1$  can be moved along the optical axis without changing the waist size at the focus. The total optical path length difference caused by tuning the lens is  $\sim 100 \lambda$  at  $\lambda = 1064 \text{ nm}$ , which is much smaller than the motion generated by the lattice frequency sweeping.

### 3.2.3 OPTICAL FEEDBACK OF ETL

We start with an Optotune EL-10-30C ETL on the experiment. We tried this one just because it is in-stock from Edmunds Optics and has the correct NIR coating. It turns out that this ETL is not stable enough for our application.



As the first step of the test, we simply create an ODT using this ETL (no lattice). We find that the focus is drifting from this ETL at constant current. This is clearly not stable enough for our application. It is widely known that the temperature will affect these types of ETLs. One possibility is stabilizing the temperature of the whole lens. The other way is using a feedback circuit that actively measures the focal power of the lens, since the optical focal length is what we care about in the end.

A simple digital PID controller is implemented based on an Arduino Micro and three external 16-bit analog-to-digital converters (ADC) (AD7686, Analog Devices) and one external 16-bit digital-to-analog converter (DAC) (AD5060, Analog Devices). The first ADC input is used to measure the total power of the beam. The second ADC input is used to measure the intensity of the center of the beam. The third ADC input is used to receive the focus position setpoint from Cicero. The calculated PID output is converted to a voltage signal by DAC and used to control the current source that drives the ETL. The response signal is measured by a photodiode behind a pinhole placed in the optical axis of the tunable lens (3.10 (a)). We observe some interference fringes when using a laser as a light source to illuminate the ETL in this measurement. We believe this originates from the surface reflections of the cover glass and tunable lens membranes appearing as fluctuations on the photodiode signal. This fluctuation is eliminated by using a single mode fiber coupled super luminescent diode (QSDM-790-30, Q-Photonics) as an incoherent light source to illuminate the ETL. This does eliminate the fringes on the photodiode signal, but turns out to be not very successful, as we still see drift of the focus with this setup over a long time scale. One explanation is that the pointing of the SLD beam is slowly drifting, and the pinhole no longer stays at the center of the SLD beam.

In the meantime, we borrowed a better ETL (EL-16-40-TC-NIR-20D, Optotune) from

Kang-Kuen Ni's group. It provides much better stability and repeatability out of the box. It also requires much less current to drive, which significantly reduced the thermal effect. We find that optical feedback is no longer necessary for this ETL. The EL-16-40-TC series ETL has a 16 mm diameter aperture, which allows longer distance transport. It can also be tuned between a convex and concave shape, with a much smaller wavefront distortion. Part of the reason that the wavefront distortion is reduced is less spherical aberration due to the longer focal length. All these features make it very suitable for this transport setup.

There are two choices of the tuning range of the EL-16-40-TC series ETL, 20 diopter (post-fix 20D) or 5 diopters (post-fix 5D). The 5D version has a stiffer membrane, which limits its tuning range, but also gives it a faster response time. It also turns out that the 20D ETL we borrowed from Ni group is an exceptionally good one that shows a transmitted wavefront error (TWE) less than  $0.09 \lambda_{\text{test}}$  over the 16 mm aperture at zero current, where  $\lambda_{\text{test}} = 525 \text{ nm}$ . The vendor can only guarantee  $\text{TWE} < 0.25 \lambda_{\text{test}}$  RMS for a new 20D class 1 ETL, and  $\text{TWE} < 0.15 \lambda_{\text{test}}$  RMS for a 5D class 1 ETL. Due to these reasons, we finally choose a EL-16-40-TC-NIR-5D for our experiment.

#### 3.2.4 DOUBLE-PASS AOD SETUP

Another challenge for longer distance transport is the ability to maintain laser power while precisely tuning the relative frequency between the ODT beam and the lattice beam over a broad range. To reach transport velocities in the tens of m/s range, the frequencies of the two beams require several MHz detuning while maintaining phase coherence. The double passed AOMs can maintain fiber coupling efficiency as the frequency is tuned, but do not maintain high diffraction efficiency.

To solve this problem, we use an acoustic beam steering acousto-optic deflector

(AOD) (ATD-801A6.1064, IntraAction) in a double-pass configuration to maintain high diffraction efficiency over a wide frequency range. The way this AOD works is very cool in my opinion, and well deserving of a short introduction here. In a normal AOM, the acoustic wave vector is fixed in the crystal, which is usually perpendicular to the surface that the piezoelectric transducer is bonded on. When the RF driving frequency changes, the wavelength of the acoustic wave changes, which requires a different Bragg angle to reach maximum diffraction efficiency. Since the input optical beam has a  $k$ -vector that is fixed to the crystal once alignment is done, the actual incident angle onto the Bragg grating will deviate from the optimal Bragg angle, causing a low diffraction efficiency and limiting the bandwidth. In this AOD, the acoustic wave vector will steer as the RF driving frequency changes and compensate the change of optimal Bragg angle.

To achieve this, the piezoelectric transducer used on this AOD is bonded to a crystal that has a step shape grounded on the side. The neighboring steps has a height difference of one half of the acoustic wavelength and the piezoelectric transducers of these two steps are driven with  $180^\circ$  out-of-phase RF signals. For a step height of  $h$ , acoustic velocity of  $v$ , and RF drive frequency of  $f$ , one would find that the phase difference between neighboring steps are  $2\pi(\frac{hf}{v} - \frac{1}{2})$ . The interference between individual transducers in this phased array creates an acoustic beam angled at  $2\pi(\frac{hf}{v} - \frac{1}{2})\frac{v}{fd} = 2\pi(\frac{h}{d} - \frac{v}{2fd})$ . Since the optimal Bragg angle is  $\theta = \frac{\lambda f}{2v}$ , one can find a design where the acoustic beam angle approximately tracks the optimal Bragg angle as the RF frequency  $f$  is swept, as shown in Figure 3.6. It is easy to see that for a specific AOD of this type, when the RF frequency is swept in one direction, the direction that the acoustic beam steers remains fixed. This means that for a specific frequency shifting direction, one has to send the laser beam in the correct direction, or the acoustic beam would steer in the wrong

direction, changing the relative angle between the acoustic beam and the laser beam away from the optimal Bragg angle. Since only an isotropic acousto-optic interaction is used in this AOD, the polarization of the light is conserved. We can simply use a quarter waveplate and a polarization beam splitter cube to realize the double-pass configuration.

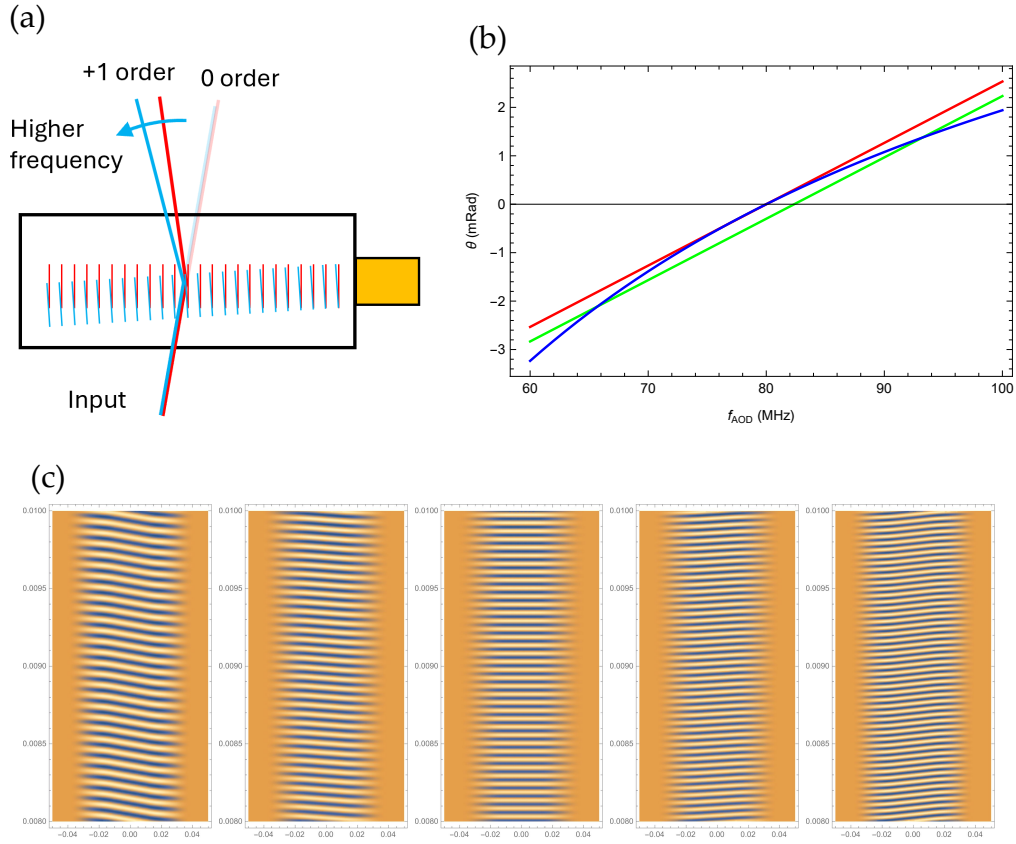


**Figure 3.6:** (a) Acoustic beam steering AOD using a stepped crystal. (b) Bragg angle of the AOD. Red curve shows the steered acoustic beam angle, and the blue curve shows the optimal Bragg angle. (c) Acoustic wave vector steered at varying RF drive frequency.

The final optical setup of the transport lattice is shown in Figure 3.7. Trapping lasers for both the focus-tunable ODT beam and the large-waist Gaussian beam are

derived from a low intensity noise narrow-linewidth ( $< 5$  kHz) laser module (RIO Orion 1064 nm) emitting over 20 mW of single frequency 1064 nm into a PM fiber. This seed laser is split by a 25:75 PM fiber splitter into 5 mW and 15 mW. 25% of the seed power is directly fed into a 50 W single-frequency PM-YDFA (denoted as “PM-YDFA<sub>1</sub>”) from Precilasers. The rest of the seed power is free space collimated, sent through a double passed acoustic optic deflector (AOD) setup, and then fed into another PM-YDFA of the same model (PM-YDFA<sub>2</sub>). The frequency shift range of this setup is  $f_{AOD} = 60$  MHz  $\sim$  100 MHz,  $2f_{AOD} = 120$  MHz  $\sim$  200 MHz.

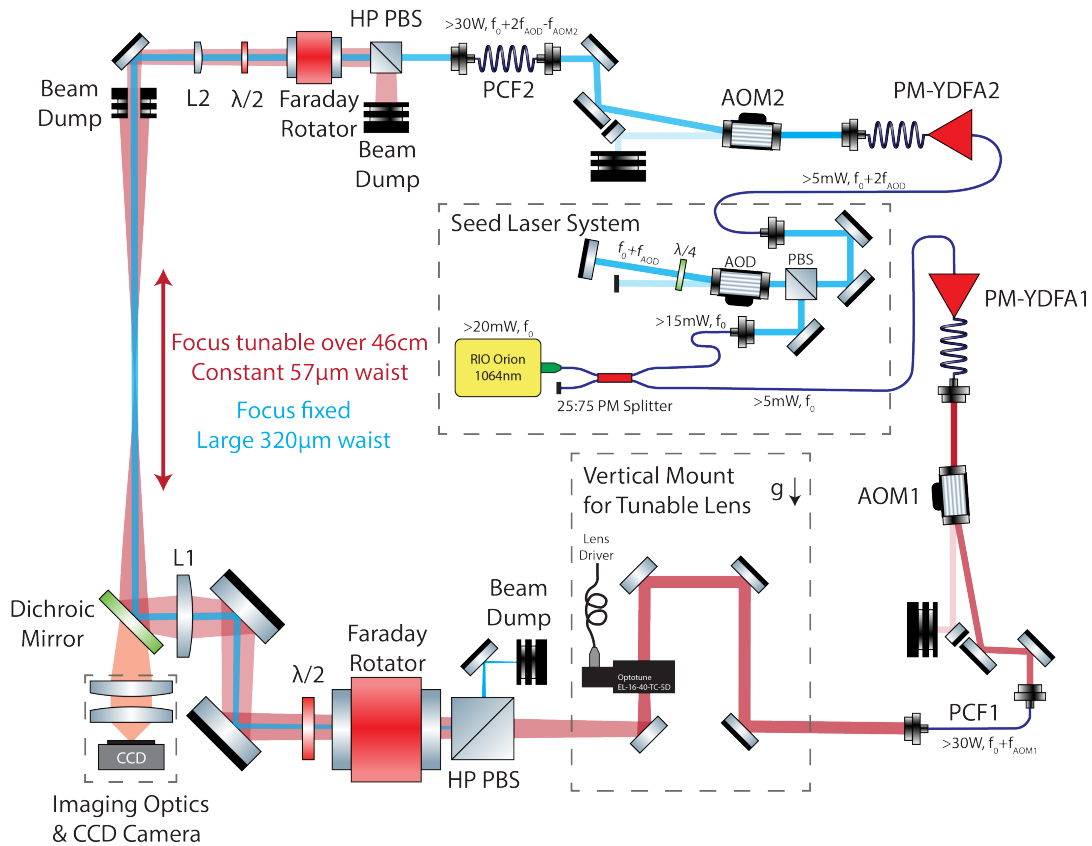


**Figure 3.7:** Final transport lattice setup view from the top. The tunable lens mount section inside the dashed box is vertically mounted on the optical table.

We obtain more than 5 mW of fiber-coupled seed power into the PM-YDFA2 over the full  $2 \times 40$  MHz tuning range of the double-passed AOD. This frequency tuning range corresponds to a maximum transport velocity of 21 m/s in both directions. The PM-YDFAs are working in a saturated regime where the output power is less sensitive to input seed power fluctuation compared to a non-saturated optical amplifier. We observe no output power fluctuation as we tune over the full  $2 \times 40$  MHz tuning range.

The outputs of both PM-YDFAs are both optically isolated and sent through AOMs used as optical switches and attenuators. The PM-YDFA1 output is frequency shifted up by an AOM driven at  $f_{\text{AOM1}} = 80$  MHz (AOM1) and then coupled into a photonic crystal fiber (PCF1). The output of this fiber is delivered to the ODT beam section. The PM-YDFA2 output is frequency shifted down by an AOM driven at  $f_{\text{AOM2}} = 80$  MHz (AOM2) and then coupled into another PCF of the same type (PCF2). The output of PCF2 is delivered to the large-waist Gaussian beam section. We obtain  $> 30$  W optical power on the experimental table for each beam. The frequency difference between the two beams after the PCFs is  $\Delta f = f_{\text{PCF1}} - f_{\text{PCF2}} = f_{\text{AOM1}} + f_{\text{AOM2}} - 2f_{\text{AOD}}$ . By driving the double passed AOD at frequency  $f_{\text{AOD}} = 80$  MHz, the frequency difference is zero, corresponding to a static lattice condition. Tuning  $f_{\text{AOD}}$  above 80 MHz moves the lattice sites towards the MOT chamber direction and tuning  $f_{\text{AOD}}$  below 80 MHz moves lattice sites towards the science cell direction.

Since the AWG70001A is a shared device between labs, we later switched to a DDS solution, which gives similar transport performance. In the permanent setup, the  $f_{\text{AOD}}$ ,  $f_{\text{AOM1}}$ , and  $f_{\text{AOM2}}$  signals are generated by two AD9910 direct digital synthesizers (DDS) based on an Analog Devices EVAL-AD9910 evaluation board. Both synthesizers are clocked by a shared 1 GHz low phase noise crystal oscillator (CCSO-914X3-1000, Crys-tek). The phase lock loop (PLL) in the AD9910 DDS is bypassed to eliminate the exces-

sive phase noise from the PLL's servo bump. The  $f_{\text{AOM1}}$  and  $f_{\text{AOM2}}$  signals are single-tone 80 MHz sine waves generated by a single AD9910. The output of this DDS is split into two paths, separately attenuated and amplified to drive AOM1 and AOM2. The driving amplitudes into these two AOMs are controlled by intensity stabilization servos (SIM960, Stanford Research Systems) that stabilize the output power after each PCF. The frequency swept  $f_{\text{AOD}}$  signal is generated by another AD9910 DDS utilizing its internal digital ramp generator (DRG). The internal DRG can only be used to sweep the frequency for one-way transport. To achieve round-trip transport for debugging, an Arduino Due microcontroller board is used to reconfigure the ramp limits of the DRG in real time to transport molecules back to the MOT chamber.

One technical note that we would like to point out is that the high power lattice beams need to be properly dumped after passing through the vacuum system. Unlike a retro-reflected optical lattice setup, in our setup, the main focusing lens L1 focuses down the counter-propagating large-waist Gaussian beam to a small spot onto the tunable lens. This high intensity focal spot can easily exceed the damage threshold of the tunable lens. Thus, a high-power large-aperture optical isolator must be installed between L1 and the tunable lens. Due to the very high intensity of the focused lattice beam in the isolator, we opt to use a high power Faraday rotator (110-23123-0003, PAVOS ULTRA series, Electro optics technology, EOT)<sup>‡</sup>.

---

<sup>‡</sup>This is a special Faraday rotator made from KTF crystal, rather than the typical TGG crystals. KTF crystals offer significantly lower absorption of optical power and much lower thermo-optic coefficient ( $\frac{dn}{dT}$ ), with a slightly lower thermal conductivity. These features make KTF a great material to reduce the thermal lensing effect in a Faraday rotator.

### 3.2.5 ALIGNMENT PROCEDURE

The alignment of a beam path with an ETL is slightly different from a static one, since ETL is a dynamical device that could change more than just the focus of the beam properties when electrically tuned. In the ETL used in this work, one optical surface is a piece of glass that is fixed, and the only tunable part is the other optical surface which is a flexible membrane. One can easily see that, if the alignment is not ideal, the focus of the lens will move away from the optical axis. The overall goal of alignment is to make sure that the  $k$ -vector of the laser beam is coincident with the focus trajectory of the ETL during tuning. To achieve this, the alignment must be carried out at different ETL focal lengths in an iterative way, with the angle and position of the beam into the tunable lens the degrees of freedom for the alignment. These degrees of freedom are provided by two kinematic mirror mounts on the top of the “tombstone” ETL mount.

To accurately determine the center of the beam profile at a given plane, a large area CMOS camera (Allied Vision, Alvium 1800 U-2050m) is used with a custom Gaussian fitting program. Note that this alignment is carried out without the final L<sub>1</sub> lens. Without the L<sub>1</sub> lens, the desired tuning range on the ETL would be from slightly focusing to slightly diverging. We hop the driving current to switch the ETL between two focal lengths and use the two kinematic mirror mounts before the ETL to minimize the beam center movement when the driving current is hopped.

To align the counter-propagating lattice beam with the focus tuning beam, the most obvious way is back coupling the lattice beam into the focus tuning beam PCF. Specifically, we place a power meter sensor at the input side of the PCF<sub>1</sub> for the focus tuning beam, turning the waveplate after the large aperture Faraday rotator to allow lattice beam power transmitting onto the PCF<sub>1</sub> output collimator. The goal is to optimize the



coupling efficiency into the PCF. However, this is not an easy task to do. In practice, one will find that there seems to be a large range of fiber coupling configurations that give very similar coupling efficiency.

The reason that simple fiber back coupling does not work out-of-the-box is that a normal fiber coupling protocol relies on the narrow range of the center position and numerical aperture of the single mode fiber to provide a penalty (reduce the coupling efficiency) when alignment is not optimal. In our case, due to the mismatch of the spatial mode of the two beams, the light has a huge  $1/e$  diameter on the facet of the fiber, causing a lot of the lattice beam power to not reach the PCF collimator. The observation is that the coupling efficiency stays low and almost invariant while walking the lattice beam at several different positions. The issue is caused by not enough penalty when the laser beam is off-center from the fiber collimator. The solution is adding penalty elsewhere in the beam path that helps overlapping the beam path. We realize this using an iris mounted on a precision X-Y translation stage between the lens  $L_1$  and the large aperture Faraday rotator. We first place a power meter sensor right after the iris and turn on the ODT beam at low power. We coarsely position the iris to be centered on the beam. We then shrink the iris so the transmitted power through the iris is reduced to less than 50% compared to when the iris is fully opened. We then use the fine adjustment knobs on the X-Y translation stage to maximize the transmitted power. This procedure aligns the iris center to the ODT beam center with high precision.

Next we turn off the ODT beam and turn on the lattice beam at low power. The power meter sensor is moved to the other side of the iris and set to measure the lattice beam power. We roughly center the lattice beam on the iris by adjusting one kinematic mirror mount that steers the lattice beam. We then shrink the iris again to reduce the power meter reading of the transmitted power of the lattice beam through the iris to less

than 50% compared to when the iris is fully opened. Finally, we move the power meter sensor to the input side of the ODT beam PCF to monitor the back coupling signal. The lattice beam is walked using the two kinematic mirror mount on the lattice beam optical bread board.

With all these implemented, we are able to extend the transport range to over 10 cm. We scan the range of the frequency sweep ( $x$ -axis in the figure), and a peak of survived molecules after round trip transport is observed for distances that are many times the Rayleigh range of the ODT beam (Figure 3.8 (a)). We also find that we are able to transport over 12.5 cm, but not 13.5 cm. Our transport is actually limited by the finite distance available in the MOT chamber, where the molecules are moved too close to the viewpoint of the MOT chamber. It is time to construct the glass cell section of the UHV system, which should allow transporting all the way from MOT chamber to the glass cell (Figure 3.8 (b)).

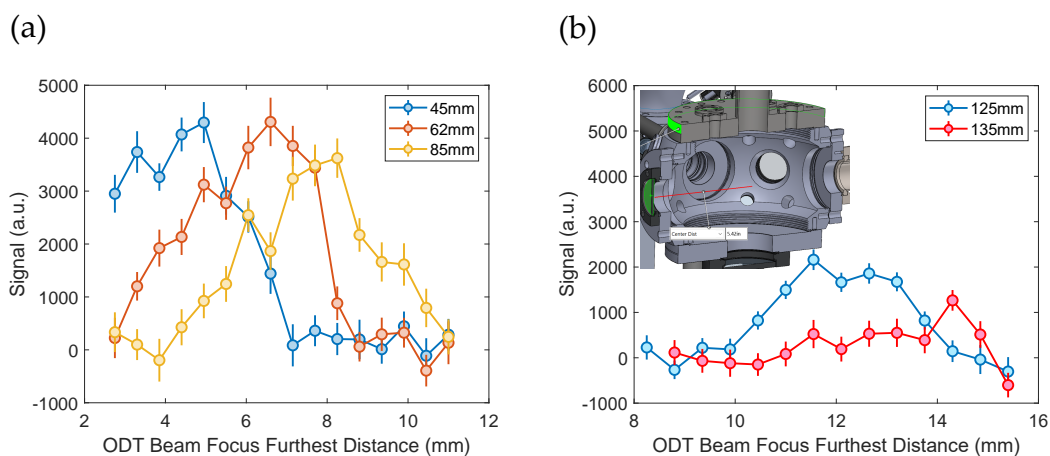


**Figure 3.8:** (a) Medium distance transport with new ETL. (b) Loss of molecules is observed when transporting too close to the viewport.

### 3.2.6 ETL WAVEFORM OPTIMIZATION

The tunable lens has mechanical resonances at frequencies below 1 kHz. Excitation of higher order mechanical modes of the lens membrane can distort the wavefront of the laser beam, causing large fluctuations of the trap depth and the focal position. These resonances can be observed in Figure 3.9. This can lead to rapid heating and loss of molecules, limiting the practical tuning speed of the tunable lens. This is typically not a problem in a tunable-lens only moving ODT transport system since the transport takes order of seconds, which is more than an order of magnitude slower than our scheme. To maintain a good beam quality while still forcing the lens to respond as fast as possible, the lens is driven with an optimized waveform instead of a simple linear ramp waveform. The optimized driving waveform is obtained by measuring the step function response of the lens, which is then input into a convex optimization algorithm to generate a waveform for the target focus trajectory<sup>65,47,46</sup>.

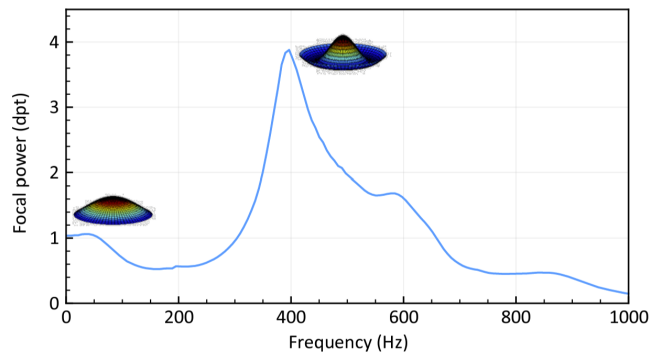


**Figure 3.9:** Typical frequency response of the EL-16-40-TC. The driving amplitude is  $-50$  mA to  $50$  mA. Reproduced from EL-16-40-TC datasheet by Optotune.

We model the tunable lens as a linear time-invariant (LTI) system. An LTI system can be described by its impulse response function. Although the early attempt to build an optical feedback circuit on the EL-10-30C ETL was not successful, the setup is used

for measuring the impulse response function of the ETL (Figure 3.10 (a)). We measure the impulse response function by applying a step function current waveform to the tunable lens. The photodiode signal is recorded by a 16-bit digitizer. For a Gaussian beam cross section with a  $1/e^2$  diameter  $w$  and power  $P$  as input, the intensity at the center of the beam follows  $I = \frac{2P}{\pi w^2}$ . where  $P$  is the total power in the beam and  $w$  is the  $1/e^2$  beam radius at the pinhole plane. The focal length  $f_{ETL}$  of the ETL satisfies the following relation, assuming the collimated light has a Gaussian waist of  $w_0$  before entering the ETL and the  $1/e^2$  beam radius at the pinhole plane is  $w$

$$\frac{f_{ETL} - d}{d} = \frac{w}{w_0} \quad (3.5)$$

It is easy to derive  $f_{ETL}$  using the relation  $I = \frac{2P}{\pi w^2}$ , where  $I$  is the measured intensity at the center of pinhole.

$$f_{ETL} = \frac{dw_0}{w_0 - w} = \frac{dw_0}{w_0 - \sqrt{\frac{2P}{\pi I}}} \quad (3.6)$$

The actual position of the ODT focus is not  $f_{ETL}$  from the ETL, since we have an extra lens ( $L_1$ ) with a focal length of  $f_{L1}$  placed at a distance of  $f_{L1}$  after the ETL. We can then convert the ETL focal length to distance between ODT focus and  $L_1$  lens. This distance  $D$  can be expressed as

$$\frac{1}{f_{L1}} = \frac{1}{D} + \frac{1}{f_{L1} - f_{ETL}} \quad (3.7)$$

We finally derive the distance between L1 lens and ODT focus  $D$  as

$$D = f_{L1} + \frac{f_{L1}^2}{d} \left( \frac{w}{w_0} - 1 \right) = f_{L1} + \frac{f_{L1}^2}{d} \left( \frac{1}{w_0} \sqrt{\frac{2P}{\pi I}} - 1 \right) \quad (3.8)$$

In reality, because of the slight misalignment between the beam and the tunable lens's optical axis, the photodiode signal deviates from the formula when  $w$  is small. We instead use an interpolated function between the photodetector output versus measured lens position to linearize the tunable lens response. The tunable lens position signal is then differentiated to derive the impulse response function  $h(t)$ . Here we provide two examples of the impulse response function from our 20 diopters (20D) range and 5 diopters (5D) range models of the lens in Figure 3.10 (b), showing very different resonant and damping characteristics. The impulse response function is also different from lens to lens. Thus, each new lens needs to be tested for its unique impulse response function before the optimization algorithm can be applied. The 5D lens with a stiffer membrane is chosen for our experiment, as it has a higher resonant frequency and can intrinsically be driven faster.

By taking the convolution of an arbitrary driving waveform  $x(t)$  with the measured impulse response function  $h(t)$ , we can simulate the tunable lens position response  $y(t) = x(t) * h(t)$  on a computer, where  $*$  denotes discrete convolution. We test the difference between a simulated response to the target response waveform  $y_0(t)$  using a customized cost function

$$c(x(t)) = x(t) * h(t) - y_0(t) + k \int |x(t') - \int_{t=t'-\tau}^{t'+\tau} x(t)|^2 dt' \quad (3.9)$$

The last term is a penalty term added in the cost function to suppress the high fre-

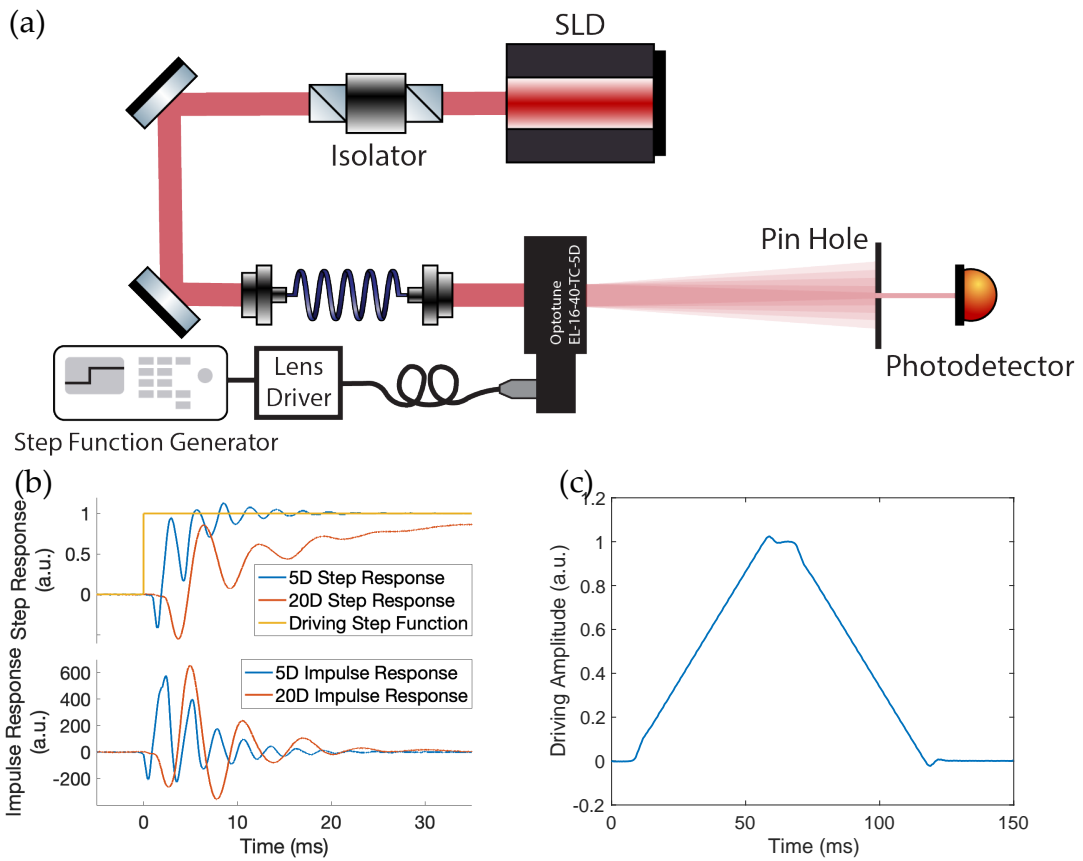


**Figure 3.10:** (a) Impulse response measurement setup (b) Measured step response and impulse response functions of the 20D and 5D lenses. (c) Optimized driving waveform for a simple linear ramp as a target trajectory.

quency noise components in the optimized waveform, in which the variable  $k$  is the weight of the penalty term and  $\tau$  is a low-pass filter time constant. We then use the CVX convex optimizer package in MATLAB to minimize this cost function to find the optimized driving waveform<sup>47,46</sup>. The typical optimized driving waveform used in this experiment is shown in Figure 3.10 (c). Since the lens is modeled as an LTI system, we linearly scale the optimized waveform to control the start and stop position of the lens without generating the optimized waveform each time.

In Figure 3.11, we show the distorted response of the tunable lens when driven with a simple linear ramp signal. Driving with an optimized waveform shows no distortion near the beginning and end of the motion. During the constant velocity transport, there is very small difference between the two waveforms. We find that using the optimized waveform is crucial in achieving high efficiency in our fast transport scheme. We see no molecules transported at the full distance when using the simple ramp signal. This can be explained by the distortion caused by higher resonant modes of the lens membrane or large deviation from the target trajectory during the acceleration period.

To explore the limits of transfer speed, we apply acceleration for longer durations, transporting the molecules one-way over a distance of 46 cm in 25 ms. We observe that the transport efficiency degrades significantly. The measured impulse response function of the tunable lens, as shown in Figure 3.10 (b), indicates a resonant cycle period around 6 ms, which is close to half of the one-way transport time 12.5 ms. We suspect that the tunable lens response is no longer linear under such a fast and large amplitude driving condition. Since our optimization is based on a linear model, it is expected that the performance of our optimized waveform would degrade.

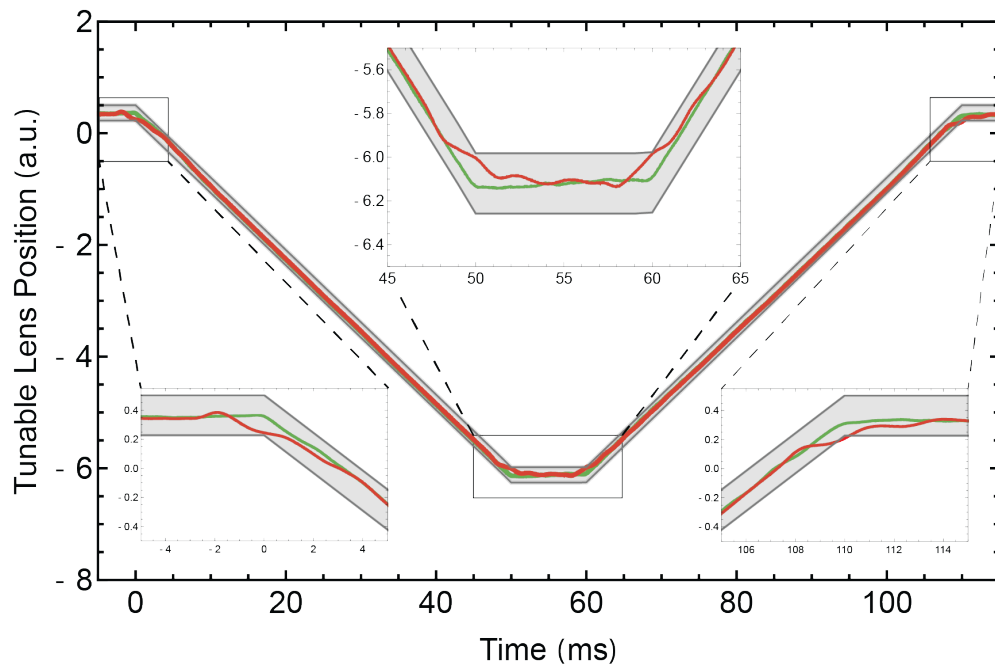


**Figure 3.11:** Lens response driven with a simple linear ramp (red) versus an optimized waveform (green). The gray area is the Rayleigh range of the ODT along the target trajectory. Key moments during lattice acceleration and deceleration are zoomed in for clarity.



### 3.3 OPTICAL TRANSPORT PERFORMANCE

We benchmark transport performance by first studying round-trip transports, starting and ending in the MOT chamber. This allows direct extraction of the transport efficiency without requiring the determination of photon collection efficiency or calibration of the camera gain in the downstream chamber (“science cell”). To vary the transport distance, we fix the acceleration and total transport duration and vary the acceleration duration, reaching different maximum velocities. We take two  $\Lambda$ -imaging pictures<sup>26</sup>, each with 20 ms exposure time, before and after the round-trip transport. We then normalize the camera signal of the second image relative to the first image to remove molecule number fluctuation. For each transport distance, corresponding to each colored trace in Figure 3.12 (a), we scan the amplitude of the tunable lens driving waveform and measure the transport efficiency. The highest transport efficiency is achieved when the trajectory of the ODT beam focus most accurately tracks the motion of the lattice sites.

Molecule signal loss is observed with no transport, i.e. holding molecules in a static lattice. As shown in Figure 3.12(a), after holding molecules in a static lattice for 100 ms, the normalized signal drops to 50%. Most of this loss is caused by the diffusion of molecules out of the low trap frequency ODT during  $\Lambda$ -imaging. A small portion of the loss can be assigned to the lattice shaking originating from technical limitations such as the phase noise picked up in the fibers and residual intensity noise of the laser. As the lattice beam power is being lowered, the lattice trap frequency decreases, and we observe a longer lifetime in the lattice. Therefore, to reduce loss during the constant velocity transport, we find it beneficial to lower the lattice beam power and release molecules back to the ODT. All data shown in Figure 3.12 is taken with the lattice beam

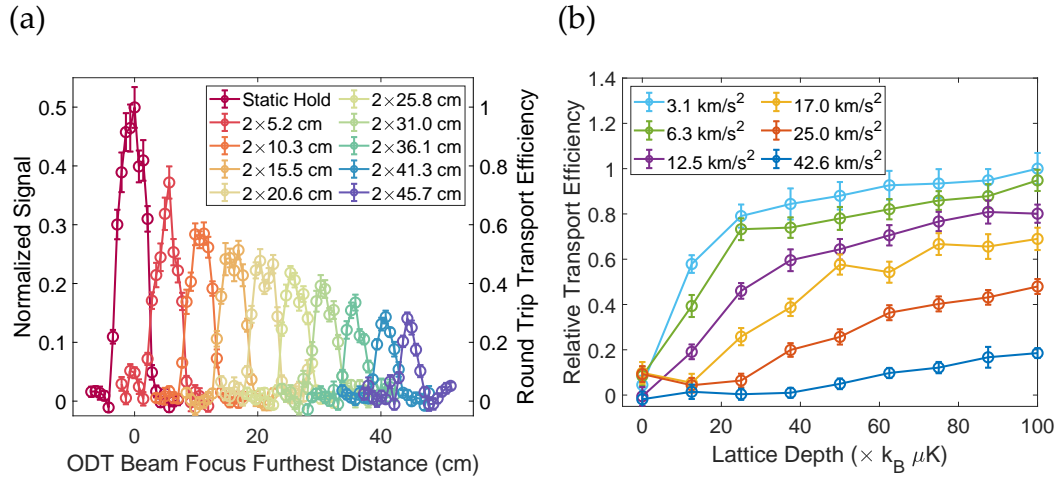


**Figure 3.12:** (a) Transport efficiency versus the furthest distance reached by the focus of the ODT beam, taken with different round-trip transport distances (indicated in the legend) defined by the lattice motion. Data points on each trace are obtained by scanning the amplitude of the tunable lens driving waveform. The left vertical axis shows the normalized fluorescence signal after transport referenced to the fluorescence signal before the transport. The right vertical axis shows the transport efficiency calculated by dividing the signal by the peak value of the static hold condition. The error bars are all referenced to the left vertical axis. All transports shown in this figure are round-trip, with the longest distance being 45.7 cm to the science cell and then back to MOT chamber. The acceleration is  $6.3 \text{ km/s}^2$  and the round-trip transport time is 100 ms. (b) Relative transport efficiency versus the lattice depth with different acceleration during acceleration phases. Relative transport efficiency is all normalized relative to the peak efficiency in this data set.

power ramped to zero during the constant velocity period of the transport.

Due to the heating from the lattice, some molecules are heated above the top of the lattice potential, but still below the ODT potential. They should be transported with almost the same velocity as other molecules inside the “optical transport tube” to the glass cell, but would fail to be decelerated at the end of transport. With our EMCCD camera monitoring from the top of the glass cell, we are able to observe this effect, where some molecules are flying out (Figure 3.13). The elongated cloud in the pictures are due to motion blur. Due to vignetting of this temporary imaging system, we cannot reliably extract the loss fraction from the data.

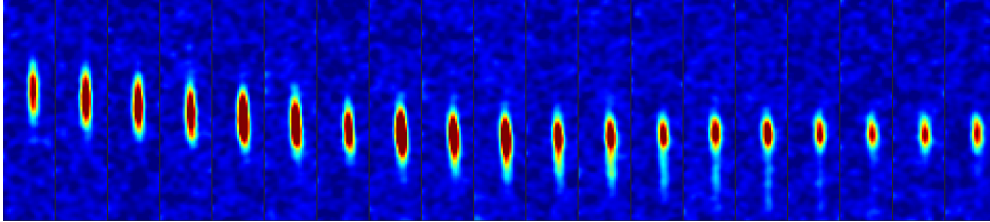


**Figure 3.13:** Heated molecules failed to decelerate at the end of transport and fly away.

We scan the lattice depth by varying the lattice beam power while keeping the ODT beam power constant. We measure the transport efficiency at roughly half of the maximum round-trip transport distance with different combinations of lattice depth and acceleration as shown in Figure 3.12 (b). An accelerating lattice can be viewed as a tilted lattice with reduced depth. For low acceleration, even a reduced depth is enough to hold molecules in the lattice sites. The data indicates that when the acceleration is low, the transport efficiency saturates as lattice depth increases. For higher acceleration, the transport efficiency increases gradually as lattice becomes deeper, but the overall transport efficiency is lower. This is expected because increasing the overall lattice depth can compensate for the larger reduction in lattice depth caused by higher

acceleration. When the lattice beam is not turned on, molecules are not transported. This demonstrates that our moving lattice can provide a higher axial acceleration than that of a simple ODT.

The highest transport efficiency is reached at an optimal acceleration. High acceleration can increase loss, while too low of an acceleration will increase the time that the lattice has to be turned on, leading to lattice heating loss. The transport efficiency reported in this work is achieved with an acceleration around  $6.3 \text{ km/s}^2$ . For one-way transport, this accelerates molecules to  $9.4 \text{ m/s}$  in  $1.5 \text{ ms}$ . With a total  $50 \text{ ms}$  transport time, molecules are transported  $45.7 \text{ cm}$  to the center of the science cell.

We measure the temperature of the trapped molecules before and after transport using the time-of-flight method. The temperature of the molecules before transport is  $32(2) \text{ } \mu\text{K}$ . This temperature is higher than the temperature of  $\sim 10 \text{ } \mu\text{K}$  achieved in free space, because the tensor AC Stark shift from the deep optical trap affects the  $\Lambda$ -cooling<sup>26</sup>. We then apply the same  $2 \times 20.6 \text{ cm}$  round-trip transport using  $6.3 \text{ km/s}^2$  acceleration and re-measure the temperature. The temperature of the molecules after transport rises up to  $53(4) \text{ } \mu\text{K}$ . However, this is still within the capture velocity of  $\Lambda$ -cooling. By applying cooling again in the science cell, we can recover the lowest trapped molecule temperature.

Using one-way transport, we take a second image of the molecular cloud in the science cell. Imaging in the science cell shows a transport efficiency of  $48(8)\%$ . The round-trip transport sequences use identical transport parameters for both the transport out and transport back legs. The efficiency of the one-way transport efficiency compared to the square root of the round-trip efficiency ( $\sqrt{28\%} \approx 53\%$ ), is consistent to within the calibration uncertainty of the imaging systems. We observe an RMS fluctuation of the center position of the transported molecular cloud to be better than  $1\%$  ( $36 \text{ } \mu\text{m}$ ) of the

length scale of the molecular cloud over one hour. This axial stability should not affect the loading of an optical tweezer array of molecules in the glass cell.

As we are going to load an optical tweezer array from this transported sample of CaF molecules, pointing stability of the ETL beam becomes a concern. When we later started loading tweezer arrays, we do see small drifts of the relative position of optical tweezer array and the transport lattice from day to day. Fortunately, this is a small effect and a relatively slow process. With a pick-off mirror sampling the ETL beam after the glass cell, the spot position can be detected on a camera or a four-quadrant photodiode. The measured position data can then be used with piezoelectric kinematic mirror mounts and corresponding PID controllers to stabilize the lattice pointing in real time.

#### 3.4 OUTLOOK

It is also possible to parallel the MOT loading and optical tweezer operation (pipeline), where a MOT can be captured and loaded into the transport lattice, while the optical tweezers are still holding molecules from the last experimental run for science applications. This would allow for quasi-continuous loading of the molecules into a tweezer array in the future.

*The Tao produced One; One produced Two; Two produced  
Three; Three produced All things.*

Laozi

# 4

## An Optical Tweezer Array of Molecules

Optical tweezer is a powerful tool for manipulating ultracold atoms and molecules. An optical tweezer can be viewed as an ODT with a very small waist. The trap volume of this ODT is so small, that when more than one atom or molecule are loaded at the same time, some type of collisions process would lead to both particles, or preferentially one

of the particle. In our case for CaF molecules, the light-assisted collision is the dominate loss process for two particles, and usually both molecules are lost from the tweezer trap, causing a parity projection effect, and gives us about 50% loading probability of each tweezer trap.

By creating an array of copies of optical tweezers, multiple atoms or molecules can be trapped in a programmable arrangement. The creation of the pattern is usually provided by some types of spatial light modulators. Dynamically updating the pattern allows for rapid rearranging of the tweezers and switch between various patterns.

#### 4.1 MICROSCOPE OBJECTIVE

To create a very tightly focused Gaussian beam (small waist  $w_0$ ), one would immediately see that the divergence angle of the beam will be large. This requires high numerical aperture (NA, defined by  $NA = n \sin \theta$ , where  $n$  is the refractive index and  $\theta$  is the half angle of the cone of the focused light) lens. The same lens can be also used to collect scattered photons from the atoms or molecules for imaging. These type of lens are usually called microscope objective lenses. We will refer to it using the short name “objective” in the following paragraphs.

Objective is nothing special other than an ideal lens. In reality, a simple lens with spherical surface has too much spherical aberration and cannot maintain diffraction limited performance at high NA. In practice, an objective is usually a multi-lens design consists of sophisticatedly designed and manufactured singlet lenses in lens groups that are precisely aligned referenced to the optical axis. A custom objective order can easily cost on the order of \$100,000 due to the small number of objectives ordered and highly customized specifications.

To see if an objective meets design specifications, the first thing that must be tested is its transmitted wavefront error (TWE). For an ideal lens, incoming light with a flat wavefront (collimated beam) will be converted into a perfect spherical wavefront (focus is at the center of the spherical surface). Any deviation from this ideal condition is considered aberration. The wavefront deviation over a circular aperture could be expanded into Zernike polynomials. For the custom objective used on Gen2 experiment, we expect most common aberration are properly corrected during the design stage. Using the Zemax OpticStudio blackbox file provided by the vendor (Special Optics), we are able to preview the performance of this microscope objective (Figure 4.1). Note that the objective is optimized for a field of view (FoV) with a radius of  $100\ \mu\text{m}$  at three wavelengths  $531\ \text{nm}$ ,  $606\ \text{nm}$  and  $780\ \text{nm}$ . It is normal that the objective performance degrades at wavelengths away from those three wavelengths or outside the radius of  $100\ \mu\text{m}$  from the center of FoV.

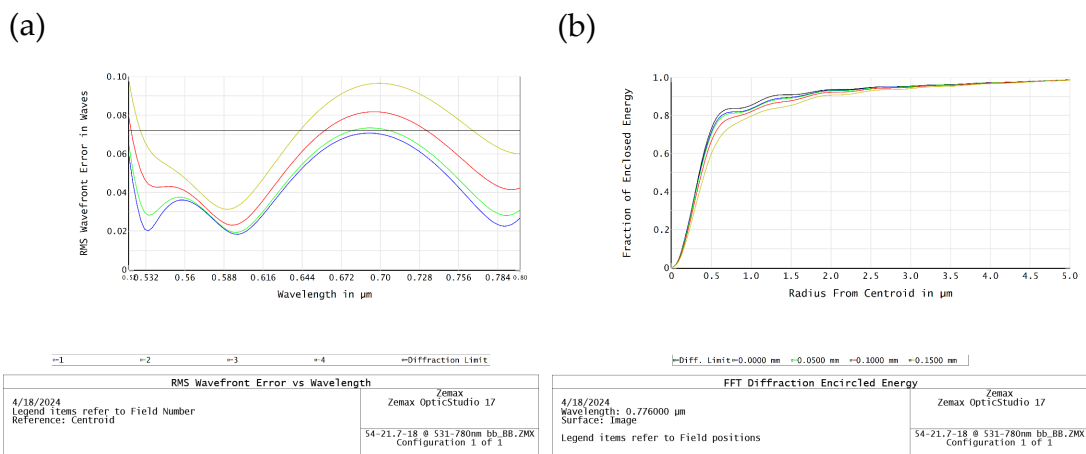


**Figure 4.1:** (a) RMS TWE of the default objective setup at different wavelengths. Blue, green, red, yellow curves are center,  $50\ \mu\text{m}$ ,  $100\ \mu\text{m}$  and  $150\ \mu\text{m}$  distance from the center of field of view. Black curve is the indication of diffraction limit. (b) FFT diffraction encircled energy of the default objective setup.



When we were deciding on the specifications for the objective, we are also considering compatibility with future upgrades. Many experiments with a 3-D optical lattice requires a lattice beam going through the mechanical axis of the objective without transmitting through the optics of the lens. This is usually realized by grinding a hole on all the elements of the objective. However, this method has several disadvantages, including loss of low spatial frequency components of the image, loss of photon collection efficiency, more scattering due to diffraction from the edge of the hole. Instead of letting the lattice beam go through, we choose to reflect it. An objective usually has a meniscus lens as its first element. Any thickness of flat optics (usually vacuum windows) can be corrected during the design stage of the objective. In a diffraction limited imaging system, reordering flat optics does not change the transmitted wavefront error, as long as all the flat surfaces are perpendicular to the optical axis. We decide to ask for 2 mm thicker fused silica to be compensated on this objective, and mechanically integrate this fused silica plate onto the objective assembly with a plastic retaining clamp. The objective as delivered come with a piece that is anti-reflective coated on both sides, where the first element can be replaced in the lab with a custom piece that is high-reflective coated on one side for the lattice wavelength.

The objective is also designed for an extra 1 mm thick piece of sapphire in vacuum. This piece can be used for a future cryogenic shield for molecules, or parallel electrodes for electric field control. In the current generation of the experiment, we are not planning to immediately install this sapphire plate into the glass cell. As we have discussed before, the order of flat optics between the focus and microscope objective does not matter. This means the sapphire plate can be moved outside of the glass cell and glued to the front flat element of the objective, without affecting the imaging performance. Furthermore, this plate is thin enough that we can just use a piece of fused silica plate

to replace the sapphire plate without sacrificing too much performance. Finally, there is another advantage, glass cell manufacturer can only guarantee the thickness of the window before fusing them onto the fused silica frame. It would be hard to change any specification of the objective once the order is placed. In our case, we can measure the thickness of the received glass cell, and custom the thickness of the compensation glass plate with a separate vendor. The delivery of the custom compensation glass plate is relatively quick. In our case, it arrives before the objective arrives, resulting in no down time on the experiment.

When the fused silica plate is placed on the objective front element, we see rainbow color rings (Newton rings) originated by white light interference under room light (Figure 4.2 (a)). This immediately tells us that the air gap between the two surfaces are not completely flat.

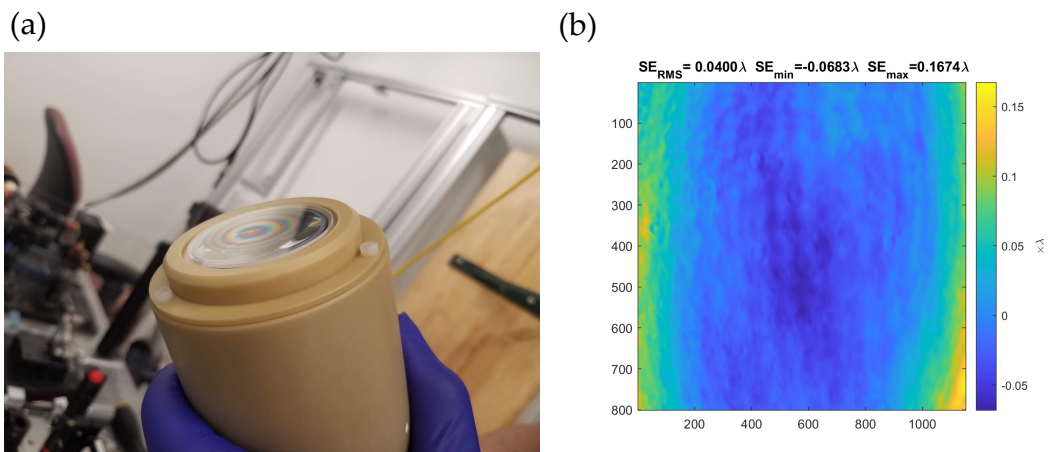


**Figure 4.2:** (a) Rainbow colored Newton rings are observed when fused silica plate is mounted on the objective flat front element. (b) Interferometric test of the surface flatness of the 1 mm fused silica plate.

It might seem problematic, but we can see from two aspects that this is actually nor-

mal and would not affect the performance of the objective. First, this piece of fused silica is specified with a transmitted wavefront error (TWE) of less than  $\lambda/10$  over the 90% clear aperture. Using the refractive index of fused silica at the wavelength range we are interested in ( $\sim 1.5$ ), this means the thickness variation is less than  $\lambda/5$  over the 90% clear aperture. The surface flatness is also tested using the interferometer (Figure 4.2 (b)). This actually suggests to the front glass plate supplied by Special Optics might be not flat. Second, the newton rings tells us that the thickness of the air gap between the flat front element of the objective and the fused silica plate varies less than  $2\lambda$  from the center to the edge with a fairly symmetric shape. The symmetric ring shape actually tells us that the plate is not tilted. Including these information into Zemax and we can see the performance is not affected (Figure 4.4).

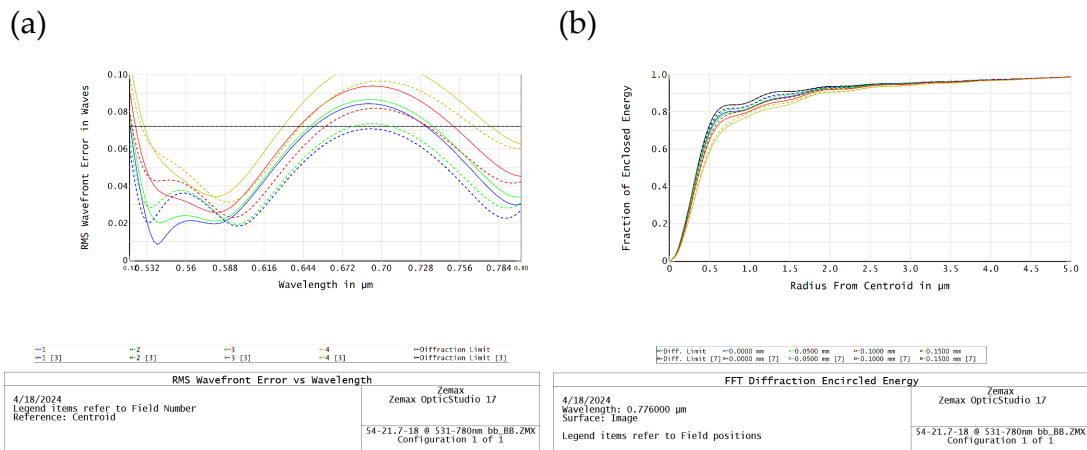


**Figure 4.3:** (a) RMS TWE of the objective setup at different wavelengths after replacing 1mm thick sapphire with 1mm thick fused silica, with (solid lines) and without (dashed lines) the effect of bowed fused silica plate. (b) FFT diffraction encircled energy of the objective setup described in (a).

## 4.2 INTERFEROMETRIC TEST OF OBJECTIVE AND GLASS CELL

To make sure that the imaging system and tweezer projection system can work at their best performance, we have to make sure that the delivered microscope objective is diffraction limited and the glass cell window has the correct thickness and flatness specification. We confirm these with a home built interferometer setup and imaging tests.

In the specification of our glass cell, we reduce the thickness of the window to 0.25 inch compared to the 0.5 inch thick off-shelf 3-inch diameter window design offered by the glass cell vendor (Precision Glassblowing of Colorado). This poses some risk of having a bent surface of the window when the glass cell is pumped down and introduce wavefront error. We choose to use COMSOL to quantitatively simulate this effect. The curvature is pretty rotational symmetric according to the simulation, as expected since the window is fused onto the skeleton that has a circular hole. The radius of the curvature of this bent surface is extracted from COMSOL and used for simulation in Zemax. We find that if the objective can be perfectly centered on the glass cell, the curvature can be simply compensated by refocus the objective a little bit and no obvious degradation of wavefront error can be observed.

To measure the flatness of the glass cell, one important aspect is that there are four surfaces in a fully assembled glass cell (two parallel windows, each one has two parallel surfaces) and they will all reflect similar amount of light. It is important to separately measure these four surfaces. To achieve that, we choose to build a "white light" Fizeau interferometer using incoherent light source that only reflection with matched optical path length can create interference. This is achieved using a 790 nm superluminescent diode (SLD) to seed a tapered amplifier. The amplified incoherent light is then fiber

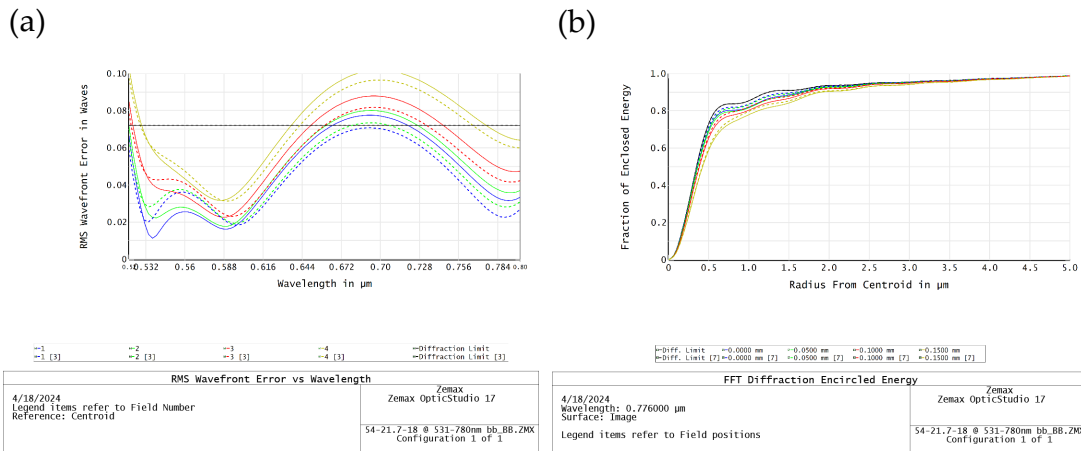


**Figure 4.4:** (a) RMS TWE of the objective setup at different wavelengths with (solid lines) and without (dashed lines) the effect of glass cell viewport bent inwards under vacuum. (b) FFT diffraction encircled energy of the objective setup described in (a).

coupled and deliver to an adjustable delay line (Figure 4.5 (a)). the light is power split and one branch delayed and recombined, finally send through a PM fiber on the interferometer board. On the interferometer board, a  $\lambda/20$  optical flat is used as a known flat reference surface. Only when the optical path length between the optical flat surface (reference surface) and the reflected surface of interest matches to the delay optical path length within the coherent length of the incoherent light, interferometric fringes can be see on the camera. The setup on the interferometer board is shown in Figure 4.5 (b).

To extract the surface geometry from the interference fringes, a technique called phase shift interferometry (PSI) is used. The delay line can be coarse scanned manually using the micrometer and there is a small piezoelectric stack actuator providing fine scan capability. The voltage on the piezoelectric actuator is scanned using a triangle wave which shifts the relative phase between the two arms of the delay line and cause the fringes to move on the camera. The interferogram are recorded as an im-

age sequence during the phase shift scan. The phase shift scan is parameterized with parameter  $t$ . We can see for two beams with intensity  $I_1$  and  $I_2$  on the detector, the detected intensity  $I(\varphi(t))$  will depend on  $t$ . By scanning the phase  $\varphi(t)$ , we can locate four intensity values  $I(\varphi(t))$  at four different  $\varphi(t)$  (Equation 4.2).

$$I(\varphi(t)) = I_1 + I_2 + 2\sqrt{I_1 I_2} \cos(\Delta\varphi + \varphi(t)) \quad (4.1)$$

$$\begin{aligned} I(\varphi(t) = 0) &= I_1 + I_2 + 2\sqrt{I_1 I_2} \cos(\Delta\varphi) \\ I(\varphi(t) = \frac{\pi}{2}) &= I_1 + I_2 - 2\sqrt{I_1 I_2} \sin(\Delta\varphi) \\ I(\varphi(t) = \pi) &= I_1 + I_2 - 2\sqrt{I_1 I_2} \cos(\Delta\varphi) \\ I(\varphi(t) = \frac{3\pi}{2}) &= I_1 + I_2 + 2\sqrt{I_1 I_2} \sin(\Delta\varphi) \end{aligned} \quad (4.2)$$

We can see that there will be enough degrees of freedom to determine  $\Delta\varphi$  with these four intensity measurement. Using the following relation, we can extract the value of a specific point  $\Delta\varphi$  on the phase diagram.

$$\tan(\Delta\varphi) = \frac{I(\varphi(t) = \frac{3\pi}{2}) - I(\varphi(t) = \frac{\pi}{2})}{I(\varphi(t) = 0) - I(\varphi(t) = \pi)} \quad (4.3)$$

Finally the phase diagram is unwrapped and both vertical and horizontal tilt (due to the surface of interest being not aligned parallel to the reference surface) is removed. Using this interferometer, we are able to measure the thickness of the glass, the parallelism between the two windows, two surfaces of each window and the flatness of each surface, completely contact-free.

We also measure the surface flatness of the glass cell primary viewport when the glass cell is pumped down to vacuum. The measurement result is shown in Figure 4.6 (a). We compare this measurement to the COMSOL simulation and find very

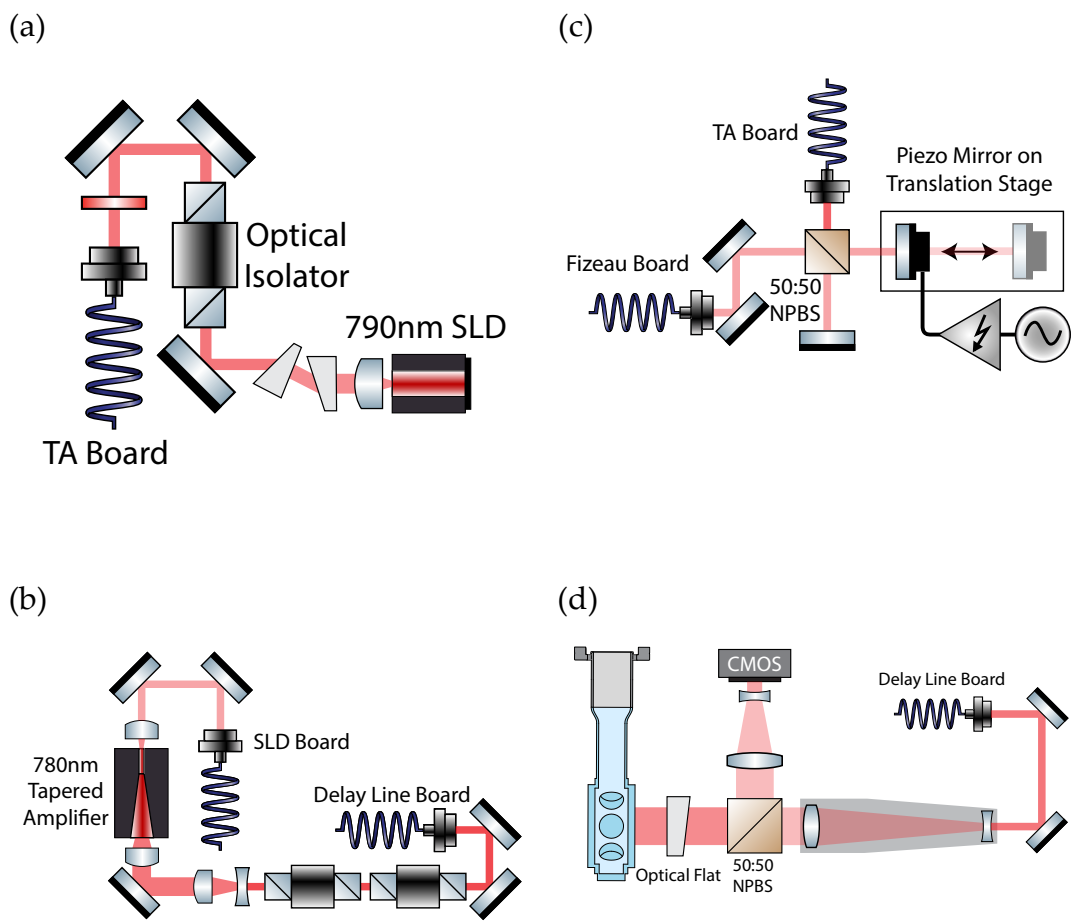


**Figure 4.5:** (a)-(b) Incoherent light source based on TA and SLD. (c) Optical delay line with coarse and fine scan capability. (d) Fizeau interferometer used in this work.

good agreement (Figure 4.6 (b)). The simulated radius of curvature is about 166 m, and Zemax suggested that this does not affect RMS TWE of the objective by more than  $0.02\lambda$  if there is a misalignment between the center of the glass cell viewport and the objective within the range allowed by the size of the viewport.

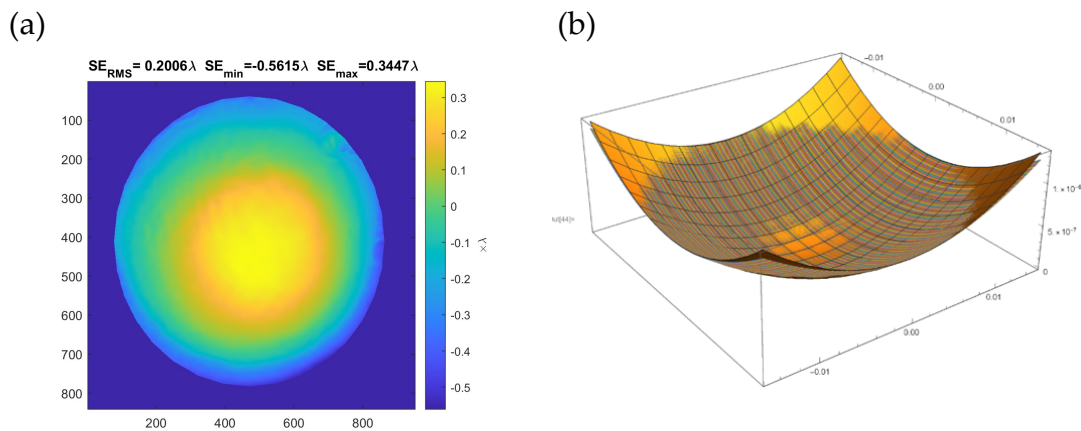


**Figure 4.6:** (a) The measured glass cell primary viewport deformation under vacuum. (b) Compare measurement to COMSOL simulation, measurement is shown in color dots.

After making this measurement, we decide to vent the glass cell to atmosphere pressure, and the image series in Figure 4.7 is what we see at the moment of vent. It is a very frightening moment, as a lot of reflection from the glass cell is observed, pointing to failure of the nano-textured AR coating on the glass cell. We quickly check the coating using a flashlight and find that the interior surface of the glass cell is indeed no longer AR. Fortunately, we find out this is due to the quick vent causing water vapor in the air to condense on the interior surface of the glass cell. The condensed water fills up the nano-textured structure, causing significant increase in reflectivity. After blowing dry nitrogen into the glass cell, the AR performance is recovered. It is a good idea to always vent these type of glass cells using dry nitrogen.



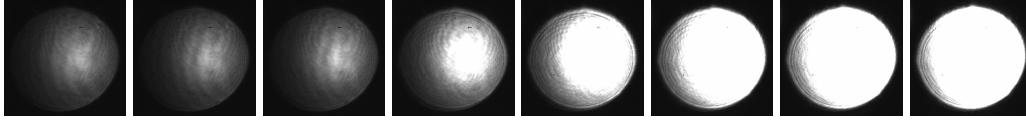


**Figure 4.7:** Interferometer raw image acquired during a glass cell vacuum vent.

The same interferometer can also be used to measure the TWE of objective. However, an interferometer usually works with a flat wavefront. To measure the performance of the objective, we could use the objective to convert a flat wavefront (optical flat) to a spherical wavefront. The wavefront error caused by the objective can then be interferometrically measured by comparing the converted spherical wavefront to a reference spherical surface. Here, we use a Grade-5 silicon carbide (SiC) bearing ball as the reference surface\*. The bearing ball is glued onto a stainless steel set screw and mounted on a 3-axis translation stage, inserted into the glass cell (Figure 4.8 (a)). We find that the objective has an RMS wavefront error of  $0.11\lambda$  at 790 nm, indicating close to diffraction limited performance. We also checked that this performance is reached when the front flat element of the objective is parallel to the glass cell. This is an important confirmation for future alignment of the objective on the experimental table, where no bearing ball is available inside vacuum for this alignment procedure. The wavefront measurement result is shown in Figure 4.8 (b).

These tests make sure that the objective meets its specification around test wavelength of 790 nm, but do not translate to other wavelengths. We also care about 606 nm for this objective, since that would be used for imaging. A simple way is to see if we can directly image a very tiny object through this objective. We use a fluorescence nano sphere (“Pink”, SPHERO™, Spherotech) with a diameter of 40 nm ~ 80 nm, well below the optical resolution of our objective. It is quite confusing that the “Pink” dye actually

---

\*The smaller the grade number, the better the quality of the bearing balls.

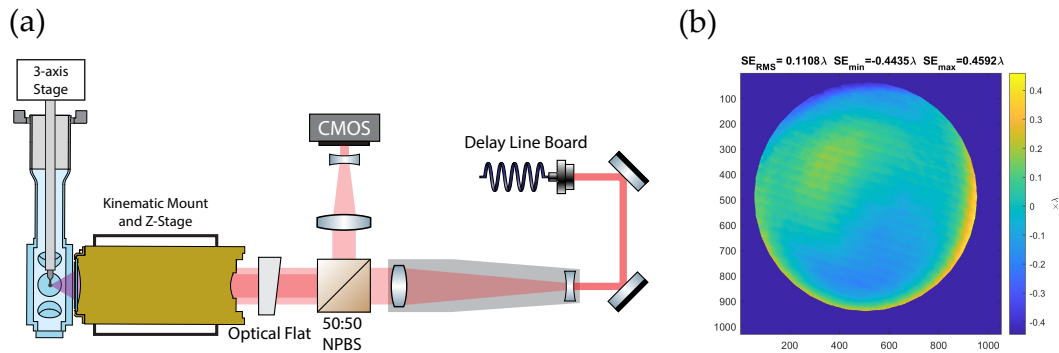


**Figure 4.8:** The setup of the objective transmitted wavefront error test using a bearing ball. (b) The transmitted wavefront error measured using a bearing ball and Fizeau interferometer.

absorb yellow-green light and emit orange light, as shown in Figure 4.9 (a). The fluorescence nano spheres are delivered in a mixture with water. We suspend them by diluting the mixture with isopropyl alcohol and then sonication the mixture for several minutes. A drop of the mixture is then applied to a piece of microscope cover glass and all the solvents are evaporated by heating on a heat plate. The dye inside the fluorescence nano spheres will be pumped by a shorter wavelength (in our case, we borrowed some 574 nm laser from CaOH experiment, which is their  $X - B$  100 repump laser) and emit around 610 nm. The microscope cover glass is replacing the bearing ball and inserted into the glass cell. We then collect that fluorescence through the aligned microscope objective and focused onto the camera with a 750 mm long focal length achromatic lens and a 610 nm narrow line interference filter. We are able to locate single fluorescence nanospheres (not clustered) and extract the point spread function (PSF) from the images. An Airy ring can also be observed in the image.

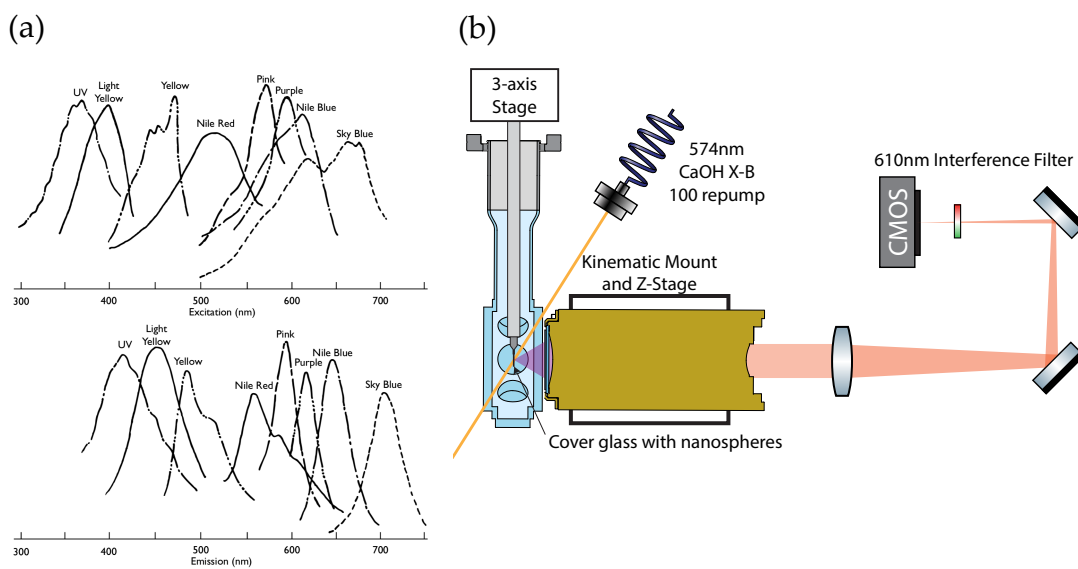


**Figure 4.9:** (a) Absorption and emission spectrum of the Fluorescence nanospheres. “Pink” nanospheres are used in this test. Reproduced from datasheet of SPHERO™ fluorescent particles. (b) Setup of the objective PSF test.

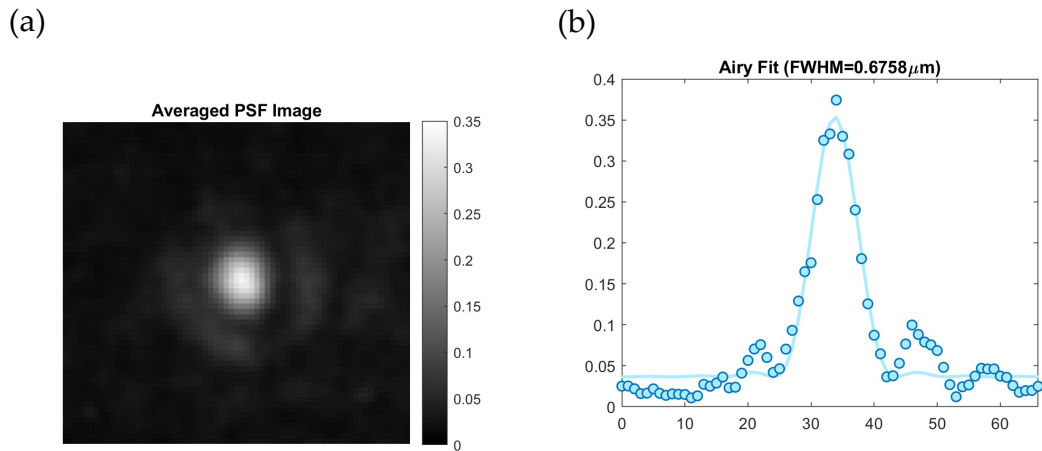


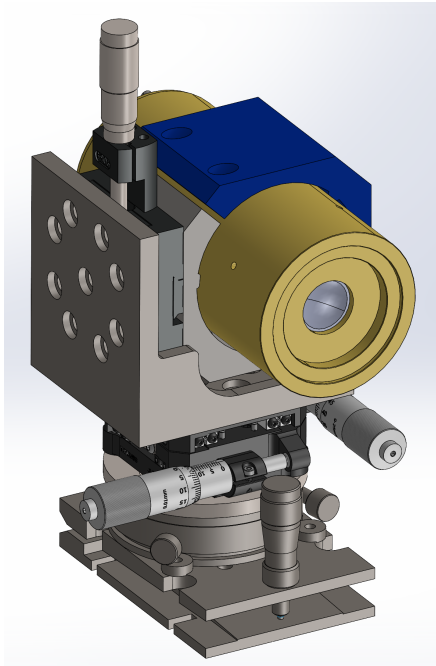
**Figure 4.10:** (a) The PSF of the objective measured at 610 nm using fluorescence nanospheres and an imaging lens with 750 mm long focal length. (b) 1D fit of the cross section of the measured PSF to an Airy model.

#### 4.3 ALIGNMENT PROCEDURE

The objective is mounted on the experimental table by a five-axis translation stage built from individual translation stages (Figure 4.11). From the table to the objective, we have a tilt platform (TGN80, Newport), a rotational stage (UTR80S, Newport), an XY translation stage (LX20, Thorlabs), a vertical translation stage (9064-X, Newport). Translation stages are assembled together using custom made stainless steel adapters. The objective is gently clamped by a 3D printed plastic clamp onto the stainless steel holder through line contacts.

Once the objective is moved onto the experimental table, aligning the objective to reach diffraction limit performance is not that hard, thanks to the flat front element of the objective. We realize this by shooting a low power visible laser beam from more

(a)



(b)

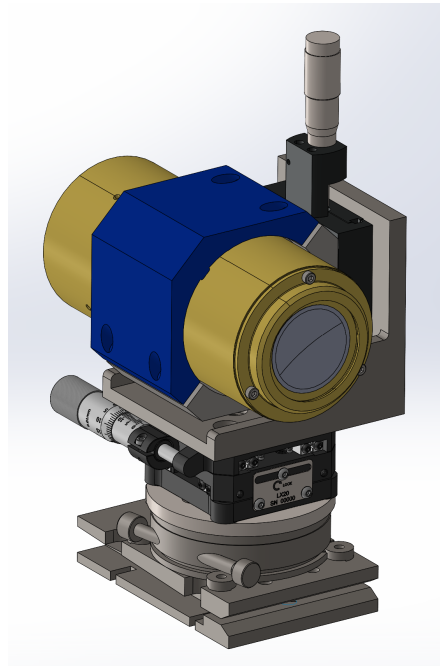
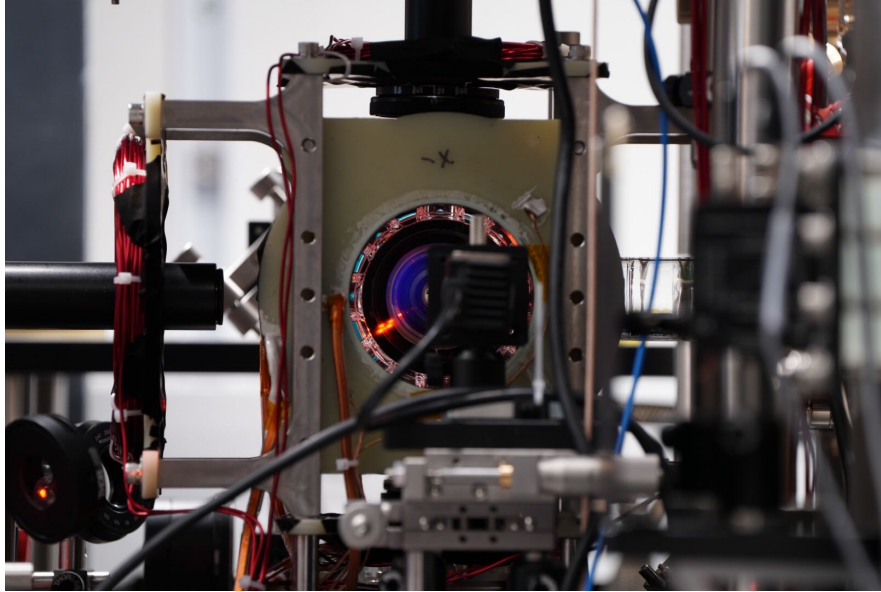


Figure 4.11: (a)-(b) Microscope objective mounted on a five-axis translation stage.

than 5 m away onto the glass cell and objective. We are able to detect the laser spots of the reflection from the four surfaces of the glass cell and the surface of the objective front element. By walking the incident angle of the visible laser beam, we can overlap the four reflection spots from the glass cell surfaces, at which point the incident laser beam is perpendicular to the glass cell surface. We then use the rotational stage and the tilt platform on the objective mount to overlap the reflection spot from the objective front element to the reflection from the glass cell surfaces. This step ensures that the objective front element is in parallel with the glass cell surface. At a distance of  $\sim 5$  m, with a laser beam diameter of  $\sim 3$  mm and assume we can distinguish one waist (radius) away from the center of the beam, we can easily achieve alignment precision of  $\sim 0.15$  m rad, which is more than enough according to Zeman simulation. Although we have discussed in the previous section that the performance of the objective is not very sensitive to the alignment of the objective and the center of the viewport, we still roughly align it. This is realized by imaging the glass cell and the objective using a long focal length ( $f = 400$  mm) camera lens on a digital camera (Figure 4.12). The circumference of the glass cell viewport and the objective is identified from the picture and marked manually. These manually marked points are fitted into a circle for viewport and another circle for objective. The amount of translation required is calculated from the distance between the centers of the two circles. We then use the translation stages to align it, and repeat the process to confirm that the centers are aligned. Similar technique could be used to record and align the position of the magnetic field coils onto the glass cell.

Next step is to align the objective field of view (FoV, which is  $\sim 100$   $\mu\text{m}$  radius) to the center of the transported ODT of molecules, which is not an easy job. The challenges are weak signals from the relative small number of molecules in the ODT, and small FoV of the objective. It is obvious that we have to locate the position of transported



**Figure 4.12:** Align objective to glass cell center using a long focal length camera lens.

ODT and use that position information to guide the alignment process.

Here, we choose to build a temporary imaging system, which is based on a low read-out noise CMOS camera (Allied Vision, Alvium 1800 U-319m). One 50 mm focal length doublet achromatic lens (AC254-050-A, Thorlabs) is used to collimate the light from a point source in the glass cell, the collimated light is then passed through a dichroic mirror angled at  $45^\circ$  and an interference filter. Finally, the filtered light is focused onto the camera sensor using another doublet achromatic lens. This setup is shown in the upper part of Figure 4.13.

This system is used to image the transported ODT on the opposite side of the objective. It is easier to locate the ODT position using this temporary imaging system, since the FoV of this system is much larger than the tweezer imaging system. We use software binning during the initial search for the transported ODT, and the relatively

low readout noise of the CMOS camera allows us to see the ODT in a single shot. We then adjust the focus of the temporary imaging system using the translation stage to minimize the fitted width of the transported ODT. The pixel coordinates of the center of the transported ODT are then written down as the reference of following alignment steps.

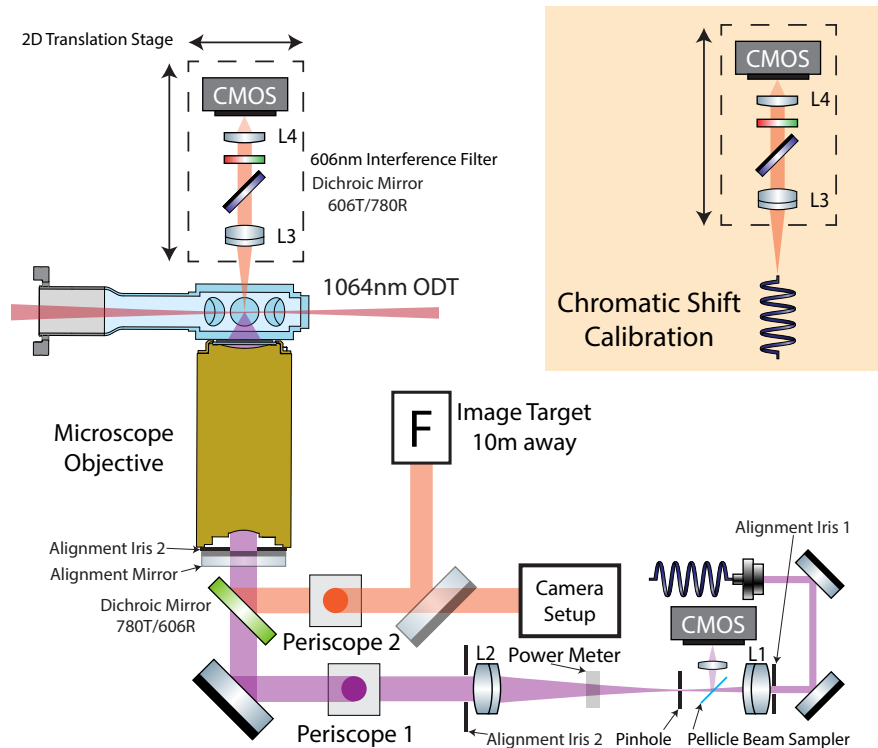


**Figure 4.13:** Objective alignment beam path.

First, we have to align the 1:4 telescope for the 776 nm tweezer beam. this is done by adding two alignment irises (alignment iris 1 and 2) on the lens tube of the two achromatic lens. We translate the lens position so most of the power is transmitted through a shrunk iris. The spacing of the telescope is adjusted so the expanded beam is collimated over  $\sim 10$  m distance. It is perfectly fine to use a shear interferometer to



check the collimation of this beam. However, one must be careful that the wedged glass plate is precisely aligned to the frame of the shear plate in factory. During the initial aligning attempts, we were badly tricked by a shear plate that was once dropped with glass plate broken off and “reassembled” by someone using 5-minute epoxy.

Next, we have to make sure that tweezer focus is inside the FoV of the objective, which is equivalent of sending collimated light that is along the optical axis of the objective. The SM2 thread on the back of the objective is precisely machined and we will use that as a reference for optical axis. We place a 25  $\mu\text{m}$  pinhole that is mounted on a X-Y translation stage at the focus of the relay imaging plane. We place a power meter sensor after the pinhole, and move the pinhole to maximize the power reading to allow the pinhole coincident with the image of the tweezer on that plane. A pellicle beam sampler is placed at 45° before the pinhole. The back reflected light from the alignment mirror can pass through the pinhole, being picked off by the pellicle beam splitter and detected by a CMOS camera. The kinematic mirror mounts of the periscope 1 is then used to align the back reflected light through pinhole and onto the CMOS camera. This finishes aligning the tweezer beam to be parallel to the objective optical axis.

Since the FoV of the objective is referenced to the optical axis of the objective, without moving the ODT, one has to mechanically translate the objective in order to place the ODT in the FoV. We simply translate the objective so the 776 nm light leaking through the filters focuses on the temporary imaging system camera where the ODT fluorescence is. Translating the objective will not change the relative position of optical tweezer compared to the FoV center (the tweezer beam is always parallel to the optical axis of the objective), but it will crop the collimated tweezer beam before the objective. This is because we are using the maximum numerical aperture of the objective and the tweezer beam is almost the same size of the objective back aperture. This is corrected

by walking the collimated tweezer beam using the same kinematic mirror mounts of the periscope 1 to maintain the same tweezer light image on the temporary imaging camera (keep the tweezer beam parallel with the optical axis of objective), while shifting the center of the tweezer beam towards the center of the objective back aperture. The tweezer beam and objective back aperture both have a large diameter, so it is hard to tell the overlap of the center. We solve this problem by placing an alignment iris 1 on the SM2 thread at the back of the objective.

Finally, one has to adjust the focus of the microscope objective to the center of ODT. However, the temporary imaging system is not achromatic enough, and has to be calibrated before used for the alignment. We took the whole temporary imaging system with the translation stages off the table and use the temporary camera to image a tip of a single mode fiber, shown in the top right corner of Figure 4.13. When switching the laser wavelength into the fiber between tweezer wavelength (776 nm) and imaging wavelength (606 nm), we have to move the temporary imaging system along the optical axis a small amount to keep the image on focus. This small distance can be measured using the micrometer on the translation stage that the temporary camera is mounted on. This distance is measured to be 280  $\mu\text{m}$  in our case, matching the specification given by the vendor. The temporary camera is then mounted back to the experiment, where the position of the camera is adjusted so image of ODT is in focus on the camera. We then move the temporary camera translation stage by the calibrated chromatic shift distance, so any objects emitting tweezer wavelength will be in focus on temporary camera. We then turn on the tweezer laser, adjust the focus of the microscope objective, so that the tweezer projection in the glass cell is on focus when imaged by the temporary camera. At this moment, the tweezer projection is overlapped with the center of ODT.

One feature of our objective is that it is achromatic for the tweezer wavelength and

imaging wavelength. As we can see from Figure 4.1 that our objective meets this criterion for three design wavelengths (apochromatic). This greatly reduce the difficulties during focusing, and is usually an option during the design stage of the microscope objective. After the alignment, as a sanity check, we place a temporary mirror to direct the 606 nm beam path to a image target that is placed  $\sim 10$  m away, and use the temporary imaging system for imaging the target. We see the image target is close to focus, confirming that the objective is achromatic.

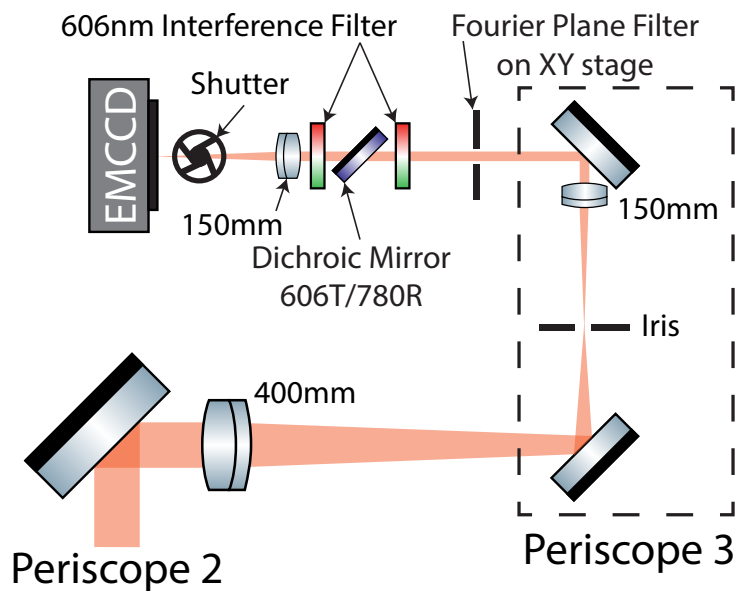


**Figure 4.14:** Tweezer imaging beam path.

The tweezer imaging system is built around a low noise electron-multiplying charge coupled device (EMCCD) camera (iXon Ultra 897, Andor). The tweezer imaging system is assembled off the table using mostly Thorlabs lens tubes and cage mount systems, with the beam path shown in Figure 4.14. The assembly is focused by imaging an object in the lab  $\sim 10$  m away. To properly align the collimated fluorescence collected

by the objective into the tweezer imaging system, we put the alignment mirror back to the objective, and reflect the tweezer beam into the tweezer imaging system (after a lot of attenuation from the interference filters and dichroic mirrors). The kinematic mirror mounts on the periscope 2 is then used to position the tweezer to the center of the camera sensor, while making sure the beam is hitting the center of the first lens of the tweezer imaging system.

After performing the full alignment procedure, fluorescence signal of single molecules in the tweezer just shows up on the camera without much effort.

#### 4.4 TWEEZER IMAGING

The upgrade to high NA objective on Gen2 experiment makes it harder to maintain orthogonal between  $\Lambda$ -imaging beams from each axis. When we initially observe tweezer loading signal, we use a imaging beam configuration shown in Figure 4.14 (a). We find the imaging lifetime is very short in such setup, much shorter than what we observed in Gen1 experiment.

We observed relative low loading efficiency after optimizing the trap depth of the optical tweezers. The highest loading probability we observed with a small waist optical tweezer is about 40%. This is lower than the loading probability we observed in the Gen1 experiment, which is very close to 50%. We tried to use the zoom collimator on Gen2 experiment to reduce the NA so the waist would match Gen1 experiment, and 50% loading efficiency can be recovered. We do not have a good explanation of this loading probability limitation in small waist optical tweezers yet.

We find that the non-destructive imaging fidelity (the survival rate of molecules after first imaging pulse) is partially limited by off-resonant photon scattering from the

imaging light. This process pumps the molecules into  $|X, v = 0, N = 3\rangle$  states through  $|A, v = 0, J = 3/2, +\rangle$  state. By adding a  $N = 3$  rotational repump laser driving the transition between  $|X, v = 0, N = 3\rangle$  and  $|B, v = 0, N = 2\rangle$ , we are able to reach detection fidelity of 98(1)% and 94(1)% non-destructive imaging fidelity (the probability that a molecule survives the imaging process in the tweezer). We use an EOM that is similar to our  $N = 1$  hyperfine EOM, but resonant at  $\sim 36$  MHz, to add sidebands to this rotational repump laser. A sample of the histogram of the camera ADC counts in the imaging region of interest (ROI) is shown in Figure 4.15.

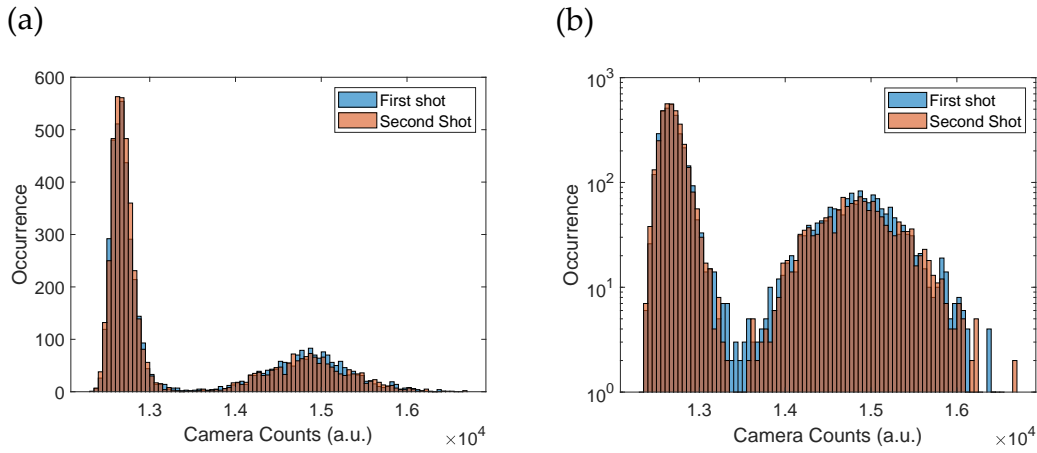


**Figure 4.15:** Tweezer ROI histogram of the first image shot and second image shot, plotted in linear scale (a) and logarithmic scale (b). Imaging exposure time is 15 ms.

#### 4.5 MAKING IT AN ARRAY

We choose 776 nm as the wavelength of our optical tweezer. The tweezer laser is generated by frequency doubling of a 15 W Erbium doped fiber amplifier. To reduce the effect of relative intensity noise (RIN) from the seed laser, we choose to use a 1552 nm semi-

conductor laser as seed laser (RIO ORION). The tweezer laser is initially provided by a NKT Photonics BOOSTIK-HP amplifier seeded by an RIO ORION 1552 nm seed and HARMONIK frequency doubler. This amplifier shows unstable relative intensity noise (RIN) performance during its early service and a monitor photodiode connected to a spectrum analyzer has to be used to make sure the RIN is within specification. After sharing it with the first generation experiment for less than 2 years, the laser failed abruptly. Later, it turns out the NKT Photonics BOOSTIK-HP amplifiers are suffering repeated quality issue, where a brand new replaced amplifier died again within 6 month. Finally, we switched to a new system (EFA-SSHG-780-8-CW, Precilasers), which shows good RIN performance at different pump current settings. The new system adopts a dual MgO:PPLN crystal design that provides up to 9.4 W of 776 nm.

The laser is then split into two branches and going through two AOMs for switching and intensity servo, and coupled into two PM780-HP fiber. To avoid beat note between the neighboring interleaved tweezer array causing heating, one AOM is shifting frequency up while the other one is shifting frequency down. This moves the beat note frequency to 200 MHz, far away from tweezer trap frequency. As a useful note on passing high power single frequency NIR lasers through optical fibers, we find that a standard 2 m long Thorlabs PM780-HP fiber patch cord can deliver 6.5 W of single frequency 776 nm power, without hitting spontaneous Brillouin scattering (SBS) limit. For long term reliability, we restrict the power for each fiber to be less than 4 W and switched to an air-gapped and end-capped fiber patch cord (OZ-optics) based on the same PM780-HP optical fiber.

The output of the optical fiber is collimated by a zoom fiber collimator (ZC618APC-B, Thorlabs). This collimator allows us to change the diameter of the collimated beam without swapping lens and realigning the beam path. This changes the numerical aper-

ture we were using and can be used to vary the tweezer waist size. The beam is then further expanded using a 2x telescope (GBE02-B, Thorlabs) and send through a 1-D AOD (DTSX-400, AA optoelectronics). We start with an 1-D array, but it is entirely possible to upgrade to a 2-D array in the near future. The AOD is driven by a high linearity (high OIP<sub>3</sub>) RF amplifier (ZHL-5W-1+, Mini-circuits), where the driving signal is generated by a PCI-E AWG card (M4i-6631-x8, Spectrum Instrumentation GmbH). The AWG card is controlled by a custom Python software detailed in Appendix E.

To avoid saturating the RF amplifier and AOD, it is important to look for an optimized phase relation between all individual frequency tones. As one can easily see, if there are  $N$  frequency tones with unity amplitude and equal starting phase, the maximum amplitude would be  $N$ . However, if an optimized phase is used, the maximum amplitude can be reduced to almost  $\sqrt{N}$ . We show here that by randomly generate

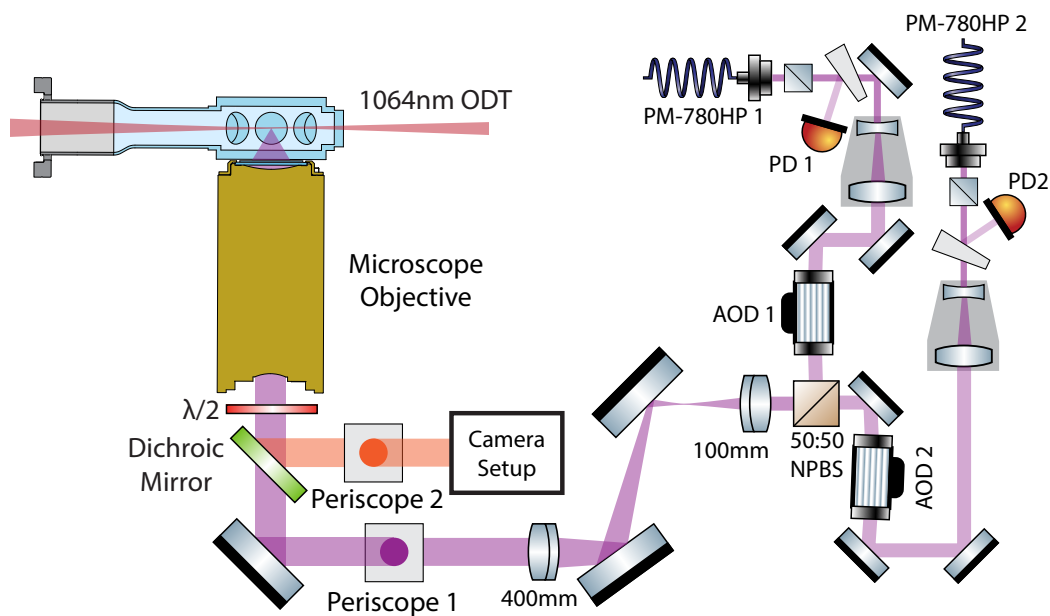


**Figure 4.16:** Dual AOD tweezer beam path.

To create a dual AOD array, two sets of fiber collimators, telescopes and AODs are installed with almost identical beam paths. The diffracted beam from the AOD is then combined with a 50:50 non-polarizing beam splitter, where half of the power is lost. The combined beam is then sent through the 1:4 Keplerian telescope and a dichroic mirror, finally into the back aperture of microscope objective. The full beam path setup for the optical tweezer array is shown in Figure 4.16. The performance of the full optical train is verified by Zemax.

Rearranging a 1-D tweezer array requires turning off the frequency tones for empty tweezers and sweep the frequency tones of the loaded tweezers to target array positions. Since we choose to pre-compute required waveforms for the frequency sweeps, phase for all the frequency tones should be continuous when switching between waveforms. When we first try rearranging, this phase was incorrectly programmed due to an error in the waveform generation code. This results in large loss observed when moving tweezers across the array. It was quite confusing, since the discontinuity of the phase is almost random for different moving distance (Figure 4.17 (a)). Once the bug is fixed and the phase is kept continuous, we observe the loss during a short rearranging distance is dominantly limited by finite surviving probability of the  $\Lambda$ -imaging (Figure 4.17 (b)). An example of the images taken before and after rearranging process is shown in Figure 4.18.

#### 4.6 PROPERTIES OF OPTICAL TWEEZERS

The geometry of the optical tweezer is defined by their waist at the focus. We could not easily measure the size of the waist in vacuum. Instead, we could measure the trap frequency of the molecules in the tweezer. Together with the measured optical



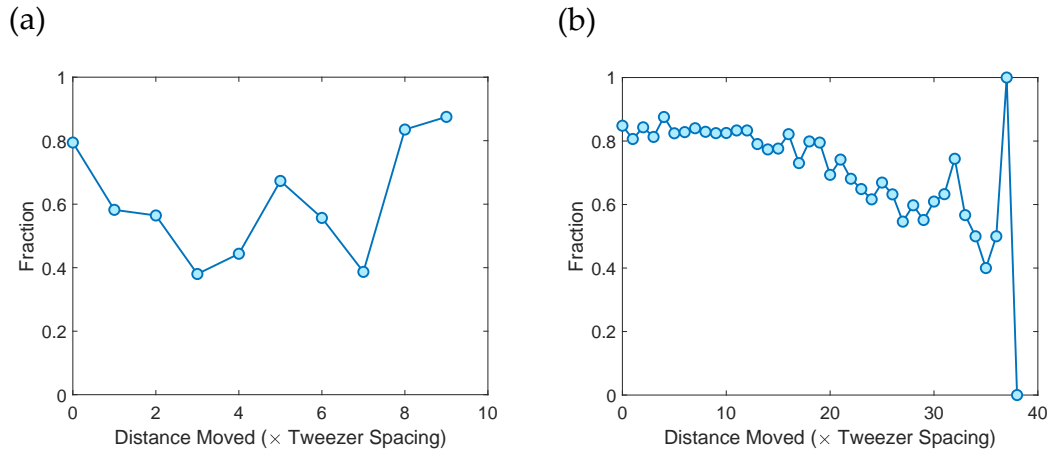


**Figure 4.17:** (a) Survival fraction versus number of tweezer spacing distance moved during rearranging in a 10-site tweezer array with incorrect phase. (b) Survival fraction versus number of tweezer spacing distance moved during rearranging in a 40-site tweezer array with correct phase.

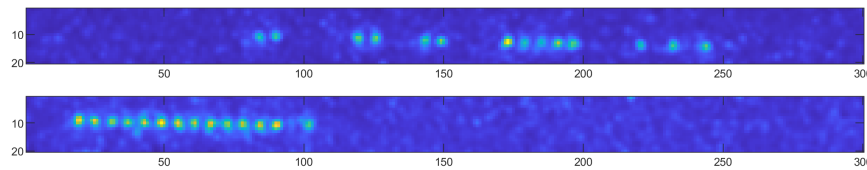


**Figure 4.18:** 1-D tweezer array rearrange. Top image is the first image of randomly loaded tweezers, and is used for identification. Second image is confirmation of rearranging towards left side of the array.

power per tweezer trap, we can compare the result using the calculated trap frequency to estimate the waist of the tweezer.

To measure the trap frequency, we use parametric heating method. Parametric heating is a phenomenon that when we modulate the trap depth of the tweezer at twice of the trap frequency, fast heating and loss of molecules can be observed. In the experiment, we use the AOM before the PM780-HP fiber to modulate the trap depth at different frequencies, while keeping the cycles of modulation the same. We then lower the trap depth adiabatically to let heated molecules leaving the trap, and finally bring the trap depth back for detection. A loss feature can then be seen on the spectrum (Figure 4.19 (a)), located at twice the trap frequency. At initial stage, we limit the NA using the zoom collimator to reduce clipping of the Gaussian beam at the back aperture of the objective. We measured our trap frequency to be 191(2) kHz in the radial direction and 33.5(5) kHz at axial direction with  $\sim 38$  mW optical power per trap delivered into the glass cell. This measurement gives us an estimation of the actual waist of the tweezer of 970 nm. The zoom collimator is later tuned to use the full aperture and we observe the waist of the tweezer is 830 nm.

The temperature of the trapped molecules in the optical tweezers is measured using the release and recapture technique<sup>120</sup>. The optical tweezers are quickly turned off for various length of time and then quickly switched back on to re-capture the molecules that are still inside the trap volume. We use the optical tweezers' beam geometry derived above as input parameters for a Monte-Carlo simulation of the trajectories of molecules during release and recapture sequence. An example of the measurement is shown below in Figure 4.19 (b).

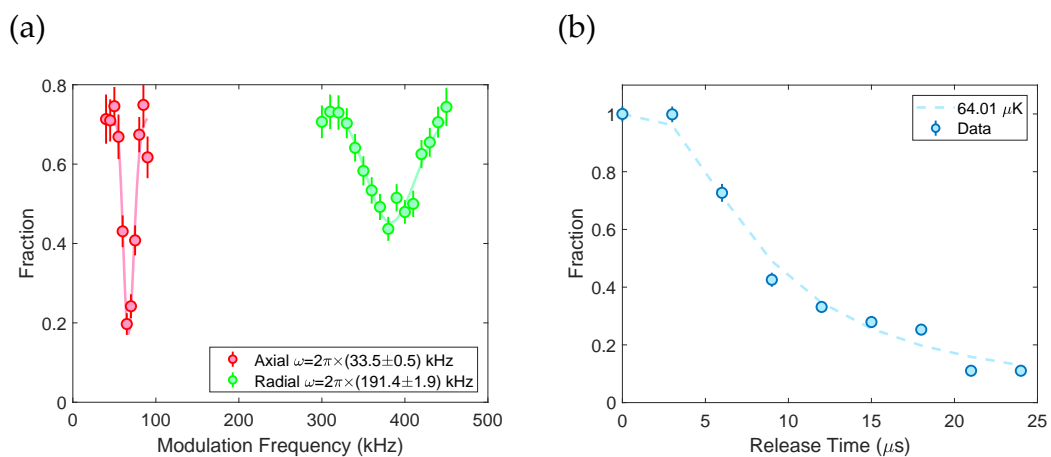


**Figure 4.19:** (a) Trap depth modulation spectroscopy showing two parametric heating loss features. The lower frequency feature is parametric heating on the axial direction. The higher frequency feature is parametric heating on the radial direction. (b) An example of release and recapture measurement of the temperature of the molecule in the optical tweezer trap. Data is fitted to a Monte-Carlo simulation.

# 5

## Dipolar Interaction Between Molecules in Optical Tweezers

One of the reason that we are interested in studying ultracold molecules is utilizing the permanent electric dipole moments of molecules. In the application of realizing a digital quantum computer, three basic ingredients are required. One is a good qubit that preserves the quantum state (storage). Second is the ability to perform high fidelity sin-

gle qubit gate (single qubit rotations/gates). Third is the ability to perform high fidelity two-qubit gate operations (two-qubit or multi-qubit gates). The first two ingredients can be apply to individual qubits. To realize the last requirement, one needs at least two qubits and some kind of robust interaction between them. Entanglement is created in a two-qubit gate, which is considered an essential resource for quantum information processing, but remains generally challenging to create experimentally.

For heteronuclear diatomic molecules, we could use their permanent electric dipole moment to mediate interaction. A key milestone towards using ultracold polar molecules for quantum simulations and multi-particle quantum gates is the generation of coherent dipole-dipole couplings between molecules<sup>45,93</sup>, which has been shown in sparsely filled 3D lattices<sup>130</sup>, 2D layers<sup>118</sup>, and in a molecular quantum gas microscope<sup>29</sup>.

### 5.1 DIPOLAR INTERACTION

Dipolar interaction has been observed in many quantum systems. Electric dipole-dipole interaction is stronger than magnetic dipole-dipole interaction by roughly a factor of  $1/\alpha = 137$ . Dipolar interaction has an characteristic scaling of  $1/r^3$ . This means to reach similar interaction strength, magnetic dipoles have to be placed  $137^{2/3}$  times closer than electric dipoles. To successfully observe coherent dipole-dipole interaction between single magnetic atoms, it would require placing atoms very close to each other and maintain a long coherence time. A good example would be Erbium atoms, which possess a large magnetic dipole moment of  $\mu = 7\mu_B$ . The interaction strength between a pair of Erbium atoms trapped in neighboring sites of an optical lattice with 266 nm lattice spacing is only  $2\pi \times 30$  Hz<sup>114</sup>. Another example is Dysprosium atoms with  $\mu = 10\mu_B$ ,

the interaction strength is around  $2\pi \times 20$  kHz at 50 nm distance between layers achieved using a method resembling super-resolution<sup>38</sup>. For CaF molecules used in this thesis, the electronic ground state has a permanent electric dipole moment of 3.07 Debye. Note that this is the electric dipole moment in the molecular frame. In the experiment, one can only observe dipole moment when the molecules is fully polarized (aligned) in the lab frame, usually requires very high DC electric field. Our apparatus currently does not have in-vacuum high voltage electrodes installed, thus polarizing the molecules in the lab frame using DC electric field is not an option. However, it is possible to use a microwave field that is close to the rotational transitions to polarize the molecules. Due to the choice of the states in this work, the effective electric dipole moment is only  $\sim 1$  Debye. As we will see in this chapter, similar interaction strength can be achieved with molecules trapped several micrometers apart, making it possible to use optical tweezer arrays for this work.

The dipolar spin-exchange interaction Hamiltonian in the absent of external DC electric field<sup>45</sup> is

$$H_{dip} = \frac{J}{2}(\hat{S}_1^+ \hat{S}_2^- + \hat{S}_1^- \hat{S}_2^+) = J(\hat{S}_1^x \hat{S}_2^x + \hat{S}_1^y \hat{S}_2^y) \quad (5.1)$$

where  $\hat{S}_i^+$  ( $\hat{S}_i^-$ ,  $\hat{S}_i^x$ ,  $\hat{S}_i^y$ ) is the spin- $\frac{1}{2}$  raising (lowering, Pauli-X, Pauli-Y) operator for molecule number  $i$  in a tweezer pair.  $J$  is the dipolar interaction strength that can be further expressed as

$$J = \frac{d^2}{4\pi\epsilon_0 r^3} (1 - 3 \cos^2 \theta) \quad (5.2)$$

where  $d$  is the transition dipole moment between the  $|\uparrow\rangle$  and  $|\downarrow\rangle$  state ( $d \approx 1$  Debye),  $\epsilon_0$  is the vacuum permittivity,  $r$  is the inter-molecular spacing and  $\theta$  is the angle between the quantization axis and the inter-molecular axis direction. Apart from molecular systems<sup>130,79,29</sup>, this XY spin Hamiltonian was previously studied with Rydberg atoms in

optical tweezers<sup>33</sup> and atoms in optical lattices<sup>34,66</sup>.

## 5.2 INITIAL STATE PREPARATION

For this work, we first start with a twenty-site array formed by a single AOD. After loading and identification of tweezers that are loaded with a single molecule using  $\Lambda$ -imaging, the population of molecules are distributed over all twelve hyperfine states in the  $(X, v = 0, N = 1)$  rotational manifold. We would like all the molecules to be initialize in a single quantum state before applying any coherent operations. We use optical pumping to initialize the population in a single state and use microwave to transfer the population to the desired state. Using short  $X - A$  laser pulses resonant with all hyperfine levels in  $(X, v = 0, N = 1)$  manifold *except* the  $|X, N = 1, F = 0, m_F = 0\rangle$  state, we pump most of the molecular population into the latter state. This is a simple but coarse optical pumping scheme, as it can be affected by off-resonant scattering, resulting in a relatively low efficiency. In the experiment, we see that the optical pumping efficiency saturated at around 80% using this method. It would be better to switch to an optical pumping scheme that has a robust dark state, for example, optical pumping into a stretched  $m_F$  state, as demonstrated in 59.

The trap depth of the tweezers is then linearly ramped down in 5 ms and a bias magnetic field of  $\approx 3.2$  G is applied. A subsequent microwave  $\pi$ -pulse transfers the population from  $|X, N = 1, F = 0, m_F = 0\rangle$  to the  $|X, N = 0, F = 1, m_F = 0\rangle$  state (Figure 5.1). Finally, an  $X - A$  laser pulse containing frequencies to drive all the hyperfine components is applied to remove any molecular population left over in the  $(X, N = 1)$  manifold. In the end, all the remaining molecules in the array are in the  $|X, N = 0, F = 1, m_F = 0\rangle$  state, initializing the qubits. We can then map  $|X, N = 1, F = 0, m_F = 0\rangle \equiv |\uparrow\rangle$  and

$|X, N = 0, F = 1, m_F = 0\rangle \equiv |\downarrow\rangle$  states, which effectively encoding a spin- $\frac{1}{2}$  model in the subspace spanned by the two hyperfine states (Figure 5.1). The total state preparation and detection efficiency is 60(2)%, limited by residual population in other hyperfine states within  $(X, N = 1)$  due to the coarse optical pumping and imperfect imaging fidelity.

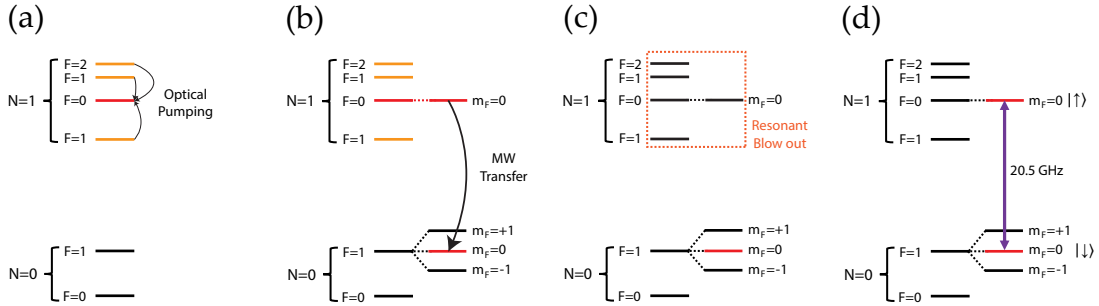


**Figure 5.1:** Relevant rotational ( $N$ ) and hyperfine ( $F$ ) states in the ground electronic state of CaF. Figure (a)-(d) show steps of state preparation using optical pumping, microwave transfer and resonant blow out.

### 5.3 ROTATIONAL COHERENCE AND MICROWAVE SETUP

To observe coherent dipolar spin-exchange interactions, a long rotational coherence time comparable to the time scale of the dipolar interaction is required. Starting with a sample of molecules at finite temperature in optical tweezers, it is important to control the differential AC Stark shift broadening due to molecule’s thermal motion in the tweezer trap<sup>90,110,24,80</sup>. We have already investigate this issue on our first generation of the CaF experiment<sup>19</sup>. To suppress this broadening, the tweezer laser is linearly polarized at a “magic” angle relative to the quantization axis defined by the applied bias magnetic field (Figure 5.2).



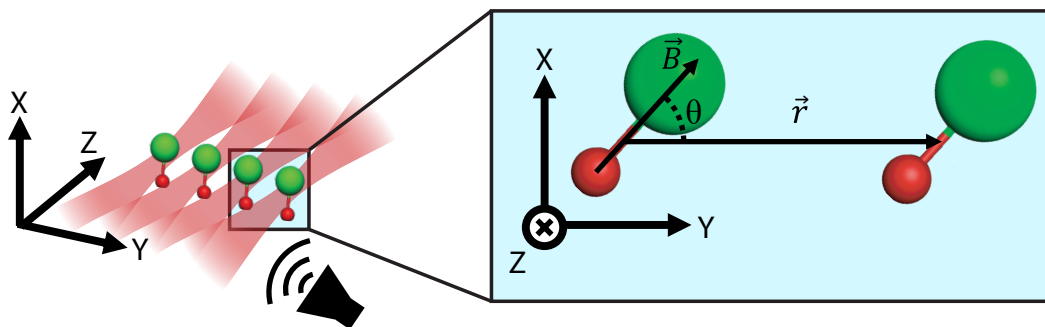


**Figure 5.2:** Cartoon of optical tweezers and the coordinate system used in this work. For visual clarity, only four sites of the realized twenty-site array are depicted. Between a pair of tweezers, we define  $\theta$  as the relative angle between the applied bias magnetic field  $\vec{B}$  (in the XY plane) and the inter-molecular vector  $\vec{r}$ . The tweezer light propagates along Z.

We first made a very simple microwave setup to drive the transition between  $N = 0$  and  $N = 1$  manifolds. Since this is a electric dipole ( $E1$ ) allowed transition, transition dipole moment is relative large and high power microwave is not required to reach a reasonable Rabi frequency. We start with a setup that consists of two signal generators, one outputs 18.5 GHz and another one outputs 2.0 GHz. A frequency mixer is used to mix the two frequencies and create 20.5 GHz microwave signal. The diagram of this simple microwave setup is shown in Figure 5.3. The microwave is delivered to the molecules in the glass cell using a commercial microwave horn antenna (PE9852B/2F-20, Pasternack). All the microwave equipment is locked to a 10 MHz reference clock provided by a GPS disciplined oscillator (FS752, Stanford Research Systems).

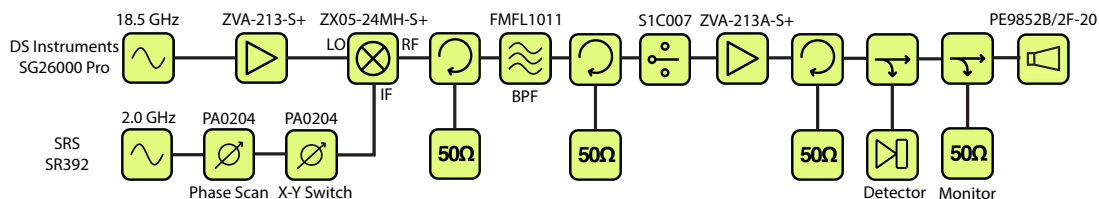


**Figure 5.3:** The diagram of the simple microwave setup.

Using this setup, we are able to drive the molecules out of the  $|N = 1, F = 0, m_F = 0\rangle$  state and observe coherent Rabi oscillations on all the tweezers in the array.

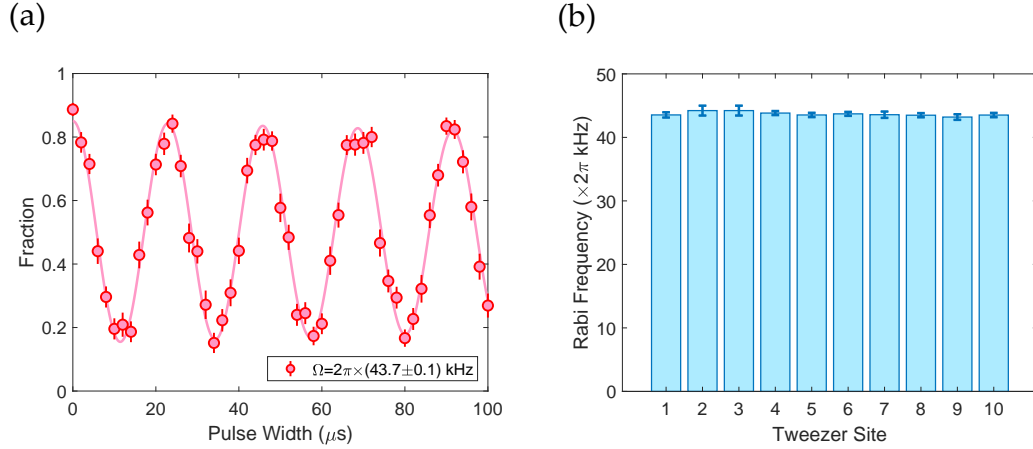


**Figure 5.4:** (a) Coherent Rabi oscillation averaged over 10 sites in an optical tweezer array. (b) Rabi oscillation frequency per tweezer site.

To maximize the single qubit coherence time, it is beneficial to adiabatically lower the trap depth as much as possible without unduly spilling molecules from the trap. We demonstrated up to 97 ms long rotational coherence time on CaF molecules trapped in optical tweezers in the first generation experiment using the “magic angle” condition. However, this is not the optimal condition for maximizing the number of observed dipolar spin-exchange oscillation cycles. At finite temperature, the instantaneous dipolar interaction strength fluctuates due to thermal motion, which becomes more prominent in a shallow trap. As we will see later in this chapter, this is the main mechanism of dephasing at current stage of the experiment. To mitigate this issue, we confine the molecules more tightly by operating the tweezer at a higher trap light intensity for which the magic angle is close to  $90^\circ$ . The work described below is performed under

these conditions.

We first start with a simple Ramsey pulse sequence. We find that the phase is fluctuating over time, causing random jumps of phase during the phase scan. If we take enough amount of data, the Ramsey contrast disappears. This finally traced down to two issues. One issue is ambient magnetic field noise. We install a fluxgate magnetometer on the experiment and monitor the vector magnetic field over time. To remove the effect of 60 Hz, the analog output of the magnetometer is sampled by a data acquisition card that is triggered by 60 Hz power line cycle. The data trace acquired during a single 60 Hz cycle is averaged and saved. We observe that there are large magnetic field noise especially on the vertical axis in the lab. We do not know where this noise comes from, until we extend the monitor time over one day (Figure 5.5). The magnetic field noise disappears between 2am and 5am, and is quite repeatable from day to day. We quickly determined that this is due to the nearby MBTA red line train. Since we cannot ask MBTA to shutdown red line, we choose to rotate our quantization axis in the horizontal direction. By making the quantization axis perpendicular to the noisy axis, the fluctuation adds in quadrature rather than linearly. Later, we also add a magnetic field cancellation system, which is detailed in Appendix G.

We also observe electric field fluctuation causing Ramsey phase shift instability. We have to be careful about the insulated surface near the glass cell. At the beginning, a piece of black flocked paper from Thorlabs is used as a light absorption backdrop for the camera, we observe random fluctuation of the phase (Figure 5.6 (a)). The fluctuation is almost eliminated after replacing this black flocked paper with Acktar Metal Velvet black sheet, as shown in Figure 5.6 (b). We also installed an air ionizer bar below our laminar flow air filter (Figure 5.8 (a)). There are four pairs of high voltage needle electrodes on the ionizer bar, which are driven with high voltage that switches polarity

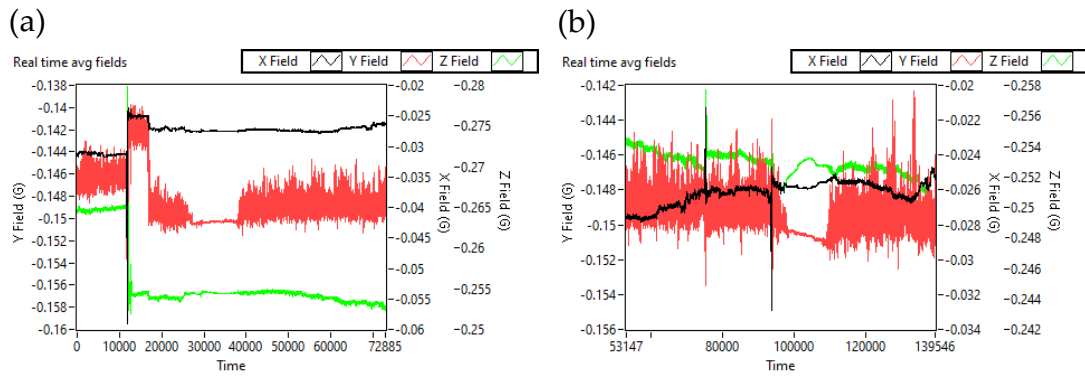


**Figure 5.5:** (a) Magnetic field noise in the lab measured by a fluxgate magnetometer. Y-axis is vertical direction. (b) Same measurement, but taken at another day. The time axis value should be multiplied by 1.2 to obtain the time in the unit of second.

quickly, ionizing the air with balanced positive and negative charges, effectively making the air slightly conductive. These charged particles can neutralize the patch charges on the surfaces that are exposed to air.

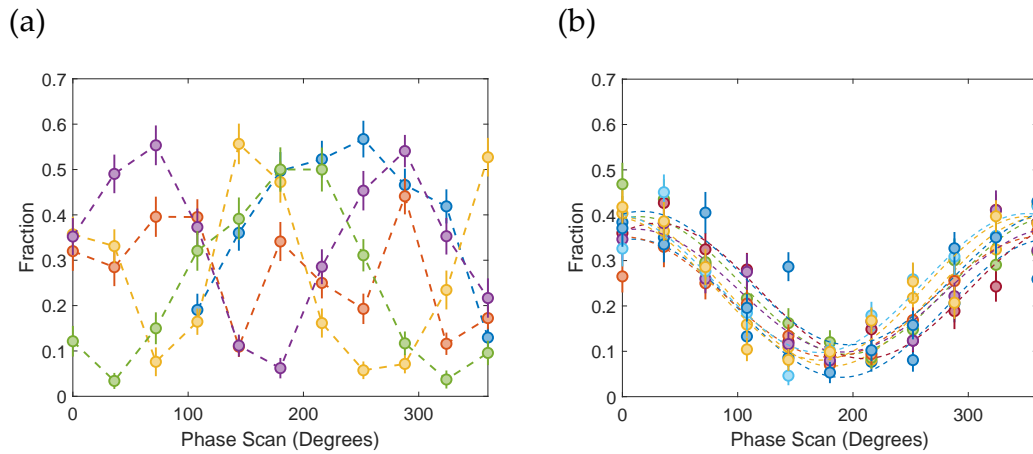


**Figure 5.6:** (a) Repeated phase scans of Ramsey sequence. Each scan take about 2 min, with the black flocked paper in place. (b) Same phase scans with the black flocked paper replaced by a piece of Acktar Metal Velvet black sheet.

We also observe surface patch charges on the interior surface glass cell generating electric field, affecting the stability of the transition. Evidence shows that even there is no direct line of sight from the glass cell to an ion source in the vacuum, surface charge in the glass cell can still be affected by the ion source. We monitor the phase of a Ramsey sequence repeatedly. At one point, we turn off the ion gauge in the glass cell section, and we see the phase immediately shifted in the next scan. One might think this could be magnetic field generated by the cable powering the ion gauge filament. However, the phase keeps drifting in the next several scans, and finally stabilizes at a new value (Figure 5.7). We suspect this is due to collision between the ions and residual gas atoms that eject new charged particles in a different direction. A continuous stream of charge particles arrive on the surface of the glass cell, reaches an equilibrium when the ion gauge is kept on. The electric field quickly shifts when this charged particle stream stops after the ion gauge is turned off, and a new equilibrium is gradually reached. We do not have the ability to confirm this is actually the cause in the current apparatus. Patch charges issues are also observed in the CaOH experiment of our group, where the transition is shifted by patch charges accumulated on the surface of in-vacuum MOT coil. The source of charged particles in their case is traced down to laser ablation inside of CBGB. Although we have not observed that ions generated in CBGB can affect surface patch charges on the glass cell, we still built and installed an ion sweeper into the beam box (Figure 5.8 (b)). The ion sweeper is made of two pieces of copper mesh, with one side grounded and the other side connected to a  $-2$  kV high voltage power supply. We also installed an UV LED to flood illuminate the glass cell. The UV LED method is mentioned in many Rydberg atom experiments<sup>77</sup>.

After fixing these issues affecting Ramsey phase scan stability, we then increase the trap depth of the tweezer and measure the rotational qubit coherence time under conditions

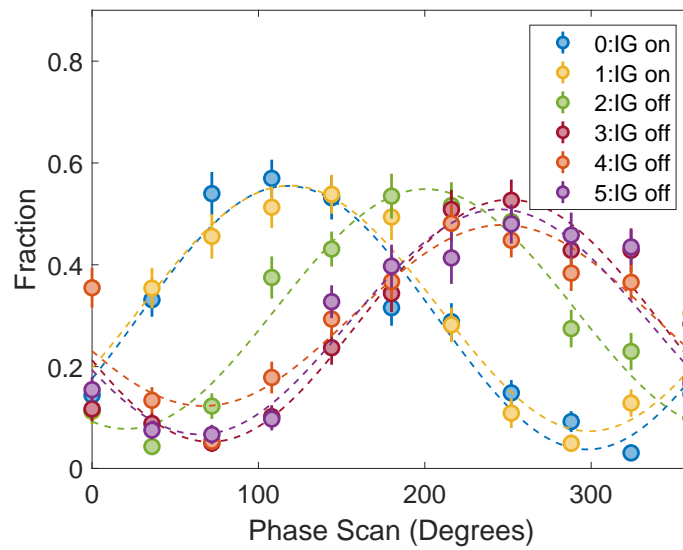


**Figure 5.7:** Repeated phase scans of Ramsey sequence. Each scan take about 2 min. Ion gauge is turned off after finishing scan 1.

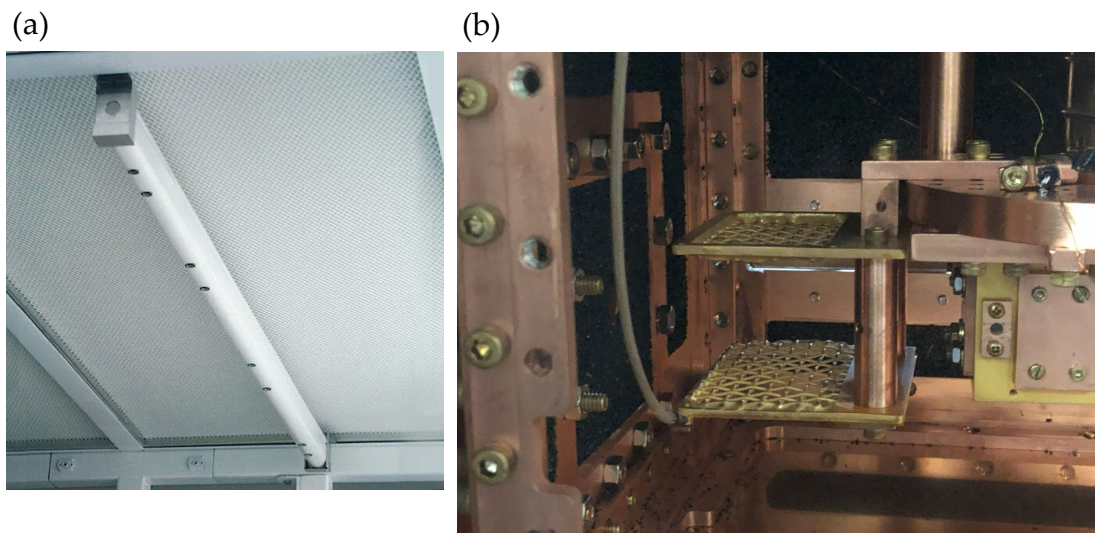


**Figure 5.8:** (a) Ionizer bar with 4 pairs of electrodes. (b) Ion sweeper installed in the beam box.

of three different microwave pulse sequences (Figure 5.9 (a)). The decay of the phase contrast is shown in Figure 5.9 (b) and fitted to a Gaussian model centered at  $t = 0$  to obtain  $1/e$  rotational coherence time.

With a Ramsey sequence, we observe a single qubit coherence time of  $\tau_C = 3.6(6)$  ms. By adding a single  $\pi$  spin-echo pulse,  $\tau_C$  is extended to  $33(5)$  ms. Active magnetic field cancellation is employed to remove long-term drift on the order of 10 mG, but the system used does not remove magnetic field fluctuation within a power line cycle time of less than  $1/(60 \text{ Hz})$ . This limits the effective interval between spin-echo pulses to be an integer multiple of  $1/(60 \text{ Hz}) \approx 16.7 \text{ ms}$ , making it difficult to measure fast dipolar oscillations with only a single  $\pi$ -pulse. Instead, we use dynamical decoupling schemes to preserve the qubit coherence. This technique is employed in a variety of quantum information systems<sup>53,37</sup>, including molecular systems<sup>130,79,59</sup>. We choose the XY8 dynamical decoupling sequence (Figure 5.9 (a)), with a cycle length of 1.6 ms. Each XY8 block has a  $\pi$ -pulse time optimized for the specific magnetic field and microwave frequency. Due to the finite  $\pi$ -pulse width, the pulse interval  $\tau$  between pulses are not exactly 100  $\mu\text{s}$  but adjusted to make each XY8 block exactly 1.6 ms. The XY8 sequence effectively acts as a band-pass filter with, in our case, its pass-band centered at 2.5 kHz<sup>28</sup>, which is higher than the dominant magnetic field noise spectrum range in our system. This is a time scale much shorter than  $1/(60 \text{ Hz})$ . We are able to achieve a coherence time of  $\tau_C = 630(90)$  ms with such kind of pulse sequence. This XY8 dynamical decoupling pulse is used for all of our measurements in following sections in this chapter, except where noted. Figure 5.9 (b) shows the measured contrast versus time for single particle oscillations between  $|\uparrow\rangle$  and  $|\downarrow\rangle$ , from which  $\tau_C$  is determined.

When we first start using these dynamical decoupling pulse sequences in the experiment, the phase between pulses are controlled using a voltage controlled phase





shifter (PA0204, Clear Microwave) on the 2.0 GHz path. This specific phase shifter maps  $0 \sim 9$  V control voltage into  $0 \sim 2\pi$  rad of phase delay with high nonlinearity. At the first attempt of dynamical decoupling, we saw an oscillating phase scan contrast as the interrogation time increases (Figure 5.10), instead of a monotonic decay. The origin of this effect is quickly narrowed down to the X and Y rotation being not around orthogonal axis (phase between X and Y pulses are not  $90^\circ$ ).

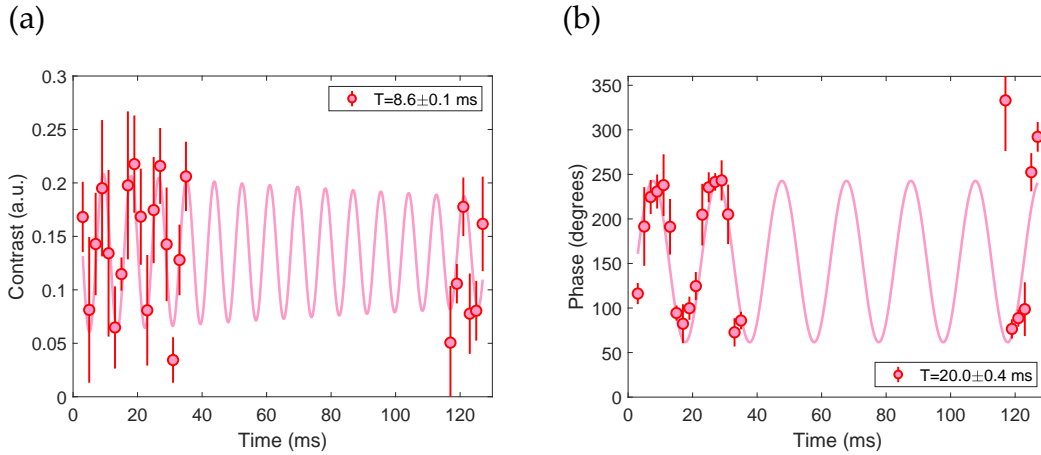


**Figure 5.10:** (a) Oscillating XY8 phase scan contrast due to X and Y rotation axis deviation from  $90^\circ$  angle between X and Y rotation. (b) Oscillating phase in the XY8 phase scan due to X and Y rotation axis deviation from  $90^\circ$

We then moved on to upgrade our system to use the I/Q modulator built into the SR392 vector signal generator. The new setup is designed to provide agile and precise amplitude, phase, and frequency tuning capability. The diagram of the new setup is shown in Figure 5.11. A high-speed dual-channel PCI-Express arbitrary waveform generator (AWG) card with synchronized digital outputs is used to generate the baseband signal and the blanking signal. The two analog channel outputs are used for the baseband signal, driving an I/Q modulator with a carrier frequency near 1981 MHz. The

output of the I/Q modulator is subsequently mixed with a 18.5 GHz microwave source, and passed to the filters, switches and amplifiers that are the same with the simple microwave setup discussed previously. The digital blanking signal is used to control two fast microwave switches in tandem, providing 160 dB suppression of microwave power when the microwaves are turned off.

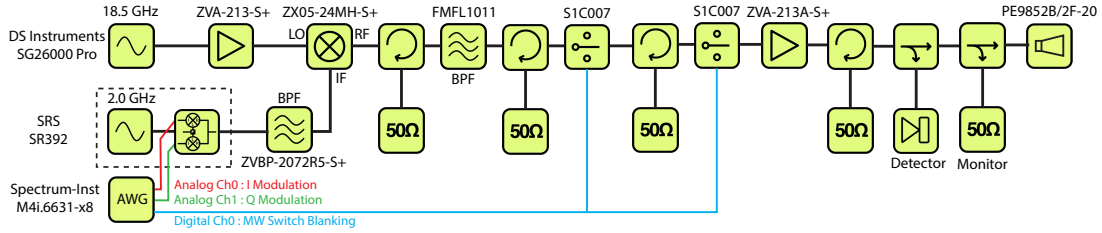


**Figure 5.11:** The diagram of the new microwave setup using I/Q modulator inside SR392. An additional microwave switch is added to increase isolation. Both microwave switches are controlled by the AWG synchronized digital output.

#### 5.4 COHERENT DIPOLAR SPIN-EXCHANGE INTERACTION

We set the bias magnetic field perpendicular to both the  $k$ -vector of the tweezer light and the direction of 1D tweezer array. The polarization of the linearly polarized tweezer light is rotated to the tweezer array direction (i.e. a magic angle close to  $90^\circ$ ). This configuration provides the largest “magic trap depth” (the tightest confinement) at a given magnetic field.

State preparation is first done with pairs of tweezers spaced at  $|\vec{R}| \sim 5 \mu\text{m}$ , with each site loaded with a single molecule prepared in the  $|\downarrow\rangle$  state (or empty), yielding the  $|\downarrow\downarrow\rangle$  state. At this separation, the dipolar interaction strength  $J$  is negligible due to the large spacing between the tweezers ( $\frac{J}{\hbar} < 3 \text{ Hz}$ ). In a time period  $\sim 1 \text{ ms}$  we then move the even numbered sites towards the odd numbered sites, by sweeping the AOD

frequency tones of the even sites, which reduces the separation and has the effect of increasing the dipolar interaction strength. A  $\frac{\pi}{2}$ -pulse is then applied to prepare both molecules in the superposition state  $(|\uparrow\rangle + |\downarrow\rangle)/\sqrt{2}$ . At this moment, the two-particle quantum state can be written in the following form, which is still a separable state.

$$[(|\uparrow\rangle + |\downarrow\rangle) \otimes (|\uparrow\rangle + |\downarrow\rangle)]/2 = [(|\uparrow\downarrow\rangle + |\downarrow\uparrow\rangle) + (|\uparrow\uparrow\rangle + |\downarrow\downarrow\rangle)]/2 \quad (5.3)$$

Then, we apply XY8 dynamical decoupling sequence of microwave pulses. Under the time evolution of dipolar spin-exchange Hamiltonian ( $H_{dip}$ ), a relative phase accumulates between  $(|\uparrow\downarrow\rangle + |\downarrow\uparrow\rangle)/\sqrt{2}$  and  $(|\uparrow\uparrow\rangle + |\downarrow\downarrow\rangle)/\sqrt{2}$ . Since the XY8 sequence only contains  $\pi$ -pulses, it will not affect the phase accumulation during the evolution under  $H_{dip}$ . After a various wait time, we apply another  $\frac{\pi}{2}$ -pulse and then move the molecules apart. To read out the final qubit state, a second  $\Lambda$ -imaging pulse projects the system to  $|\uparrow\uparrow\rangle$ . We select the data where both sites in a tweezer pair are initially loaded with single molecules. Our measurement yields the probability  $P_{\uparrow\uparrow}$  of detecting both molecules being in the  $|\uparrow\rangle$  state. To summarize, starting from the initial state  $|\downarrow\downarrow\rangle$ , a microwave pulse sequence creates a final state that evolves in time as  $|\psi(t)\rangle = \frac{1}{2}((1 - e^{-i\frac{Jt}{2\hbar}})|\downarrow\downarrow\rangle - (1 + e^{-i\frac{Jt}{2\hbar}})|\uparrow\uparrow\rangle)$ , resulting in the probability  $P_{\uparrow\uparrow} = \cos^2 \frac{Jt}{4\hbar} = \frac{1}{2}(1 + \cos \frac{Jt}{2\hbar})$ , which oscillates at an angular frequency of  $\omega_J = \frac{J}{2\hbar}$ .

This is indeed observed in our experiment. At smaller tweezer spacings, we observe increased  $\omega_J$  due to the stronger dipolar interaction between the two molecules (Figure 5.13 (a)). By fitting the data to an exponentially decaying sinusoidal model, we extract the dipolar oscillation cycle period  $T$  and contrast decay time constant  $\tau_D$ . The dipolar spin-exchange strength  $J$  at different tweezer spacings can be then calculated from  $T$ . We find that the measured  $J$  is slightly smaller than the theoretical prediction

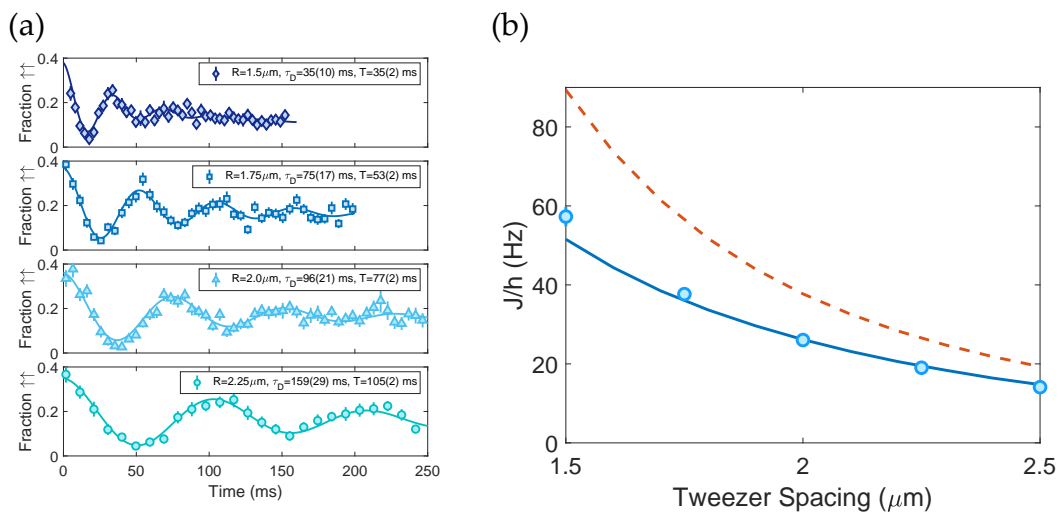


**Figure 5.12:** (a) Dipolar spin-exchange oscillation at various tweezer spacings, with fitted decay time constant and oscillation period shown in the legends. (b) Dipolar spin-exchange interaction strength  $J$  versus the tweezer spacing  $|\vec{R}|$ . Orange line (dashed) is the theoretical prediction of  $J$  at zero temperature. Blue line (solid) is the simulated result of  $J$  with the thermal motion of the molecules taken into account.

and deviates more as the spacing decreases (Figure 5.13 (b)). This can be explained by the finite temperature of the molecules causing the effective inter-molecular spacing  $\langle |\vec{r}| \rangle$  to be larger than the tweezer spacing  $|\vec{R}|$ . We Monte-Carlo simulate the behavior of the molecules in the tweezer, including the thermal motion of the molecules, and show in Figure 5.13 (b) that the simulated results agree with the experimental data. Additionally, the simulation captures the behavior that the thermal motion decreases the observed number of coherent dipolar oscillations at reduced tweezer spacing.

The Monte-Carlo simulation is used to predict the dephasing effect described by a thermal dephasing model and that is compared to the experimental measurement. We randomly seed the simulation with molecules with an initial position vector and velocity vector following a Gaussian distribution on each axis. The standard deviations of the Gaussian distributions are calculated for a particle at the measured temperature in a harmonic trap. Since we are loading with a large trap depth to temperature ratio, the harmonic approximation works well. We propagate the position and velocity vector of the molecule in the trap using the equation of motion and extract the trajectory of the molecule. Next, we adiabatically lower the trapping potential, keep it at low trap depth and then evolve for various amount of time. We then use the relative geometry between two trajectories  $i$  and  $j$  of the molecules to calculate the instantaneous  $J_{i,j}(t)$ .

$$J_{i,j}(t) = \frac{d^2}{4\pi\epsilon_0|\vec{r}_{i,j}(t)|^3} \left(1 - 3\left(\frac{\vec{r}_{i,j}(t) \cdot \vec{n}}{|\vec{r}_{i,j}(t)||\vec{n}|}\right)^2\right) \quad (5.4)$$

$$\vec{r}_{i,j}(t) = \vec{r}_i(t) - \vec{r}_j(t) + \vec{R} \quad (5.5)$$

Here,  $\vec{r}_i(t)$  is the 3D position vector at time  $t$  in a trajectory  $i$ , relative to the center of the tweezer.  $\vec{R}$  is the vector pointing from the center of the left tweezer to the right tweezer in a pair.  $\vec{n}$  is the vector pointing at the orientation of the quantization axis.

Next, we integrate  $J_{ij}(t)$  to get the accumulated phase  $\varphi_{ij}(T) = \int_0^T J(t)dt$ . By averaging all the oscillation traces from different trajectory pairs, we get the final probability  $P_{\uparrow\uparrow}(T) = \sum_{ij} \frac{1}{2}(1 + \cos(\varphi_{ij}(T)))$  where the summation is over all mutual trajectory pairs. Finally, we scale the simulated  $P_{\uparrow\uparrow}(t)$  to match the amplitude of experimental data in Figure 5.13 (a). We then scan the tweezer spacing  $|\vec{R}|$  and for each spacing we use the same exponential decaying sinusoidal model to fit the simulated result and produce the blue solid line in Figure 5.13 (b).

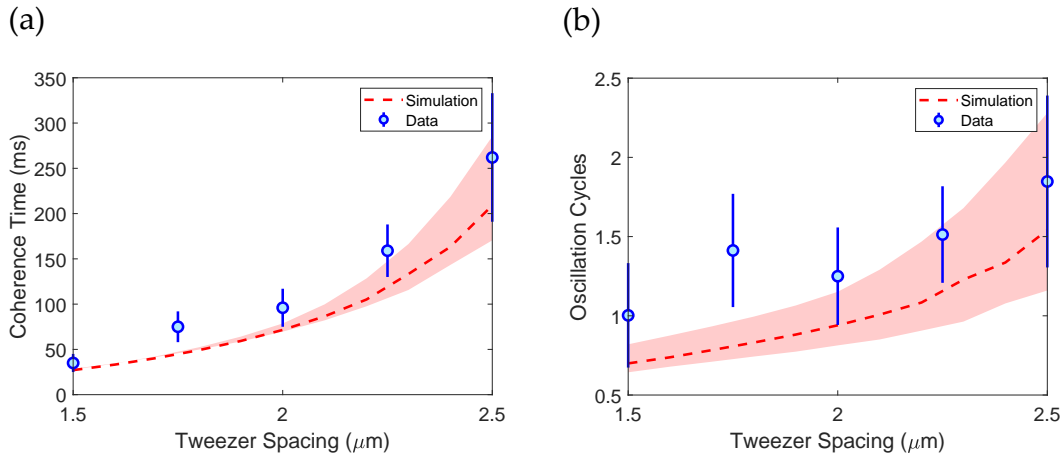


**Figure 5.13:** (a) Simulated  $1/e$  dipolar coherence times at different tweezer spacings are shown in the red.  $1/e$  dipolar coherence times fitted from the measured data are shown in blue. (b) Simulated number of dipolar oscillation cycles (contrast decayed to  $1/e$ ) at different tweezer spacings are shown in the red. Fitted data from measured oscillations are shown in blue.

More insights can be gained from the result of this Monte-Carlo simulation. In Figure 5.13 (a), we show the  $1/e$  dipolar interaction coherence time fitted from the simulation, and the same coherence time fitted from the measured oscillation data. The agreement with the simulation supports the expectation that a lower temperature can potentially increase the dipolar interaction coherence time, and hence the fidelity of

the Bell state generated by this system. Number of dipolar oscillation cycles seen in the  $1/e$  dipolar coherence time versus the trap spacing is shown in Figure 5.13 (b), the observed number of oscillation cycles grows as the tweezer spacing increases, matching the observation on the experiments up to  $2.5 \mu\text{m}$ . However, this simulation does not take into account the finite single molecule rotational coherence time ( $\sim 630 \text{ ms}$  in our case), which will ultimately limit the number of oscillation cycles.

### 5.5 ANISOTROPY OF THE DIPOLAR INTERACTION

The general dipole-dipole Hamiltonian described in Equation 5.1 and Equation 5.2 is inherently anisotropic due to the  $\theta$ -dependent term. We would like to study the effect of the anisotropy of spin exchange experimentally by varying the angle  $\theta$ , and measuring the corresponding dipolar interaction strength. At the low magnetic field that we are applying here, the rotational angular momentum has not been decoupled from the electron spin, by adiabatically prepare the molecule in a specific magnetic sublevel with varied magnetic quantization axis, we could change  $\theta$  by rotating the quantization axis relative to the line between the centers of the tweezers. The quantization axis is set by the applied bias magnetic field and can be changed by tuning the current through two pairs of magnetic field coils while simultaneously rotating the tweezer light polarization to maintain the same magic angle.

In Figure 5.14 (a), we show  $P_{\uparrow\uparrow}$  at three characteristic angles  $\theta = 0^\circ$ ,  $54.7^\circ$  and  $90^\circ$ , all taken with a  $|\vec{R}| = 2 \mu\text{m}$  tweezer spacing. We observe dipolar spin-exchange oscillations in both  $\theta = 0^\circ$  and  $\theta = 90^\circ$  configurations, with the oscillation at  $\theta = 0^\circ$  being twice the frequency as that of  $\theta = 90^\circ$ . No clear oscillation is observed for  $\theta = 54.7^\circ$  configuration, as expected because the dipolar interaction averages to zero at this an-

gle. These results agree with the absolute value of the magnitude of the anisotropic term in each configuration. We also observe a larger number of oscillation cycles at  $\theta = 90^\circ$  than  $\theta = 0^\circ$ . By changing the orientation of  $\vec{n}$  in the Monte-Carlo simulation, the anisotropy effect of the dipolar spin-exchange interaction shown in Figure 5.14 (b), which agrees with the measured result. Our Monte-Carlo simulation result also supports the prediction that thermal motion is the dominant cause of dephasing. At  $\theta = 0^\circ$ , the larger motional wavefunction spread in the more weakly trapped axial direction of the optical tweezers results in a large fluctuation of the instantaneous value of  $\theta$ . The  $\theta = 90^\circ$  configuration is less affected due to the tight confinement of the optical tweezers in the radial direction.

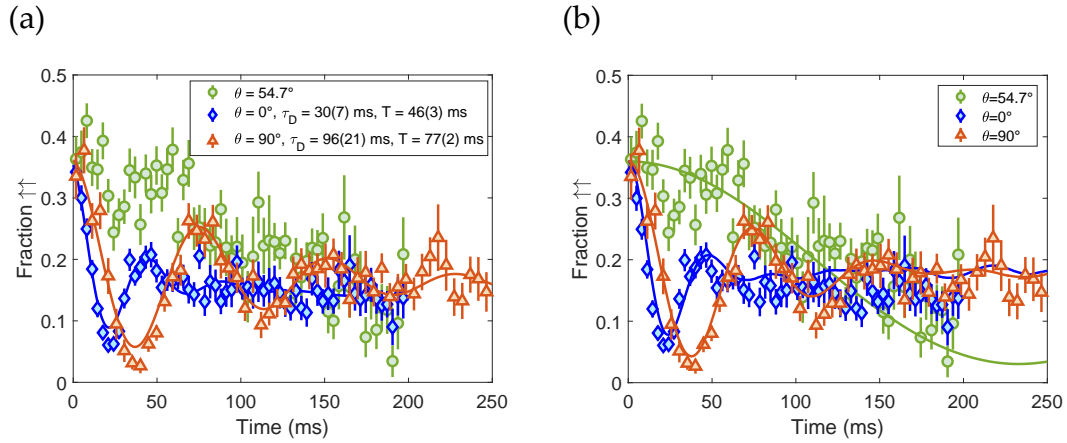


**Figure 5.14:** (a) Dipolar spin-exchange interaction at different angles  $\theta = 0^\circ, 54.7^\circ$  and  $90^\circ$ . The  $\theta = 0^\circ$  and  $90^\circ$  data is fitted to an exponentially decaying sinusoidal model with decay time constant  $\tau_D$  and oscillation cycle time  $T$ , shown in solid lines. (b) Simulated  $P_{\uparrow\uparrow}$  at different  $\theta$  angle and a tweezer spacing  $|\vec{R}| = 2 \mu\text{m}$ . Solid lines are the simulation results while the data is the same as (a).



## 5.6 FIDELITY OF CREATED BELL STATES

Dipolar spin-exchange can be used in a two-qubit iSWAP gate to generate entanglement between molecules in neighboring tweezers<sup>93</sup>. At a dipolar spin-exchange interaction time of  $t = T/4 = 19.2$  ms, where  $T$  is the oscillation period of the spin-exchange oscillation, the system has evolved into a maximally entangled state known as a Bell state. To test the fidelity of the Bell state generated in our system, we apply a third  $\frac{\pi}{2}$ -pulse (see Figure 5.15 (a) caption) around a variable rotation axis on the Bloch sphere (angled  $\varphi$  relative to the x-axis on the equatorial plane). By varying  $\varphi$  and measuring the survival probability of all four possible final state outcomes, one can construct the parity quantity  $\Pi$ <sup>121,106</sup>.

$$\Pi = \langle \hat{\Pi} \rangle = \langle \hat{S}_1^z \hat{S}_2^z \rangle = P_{\uparrow\uparrow} + P_{\downarrow\downarrow} - P_{\uparrow\downarrow} - P_{\downarrow\uparrow} \quad (5.6)$$

Here  $\langle \rangle$  denotes averaging over all occurrences where both sites in a tweezer pair are initially loaded with single molecules.  $\hat{S}_i^z$  represents the Pauli-Z operator on the number  $i$  molecule in a pair.

Starting from a Bell state, this sequence will result in a  $4\pi$  oscillation in  $\Pi$  as  $\varphi$  is varied from 0 to  $2\pi$ <sup>100</sup>. Displayed in Figure 5.15 (b) is  $\Pi$  for both  $\theta = 0^\circ$  and  $\theta = 90^\circ$  configurations. Extracting the contrast of the oscillation for the  $\theta = 90^\circ$  case, we measure a Bell state fidelity of  $\mathcal{F} = 0.32(2)$  and a state preparation and measurement (SPAM) corrected fidelity of  $\mathcal{F}_{SPAM} = 0.89(7)$ . The phase of the parity oscillation reveals the sign of the anisotropic term  $(1 - 3 \cos^2 \theta)$ , also seen in 58. Our data shows that the  $\theta = 0^\circ$  configuration leads to a negative  $J$ , corresponding to a ferromagnetic interaction, and the  $\theta = 90^\circ$  configuration leads to a positive  $J$ , corresponding to an anti-ferromagnetic interaction.

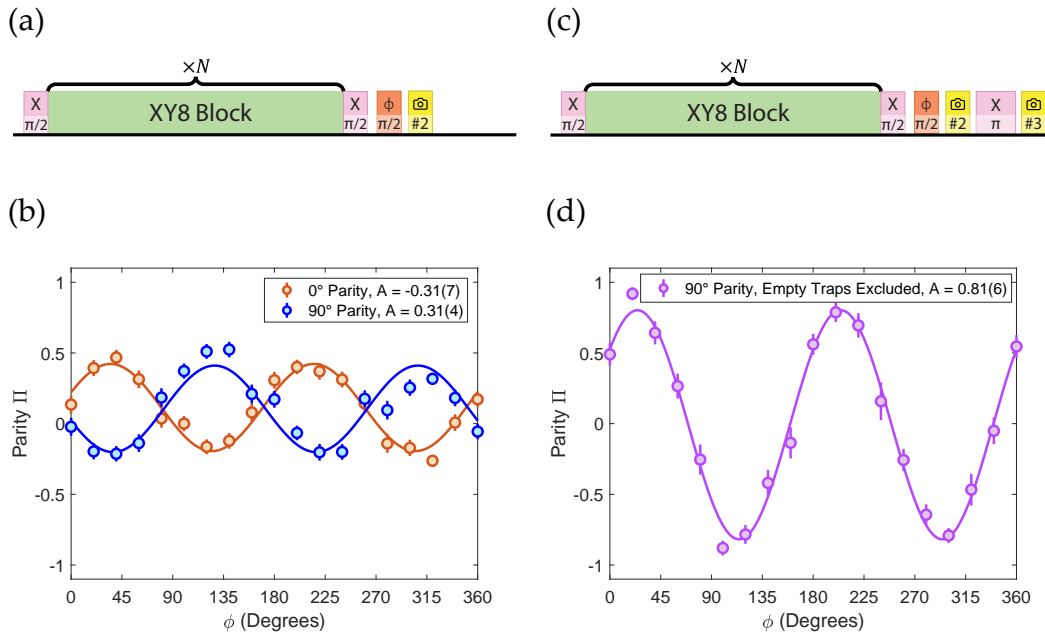


**Figure 5.15:** (a) Microwave pulse and detection sequence used in the parity oscillation measurement.  $\frac{\pi_\phi}{2}$  denotes a  $\frac{\pi}{2}$ -pulse with a microwave phase shifted by  $\phi$  relative to the first  $\frac{\pi_x}{2}$  pulse in the sequence, effectively rotating the quantum state around an axis that is angled  $\phi$  relative to the  $x$ -axis on the Bloch sphere. The pulse ( $\text{📷}$  icon, in yellow) represents imaging of the molecules. Note that the first imaging pulse for tweezer loading identification, as well as the microwave pulses for initial state preparation, are applied before this sequence and not shown in this figure. (b) Parity oscillation at  $\theta = 0^\circ$  and  $\theta = 90^\circ$ .  $A$  is the fitted parity oscillation amplitude. (c) With the addition of a  $\pi$ -pulse and a third imaging step to the sequence in (a), molecules are verified to be present throughout the entanglement and readout process. (d) Parity oscillation for  $\theta = 90^\circ$  with empty traps excluded and corrected for measurement error, using the sequence depicted in (c).

$\mathcal{F}_{SPAM}$  is measured to be significantly higher than  $\mathcal{F}$ , with imperfect state preparation and detection being the surmised cause. In detail, during initial state preparation, molecules that fail to be prepared in the desired  $|N = 0, F = 1, m_F = 0\rangle$  ( $|\downarrow\rangle$ ) state are intentionally removed by a resonant laser pulse, resulting in an empty trap(s). During the final readout, the cases that the molecule is in the  $|\downarrow\rangle$  state or that the trap is simply empty would both appear dark. A  $\pi$ -pulse and additional imaging pulse are employed (Figure 5.15 (c)) to distinguish between these two cases. If the molecule is in the  $|\downarrow\rangle$  state, it will be transferred to the  $|\uparrow\rangle$  state and detected, while an empty trap will remain dark. This information is used to exclude the cases of empty traps during the final readout, improving the contrast of the parity oscillation (Figure 5.15 (d)). The resulting Bell state fidelity corrected for measurement error is determined to be  $\mathcal{F}_{ex} = 0.89(6)$ , higher than the threshold of  $\mathcal{F}_{th} = 0.5$ <sup>106</sup>, showing under these conditions the conditional preparation of entanglement of two molecules in a tweezer pair. The evolution of the system to create a Bell state is an iSWAP operation and although we have not fully characterized the system as an iSWAP gate, the Bell state fidelity indicates how it would perform.

### 5.6.1 ESTIMATION OF THE SPAM CORRECTED BELL STATE FIDELITY

We use a reduced tomography procedure to determine the fidelity. The fidelity between a Bell state  $|\Psi\rangle$  and an arbitrary density matrix produced in the experiment  $\rho$  is  $\mathcal{F} = \langle\Psi|\rho|\Psi\rangle$ , where the density matrix has form

$$\rho = \begin{pmatrix} \rho_{\uparrow\uparrow,\uparrow\uparrow} & \rho_{\uparrow\uparrow,\uparrow\downarrow} & \rho_{\uparrow\uparrow,\downarrow\uparrow} & \rho_{\uparrow\uparrow,\downarrow\downarrow} \\ \rho_{\uparrow\downarrow,\uparrow\uparrow} & \rho_{\uparrow\downarrow,\uparrow\downarrow} & \rho_{\uparrow\downarrow,\downarrow\uparrow} & \rho_{\uparrow\downarrow,\downarrow\downarrow} \\ \rho_{\downarrow\uparrow,\uparrow\uparrow} & \rho_{\downarrow\uparrow,\uparrow\downarrow} & \rho_{\downarrow\uparrow,\downarrow\uparrow} & \rho_{\downarrow\uparrow,\downarrow\downarrow} \\ \rho_{\downarrow\downarrow,\uparrow\uparrow} & \rho_{\downarrow\downarrow,\uparrow\downarrow} & \rho_{\downarrow\downarrow,\downarrow\uparrow} & \rho_{\downarrow\downarrow,\downarrow\downarrow} \end{pmatrix} \quad (5.7)$$

For a given Bell state  $|\Psi\rangle = \frac{1}{\sqrt{2}}(|\downarrow\downarrow\rangle + e^{i\psi}|\uparrow\uparrow\rangle)$ , the fidelity is then quantified as:

$$\mathcal{F} = \frac{1}{2}(\rho_{\downarrow\downarrow,\downarrow\downarrow} + \rho_{\uparrow\uparrow,\uparrow\uparrow}) + \frac{1}{2}(e^{i\psi}\rho_{\uparrow\uparrow,\downarrow\downarrow} + c.c.) = \frac{1}{2}(P_{\downarrow\downarrow} + P_{\uparrow\uparrow} + 2\mathcal{C}) \quad (5.8)$$

where  $P_{ij} \equiv \rho_{ij,ij}$  ( $i, j = \{\uparrow, \downarrow\}$ ) and  $\mathcal{C} \equiv \text{Re}(\rho_{\downarrow\downarrow,\uparrow\uparrow})$  is the coherence between states  $|\downarrow\downarrow\rangle$  and  $|\uparrow\uparrow\rangle$ . The population sum  $P_{\downarrow\downarrow} + P_{\uparrow\uparrow}$  can be directly determined from projective measurements onto detection basis  $\{|\uparrow\rangle, |\downarrow\rangle\}$ , while the coherence  $\mathcal{C}$  can be assessed through parity oscillations. Specifically, to measure the coherence term a single-qubit  $\frac{\Pi}{2}$  rotation with a variable phase  $\varphi$  is applied to both molecules as an ‘‘analysis pulse’’ and we measure the parity observable  $\Pi$  defined in Equation 5.6<sup>121,106</sup>.

The fidelity  $\mathcal{F}$  calculated above contains state preparation imperfections due to empty tweezer sites being identified as  $|\downarrow\rangle$  and detection infidelity in our system, in addition to the actual gate errors. Calculating the SPAM-corrected fidelity thus amounts to obtaining the full distribution of all the following probable events in the experiment:  $\{P_{\uparrow\uparrow}, P_{\uparrow\downarrow}, P_{\downarrow\uparrow}, P_{\downarrow\downarrow}, P_{\uparrow e}, P_{\downarrow e}, P_{e\uparrow}, P_{e\downarrow}, P_{ee}\}$ , where the subscript  $e$  denotes an empty site.

Our Bell state detection provides the following set of measured quantities:  $\{A_{11}, A_{10}, A_{01}, A_{11}\}$ , where  $A_{kl}$  is the probability of detecting the molecule bright ( $k, l = 1 \equiv |\uparrow\rangle$ ) or dark ( $k, l = 0 \equiv |\downarrow\rangle$  or  $|e\rangle$ ). By adding a subsequent  $\pi$ -pulse, we obtain another set of measured probabilities  $\{B_{11}, B_{10}, B_{01}, B_{11}\}$ . Using these eight measured

quantities, we construct the following relations:

$$A_{11} = P_{\uparrow\uparrow} \quad (5.9a)$$

$$A_{10} = P_{\uparrow\downarrow} + P_{\uparrow e} \quad (5.9b)$$

$$A_{01} = P_{\downarrow\uparrow} + P_{e\uparrow} \quad (5.9c)$$

$$A_{00} = P_{\downarrow\downarrow} + P_{\downarrow e} + P_{e\downarrow} + P_{ee} \quad (5.9d)$$

$$B_{00} = P_{\uparrow\uparrow} + P_{\uparrow e} + P_{e\uparrow} + P_{ee} \quad (5.9e)$$

$$B_{10} = P_{\downarrow\uparrow} + P_{\downarrow e} \quad (5.9f)$$

$$B_{01} = P_{\uparrow\downarrow} + P_{e\downarrow} \quad (5.9g)$$

$$B_{11} = P_{\downarrow\downarrow} \quad (5.9h)$$

Imposing additional physical constraints

$$P_{\uparrow\uparrow} + P_{\uparrow\downarrow} + P_{\downarrow\uparrow} + P_{\downarrow\downarrow} + P_{\uparrow e} + P_{\downarrow e} + P_{e\uparrow} + P_{e\downarrow} + P_{ee} = 1 \quad (5.10a)$$

$$P_{ee} = (1 - \beta)^2 \quad (5.10b)$$

$$P_{\uparrow e} + P_{\downarrow e} + P_{e\uparrow} + P_{e\downarrow} = 2\beta(1 - \beta) \quad (5.10c)$$

$$P_{\uparrow\downarrow} = P_{\downarrow\uparrow} \quad (5.10d)$$

$$P_{\uparrow e} = P_{\downarrow e} \quad (5.10e)$$

$$P_{\downarrow e} = P_{e\uparrow} \quad (5.10f)$$

where  $\beta$  accounts for the single-molecule state preparation and detection fidelity (i.e., the probability of successfully preparing a molecule in  $|\downarrow\rangle$ ), probabilities of all probable events in Equation 5.9 can be readily expressed in terms of the eight measured quantities  $A_{kl}$  and  $B_{kl}$ . Finally, we calculate the value  $\beta = 1 - \sqrt{P_{ee}}$  and use this factor to obtain

the SPAM-corrected Bell state fidelity  $\mathcal{F}_{\text{SPAM}} = \mathcal{F}/\beta^2$ . Figure 5.16 (a) and (b) show the measured probabilities of  $A_{kl}$  and  $B_{kl}$ , respectively. Figure 5.16 (c) shows the full distribution of all the probabilities determined from above reduced tomography that we use for SPAM correction.

## 5.7 TOWARDS ARBITRARY INITIAL STATE PREPARATION

Motivated by the desire to perform robust single site addressing, instead of using a single AOD to generate all sites in the array, we switch to using one AOD to generate the odd numbered sites and another AOD to generate the even number sites. This allows for convenient independent trap depth control over each molecule in a pair, and uniformity across the array. Additionally, by offsetting the frequency of the tweezer light of the even and odd sites, molecules can be moved in close proximity without experiencing the heating that can arise in a single AOD system<sup>42,137</sup>. For a given trap depth, the differential AC Stark shift results in molecules in even number sites being away from the resonance of the  $|\uparrow\rangle \rightarrow |\downarrow\rangle$  microwave transition, therefore allowing separate microwave addressing of the odd sites. By applying a microwave  $\pi$ -pulse when odd sites are detuned away, we can prepare an anti-ferromagnetic initial state  $|\uparrow\downarrow\rangle$ . Under  $H_{\text{dip}}$ , an initial state  $|\uparrow\downarrow\rangle$  evolves as  $|\psi(t)\rangle = \cos\frac{Jt}{2\hbar}|\uparrow\downarrow\rangle - i\sin\frac{Jt}{2\hbar}|\downarrow\uparrow\rangle$ , and  $P_{\downarrow\uparrow} = \cos^2\frac{Jt}{2\hbar} = \frac{1}{2}(1 + \cos\frac{Jt}{\hbar})$  will thus oscillate at an angular frequency of  $\frac{J}{\hbar}$ .

Here we describe the details about the optical setup used to generate the dual AOD optical tweezer arrays. The tweezer light is delivered to the experiment through a polarization maintaining single mode optical fiber. The light after the optical fiber is then polarization cleaned by a polarized beam splitter (PBS) and actively power stabilized before sent into an AOD. The phase between the frequency tones in the AOD driving

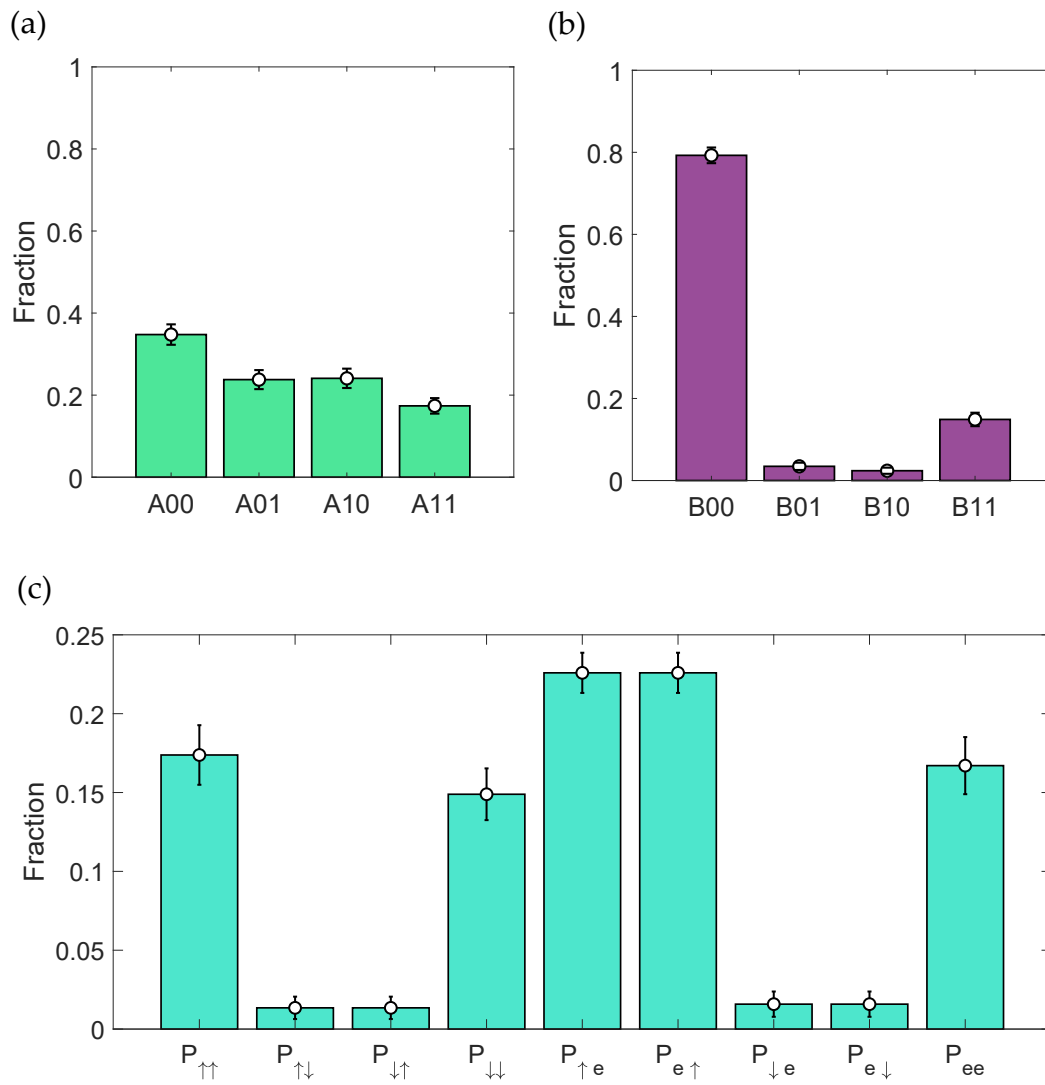


**Figure 5.16:** (a) The measured probability of the four outcomes after the creation of Bell state. (b) The measured probability of the four outcomes with an additional  $\pi$ -pulse added after the creation of Bell state. (c) The full distribution of all the probable events.

waveform is optimized to achieve the lowest peak amplitude, which is crucial to maintain array uniformity and avoid saturation of the RF amplifier. The dual AOD setup consists of two identical single AOD setups. The light beams coupled into the optical fibers are derived from the same laser, but one is frequency shifted +100 MHz using an acousto-optic modulator, while the other one being shifted down by -100 MHz. This setup achieves a 200 MHz detuning between each tweezer pairs, avoiding the parametric heating due to the  $\sim$  MHz beat note created when two sites in a single AOD setup are brought in close proximity<sup>42,137</sup>. The diffracted beams from the two setups are then combined using a non-polarizing beam splitter, maintaining the same polarization in odd and even sites. The combined beams from the AODs are then expanded with a telescope and sent into the microscope objective. A dichroic mirror is used to reflect 606 nm fluorescence collected from the molecules into the EMCCD while transmitting the 776 nm tweezer light. A half waveplate is placed between the dichroic mirror and the microscope objective to rotate the polarization of the tweezer light for tuning the magic angle.

To demonstrate individual addressing, we first prepare the molecules (both in the even and odd sites) in initial state  $|\downarrow\downarrow\rangle$ . We then adiabatically ramp the trap depth of the odd sites to seven times that of the even sites, so as to detune the transition of the molecules in the odd sites out of resonance. The microwave  $\pi$ -pulse then only transfers the molecules in the even sites from  $|\downarrow\rangle$  to  $|\uparrow\rangle$ . This creates an anti-ferromagnetic state  $|\downarrow\uparrow\rangle$ . By then applying a microwave pulse with variable length of time and detecting molecules in the  $|\uparrow\rangle$  state, we observe Rabi oscillations in both even and odd sites with opposite phase (Figure 5.18 (a)). To observe dipolar spin-exchange, we move the tweezers to a smaller spacing ( $|\vec{R}| = 2 \mu\text{m}$ ). As with the single AOD system, the XY8 dynamical decoupling pulses are applied and then the pairs separated for detection.



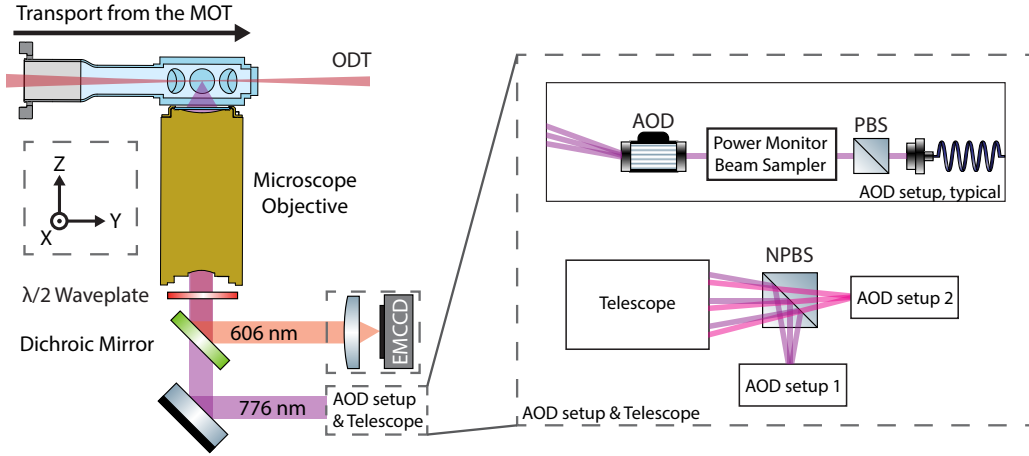


**Figure 5.17: Optical setup for generating the optical tweezer array.** A cartoon of the optical setup around the glass cell is shown on the left. A zoomed in sketch of the dual AOD setup is shown on the right. The typical AOD setups are used to create separate array for the odd and even sites. The purple and pink beams denote the laser beams generated by AOD setup 1 and 2.

The resultant outcome probabilities are shown in Figure 5.18 (b), with a clear display of spin exchange.

## 5.8 SUMMARY

In conclusion, we observe dipolar spin-exchange interactions and create Bell state entangled pairs with single CaF molecules trapped in optical tweezers. We study the dipolar interaction and entanglement by tuning the spacing of the optical tweezers and the angle of the electric dipole quantization axis. By applying detection at the end of the entanglement sequence to include only cases where two molecules are present, we determine a Bell state fidelity of  $\mathcal{F}_{ex} = 0.89(6)$  through a parity oscillation measurement. Parity measurements confirm that the interaction in this system can be tuned between ferromagnetic and anti-ferromagnetic.

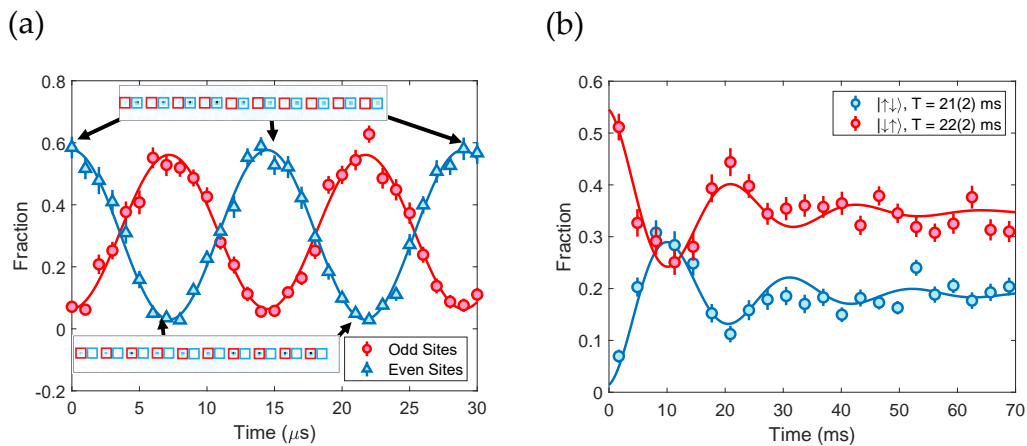


**Figure 5.18:** (a) Rabi oscillation after preparation of the molecular pair in  $|\uparrow\downarrow\rangle$ . (b) Dipolar spin-exchange oscillation with a initial  $|\uparrow\downarrow\rangle$  state at  $\theta = 90^\circ$ . Shown here is the outcome of  $|\uparrow\downarrow\rangle$  and  $|\downarrow\uparrow\rangle$ .

The coherence time of dipolar interactions and the single molecule rotational coherence time are both limited by the finite temperature of the molecules. Implementation of further cooling using other techniques, for example, Raman sideband cooling<sup>22</sup>, would dramatically reduce motional dephasing, extend the single qubit rotational coherence time<sup>19</sup>, and thus increase the two-qubit gate fidelity<sup>93</sup>. This brings in main topic for the next chapter.

# 6

## Raman Sideband Cooling of Molecules

$\Lambda$ -cooling has been used in many crucial steps during the laser cooling of CaF molecules. However, due to differential AC Stark shift of tweezer trap light destabilizing the dark states, the temperature of molecules in the tweezer trap is significantly higher than what can be achieved in free space with  $\Lambda$ -cooling. An obvious way

of reaching even lower temperature is forced evaporative cooling, which successfully create Bose-Einstein condensates. Another possibility is sympathetic cooling between molecules and atoms that are already cooled to ultracold temperature. These methods both require good collisional properties between the particles where efficient thermalization happens faster than collisional loss of the molecules. It is thus challenging to cool a molecule in an optical trap in the absence of a narrow-line transition, as is the case with most (but not all<sup>129</sup>) laser cooled molecules. One feature of the optical tweezer is that when the molecules are trapped close to the center, the potential can be very well approximated by a 3D harmonic potential. The motion is quantized in each direction in such potential. This brings up the idea of Raman sideband cooling (RSC), which uses a two-photon Raman transition to individually address these motional states and uses optical pumping for entropy removal. RSC techniques have been used to cool ions in traps<sup>88</sup> and neutral atoms in optical lattices and optical tweezers<sup>124,57,99,68,117</sup>, to their motional ground state.

## 6.1 INTRODUCTION TO RAMAN SIDEBAND COOLING

RSC typically consists of two key steps. First, a motional-sideband-resolved two-photon Raman transition is driven, reducing the motional quantum number  $|n\rangle$  of the harmonic trapping potential, while also changing the internal state of the atom. Second, optical pumping restores the internal state of the atom without affecting the motional state. By repeatedly applying these two steps, the trapped atom can be driven to the motional ground state of the trapping potential. To reach the motional ground state using RSC, it is crucial to optically resolve the motional sidebands in all three dimensions and to achieve efficient optical pumping.

As we have mentioned before, in a deep optical tweezer, the potential can be approximated as a 3-D harmonic oscillator. We know from undergraduate quantum mechanics that the wavefunction in such kind of potential is separable into three 1-D harmonic oscillators. And for each harmonic oscillator, the energy of eigenstates are spaced evenly from the ground state up to infinite. In a real optical tweezer generated by focusing an Gaussian beam, anharmonicity appears near the edge of the trap. Nevertheless, the trapping potential can still be well approximated by harmonic trap near the center. With the typical numerical aperture available for optical tweezer experiments, the axial direction always has lower trapping frequency than the radial direction. For the same initial temperature, a lot more harmonic oscillator states are occupied for axial direction than radial direction, and greatly increase the difficulties of cooling. If motional ground state RSC in the axial axis is proved to be hard for molecules, the addition of a accordion lattice on the axial direction could help by boosting the axial trap frequency. This solution of course adds additional complexity, thus is less ideal.

For molecules trapped in deep optical tweezers, differential AC Stark shifts can broaden the Raman transition, making it challenging to resolve the motional sidebands. Adiabatically ramping the tweezer trap depth does not really help with this broadening, as we will see in the following analysis of the scaling. the population on each motional states is kept the same during an adiabatic tweezer ramp. As the trap depth is lowered from  $U$  to  $\alpha U$ , the trap frequency lowers from  $\omega$  to  $\sqrt{\alpha}\omega$ . For a harmonic trap, the spring constant ( $k$ , related to trap frequency  $k = m\omega^2$ ) drops to  $\alpha k$ . The width of the wavefunction drops to  $\alpha^{-1/4}$ , reduces the differential AC Stark shift to  $\sqrt{\alpha}$ . Unfortunately, this scaling of the differential AC Stark shift matches the scaling of trap frequency. On the experiment, this means one can use lower Rabi frequency due to lower differential AC Stark shift, but the frequency spacings between sidebands are

also reduced by the same amount, the ability to resolve sidebands does not change. One has to locate a transition with low enough differential AC Stark shift.

We realize Raman sideband cooling (RSC) of ultracold CaF molecules trapped in optical tweezers and cool the molecules to near the three-dimensional motional ground state in about 100 ms. The experimental approach is guided by the proposal of Caldwell and Tarbutt<sup>22</sup>, whereby a high magnetic field decouples the electron spin and nuclear spin from the molecular rotation, significantly reducing the number of quantum states in the RSC scheme. With our choice of states at high magnetic field, these difficulties are overcome, resulting in a simple scheme for applying RSC on molecules.

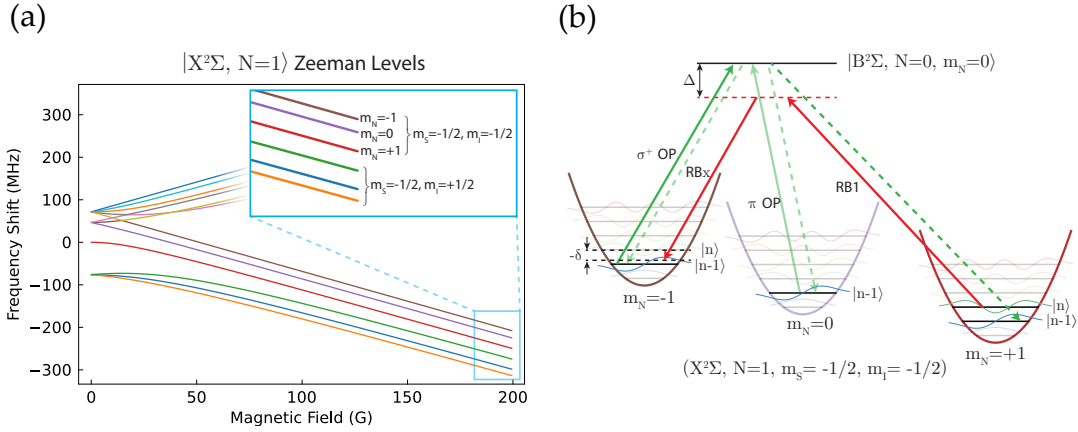


**Figure 6.1:** (a) Zeeman energy levels of the  $|X^2\Sigma, N=1\rangle$  manifold. The  $(m_S = -1/2, m_l = -1/2)$  subspace used for RSC in this work is highlighted in the blue inset. (b) Motional eigenstates  $|n\rangle$  in a harmonic trap. Red arrows labeled RB1 and RB $x$  ( $x = 2, 3$  or  $4$ ) represent the Raman transition driven to lower the motional quantum number  $n$  by 1 for a specific trap axis. The green arrows represent the  $\sigma+$  and the  $\pi$  optical pumping transitions. The dashed green arrow indicates spontaneous emission. The  $\pi$ -polarized transition is driven to prevent accumulation of population in  $|X^2\Sigma, N=1, m_N=0\rangle$  state during OP. Note the negative sign in front of the Raman two-photon detuning  $\delta$ , indicating cooling sidebands have a negative  $\delta$  value. The  $m_N = +1$  state is the final state to which the molecules are cooled by RSC.

The Lamb-Dicke parameter of the Raman transition is defined as  $\eta^R \equiv \Delta k x_0$ , where

$\Delta k$  is the difference between the wave-vectors of the two Raman beams and  $x_0$  is the spread of the ground-state wave-function of the molecule.  $x_0$  can be expressed as  $\sqrt{\hbar/(2m\omega)}$  where  $\hbar$  is Planck constant and  $\omega$  is the trap angular frequency in the specific motional axis. In our application of RSC, the cooling is initiated outside of the Lamb-Dicke (LD) regime due to a combination of factors, with  $\eta_x^R = 0.57$ ,  $\eta_y^R = 0.61$ ,  $\eta_z^R = 0.62$ . These factors are dominantly the relatively light mass of CaF, the low trap frequencies in both the radial and axial directions of the tweezer trap, and the initial temperature set by the limits of  $\Lambda$ -enhanced gray molasses cooling ( $\sim 60 \mu\text{K}$  in a  $\sim k_B \times 1.3 \text{ mK}$  deep trap, equivalent to  $\bar{n}_{\text{radial}} \sim 6$  and  $\bar{n}_{\text{axial}} \sim 40$ ). We perform the cooling by setting the two-photon detuning  $\delta$  of the Raman lasers to address higher-order motional sidebands ( $|\Delta n| > 1$ , where  $\Delta n$  is the change of the motional quantum number) in the initial cooling steps<sup>134</sup>. This allows the removal of more motional energy in a single RSC cycle while leaving the amount of heating from the optical pumping step unchanged. We then switch to driving only one or two states to finish the cooling process.

## 6.2 INITIAL STATE PREPARATION

RSC necessarily requires many steps of optical pumping and two-photon Raman transitions. However, this is challenging with molecules due to the large number of internal states, which can lead to population leakage to states outside the cooling cycle. In order to minimize leakage, a high ( $\sim 200 \text{ G}$ ) magnetic field is applied, resolving and isolating the state manifold for RSC<sup>22</sup> by decoupling the electron spin  $S$  and nuclear spin  $I$  from rotational angular momentum  $N$  (Figure 6.1 (a)). These decoupled angular momentum eigenstates of the molecule are written as  $|S, m_S\rangle |I, m_I\rangle |N, m_N\rangle$ , where  $m_S$  ( $m_I$ ) is the projection of the electron (nuclear) spin angular momentum onto the

quantization axis. When driving optical pumping transitions between the  $X^2\Sigma$  and  $B^2\Sigma$  electronic states in CaF at this magnetic field strength, the transitions that change  $m_I$  and  $m_S$  are suppressed. This reduces the number of scattered photons needed for cooling and therefore results in good state-preserving efficiency and lower heating<sup>22</sup>. A small subspace ( $m_S = -1/2, m_I = -1/2$ ) in the  $X^2\Sigma$  electronic ground state is used, with only three relevant RSC states,  $|m_N = 0, \pm 1\rangle$  (Figure 6.1 (b)). We would like to emphasize that the FCFs of the transitions between the CaF  $X^2\Sigma$  and  $B^2\Sigma$  states are highly diagonal ( $\sim 0.998$ ), that the loss into excited vibrational states is minimal.

To reach such high magnetic field, a special coil with sufficient cooling is required. We design a water cooled coil based on hollow copper wires and fabricate it in house. Details of the construction of this coil can be find in Appendix A. The coil is driven by a low noise programmable switching power supply (SM18-220, Delta Electronika). We use a high current solid state relay (SSR, D1D100, Crydom) to switch the on and off state of the coil, which limits the maximum current to 100 A we can apply to the coil at this stage of the experiment. The coil has been tested up to 220 A under continuous working condition with adequate water cooling. The current regulation is achieved by using the analog programming input of the constant current value in the power supply, which is relatively noisy and drifts over time. This could be improved in the future by adding an insulated-gate bipolar transistor (IGBT) based linear constant current regulator after the power supply.

To prepare the molecules in this ( $m_S = -1/2, m_I = -1/2$ ) manifold seems trivial at first glance. Similar to the dipolar interaction experiment, after  $\Lambda$ -imaging, the molecular population is distributed among multiple hyperfine states of the  $X^2\Sigma, N = 1$  rotational manifold. We first optically pump them into the  $|i\rangle \equiv |N = 1, F = 0, m_F = 0\rangle$  state (Figure 6.2 (a)). Next, the trap depths of the tweezers are ramped down from



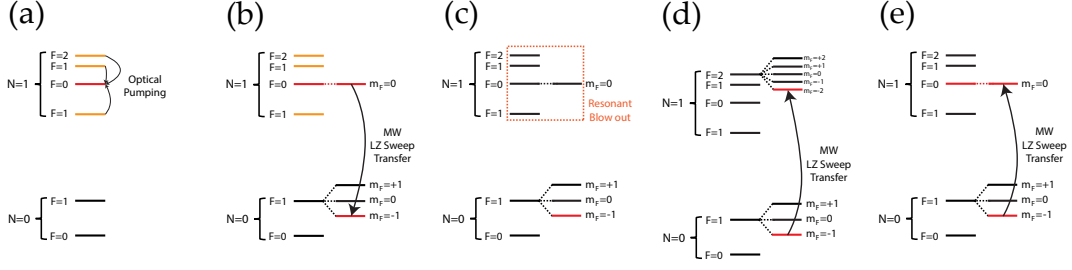


**Figure 6.2:** Relevant rotational ( $N$ ) and hyperfine ( $F$ ) states in the ground electronic state of CaF. Figure (a)~(c) show steps of state preparation using optical pumping, microwave Landau-Zener transfer and resonant blow out. Figure (d) shows the final step of preparing molecules in  $|N = 1, F = 2, m_F = -2\rangle$ . Figure (e) shows the final step of preparing molecules in  $|N = 1, F = 0, m_F = 0\rangle$ .

$\sim k_B \times 1.3 \text{ mK}$  to  $\sim k_B \times 220 \mu\text{K}$ . This adiabatically cools the molecules from a temperature of  $\sim 60 \mu\text{K}$  to  $\sim 25 \mu\text{K}$ , leaving  $\bar{n}$  on all three directions unchanged. A small bias magnetic field along the vertical  $y$ -axis,  $B_y \sim 2.8 \text{ G}$ , is then applied to lift the degeneracy between  $m_F$  states. This allows the use of a microwave Landau-Zener (LZ) sweep to shelve the population into the  $|N = 0, F = 1, m_F = -1\rangle$  state (Figure 6.2 (b)). A laser pulse resonant with the  $|X^2\Sigma, N = 1\rangle - |A^2\Pi_{1/2}, J = 1/2\rangle$  transition removes the residual molecules left in the  $N = 1$  manifold while not affecting the shelved population in the  $N = 0$  manifold (Figure 6.2 (c)).

After this, we apply a LZ sweep to transfer the molecules back into the  $|N = 0, F = 2, m_F = -2\rangle$  state (Figure 6.2 (d)). We then only need to slowly increase the magnetic field, where the molecules will adiabatically follow the Zeeman shift curve to the targeted  $|m_N = -1\rangle$  state in the  $(m_I = -1/2, m_S = -1/2)$  manifold at high magnetic field. When we engage a round trip magnetic field ramp, we find that molecules are lost during the ramp. We then tried to ramp the magnetic field to different level, and find that there is no loss if the magnetic field is not ramped high enough, and there are

sharp loss features when the magnetic field is ramped beyond some special values, as shown in Figure 6.3 (a). With identical ramp profiles, there is no loss feature observed when we initially prepare the molecule in  $|F = 2, m_F = +2\rangle$ , as shown in Figure 6.3 (b).

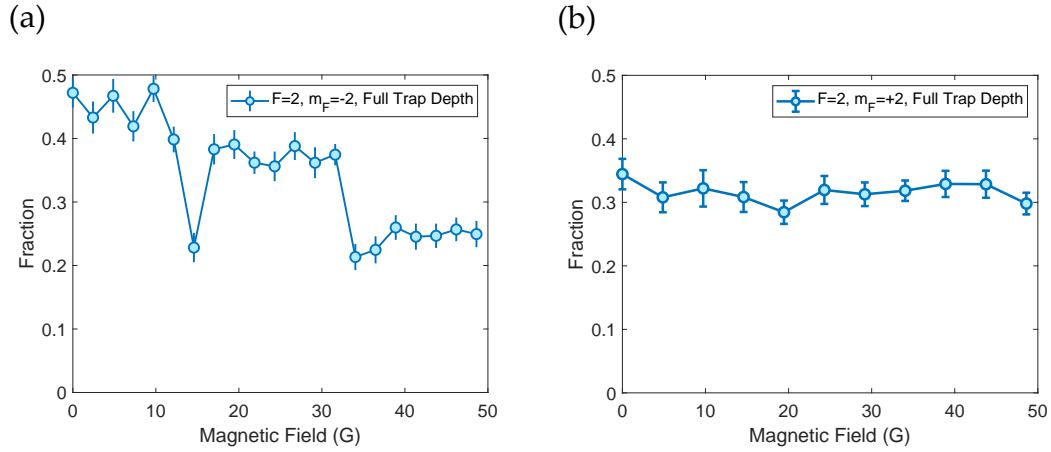


**Figure 6.3:** (a) Loss from  $|F = 2, m_F = -1\rangle$  is observed as the amplitude of the magnetic field ramp is scanned. (b) No loss is observed from  $|F = 2, m_F = -1\rangle$  as the amplitude of the magnetic field ramp is scanned.

The origin of this issue is quickly figured out using our state-sensitive detection recipes, by measuring the population on each state in  $N = 1$  manifold to locate the lost population. It seems the population is dominantly lost to  $|F = 1+, m_F = 0\rangle$  state. It is actually obvious when looking at the Zeeman structure of the  $N = 1$  manifold (Figure 6.4 (a)), due to the tensor AC Stark shift,  $|F = 2, m_F = -2\rangle$  state can mix with  $|F = 1+, m_F = 0\rangle$ , creating an avoided crossing on the Zeeman shift curve. The position of this avoided crossing coincident with the sharp loss feature observed in the data. If we reduce the tweezer trap depth, the energy gap becomes smaller compared to the scale of magnetic field ramp rate, we observe that the loss is reduced (Figure 6.4 (b)). It

is also possible to reduce the ramp by increasing the ramp rate. Both these two methods cannot completely eliminate leakage into  $|F = 1+, m_F = 0\rangle$  states. To solve this problem in a robust way, we decide to instead initialize the molecules in  $|F = 0, m_F = 0\rangle$  (Figure 6.2 (e)) and ramp the magnetic field to prepare  $|m_I = -1/2, m_S = -1/2, m_N = +1\rangle$ , since this state does not have any avoided crossing in the magnetic field ramp range.

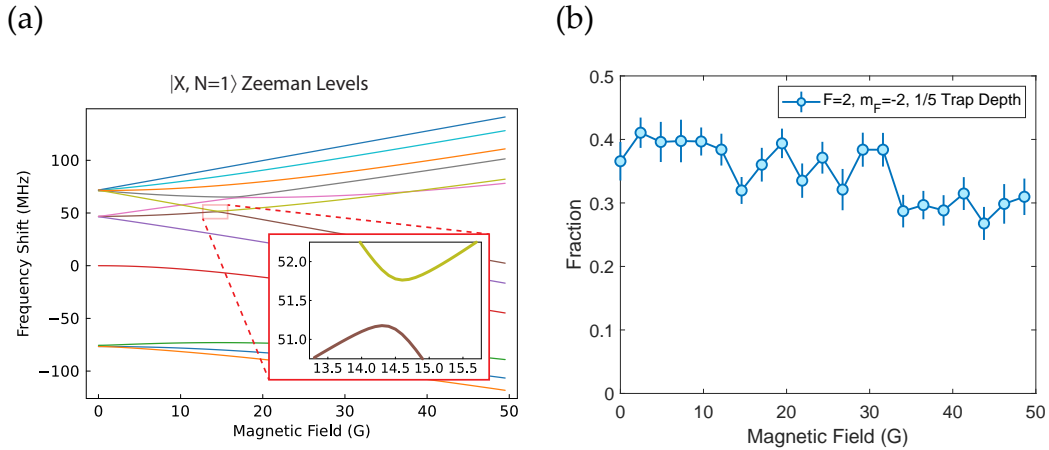


**Figure 6.4:** (a) Avoided crossing between  $|F = 2, m_F = -2\rangle$  state and  $|F = 1+, m_F = 0\rangle$  state around magnetic field  $B_{\text{cross}} \approx 14.5$  G. (b) Loss is much reduced after tweezer trap depth is reduced to  $1/5$

### 6.3 RESOLVING MOTIONAL SIDEBANDS USING RAMAN TRANSITIONS

After prepare the molecules on the correct initial state at high magnetic field, we try to see if we could drive Raman transition between different  $m_N$  states. We uses a Raman laser optical breadboard to prepare all the frequencies required for this task and later RSC.

The layout of the Raman laser optical breadboard are shown in the Figure 6.5. The

Raman laser beams are derived using AOMs from a single frequency 531 nm laser. All beams are set to have a single photon detuning of  $\Delta \sim 2\pi \times 44$  GHz, red-detuned from the  $|X^2\Sigma, N = 1\rangle$  to  $|B^2\Sigma, N = 0\rangle$  transition (Figure 6.1 (b)). The laser frequency is monitored by the wavemeter but remains unlocked, since optical path length difference between all fibers are short enough compared to the instantaneous linewidth of the laser ( $< 1$  MHz). Each Raman beam is separately prepared with an acousto-optic modulator to define both its frequency and intensity. The two arms of each pair of beams are set with a frequency difference  $\sim 41$  MHz (defined as the carrier frequency), chosen to match the energy difference between the RSC ground states,  $|m_N = \pm 1\rangle$ , at  $B_z \sim 200$  G. The RB2 – 4 beams in our experiment are turned on as a square pulse, whereas RB1 is a Blackman pulse, which greatly reduces off-resonant driving and helps to resolve closely spaced sidebands.

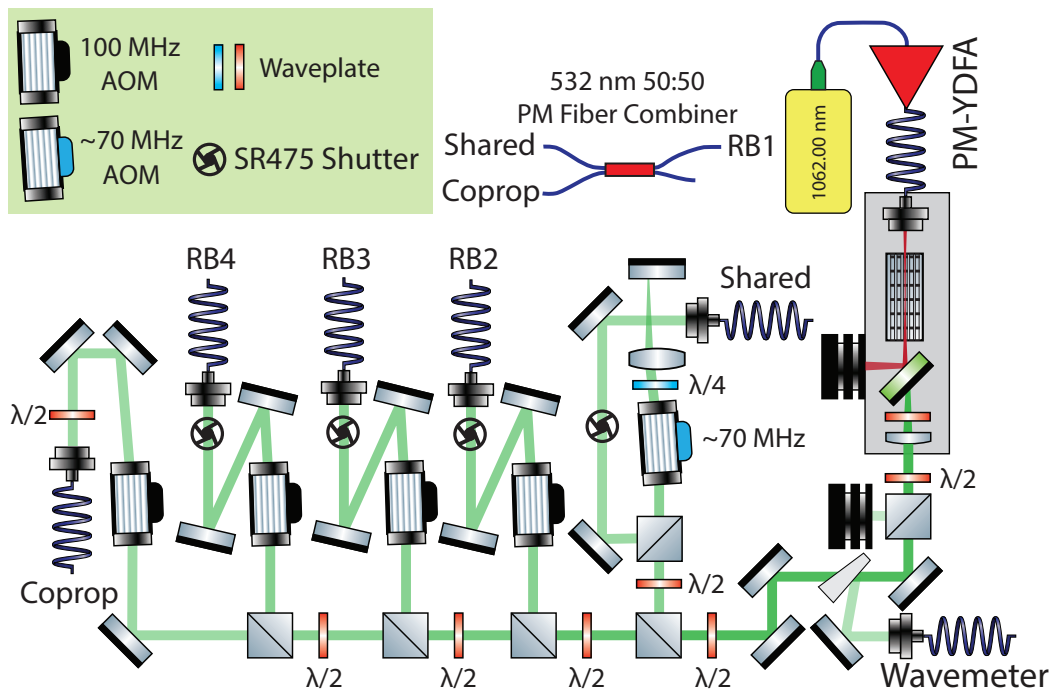


Figure 6.5: Raman laser optical setup

For initial alignment of the Raman beam paths onto the molecules, we first reduce the detuning of the Raman laser, and steer the Raman beams until molecule loss in the tweezers is observed. We are quite ambitious to resolve the sidebands right after this alignment. The Raman transition couples to motional degrees of freedom by the momentum kicks due to the absorption of one photon from one Raman beam and stimulated emission of one photon into another beam. The direction of the motion is defined by the difference of the  $k$ -vectors between two Raman beams. We quickly setup RB<sub>1</sub> and RB<sub>2</sub> in the arrangement shown in Figure 6.6 (a) to probe the motional sensitive transition.

Due to the geometry of the high magnetic field coil and its relative position to the glass cell, it is hard to apply the magnetic field in the direction of tweezer polarization. Although it is doable with our coil design, installing those extra coils greatly reduce the optical access to the molecules. Thus we did not do that at this moment. At this moment, there are two options in front of us, either use high magnetic field (up to  $\sim 200$  G with current SSR) in the tweezer  $k$ -vector direction (configuration A), or use a relatively high field ( $\sim 40$  G) in the tweezer polarization direction (configuration B).

We first tried configuration A, where a quick two-photon detuning scan of the Raman beams shows a broad single peak, which we assume is the carrier at that time. We tried to vary the Raman beam power, hoping that the peak is broad due to power broadening (Figure 6.6). That's clearly not the case, although we can broaden it even more with higher Raman beam power, but it does not get any narrower for very low Raman beam power. We failed to resolve Raman sidebands using this configuration.

We then tried configuration B, and switched to a co-propagating motion insensitive Raman beams. This is achieved by combined two frequencies of the Raman transition into a single polarization-maintaining fiber and delivered to the molecules. By scan-

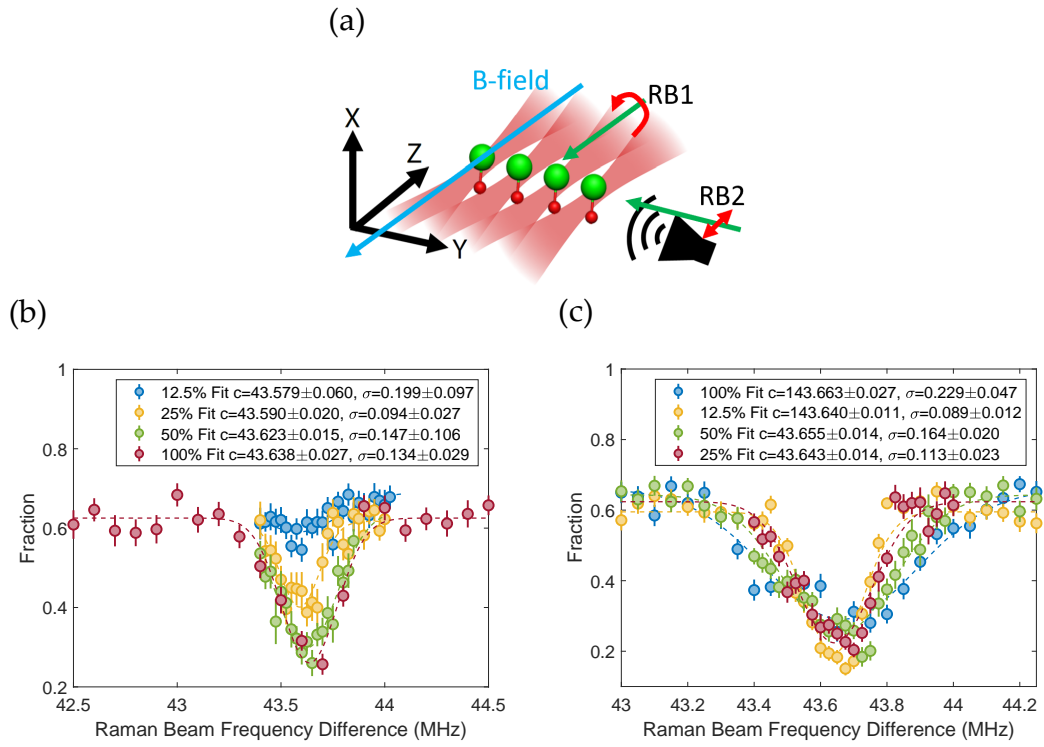


**Figure 6.6:** (a) Motion sensitive Raman transition driven with B-field aligned with tweezer  $k$ -vector (configuration A). (b) Scanning frequency difference between Raman beams at different Raman beam power. (c) Scanning frequency difference between Raman beams at different tweezer trap depth.

ning the relative frequency between the two frequency components, maximal population transfer between the  $|m_N = \pm 1\rangle$  should be observed at the carrier resonance. This resonance frequency can also be used later to locate the  $\Delta n = 0$  transition in the Raman sideband thermometry (RST) spectra.

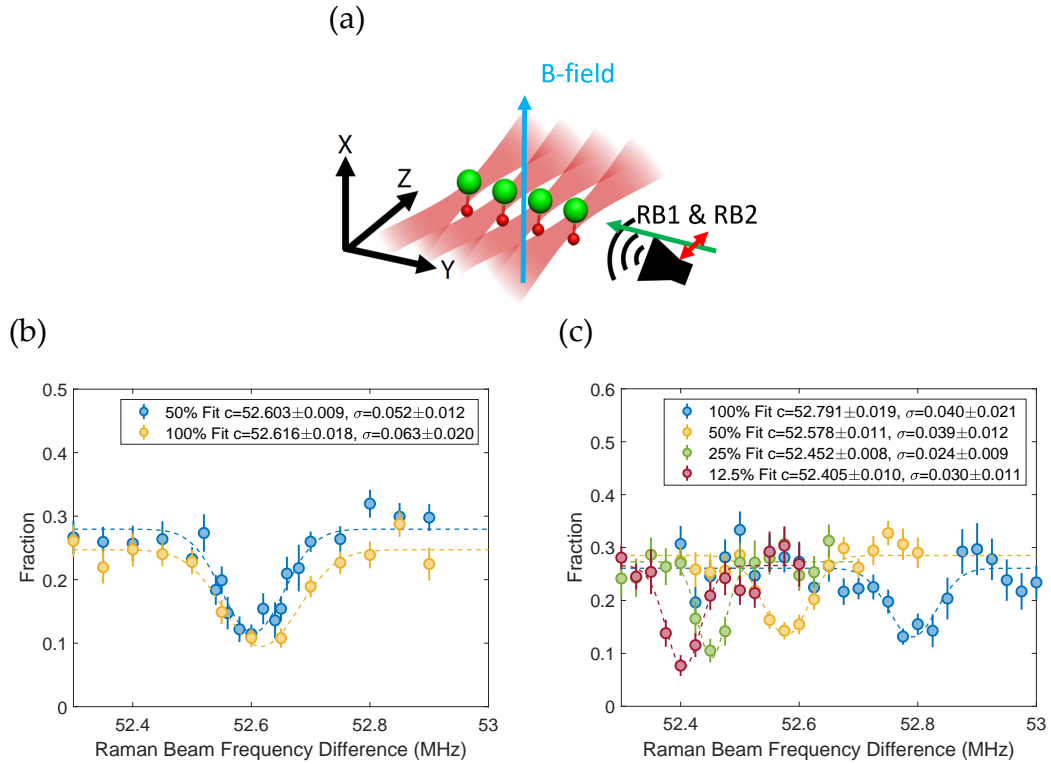


**Figure 6.7:** (a) Motion insensitive Raman transition driven with B-field aligned with tweezer polarization (configuration B). (b) Scanning frequency difference between Raman beams at different Raman beam power. (c) Scanning frequency difference between Raman beams at different tweezer trap depth.

We find that the broadening of this scan is almost equally bad, shown in Figure 6.7 (a). When the Raman beam power is reduced, we find the transition is narrower, but not narrow enough. Next, we ramp the trap depth of the tweezer to different values, and

find that the frequency shifted significantly, as shown in Figure 6.7 (b). Such broadening would definitely prevent us from resolving motional sidebands. We quickly realize that, although the choice of different  $(m_I, m_S)$  does not matter much for tensor AC Stark shifts at high magnetic field, it does matter at relative low magnetic field before the spins are fully decoupled. In the  $(m_I = -1/2, m_S = -1/2)$  manifold that we were using,  $m_N = \pm 1$  states actually have large differential tensor AC Stark shift, switching to  $(m_I = -1/2, m_S = -1/2)$  manifold could be potentially better.

Since we know that we have to apply high magnetic field later for the optical pumping step, if configuration B is required to resolve sidebands, we probably have to replace the vertical coil with the high magnetic field version. We did not try to switching to  $(m_I = 1/2, m_S = 1/2)$  manifold and give it a try in configuration B. Instead, we go back to configuration A and try motion insensitive transition. We find that the transition is much narrower than the previous motion sensitive result. It can be made even narrower by reducing the Raman beam power, indicating the width of the transition is dominated by power broadening (Figure 6.8 (a)). We also tried changing tweezer trap depth, and find it does not have a strong effect on the transition frequency (Figure 6.8 (b)).

When we review the data in Figure 6.6, the slight asymmetry of the broad peak catches our eye. Due to the direction of RB1 and RB2 chosen for this data set, many orders of radial and axial motional sidebands are overlapping with each other. The broadening we observed when tweezer trap depth is increase is not just coming from differential tensor AC Stark shift, but increased radial trap frequency causing sidebands moving further away from the carrier. Due to the initial high temperature of the molecules, it is clear that at high trap depth (high trap frequency), there are more sidebands on the low frequency side, which corresponding to cooling sidebands (re-



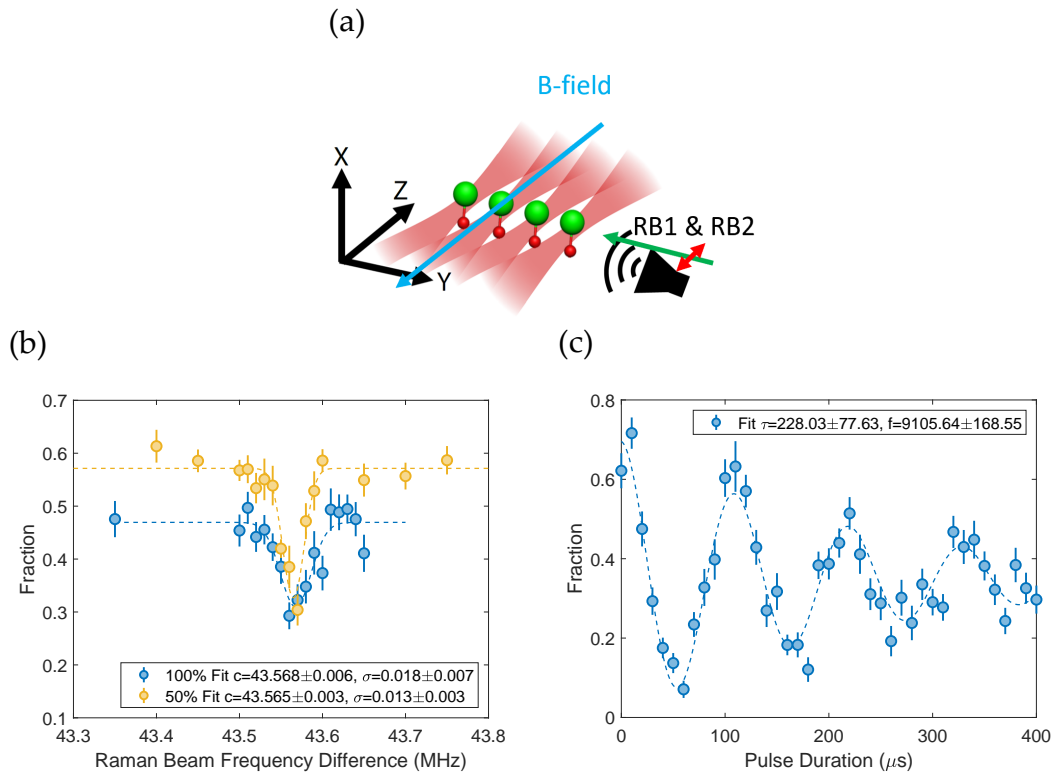


**Figure 6.8:** (a) Motion insensitive Raman transition driven with B-field aligned with tweezer  $k$ -vector (configuration A). (b) Scanning frequency difference between Raman beams at different Raman beam power. (c) Coherent Rabi oscillation observed.

duce motional quantum number).

We decide this is a good start, even though the differential tensor AC Stark shift is not zero theoretically in configuration A. We could still potentially make it work if the temperature is progressively cooled, when the effect of differential AC Stark shift greatly reduces after the molecules are localized near the center of the tweezer.

We then realign the RB1  $\sim 4$  in the arrangement shown in Figure 6.9. In this new alignment, The RB1 beam is the shared arm for all three pairs of RSC beams. RB2 and RB3 are perpendicular to RB1 but propagate in the opposite direction. RB4 is propagating at an angle  $\sim 40^\circ$  relative to RB1. RB2 – 4 are used in conjunction with RB1 to separately address the three orthogonal axes of the trap. For example, RB1 and RB2 is used to address x direction, RB1 and RB3 is used to address y direction. RB1 and RB4 address mostly z direction, but with some x and y components. The plan is to achieve radial cooling on the XY plane first, and tackle the challenge on the axial Z direction later.

To align the center of the Raman beams onto the molecules with higher precision, we couple two frequencies for driving the motion-insensitive Raman transition into each of the RB1 – 4 fiber collimators. We then maximize the Rabi frequency of this motion-insensitive Raman transition by steering the beam. A subset of six tweezers in the full array is used in this work. Over this subset, we measure a root-mean-squared (RMS) deviation of Rabi frequency of less than 3%, verifying the uniform illumination over the tweezer subset. This procedure is repeated for each of the RB1 – 4 beam paths to finish the alignment. Later, we also use this motion-insensitive Raman transition as a convenient way to transfer population between  $|m_N = \pm 1\rangle$ . This is utilized in the experiment sequence to realize state-sensitive detection on  $|m_N = -1\rangle$  state required by

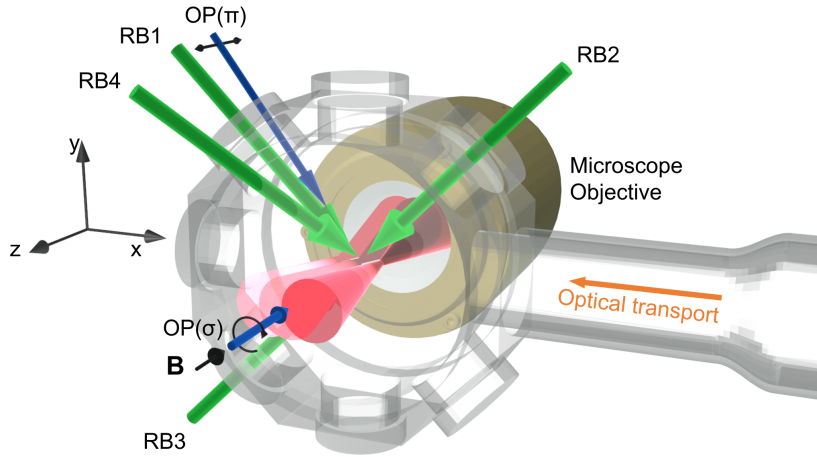


**Figure 6.9:** Configuration of Raman beams and optical pumping beams used in RSC. RB1 and RB2 address the radial motion in  $x$ -direction, RB1 and RB3 address the radial motion in  $y$ -direction, and RB1 and RB4 mainly address the axial motion in  $z$ -direction. The RB1 path is also be employed to drive a motion-insensitive Raman  $\pi$  pulse for population swapping between  $|m_N = \pm 1\rangle$  states.

RST\*.

#### 6.4 OPTICAL PUMPING

The optical pumping (OP) light is derived from our 531 nm slowing laser, since they are both close to resonance of  $(X, v = 0, N = 1)$  and  $(B, v = 0, N = 0)$  transition. The frequency is quickly hopped to the optical pumping frequency for RSC using the optical PLL setup.

In the OP steps of RSC, both  $\sigma^+$  and  $\pi$  transitions are driven to create a dark state in  $|m_N = +1\rangle$ . Two OP beams are used, where one propagates perpendicular to the magnetic field direction (linearly polarized along the magnetic field so as to address the  $\pi$  transition), and the other propagates along the magnetic field direction (circularly

---

\*You might notice the ugly negative peaks for all the data taken before this is implemented. We can now finally flip the population and make it look nicer.

polarized to address the  $\sigma^+$  transition) (Figure 6.9). During each OP step,  $\sim 3$  photons on average are estimated to be scattered based on calculated branching ratios.

This also sounds like an easy task and seems nothing could go wrong. We first locate the optical pumping frequencies by measure the population that is pumped into  $m_N = 0$  and scan the optical pumping laser frequency. This is done by apply state-sensitive detection on  $F = 1, m_F = -1$  after high magnetic field is ramped down. For the  $\sigma^-$  transition, we prepare population in  $m_N = +1$ , apply  $\sigma$ -OP light to pump population into  $m_N = 0$ . For the  $\sigma^+$  transition, we prepare population in  $m_N = +1$ , then use the motion-insensitive transition to transfer the population to  $m_N = -1$ , and then apply  $\sigma$ -OP light with opposite circular polarization to pump population into  $m_N = 0$ . For the  $\pi$  transition, we simply prepare population in  $m_N = 0$ , and pump the population out of  $m_N = 0$  using  $\pi$ -OP light. The OP frequency scan result is shown in Figure 6.10. We find good agreement between the measured frequency spacings and the calculated level spacings.

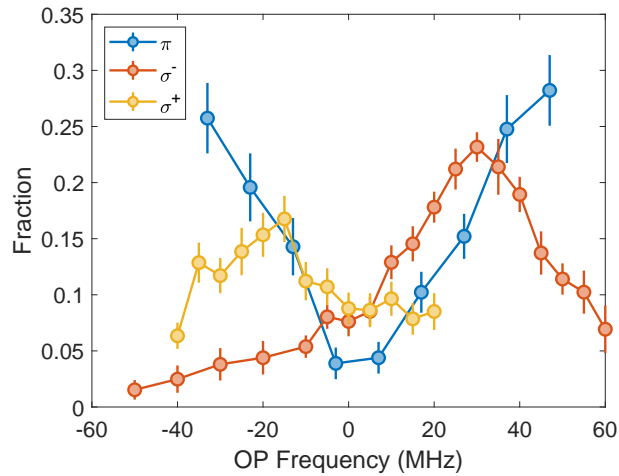


**Figure 6.10:** Optical pumping frequency scan.

We then check the purity of each optical pumping beam. We prepare population on

$m_N = +1$  state and then detect population on  $m_N = 0$  after driving  $\sigma^-$  transition or drive  $\sigma^+$  transition by rotating the waveplate to create the opposite circular polarized light. The OP frequency is fixed on the frequency that is on resonance with  $X, m_N = +1$  to  $B, m_N = 0$ . We should be able to observe population transferred to  $m_N = 0$  state quickly when  $\sigma^-$  transition is driven, but slowly when  $\sigma^+$  transition is driven (since it is forbidden). However, the measurement shows the  $\sigma^+$  is also quickly pumping population into  $m_N = 0$ , the optical pumping rate is only different by 3 times between the two configurations, as shown in Figure 6.12 (a). We also checked that the  $\pi$ -OP works fine, with a difference of optical pumping rate over 30 times between the two opposite polarization of the  $\pi$ -OP beam, as shown in Figure 6.12 (b).

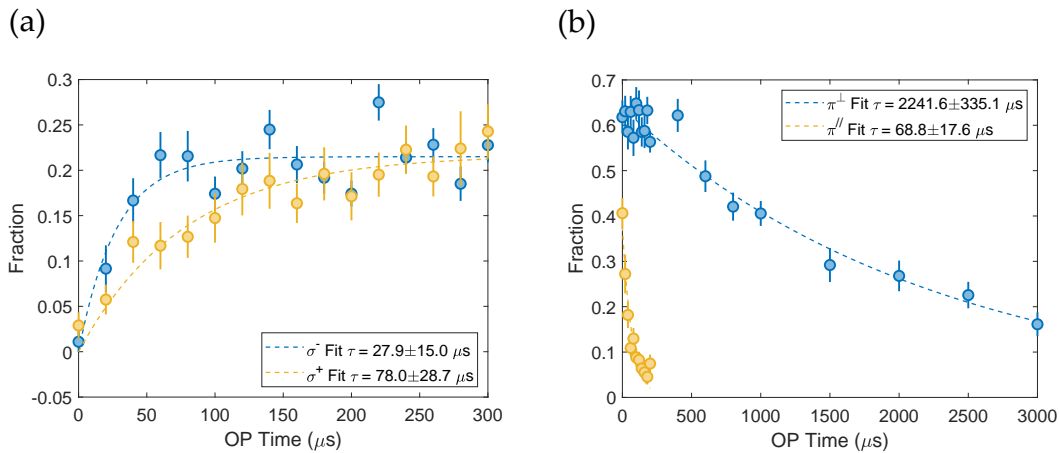


**Figure 6.11:** (a) Bad  $\sigma$  optical pumping data, showing polarization is not pure enough. (b)  $\pi$  optical pumping is working properly.

It is quite clear this is probably due to some stray OP light hitting the molecules with the wrong polarization. Since the  $\sigma$ -OP light is shooting towards the objective, we have suspected that objective reflection could be the issue, but the reflectivity on all the AR

coating used in the objective does not support this explanation. In addition to that, most of the head-on reflection from a surface will simply mirror the polarization, and since its  $k$ -vector also reverses, it will drive the same  $\sigma^\pm$  transition as the original OP beam. We did not figure the cause of this OP purity issue, until we move our attention to optics behind the objective. We almost forget that there is a piece of 2-inch 808 nm polymer half waveplate, coated for NIR, between the dichroic mirror and the objective. This waveplate has  $\sim 20\%$  reflectivity at our OP wavelength 531 nm for each surface. The major issue is the reflection from the surface that is on the far side from the objective, causing the  $\sigma$ -OP light transmits through the 808 nm waveplate twice, which obviously changes polarization, and hit the molecules again. After moving this waveplate before the dichroic mirror (no longer between the dichroic mirror and the objective), we are able to observe a difference of optical pumping rate over 70 times between  $\sigma^+$  and  $\sigma^-$  OP light.

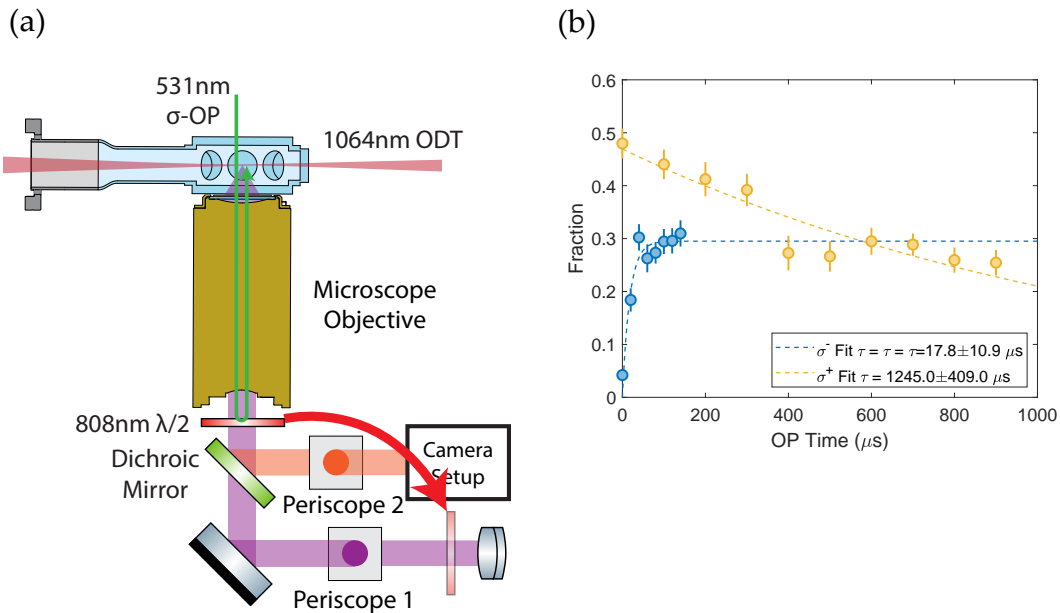


**Figure 6.12:** (a) The reflection from the 808 nm waveplate causing OP issues with the  $\sigma$ -OP beam. (b)  $\sigma$ -OP purity recovers after moving the 808 nm waveplate (red arrow in (a)).

## 6.5 RAMAN SIDEBAND THERMOMETRY

We employ RST to determine the temperature of the molecules (or, equivalently, the average motional occupation number  $\bar{n}$ ). In this technique, Raman transitions (the same that are used in RSC) are driven for a fixed duration, and the population transferred to  $|m_N = -1\rangle$  is then measured using a state-sensitive detection scheme. The two photon detuning  $\delta$  (Figure 6.1 (b)) of the Raman transition is scanned, forming a Raman sideband thermometry spectrum. In the state-sensitive detection scheme, the first step is to drive a  $\pi$ -pulse on the motion-insensitive Raman transition to transfer the population from  $|m_N = -1\rangle$  to  $|m_N = +1\rangle$ . Subsequent purification and detection of population in

$|m_N = +1\rangle$  is done in a similar way to the state initialization procedure. Specifically, we ramp the magnetic fields back to  $B_z = 0$  and  $B_y \sim 2.8 \text{ G}$ , apply a LZ sweep to transfer population from state  $|i\rangle$  into the  $N = 0$  manifold, remove the remaining population in the  $N = 1$  manifold, and finally apply a LZ sweep to transfer the shelved  $N = 0$  molecules back to  $|i\rangle$ . The molecules survived at this point of the experiment are considered Raman sideband cooled, where molecules leaked out of the photon cycling states ( $m_S = -1/2, m_J = -1/2$ ) of the RSC are removed. The tweezers are then ramped back to full depth and a third  $\Lambda$ -imaging pulse (“Img 3” in Figure 6.13 is used to detect the molecules. The fraction of molecules in  $|m_N = -1\rangle$  is calculated by dividing the number of detected molecules in “Img 3” by the number detected in “Img 2”.

Generally, an RST spectrum contains a center peak at the carrier frequency ( $\Delta n = 0$ ), with “cooling” ( $\Delta n < 0$ ) and “heating” sideband peaks ( $\Delta n > 0$ ) at lower and higher frequencies. The average occupation number of the motional states,  $\bar{n}$ , can be related to the ratio of the peak heights of the first cooling sideband to the first heating sideband,  $\alpha$ , using the relation  $\bar{n} = \frac{\alpha}{1-\alpha}$ <sup>88,134</sup>. The signature of a low temperature sample is the strong asymmetry between the peak height of the cooling and heating sidebands.

To see how this is derived, we assume the Rabi frequency of a Raman transition between motional states  $|n\rangle$  and  $|n'\rangle$  is denoted as  $\Omega_R^{n,n'}$ . It is related to the Rabi frequency of the carrier transition by a factor denoted as  $M_{n,n'}$ .

$$\Omega_R^{n,n'} = M_{n,n'} \Omega_R^0 \quad (6.1)$$



An analytical form of  $M_{n,n'}$  is given by 128

$$\begin{aligned} M_{n,n'} &= \langle n | e^{i\eta^R(\hat{a}+\hat{a}^\dagger)} | n' \rangle \\ &= e^{-(\eta^R)^2/2} \sqrt{\frac{n_{<}!}{n_{>}!}} (\eta^R)^{|n-n'|} L_{n_{<}}^{|n-n'|} ((\eta^R)^2) \end{aligned} \quad (6.2)$$

Where  $\eta^R$  is the Lamb-Dicke parameter of the Raman transition. It is defined as  $\eta^R \equiv \Delta k x_0$ , where  $\Delta k$  is the wave-vector difference between the two Raman beams and  $x_0 = \sqrt{\hbar/(2m\omega)}$  is the spread of the ground-state wave-function of the molecule. In our experiment, we have  $\eta_x^R = 0.57$ ,  $\eta_x^R = 0.61$ ,  $\eta_z^R = 0.62$ .  $n_{<(>)}$  is the smaller(larger) one between  $n$  and  $n'$ .  $L_n^\alpha(x)$  is the generalized Laguerre polynomial.

The population transferred after a  $\Delta n = \pm 1$  sideband thermometry pulse is  $P_\pm$ .

$$P_\pm = \sum_{n=0}^{\infty} p_n \sin^2(\Omega_R^{n,n\pm 1} t/2) \quad (6.3)$$

Where  $t$  is the width of the pulse applied and  $p_n$  is the probability to find the molecule in  $|n\rangle$ . Note that

$$\begin{aligned} \Omega_R^{n,n'} &= \Omega_R^{n',n} \\ \Omega_R^{n,-1} &= 0 \end{aligned} \quad (6.4)$$

and for a thermal distribution

$$p_n = (1 - e^{-\frac{\hbar\omega}{k_B T}}) e^{-\frac{n\hbar\omega}{k_B T}} \quad (6.5)$$

$$\begin{aligned}
P_+ &= \sum_{n=0}^{\infty} p_n \sin^2(\Omega_R^{n,n+1} t/2) \\
&= \sum_{n=0}^{\infty} (1 - e^{-\frac{\hbar\omega}{k_B T}}) e^{-\frac{n\hbar\omega}{k_B T}} \sin^2(\Omega_R^{n,n+1} t/2) \\
&= \sum_{m=1}^{\infty} (1 - e^{-\frac{\hbar\omega}{k_B T}}) e^{-\frac{(m-1)\hbar\omega}{k_B T}} \sin^2(\Omega_R^{m-1,m} t/2) \\
&= e^{\frac{\hbar\omega}{k_B T}} \sum_{m=1}^{\infty} (1 - e^{-\frac{\hbar\omega}{k_B T}}) e^{-\frac{m\hbar\omega}{k_B T}} \sin^2(\Omega_R^{m-1,m} t/2) \\
&= e^{\frac{\hbar\omega}{k_B T}} \sum_{m=1}^{\infty} p_m \sin^2(\Omega_R^{m,m-1} t/2) \\
&= e^{\frac{\hbar\omega}{k_B T}} \left[ \left( \sum_{m=1}^{\infty} p_m \sin^2(\Omega_R^{m,m-1} t/2) \right) + p_0 \sin^2(\Omega_R^{0,-1} t/2) \right] \\
&= e^{\frac{\hbar\omega}{k_B T}} \sum_{m=0}^{\infty} p_m \sin^2(\Omega_R^{m,m-1} t/2) \\
&= e^{\frac{\hbar\omega}{k_B T}} P_-
\end{aligned} \tag{6.6}$$

$e^{-\frac{\hbar\omega}{k_B T}}$  is directly linked to the sideband thermometry peak height ratio  $\alpha$  and is independent of the specific choice of sideband thermometry pulse width  $t$ .

$$e^{-\frac{\hbar\omega}{k_B T}} = \frac{P_-}{P_+} = \alpha \tag{6.7}$$

The average harmonic potential occupancy number  $\bar{n}$  can be determined from  $\alpha$

$$\begin{aligned}
 \bar{n} &= \sum_{n=0}^{\infty} p_n n \\
 &= \sum_{n=0}^{\infty} (1 - e^{-\frac{\hbar\omega}{k_B T}}) e^{-\frac{n\hbar\omega}{k_B T}} n \\
 &= \sum_{n=0}^{\infty} (1 - \alpha) \alpha^n n \\
 &= \frac{\alpha}{1 - \alpha}
 \end{aligned} \tag{6.8}$$

Experimentally, it is desirable to choose a sideband thermometry pulse width  $t$  that results in the largest  $P_+$  and  $P_-$ , so as to increase the sensitivity of the temperature measurement.

## 6.6 RSC RESULTS

The full experimental sequence for RSC is shown in Figure 6.13.

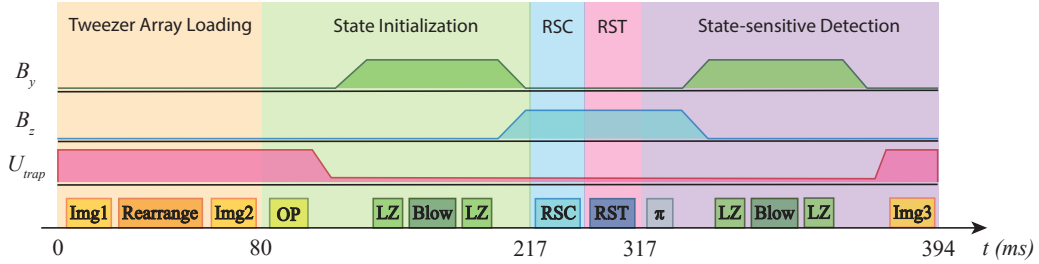


**Figure 6.13:** Experimental sequence of tweezer array preparation, state initialization, RSC, RST, and state-sensitive detection.  $B_y$  and  $B_z$  are the applied magnetic field along  $y$  direction and  $z$  direction.  $U_{trap}$  is the trap depth of the optical tweezer trap.  $\pi$  denotes the motion-insensitive Raman  $\pi$ -pulse used to transfer the population from  $|m_N = -1\rangle$  to  $|m_N = +1\rangle$ .

To characterize the initial temperature of molecules loaded into tweezers, RST is applied just after state initialization (without RSC). Although RST does not have good sen-

sitivity for thermometry at this high temperature, the measured temperature still agrees with release and recapture method and provides important information of our system. In the RST data (before RSC), motional sidebands are clearly resolved in all three directions (see Figure 6.15, orange data). The data show cooling sidebands (to the left of the carrier peak) of up to  $\Delta n = -4$  in the radial directions and  $\Delta n = -6$  in the axial direction, where  $\Delta n$  is the difference in the motional quantum number between the carrier and the sideband. These values of  $|\Delta n| > 1$  indicate that the cooling must start outside of LD regime. We used a model with multiple Lorenzians with equal frequency spacings to fit the spectrum. The model can be described as  $P(\delta) = \sum_k P_k \frac{\Omega_k^2}{(\delta - k\omega)^2 + \Omega_k^2} + \mathcal{C}$  where Rabi frequency  $\Omega_k$ , peak height coefficient  $P_k$  for peak  $k$ , trap angular frequency  $\omega$  and offset  $\mathcal{C}$  are free parameters in the model. The resolved sidebands are used to determine the trap frequencies for creating the RSC recipe, in our case,  $\omega_x = 2\pi \times 75(1)$  kHz,  $\omega_y = 2\pi \times 65(2)$  kHz (radial directions) and  $\omega_z = 2\pi \times 13.6(3)$  kHz (axial directions).

Starting again with molecules in this initial loading and state initialization condition, we apply the RSC sequence. As we start outside of the LD regime, we initially address  $\Delta n = -3$  motional sidebands for radial cooling and  $\Delta n = -5$  motional sidebands for axial cooling. As cooling proceeds we switch over to driving only the first and second order motional sidebands to finish the cooling. The Raman sideband cooling pulse sequence used in this work is shown in Figure 6.14. The pulse shape of RB1 is Blackman while those of RB2–4 are rectangular. Optical pumping (OP) pulses in the figure apply to both  $\pi$  OP and  $\sigma+$  OP beams.

After RSC, RST is performed. The data show that cooling sidebands are strongly suppressed relative to the heating sidebands in all three directions (Figure 6.15, blue curves). The average motional occupation numbers are  $\bar{n}_x = 0.16(12)$ ,  $\bar{n}_y = 0.17(17)$  (radial directions) and  $\bar{n}_z = 0.22(16)$  (axial direction), giving a  $54 \pm 18\%$  probability for

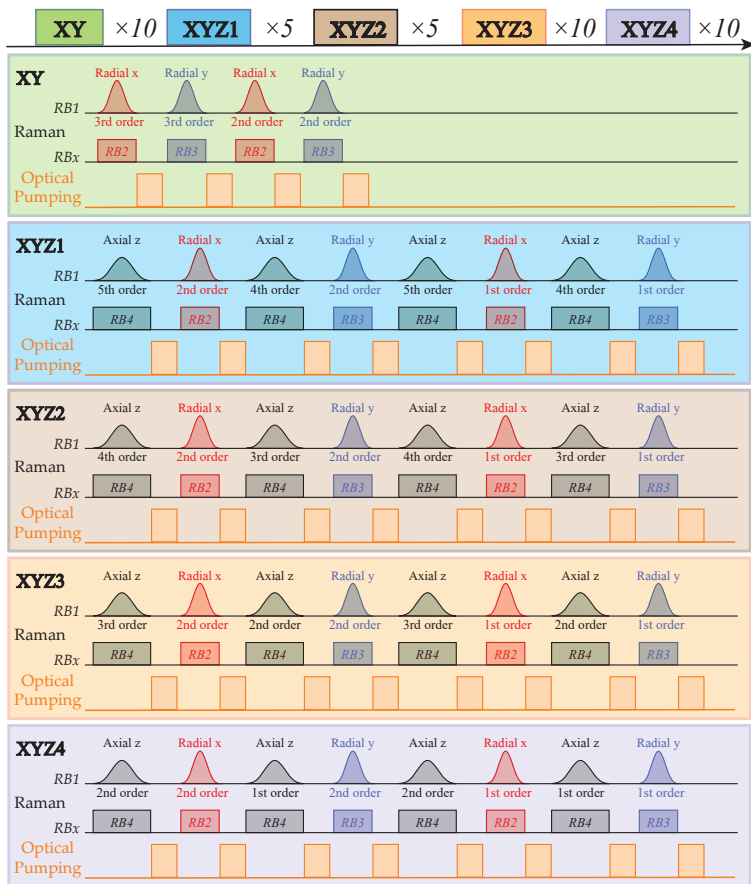
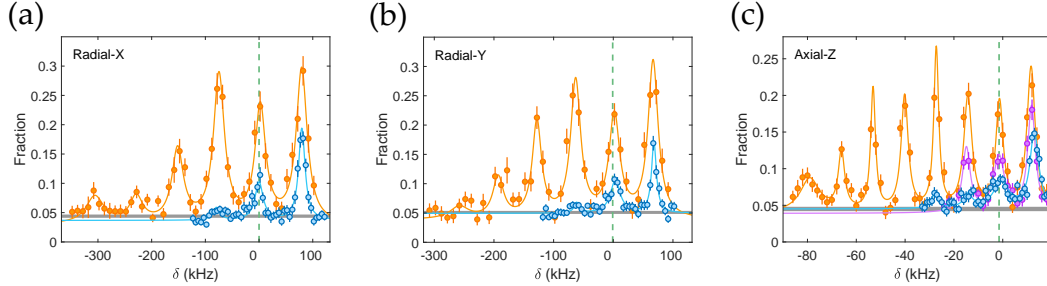


Figure 6.14: Raman sideband cooling pulse sequences used in this work.

preparing the molecules in the motional ground state of the molecules that survived RSC.



**Figure 6.15:** Raman sideband thermometry spectra: (a) radial  $x$  direction; (b) radial  $y$  direction; and (c) axial  $z$  direction. Blue curves are the spectra obtained after RSC, orange curves are the spectra obtained before RSC. For the axial  $z$  direction, an additional purple curve represents the spectrum obtained without the last step of RSC applied (partial cooling). The Raman pulse durations used for these RST spectra are  $t_x = 75 \mu\text{s}$ ,  $t_y = 110 \mu\text{s}$  and  $t_z = 350 \mu\text{s}$ . Green dashed line indicates the carrier frequency for each spectrum. Gray bands indicate the baseline for the spectra measured at the far detuned limit.

The coherence of Rabi oscillations driven on the sideband or carrier transitions can also provide information on the temperature of molecules. Since the Rabi oscillation frequencies for transitions with  $\Delta n = 0, \pm 1$  depend on  $n$ , if the molecules occupy a large number of motional  $|n\rangle$  states, rapid dephasing would be expected. We observe this behavior when attempting to drive Rabi oscillations in the initial configuration (without applying RSC, Figure 6.16, orange data). In contrast, if the molecules occupy a single  $|n\rangle$  state, coherent Rabi oscillations should be observable. After applying RSC, coherent Raman Rabi oscillations on both the carrier and the first heating sideband are clearly observed in all three directions (see Figure 6.16, blue data), showing this effect of the cooling. We use a single exponential decay model for the data before RSC is applied. The Rabi oscillation data after RSC is applied are fitted to a numerically simulated model. This model is based on the form of Equation 6.3. Due to dephasings

coming from the instability of magnetic field and Raman beam intensity, the fit predicts a higher final temperature with large uncertainty for radial directions. For axial direction with smaller Rabi frequency, the fit is dominated by these dephasings and cannot give a reliable prediction of the temperature. These instabilities are technical and can be improved by implementation of active feedback control.

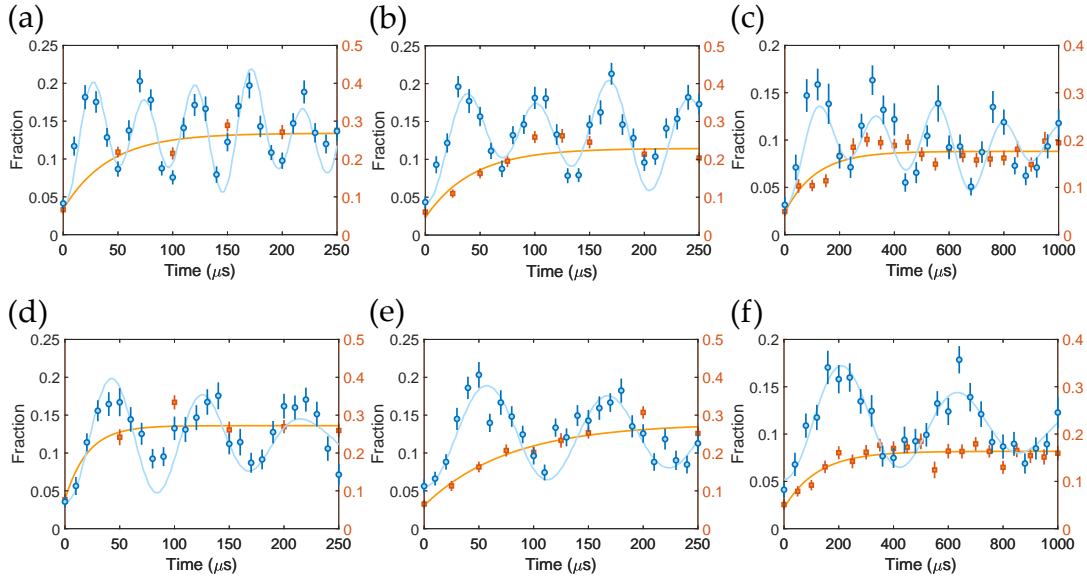


**Figure 6.16:** Rabi oscillations of the carrier transition: (a) radial  $x$  direction; (b) radial  $y$  direction; and (c) axial  $z$  direction. Rabi oscillations of the first heating sideband: (d) radial  $x$  direction; (e) radial  $y$  direction; and (f) axial  $z$  direction. In each figure, the data showing rapid dephasing before the application of RSC are plotted as orange squares, fitted to an exponential decaying model. Coherent Rabi oscillations after the application of RSC are plotted as blue circles, fitted to a numerically simulated model.

In order to study the efficiency of our RSC procedure, we varied the number of Raman and OP steps. As more RSC steps are applied, apparent increased loss of molecules is observed. The survival rate is around 40% after the application of the full RSC procedure. In order to understand the cause of this observation, we turn off the state-sensitivity of the detection in order to detect all the molecules in the  $N = 1$  manifold.

We verify that the total population in the  $N = 1$  manifold remains the same within the measurement error, indicating that this loss is not caused by loss of molecules from the trap, but by decay into other  $(m_S, m_I)$  subspaces. We attribute this to residual mixing between different  $(m_S, m_I)$  subspaces<sup>22</sup>. The observed loss scales with the number of photons scattered during the optical pumping steps of RSC, and a large number of RSC cycles are applied due to the high initial temperature of the molecules. This loss could be mitigated in the future by applying RSC simultaneously on four  $m_S$  and  $m_I$  subsets of states<sup>22</sup>. In an alternative method, one may be able to ramp down the magnetic field in the middle of the RSC pulse sequence and apply  $m_F$  optical pumping to re-initialize the molecules in  $|N = 1, F = 0, m_F = 0\rangle$  state. Since the molecules are already partially Raman sideband cooled, a smaller number of additional RSC cycles would be needed in the final cooling step. Furthermore, instead of blowing away the population in the state-sensitive detection, we can detect the molecules leaked out of the using standard  $\Lambda$ -imaging. A bright tweezer in the image indicates the molecule in that specific tweezer failed to stay in the  $(m_S = -1/2, m_I = -1/2)$  manifold. A dark tweezer in the image indicates the molecule survives the full Raman sideband cooling procedure. Using this piece of information, we could rearrange the dark tweezers into a smaller defect free array where all the molecules are Raman sideband cooled.

## 6.7 CONCLUSION AND OUTLOOK

In summary, we have demonstrated Raman sideband cooling of CaF molecules in an optical tweezer array. Motional sidebands in all three orthogonal directions are spectrally resolved. After applying Raman sideband cooling, resolved sideband thermometry measures the temperature of the molecules in the tweezers, indicating a 3-D mo-



tional ground state probability of  $54 \pm 18\%$  of the molecules that survived RSC. Dephasing of Raman Rabi oscillations is highly suppressed after cooling. Currently, the cooling performance is mainly limited by the off-resonance driving in the Raman steps and heating from the optical pumping steps. To overcome these limitations, the high magnetic field could be better stabilized to allow for lower Raman Rabi frequency and reduced off-resonance driving. In addition, by choosing the high magnetic field direction perpendicular to the trap axial axis, the heating effect from the  $\sigma^+$  optical pumping could be suppressed<sup>22</sup>.

The successful application of Raman sideband cooling on laser-cooled molecules in optical tweezers is an important step toward increasing molecular rotational coherence times and reducing motional dephasing for two qubit dipolar gate operations. It also shows that we now have full control over the degrees of freedom of CaF molecules in the optical tweezers. We note that motional ground state fraction achieved here with directly laser-cooled molecules is on par with that of the molecules formed by association of motional-ground-state cooled atoms in tweezers ( $65(3)\%$ <sup>137</sup>). This work increases the possibilities of molecular optical tweezer arrays for use in the applications of quantum computation, quantum simulation and precision searches for physics beyond the Standard Model.

*Your next beam box is always going to be better.*

The author

# 7

## Next Generation Beam Box

The beam box for CaF Gen2 is already working nicely and meets all our needs. However, there are still many aspects that could be further improved. For example, we find the heat load on 40 K and 4 K stages are both higher than expected. Although this can be solved by upgrading to a more powerful pulse tube, one can still increase the safety factor by improving its design.

## 7.1 POTENTIAL IMPROVEMENTS

### 7.1.1 NO 1K CIRCULATION

In our CaF Gen2 beam box, the 1K circulation system still requires regular warm-ups every 2 weeks if running without a cold trap. As long as the operator can follow the warm-up schedule and adhere to the operation protocols, the 1K circulation volume and helium gas can be kept free from contamination. The 1K circulation system on CaF Gen2 has been running for more than 3 years without an issue. However, it would still be ideal if 1K circulation can be eliminated from the next generation beam boxes, due to its high cost and potential failure modes due to human factor in the operation.

One might think, to maximize the population in  $N = 1$  rotational manifold for CaF molecules, one must cool the CBGB to  $\sim 2$  K. We recently test on CaF Gen2 beam box that increasing the cell temperature from 2 K to 3.5 K (this is realized by throttling the circulation pump on the 1K system) does not have an obvious negative effect on the molecule numbers in the CaF RF MOT. The data are shown in the Figure 7.1. This can be explained by collision between CaF molecules and helium buffer gas near the exiting aperture of the cell, where helium gas is isentropically expanded and cooled. Similar effects are demonstrated on ThO molecules by the ACME collaboration<sup>64</sup>. This gives us confidence to proceed with a new beam box design that is entirely based on a PT310 pulse tube cryocooler providing 1.0 W cooling power at 3 K temperature.

### 7.1.2 CHARCOAL SORB PLATES

We did not have enough sorb plates in the CaF Gen2 beam box. Usually this does not cause any issue, since the experiment is run for half a day everyday, and we warm up

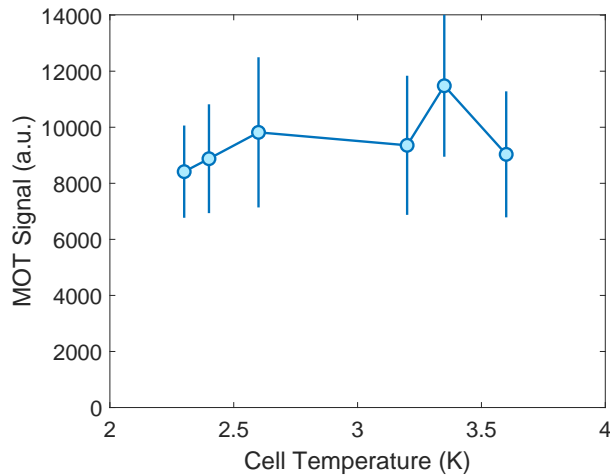


**Figure 7.1:** Molecule numbers in CaF MOT versus cell temperature. Laser ablation energy and slowing time are optimized slightly for different temperatures.

every two weeks to regenerate the sorbs. However, as the whole experimental system becomes more and more stable and automatic, running the experiment 24x7 is no longer a dream for molecule laser coolers. This causes the charcoal sorb to fill up in two weeks on Gen2 apparatus and a thermal run away would occur. This is sad but also proves the great stability of the Gen2 CBGB. To solve this problem, we simply just need to add more charcoal sorbs. For the next generation beam box, we redesign the sorb plate and sorb plate mount to double the density of charcoal sorb plates without increasing the footprint of charcoal module (Figure 7.2).

### 7.1.3 WHERE ARE THE HEAT LOADS?

#### 40K WINDOWS

Glasses are considered black body at Room temperature black-body spectrum range (emissivity is usually over 0.9 for N-BK7 glass, which is typically used in our beam

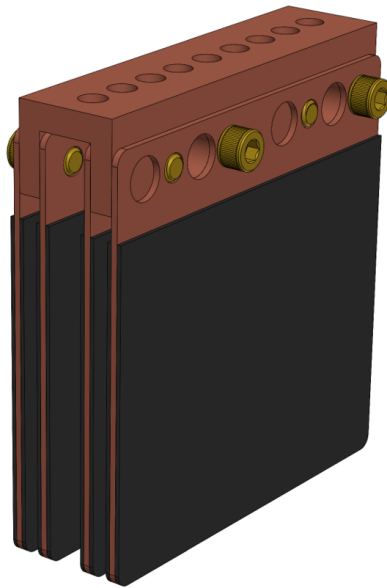


**Figure 7.2:** Double density sorb plate module

boxes). All the cold glass surfaces exposed to 300 K environment are going to absorb black-body heat load and transfer to the 40 K pulse tube stage. In CaF Gen2 beam box design, the 40 K window is mounted outside of the shield, with large areas of high emissivity area exposed (Figure 7.3 (a) and (b)). These surfaces are dominantly the thick outline of the glass and the window clamps. We estimate that up to 5.7 W BBR heat load is absorbed by a single window if the copper window clamp has an emissivity of 0.6 (tarnished). This heat load reduces to 2.77 W if the copper window clamp has a low emissivity of 0.03 (gold plated). The simulation also shows that the center hot spot of the window can be cooled down to  $\sim 50$  K, making its BBR into the 4 K section negligible. It is easy to see that the best solution is simply install this window inside, where the simulation shows the heat load is further reduced to 1.12 W (Figure 7.3 (c) and (d)).

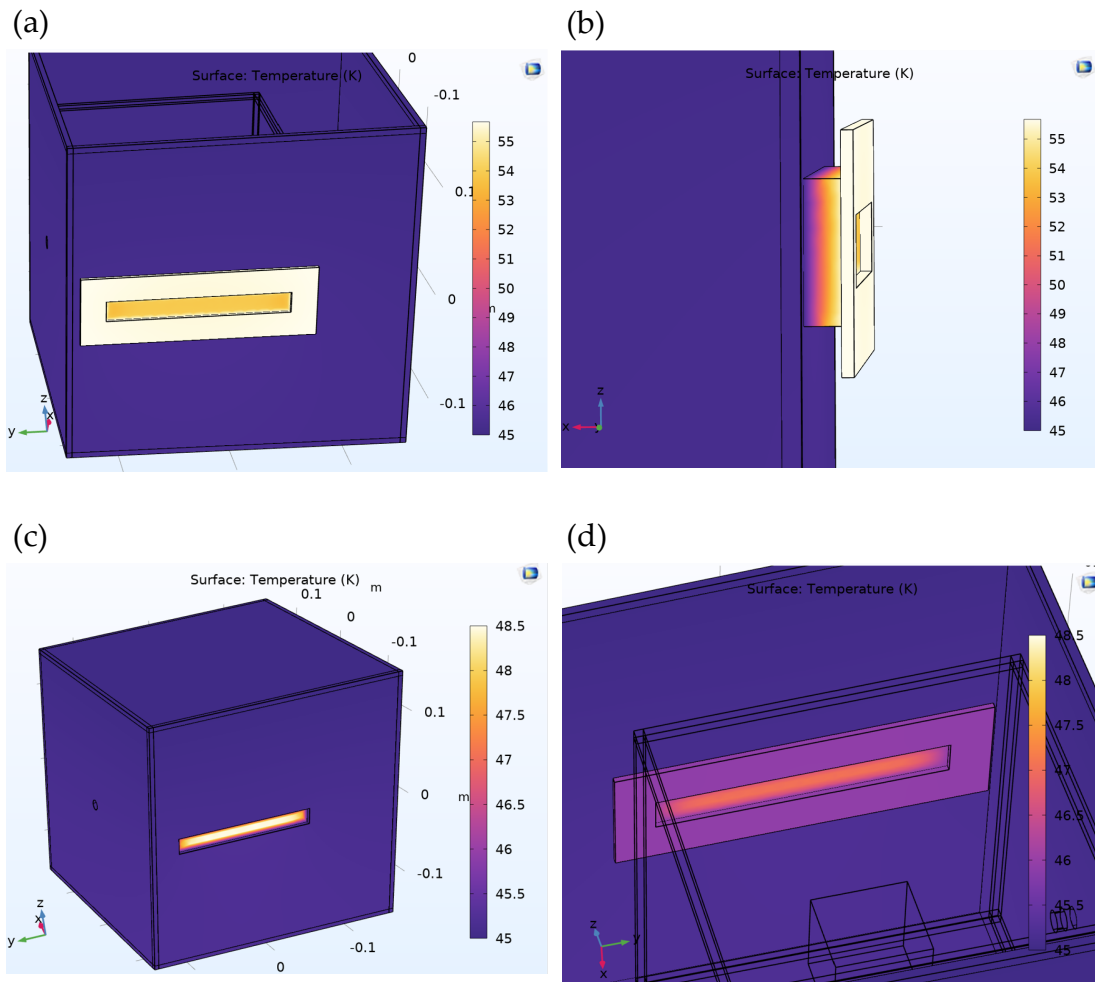


**Figure 7.3:** COMSOL simulation of the temperature of 40 K shield. (a) and (b) shows the design where window is mounted outside. (c) and (d) shows the design where window is mounted inside.

## EXPOSED BARE COPPER SURFACE

Since we have no superinsulation in CaF Gen2 beam box, it is crucial to keep track of all high emissivity surfaces. There are five frames (“donuts”) that are used to adapt the 40 K shield panel onto the structure (Figure 7.4 (a)). They are not gold plated and has significant exposed area to room temperature BBR. We estimate a heat load of  $\sim 10$  W if these surfaces are tarnished with a emissivity of 0.25. The solution to this issue could be gold plating the surface. However, one must notice that a large number of brass screws used here are also exposed, and have a high emissivity. We choose to extend our 40 K panel to cover both the “donut” and the brass screws (Figure 7.4 (b)).

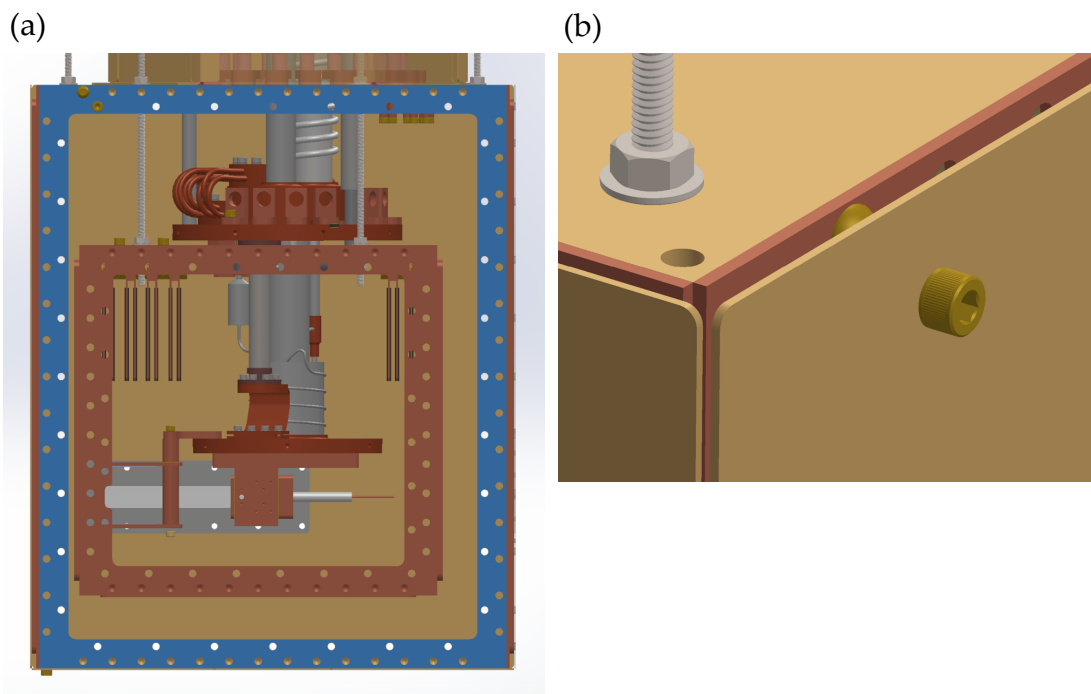


**Figure 7.4:** (a) “Donut” on the 40 K shield highlighted in blue. (b) A design that extends the 40 K panel to cover the “Donut” and brass screws.

#### 40K INTERIOR BLACKENING

One would think the emissivity of 40K interior surface does not matter, since its BBR radiation power is very low at 40 K. However, it matters when we have finite room temperature black body radiation leaking between the 40 K and 4 K surface. Assuming 40K interior surface and 4 K outside surface has similar emissivity, the space between them becomes a cavity for black body radiation photons.

Since gold plating service is usually applied on both surface of the part, it is a good idea to apply thermal blackening coating on the interior surface of 40 K shield. Due to the large temperature difference on these surfaces, black paint is not an ideal choice and often leads to paint flaking or peeling off during thermal cycles. A proven method is to apply copper blackening (oxide copper) on these surfaces, where a detailed recipe provided in<sup>95</sup>.

We simulate this effect using COMSOL and find the real answer is not straight forward. One must take into account all possible BBR leaks and compared that to the black-body radiation from 40 K onto 4 K shield. This also points out that it would be beneficial to also gold plate the exterior of 4 K shield, independent of the amount of BBR leakage into 40 K shield.

#### HEATED SF<sub>6</sub> FILL LINE

The heated SF<sub>6</sub> fill line is initially exposed to the interior of 4 K shield, which emits significant amount of thermal radiation. We are lucky that SF<sub>6</sub> has a relatively low freezing point, which is not the case for water that is used in the production of CaOH and SrOH. We would like them to be covered by a shield that is thermally anchored on the 40 K shield. There are already designs came up in our group trying to address this



issue, and I would point reader to Sean Burchesky's thesis<sup>18</sup>.

## 7.2 CONSIDERATION OF THE NEW DESIGN

### 7.2.1 CHARCOAL SORB TEMPERATURE

Since our goal is to let PT<sub>310</sub> pulse tube cryocooler running with its second stage around 3.0 K temperature, it becomes a concern that helium diffusion in the sorb will be affected at this low temperature<sup>23,76</sup>. This was not an issue with previous CaF Gen<sub>1</sub> or Gen<sub>2</sub> experiment, since both experiment has a separate 1 K pot that cools the cell below 4 K and the pulse tube cryocooler second stage is around 4 K that puts the charcoal sorbs in their comfortable working temperature. It would be important to engineer a thermal stand-off ("thermal impedance") between the pulse tube second stage and the 4 K shield that hosts the sorb plates. This can be done by carefully control the number of heat links, or inserting a piece of material with calculated thermal impedance. If the cool down time becomes of an issue due to the thermal impedance, a helium gas heat switch might be added.

### 7.2.2 TEMPERATURE VARIATION OF THE PULSE TUBE

We have seen molecular beam properties change as cell temperature changes. For example, in our previous test on molecule number in a MOT versus the cell temperature, although similar molecule number can be achieved with different cell temperatures in the range between 2 ~ 4 K, optimal ablation and slowing parameters need to be tuned for different temperature. There are also various molecule laser cooling experiments reported that the temperature fluctuation on the pulse tube second stage could affect molecular beam stability<sup>12</sup>. One option is to synchronize the experiment trigger with

the pulse tube rotary valve motor. We choose to use the liquid helium damping pot instead, since it provides more flexibility on the trigger timing of the experiment. The performance of liquid helium damping pot with a PT420 pulse tube, integrated and delivered by Cryomech, has been tested in Prof. Daniel McCarron group<sup>112</sup>. It is estimated by Cryomech that  $\sim 20\%$  of cooling power would be lost on a PT310 pulse tube at 3.0 K due to the addition of the damping pot. The heat loads coming from 4 K shields can be off loaded directly onto the second stage heat exchanger of PT310 (bypassing the damping pot), which should reduce the burden on the damping pot.



## Conclusion and Outlooks

In conclusion, we built a new apparatus of optical tweezer array of laser cooled CaF molecules. Thanks to the tighter tweezer traps in the new system, dipolar interaction between individual molecules are observed and are used to create quantum entanglement in a pair of molecules. To reaching lower temperature in the tweezer arrays, we push the limits of laser cooling for molecules to the next level, cool CaF molecules to near motional ground state in the tweezers using Raman sideband cooling.

We hope these advances in experimental techniques can improve the molecular tweezer array as a new platform for quantum information processing and quantum simulation. To make laser cooled molecules as a robust platform, a reliable 3D MOT of a lot more molecules is desired. Instabilities of the state-of-art molecular MOT is mainly coming from the molecular source and the inefficient slowing and MOT capturing. We have engineered an improved CBGB source for CaF Gen2 that can handle 24x7 unattended experiment running without major problems. As for enhanced slowing and MOT, new ideas are constantly showing up among the community. A very good example is the recent development of blue detuned MOT for molecules, which greatly enhances the density in a MOT and boosts the transfer efficiency into ODT. With the help from robust and powerful simulation programs, a lot more ideas can be quickly simulated and optimized on computer.

As for the future of molecules in tweezer array, the current 1D tweezer array can be easily upgraded to a 2D or even 3D array, where arbitrary pattern can be created using liquid crystal on silicon (LCoS) based spatial light modulators (SLM), as already demonstrated in many optical tweezer arrays of atoms<sup>9,10</sup>. This would enable the quantum simulation of interesting physics systems with dipolar interactions in a 2D geometry in such setup with ultracold molecules<sup>84,14</sup>. Furthermore, laser cooled polyatomic molecules have also been successfully loaded into 3D MOT, ODT and optical tweezer arrays. The near degenerate opposite parity states in the bending mode of a linear triatomic molecules like CaOH or symmetric top molecules like CaOCH<sub>3</sub> requires a much lower field to polarize. These features can provide more possibilities for engineering transitions that are not sensitive to external field<sup>115</sup>.

With the ability to entangle single molecules, the entanglement can be used as a resource that leads to quantum metrological gain. Spin squeezing is one example which

has been realized and benchmarked in many atomic systems, including BEC<sup>52,103</sup>, atoms in cavities<sup>75,111</sup>, hot atoms in a vapor cell<sup>7</sup> and Rydberg atoms<sup>41,15</sup>. Similar ideas can be used for the next generation of precision measurement experiments with molecules. One can imagine loading an optical tweezer array of molecules, where the molecules have two energy levels that are sensitivity to a fundamental constant. The molecules can then be spin squeezed before starting the phase accumulation, and the final readout could overcome the standard quantum limit (SQL) of quantum projection noise (QPN). The dipolar interactions are not just limited to molecules of the same specie, it is also possible to use it as a bridge connecting between different species of molecules, or even molecules and Rydberg atoms. This could potentially allow a hybrid system for quantum computing or separating the spin squeezing preparation and precision measurement interrogation into two subsystems<sup>136,126</sup>.



## High Magnetic Field Coil

The high magnetic field coil used in this work is made in house. I will explain the process of design and fabrication here. The design goal of the high magnetic field coil is to generate high magnetic field with good uniformity in the tweezer array region, while reducing the time required for stabilizing the field.

## A.1 DESIGN

In theory, if we consider a simple ring shaped conductor with current flowing through it, the magnetic field is invariant when the cross section of the conductor is split into smaller insulated sections and keeping the total current the same (the integrated current density over the cross section). The total Joules heating loss on the coil will also be invariant, since it is the integration of loss density in over the volume of the coil, where current density and volume resistivity is kept the same. This shines some insights into the choice of wire thickness for packed solid conductors. If we assume same packing density and target magnetic field strength, a thicker wire does not reduce the heat generated, it reduces the number of turns needed, thus reduce the inductance of the coil. Note that the inductance of a simple coil scales as  $N^2$ , and the current required to generate same magnetic field strength scales as  $1/N$ , the time constant  $t$  that the magnetic field can be ramped up to target current  $I$  with available compliance voltage  $U$  is  $t = I * L / U$ . One would find that if the available compliance voltage are the same, the time constant  $t$  scales as  $N$ . That means it is beneficial to reduce the number of turns  $N$  in a coil for faster response. In reality, one must consider that the cost of most power supplies scales as the maximum power, not just voltage. So when an small  $N$  coil is not available, one could use a power supply with same power rating, higher maximum voltage (thus lower maximum current), and still obtain similar rise time of the magnetic field strength. This is of course only possible if the control elements (either constant mode of the power supply or an external feedback circuit) is fast enough to remain stable at high frequency. And one must be careful if they choose to use hollow copper tubing with cooling water, since corrosion inhibitor used in cooling water might have a finite and too high voltage across the coil could cause current leaking through the cooling

water.

In the coil design for this experiment, the method of removing heat from the coil is also an important choice to make. We choose to use water cooling through hollow copper wires (or maybe I should call them tubes) for cooling. In our case, we choose a size of wire that is square in cross section with  $4\text{ mm} \times 4\text{ mm}$  outside dimension and  $2\text{ mm} \times 2\text{ mm}$  inside dimension. The wire is protected by two layers of Kapton tape that also serve as an insulator. Water is fed through the coil by a custom copper lug.

## A.2 CONSTRUCTION OF THE COIL

The bobbin must be made of a material that is strong, stiff, but not conductive or magnetic. Here we choose G-10 as the material for the bobbin. G10 is usually supplied as a laminated sheet, and we decide to use epoxy to assemble the bobbin. Each bobbin is made of a 1/4 inch thick G-10 plate that is water jet machined into the correct outline, and a G-10 tubing that is cut to length is inserted into the hole on the plate. Duralco NM25 epoxy (Cotronics) is used to hold the parts together. This epoxy is chosen because it is nonmagnetic and can withstand high temperature. One downside is, the epoxy is white color and can cause light scattering if the surface is placed very close to the experiment. Duralco also sells a high temperature epoxy in black color 4525IP, which is used for the construction of magnetic coils in Greiner group Erbium lab. It turns out the epoxy contains iron oxide ( $\text{Fe}_3\text{O}_4$ ) as a filler material (which also gives its black color), making it quite magnetic.

A side note on water jet machining G-10. G-10 is a laminated material, it is constructed from layered fiberglass cloth soaked in epoxy resin. During water jet machining, a high pressure water jet will start drilling a hole on the material (piercing). The



pressure of the jet needs to be released once it touches the surface of the material. In the case of laminated material like G-10 or carbon fiber composite, the water can be pushed into the layers of the lamination, causing delamination. Here I show a photo of the delamination on a 1/4 inch thick G-10 (Figure A.1), which jammed the water jet mixing tube during cutting. We have tried to use low pressure settings on our OMAX 2626 water jet for piercing and it still cause delamination. The best way to prevent delamination is avoid using water jet for piercing the material. For an outline that does not have a hole, we can always start the jet outside of the material and gradually moved across the edge to begin cutting, this works reliably on G-10 for us. There is also an option to install a drill head on the machining head of the water jet, so jet piercing can be replaced by drilling. Unfortunately this option is not available on our water jet. We circumvent this by first water jetting the required pattern on a sacrifice material to locate the hole positions, and use that sacrifice material as a drilling guide to manually drill small holes on the G-10 stock. The water jet tool path is then edited to make sure that the jet starts inside of the manually drilled hole, essentially solves the problem by converting the hole piercing into a “start outside of material” condition.

We wind the coil on a big lathe in the Harvard instructional machine shop (Figure A.2 and Figure A.3 (a)). This is a quite risky operation so we take a lot of safety precautions. It is strictly a two persons job, where one person’s task is solely monitoring the situation and putting his hand on the emergency stop button all the time. To tension the wire during winding, we made a custom wire feeding clamp out of Teflon, shown in Figure A.3 (b). Teflon is chosen for its self-lubricant property and softness. The depth of the notch machined is set to be smaller than the thickness of the wire, so we can use the tool clamping screw on the lathe to apply adjustable force on the wire and tune the friction. During coil winding, a G-10 rod is used together with a hammer to hammer

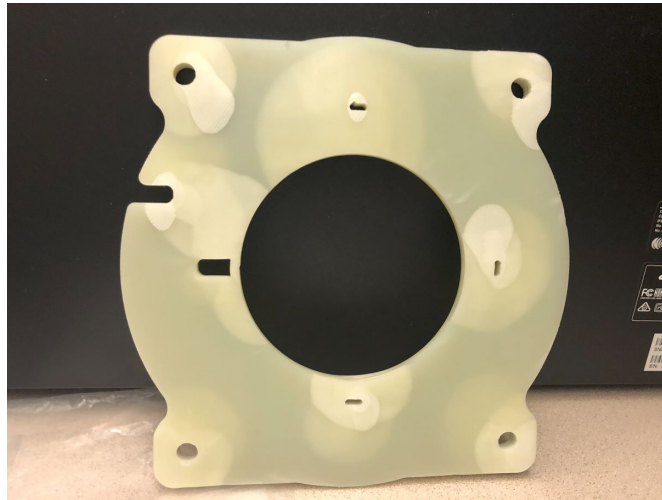


**Figure A.1:** Delamination of a 1/4 inch thick G-10 sheet that was pierced and cut using water jet machining.

down the gap between coil windings. The NM25 epoxy has a pot life around 30 min, so it is better to prepare small batched of unmixed epoxy resin and catalyst and mix a batch every half an hour. The epoxy can take up to 16 h to cure, and that means we can only make one coil per day. To increase the efficiency, we make one leads of the coil long enough to go through the hole in the shaft of the lathe, and use a 50 A power supply to run current through the coil to heat up the epoxy. The epoxy can be partially cured in about 2 hours, and the coil can be taken off the lathe, where winding of the next coil can begin.

### A.3 COIL MOUNTING

The winded coil is mounted around the glass cell using a custom structure made from Grade-5 titanium. Titanium is chosen because it is nonmagnetic and strong. The assembled coil is shown in Figure A.4



**Figure A.2:** The coil winding setup on the lathe.

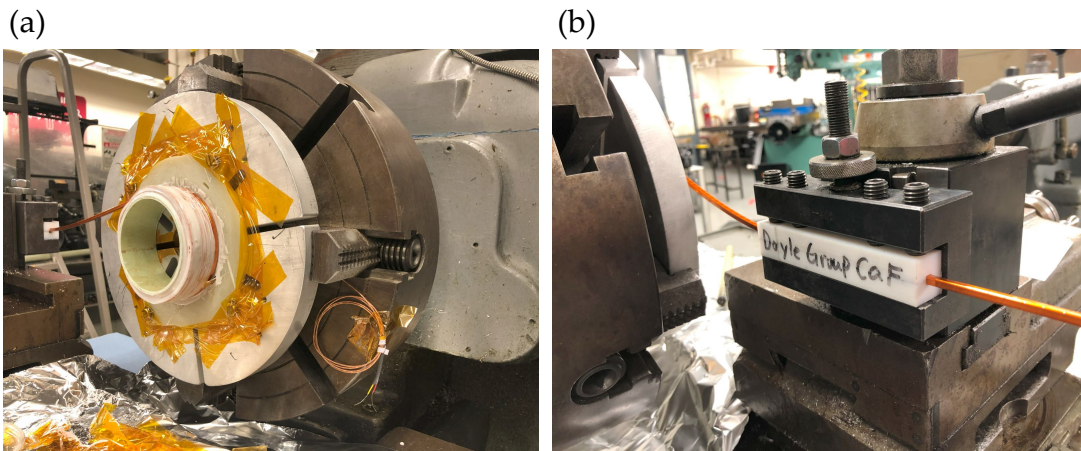


**Figure A.3:** (a) The zoomed in photo of the coil winding setup on the lathe. Teflon wire tensioner can be seen in this photo, installed on the cutting tool clamp. Low-profile thermocouples are inserted from the back of the winding adapter disk, through pre-cut slots on G-10 bobbin and clamped inside the coil windings. (b) Teflon tensioner designed to clamp on the wire with rectangular cross section. Tension can be tuned by adjusting the clamping screws on the lathe tool holder.

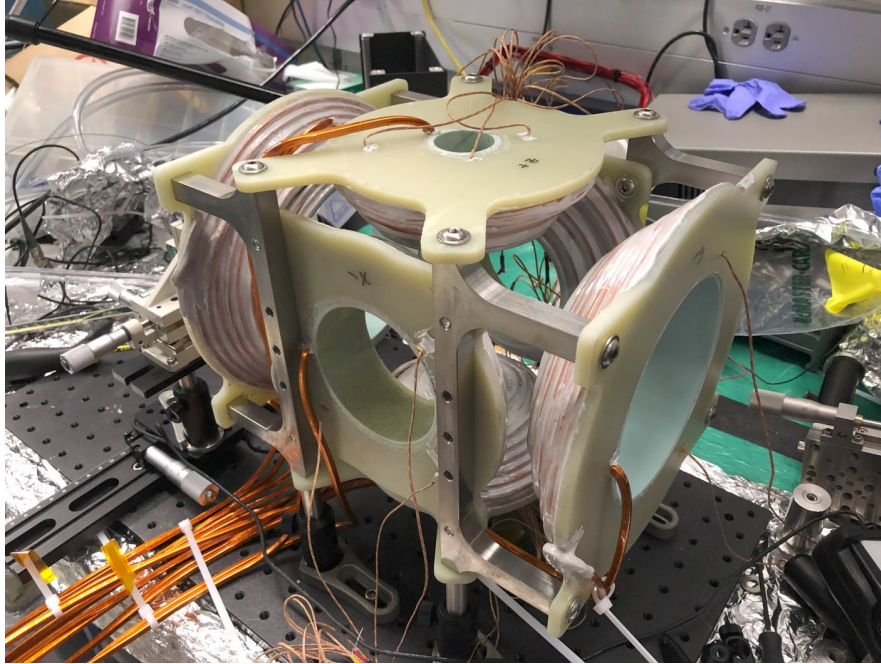


**Figure A.4:** Three pairs of high magnetic field coils mounted on titanium mounts

#### A.4 BLACKENING THE COIL

The coil will be very close to our glass cell, and we have to make sure that the paint does not flake off from the coil surface. Since the flakes or dust could fall onto the nano-textured glass cell and catch on fire when high power laser shoot through it.

In search for high performance black paint, we find MH2200 (Alion Science and Technology) is a pretty good black paint for use in UHV environment. However, it does not adhere to cured NM25 epoxy surface very well in our tests and the paint film is quite easily scratched off using nail. We find a polyurethane based black paint Aeroglaze Z307 (SOCOMORE). To apply it properly, it is required to sand the surface of cured NM25 epoxy, then spray paint the surface using Aeroglaze Z307 thinned in Aeroglaze 9958 thinner. The spray painted surface must be cured in an environment with at least

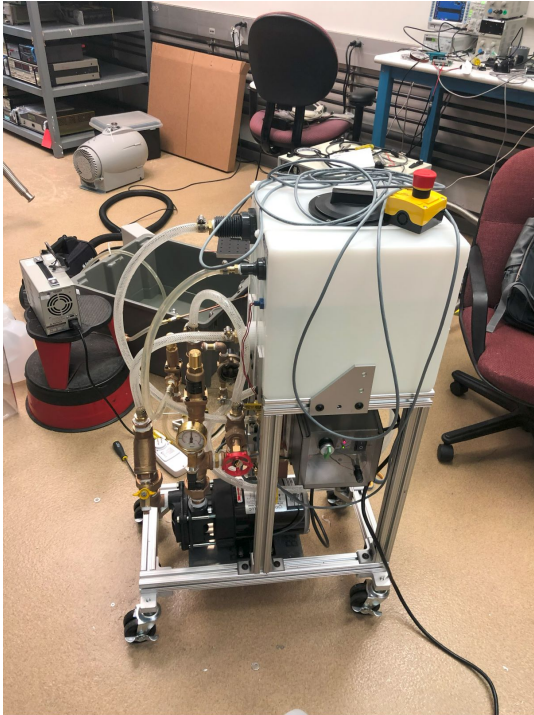
50% humidity for 24 h. We simply leave it in a plastic storage box with a cup of water next to the part. We cannot scratch the paint off the surface using nail or wooden tongue depressor with reasonable force. Note that this black paint is not good enough for strict UHV tasks and should not be used inside a UHV chamber. We use MH2200 for black paint in UHV, detailed measurement can be find in the appendix of Loïc Anderegg's thesis.

#### A.5 COIL TESTING

We build a homemade high pressure water cooling system based on a regenerative turbine pump that is capable of generating 250 PSI of pressure while providing plenty of flow rate. The cooling system has a heat exchanger that exchange the water in the coil cooling loop with temperature controlled water from an Optitemp chiller (Figure A.5 (a)). This cooling system is reserved for future use when higher current is required. To handle the high pressure and still insulate between coil inserts, a copper lug is machined, where 1/4-inch OD copper tubing and rectangular hollow copper wire is inserted on two ends and silver brazed onto the lug (Figure A.5 (b)). There are four countersink holes for mounting the lug onto a insulated panel and a 1/4-20 Helicoil tapped hole on the lug for mounting the high current leads.

We ran the high pressure water cooling manifold at 150 PSI during the test, and apply full 200 A current through the coil. We measured a temperature rise of 4 °C, 8 °C and 9 °C of the three sensors relative to the inlet cooling water temperature. Note this is an extreme test of the coil, since we don't expect the coil will run at full power continuously. In the Raman sideband cooling experiment, the coil is only turned on for about 150 ms and the experiment cycle time is around 1 s. This also shows that we can easily

(a)



(b)

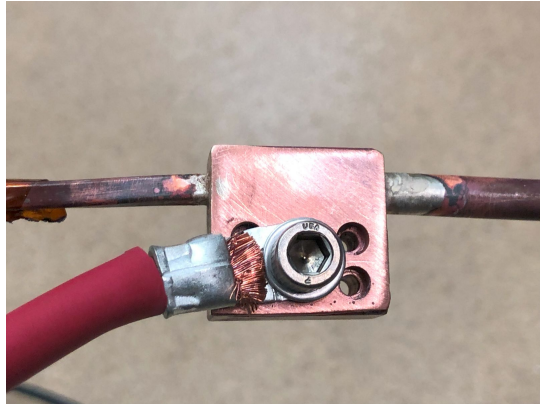


**Figure A.5:** (a) Homemade high pressure water cooling system. (b) Brazed copper lug with a high current lead attached.

run the coil at much higher current with lower duty cycle, for example, running the coil at 500 A should not be a problem, where 500 G magnetic field can be obtained.

The magnetic field uniformity is important for Raman sideband cooling if the tweezer array size expand to the full FoV of the objective in the future. We use COM-SOL to simulate the uniformity. Measurement on the home made coil matches the simulation, as shown in Figure A.6. The deviation from the center to 100  $\mu\text{m}$  away is less than 0.0042% for X coils (tweezer  $k$ -vector direction), 0.0025% for Y coils (transport direction), 0.0059% for Z coils (vertical direction).

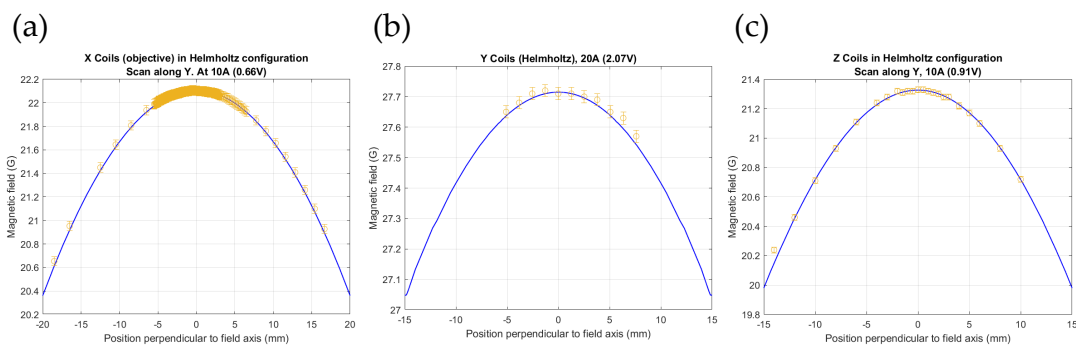


**Figure A.6:** Magnetic field measurement of coils built.



# B

## Triple Seeded SFG

When we first starting build our own SFG systems in the lab, there is no such kind of pre-built commercial solutions available\*. The implementation of homemade SFG system on the CaF Gen2 experiment turns out to be a success. We only touched the alignment once when a NP Photonics fiber amplifier died, and it works almost 24/7

---

\*There are a few companies providing a turn-key solutions these days, to name a few, Precilasers and NKT Photonics. However, in my opinion, building a SFG is a really nice optical start-up project for a young graduate student.

without any realignment. More than 5 of similar systems has been running in Doyle group for a while, without any problem. The benefit of a homemade SFG system includes: easy backup of individual components (potentially sharing backups between experiments in a research group, since doped fiber amplifiers usually has a bandwidth larger than 20 nm), changing poling tracks on the same crystal for wide wavelength tuning range. I hope these experiences in this appendix can help people build a reliable homemade single pass SFG laser system. It is a game changer.

### B.1 LITHIUM NIOBATE AND QUASI-PHASE MATCHING

Lithium Niobate is a non-linear optical material that has a high non-linear coefficient and a wide transparent window from visible to infrared. It also has a high electro-optical coefficient, making it a good material for electro optical modulator.

The refractive index of the crystal can be calculated using Sellmeier equation.

$$n_e(\lambda, T) = \sqrt{a_1 + b_1f(t) + \frac{a_2 + b_2f(T)}{\lambda^2 - (a_3 + b_3f(t))^2} + \frac{a_4 + b_4f(T)}{\lambda^2 - a_5^2} - a_6\lambda^2} \quad (\text{B.1})$$

Where the coefficients for 5% MgO doped lithium niobate are listed below<sup>44</sup>. Note the unit of  $\lambda$  is  $\mu m$  for Equation B.1.

$$a_1 = 5.756 \quad a_2 = 0.0983 \quad a_3 = 0.2020 \quad (B.2)$$

$$a_4 = 189.32 \quad a_5 = 12.52 \quad a_6 = 0.0132$$

$$b_1 = 2.860 \times 10^{-6} \quad b_2 = 4.700 \times 10^{-8} \quad (B.3)$$

$$b_3 = 6.113 \times 10^{-8} \quad b_4 = 1.516 \times 10^{-4}$$

$$f(T) = (T - 24.5)(T + 570.82) \quad (B.4)$$

Using these relations, we can plot the refractive index of lithium niobate versus wavelength at different temperature. One would notice lithium niobate has a quite high refractive index, which would cause high Fresnel reflection loss if light incident the crystal from air without an AR coating.

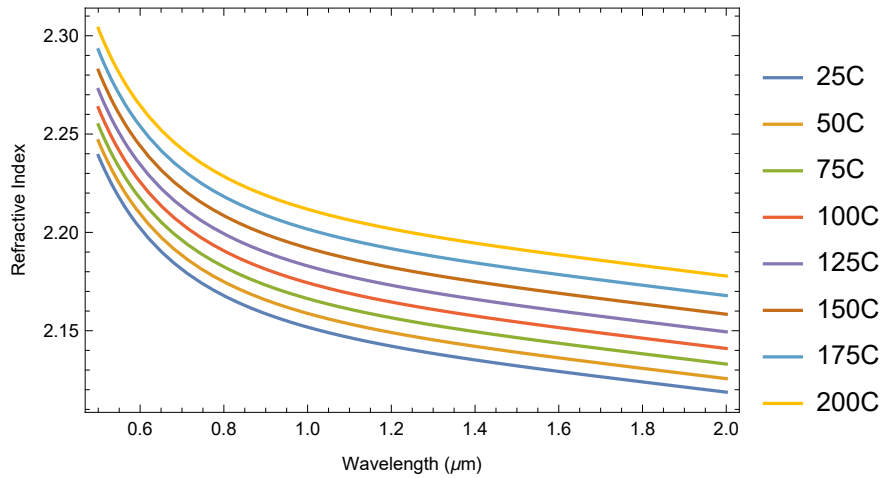


**Figure B.1:** Refractive index of lithium niobate versus wavelength at different temperature.

And the quasi-phase matching condition is met when

$$\frac{1}{n_e(\lambda_{SFG}, T)} - \frac{1}{n_e(\lambda_{p1}, T)} - \frac{1}{n_e(\lambda_{p2}, T)} = \frac{1}{\Lambda} \quad (\text{B.5})$$

where  $\Lambda$  is the poling period of the PPLN track.  $\lambda_{p1}$  and  $\lambda_{p2}$  are the wavelengths of the two pump light.  $\lambda_{SFG}$  is the wavelength of SFG output.

Using this relation, one could easily calculate the QPM temperature for their target SFG wavelength and poling period. For example, for CaF  $v = 1$  repump, we were using  $\lambda_{p1} = 1.0530 \mu\text{m}$  and  $\lambda_{p2} = 1.5594 \mu\text{m}$  and a PPLN crystal with poling period of  $11.65 \mu\text{m}$ , the solution of the equation suggests QPM temperature is around  $60.4^\circ\text{C}$ . We experimentally find the QPM temperature around  $65.3^\circ\text{C}$ , which is fairly close to the calculation.

## B.2 TIPS

Although it is entirely possible to place the  $1.5 \mu\text{m}$  and  $1.0 \mu\text{m}$  combining dichroic mirror right before the MgO:PPLN crystal, and use BB1-E04 mirrors for  $1.5 \mu\text{m}$  path and use BB1-E03 mirrors for  $1.0 \mu\text{m}$  path. We find it is much easier to align the system by combining the two wavelengths first, and then use a pair of mirrors to walk the combined beam into the crystal. However, a mirror with dielectric coating that works for both wavelengths is usually not an on-the-shelf product. The first SFG setup in the lab was built using protected silver mirrors, and the coatings were damaged after several month of use. It is apparent that a mirror with dielectric coating is required. We find a solution by using a Thorlabs short pass dichroic mirror as a mirror, which has a dielectric coating with high damage threshold. As we can see from the transmission and reflection plot of this dichroic (Figure B.2), it has a very high reflectivity for both  $1.0 \mu\text{m}$

and 1.5  $\mu\text{m}$  lasers.

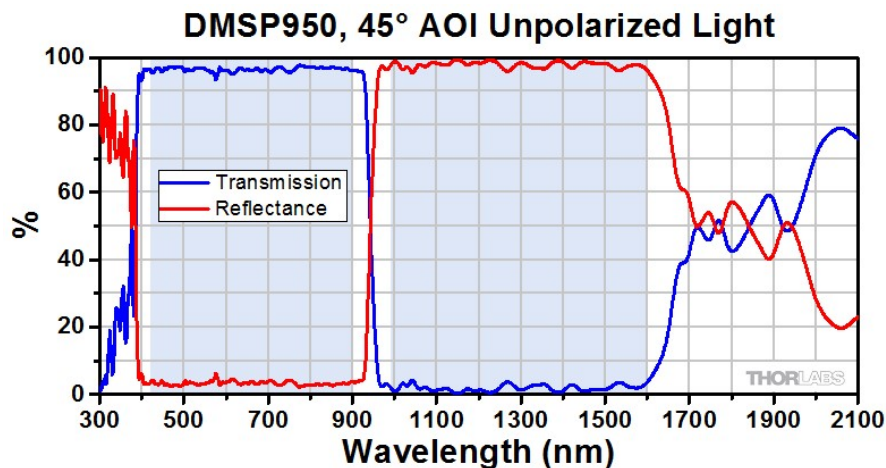


**Figure B.2:** Transmission and reflectance of Thorlabs DMSP950. Reproduced from Thorlabs Inc.

We used the PV<sub>40</sub> crystal oven from Covesion to temperature regulate our MgO:PPLN crystal (MSFG637-0.5-40). The crystal oven has a black plastic body and two plastic cover plates for thermal insulation. It turns out to be not a user friendly design, since any misalignment of the pump beam, especially on the vertical direction, could set the plastic cover plate on fire. The fume from the burnt plastic will contaminate the optical surface of the crystal, where permanent damage of the crystal or the coating can occur if high power pump beam hit the contaminated surface afterwards. In Doyle group, the first step after receiving a PPLN crystal oven from Covesion is to replace the two plastic cover plates with aluminum ones that are water jet machined in house.

The crystal oven is then mounted on a XY translation stage (460A-XY, Newport) through a custom adapter plate. One translational axis is used for switching the poling track on the crystal. The other translational axis is used for fine tuning the waist of the

pump beams inside the crystal. We find that five or six-axis stages are not necessary for aligning SFG crystals, and usually the less degrees of freedoms in a system, the more stable the alignment is.

### B.3 ALIGNMENT PROCEDURE

It is quite important to measure the beam profile out of the fiber amplifiers as the first step of building an SFG system. It is usually an easy job for 1.0  $\mu\text{m}$  lasers since silicon based CCD/CMOS beam profiler works fine in that range. To measure the beam size of 1.5  $\mu\text{m}$  laser, we use a homemade scanning knife-edge beam profiler built from razor blade and a precision translation stage.

To build the SFG board, we first perfectly overlap the 1.0  $\mu\text{m}$  beam and 1.5  $\mu\text{m}$  beam after the dichroic mirror. This can be accomplished by placing two irises spaced by tens of centimeters along the combined beam path. After that, using two mirrors to walk the beam into the MgO:PPLN crystal. Initial alignment should be always done at low pump power,  $\sim 100$  mW is a safe power level to start. Note that the pump light should be linearly polarized and perpendicular to the PPLN chip. When adjust the alignment, one could use the reflection from the edge of each track as an align aid. A good alignment should give a near circular (Gaussian) pump beam after PPLN crystal. The theoretical QPM temperature is calculated using Equation B.5 and is used as the starting point. By tuning the temperature of the crystal across the theoretical calculated QPM temperature, one could observe the  $\text{sinc}^2$  function relation between the SFG conversion efficiency and crystal temperature. The temperature setpoint is then parked where the SFG conversion efficiency is maximized. Note that this would not be the final temperature to use, since crystal self heating due to light absorption will brings

the optimal temperature to a lower value at high pump power. To properly measure the relatively weak visible laser when looking for optimal temperature with low pump power, it is very important to make sure that residual pump light, especially the 1.0  $\mu\text{m}$  pump light, is properly filtered out. We found that a single interference filter does not provide enough attenuation for this job, two interference filter with a color glass filter (e.g. FGS900 from Thorlabs) in between is always a safe choice at low power.

Once everything is optimized at low power, the pump power can be increased in steps. One should always monitor the crystal oven temperature when increasing the pump power. If the crystal temperature quickly rises, the pump power should be set back to last step to avoid damage to the crystal. After increase the pump power, re-scanning the optimal crystal temperature is needed to maximize the conversion efficiency. Note that due to local heating and thermal lensing inside the crystal, it is normal that normalized conversion efficiency will drop as pump power is increased. For our setup, we see a typical conversion efficiency around 2 %/W/cm, while this efficiency can approach 5 %/W/cm at low pump power. The focus position of the crystal also needs to be optimized by translating the crystal oven along the laser beam direction. It is possible to walk the beam a little bit to further optimize the efficiency. When doing any alignments at high pump power, it is always a good idea to place a pick off glass plate after the oven, and use an IR viewing card to monitor the pump beam profile. Once the beam profile degrades, the pump beam alignment should be moved back to its original position quickly to prevent crystal damage.

Aligning the  $v = 2$  and  $v = 3$  crystals are simply repeating these steps. Due to the chromatic shift between the two pump wavelengths, overlap between the focus of the two pump beam will degrade for the second and the third crystal, resulting in lower conversion efficiency. Fortunately, we need way less power for  $v = 2$  and  $v = 3$

repumps and it does not pose an issue.





# White-light EOM

## C.1 RLC RESONANT CIRCUIT

The goal of efficiently driving an EOM is to create electric field inside the EO crystal. The EO crystal can be simply approximated by a parallel capacitor with a small capacitance. To let power from the amplifier reaching the EO crystal without being reflected back, it is important to ensure the impedance of the EO crystal is matched to the ampli-

fier. The impedance matching goal is matching both the real and imaginary part of the source and load impedance. One would quickly realize that it is impossible to reach this goal with just reactive elements (ideal inductors and capacitors that does dissipate energy). This can also be viewed that if there is no loss in the load, no power should be transmitted into the load, and for an amplifier with only real part of the impedance ( $50\ \Omega$ ), the impedance matched load should look like open circuit (infinite resistance, zero current). In reality, there are loss due to wire resistance, loss in dielectric and magnetic materials. The resonant circuit reaches equilibrium when

Here, we use a impedance matching scheme based on a transformer, which is easy to understand and can be intuitively tuned in practice. We form a LC resonant tank circuit by adding a low loss inductor  $L$  in series with the EO crystal capacitance  $C$ . It is easy to see that the resonance frequency is  $f = \frac{1}{2\pi\sqrt{LC}}$  if all components are lossless, and the impedance drops to zero when driving frequency is on resonance. As we discussed above, there are loss in a real circuit, and we can model it as a series resistor  $R$ . One would find that the addition of  $R$  does not change the resonance frequency  $f$ . To reduce loss in this resonance circuit (minimize  $R$ ), the inductor must be carefully built. We choose to build the inductor using a toroid iron powder core made of material 2 for our white-light EOM. The required number of turns are calculated using the formula  $N_L = \frac{1}{2\pi f\sqrt{CA_L}}$ , where  $C$  is the capacitance of the EO crystal,  $f$  is the target resonant frequency, and  $A_L$  is the inductance per turn value for the toroid used.

To impedance match load impedance  $R$  to the source impedance  $50\ \Omega$ , we can use a transformer. To design such transformer, we have to know the impedance ratio. But it is usually hard to estimate  $R$ , since it can be affected by many parameters (wire thickness, inductor core loss, etc). In practice, we first build the resonance circuit and measure  $R$  using an impedance analyzer or antenna analyzer (MFJ-259D in our case). There

is one very important pitfall regarding attempts of using a scalar or vector network analyzer for this task. A small peak on measured  $S_{11}$  frequency sweep does not mean a bad tank circuit. These instruments are designed for  $50\ \Omega$  impedance. Since we have not impedance matched our resonance circuit to  $50\ \Omega$ , it is totally normal that a lot of power is reflected back into the network analyzer. A small dip on  $S_{11}$  is actually the ideal condition, since we want the loss to be as low as possible, corresponding to a small  $R$ , almost resemble a short circuit, which reflects most of the power. If you would like to use a network analyzer, you have to convert  $S_{11}$  measurement to impedance.

Once we have the measured  $R$  (in our case,  $R \sim 5\ \Omega$ ), we can wind a transformer with turns ratio of  $N_p/N_s = \sqrt{50\ \Omega/R}$ , where the primary side is connected to  $50\ \Omega$  amplifier output. The core of the transformer must be made from a magnetic material that is low loss at the frequency of operation. We choose ferrite material 61 for our white-light EOM, which maintains reasonable loss around 5 MHz. Due to leakage inductance and parasite capacitance of the windings of the transformer, resonance frequency will usually shift a little bit from previous measurement. We usually test the impedance with the transformer installed again, and a close to  $50\ \Omega$  impedance can be measured. The impedance matching can be further improved by optimizing the turn ratios of the transformer guided by the measured impedance.

## C.2 DESIGN

Previous designs of the white-light EOM suffers from unstable center frequencies and low  $Q$ . To solve this issue, a new design is constructed and tested.

Since any dielectric material between two electrodes could cause loss and decrease the  $Q$  of the resonant circuit, the stray capacitance between the electrodes should be

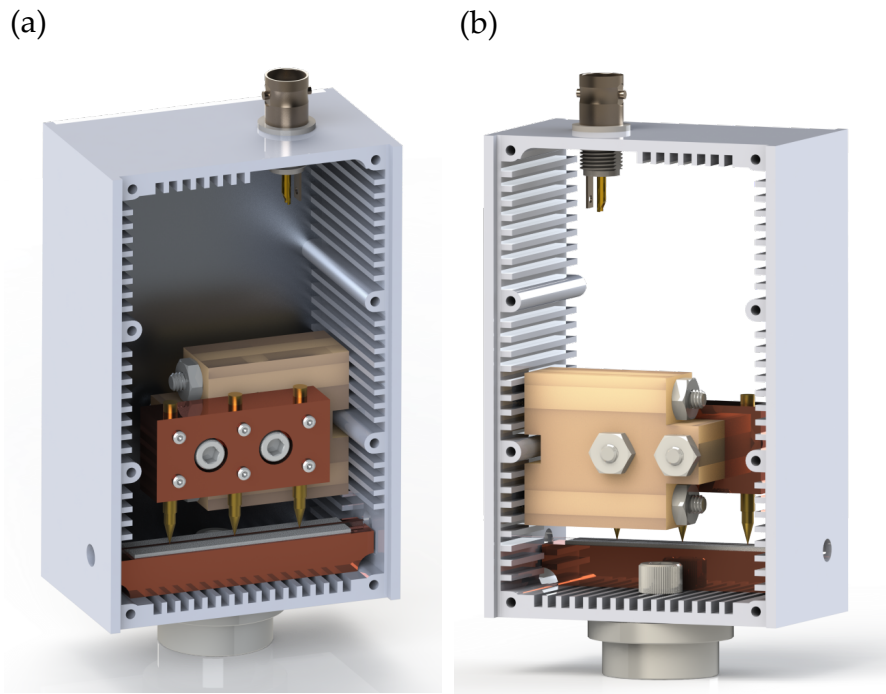


**Figure C.1:** White-light EOM 3D rendering, front view (a) and rear view (b).

reduced. These stray capacitance also cause much higher current in the tank circuit at the same voltage across the electrodes. Since the resistive loss is  $I^2R$ , where I is the current and R is the real part of the resistance in the tank circuit. A large stray capacitance will typically causes a higher loss. These stray capacitance should also be stable, since variation of the capacitance also changes the resonant frequency, causing drifts of EOM performance when the resonance is narrow (Q is high). In the old design, thin Kapton films are used between the metal block that is electrically connected to the top electrodes and the case. Since the case the the button electrodes, there is a large area of the Kapton film that serves as a parallel capacitor. To make sure the two electrodes are not shorted together, the metal block is also attached to the case through a Nylon screw. In this old design, neither Kapton nor the Nylon screw is a rigid material, and slow creep happens over time, especially under thermal stress when excessive driving power is added to compensate the low Q of the EOM. In the new EOM design, the top electrode is rigidly mounted on a piece of Ultem plastic. All the fasteners are made of stainless steel for strength and long-term stability. The 3D rendering of the new EOM design is shown in Figure C.1. The constructed EOM is shown in Figure C.3.

### C.3 PERFORMANCE

The performance of the EOM is tested by measuring the beat note of the broadened laser with the frequency shifted (with an AOM) original single frequency laser. The result is shown in Figure C.3.

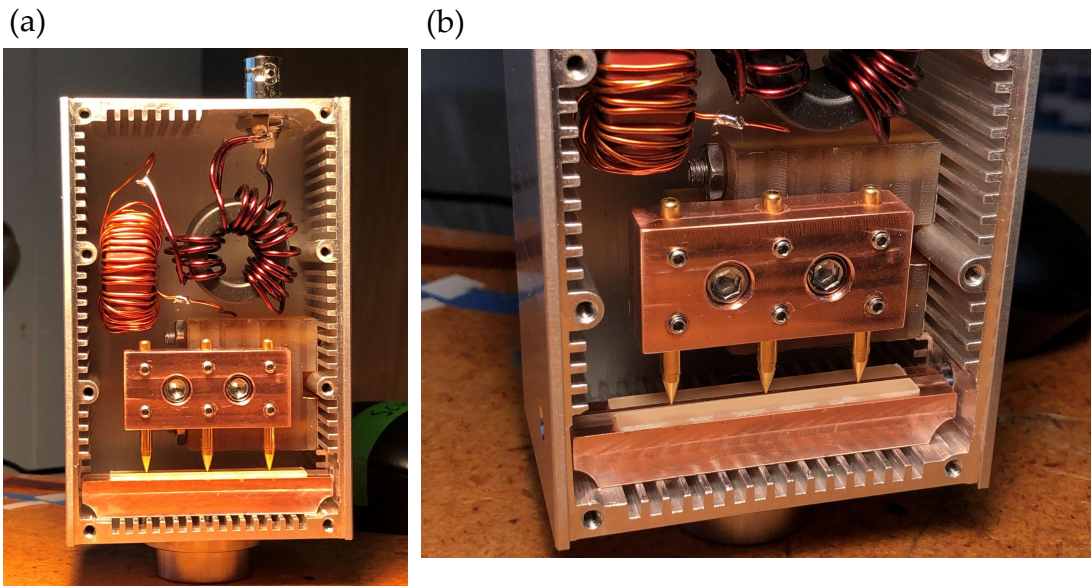


Figure C.2: White-light EOM as constructed, front view (a) and details of the crystal mount (b).

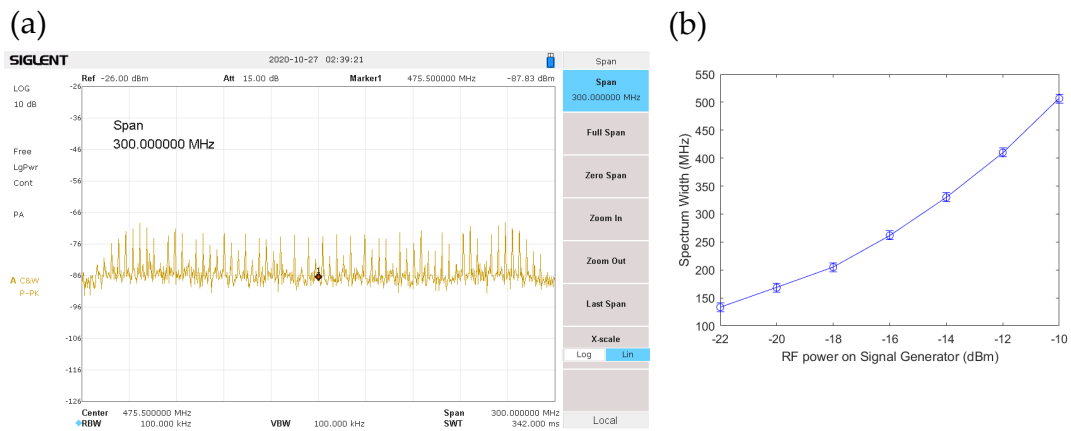


Figure C.3: White-light EOM performance. (a) Beat note measurement of the broadened laser. (b) Spectrum bandwidth versus driving power into the ZHL-5W-1+ amplifier, gain is about 44 dB.

# D

## Cryogenic Beam Box Details

### D.1 1K PULSE TUBE CRYOCOOLER

The 1K pulse tube cryocooler requires a separate gas handling system to work. Details of the adventure with an early version of the 1K system can be found in Louis Baum's thesis. Here I will focus on the operation of a similar system on the CaF Gen2 apparatus. The diagram of the gas handling system is shown in Figure D.1.

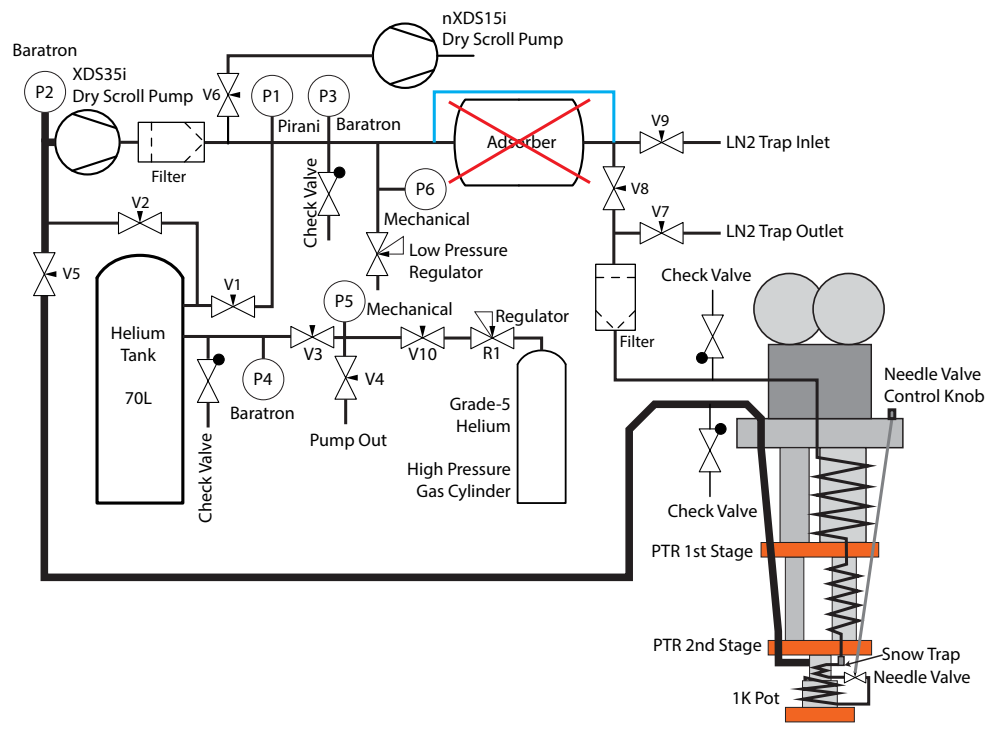


**Figure D.1:** Diagram of the gas handling system for the 1K circulation system.



The closed cycling nature of the 1 K system means any contamination in the helium gas in the gas handling system will condense at the coldest section of the loop (which is less than 4 K) and causes a clog. The only safe way to recover from this situation is warming up the whole system to room temperature and pumping out all the volatile contamination. We find that the original gas handling system provided by Cryomech does not support long term continuous running (>1 weeks). One trick is removing the “adsorber” from the system. The adsorber is installed by the vendor to adsorb moisture or other contamination in the system. However, this adsorber material has too much outgassing and actually contaminate the system in reverse. After removing the “adsorber”, we can consistently run the experiment continuously for more than 2 weeks without a cold trap. After more than 2 weeks of running, we do inevitably collect enough contamination that could causing the impedance of the system to change, that’s why we recommend a full warm up every 2 weeks. This warm-up usually happens over weekend with the help of heaters, and also regenerates the charcoal sorbs as well as melts the SF<sub>6</sub> ice in the cell, causing almost no down time of the experiment.

The pressure relief valves (“blowoffs”) on the 1K pulse tube cryocooler comes with an exposed valve piston. It cannot re-seat and form a reliable seal after it is activated or bumped. This causes air leaking into the system and immediately forming a clog. A partial solution is replacing all the “blow-offs” with a low pressure Swagelok check valve, which has the valve piston protected by the enclosure (SS-4C-5 with SS-4-TA-1-4ST adapter). By properly operate the gas handling system, no over pressure event should ever occur that can trigger the blow-offs. However, one should still leak check all the blow-offs if they suspect a potential over pressure event has happened.

The general protocol of operating the 1 K circulation system on the CaF Gen2 experiment is summarized below.

Cooling down the beam box and start circulation

1. Temporarily open the UHV shutter, pump down the beam box. Remember to use gas ballast on the multistage roots pump to handle the water vapor if the beam box is opened to air previously.
2. Turn on the pulse tube compressor and wait till the second stage reaches base temperature and the first stage temperature reaches below 50 K.
3. Isolate the 1 K system from the dry scroll vacuum pump. The 1 K circulation pump is always kept running.
4. Open V<sub>10</sub> and V<sub>3</sub> to charge the helium tank to 400 Torr through the regulator R<sub>1</sub> on the high pressure helium cylinder.
5. Open valve V<sub>2</sub> to slowly flow the helium from the helium tank to the system. The pressure reading at gauge P<sub>2</sub> should be kept below 50 Torr and gauge P<sub>3</sub> should be kept below 700 Torr
6. Temperature of the 1 K pot should drop to  $\sim 2$  K. After the helium tank is almost pumped out (indicated by P<sub>4</sub>).
7. V<sub>2</sub> and V<sub>5</sub> are kept fully open during normal operation. Rapid boiled off helium can be safely contained in the helium tank when there is an emergency warm-up.

Stop the circulation and warm up the beam box

1. Close the pneumatic gate valve between the UHV chamber and the beam box. turn off ion sweeper high voltage.
2. Turn on the nXDS 15i dry scroll vacuum pump.

3. Close valve V8 and V2, open valve V1 to compress the helium gas into the tank.
4. Close valve V1, open valve V6 and V8, to pump the residual helium out of the system. Note that all the helium collected in the helium tank is considered clean helium. Opening V8 allows pumping contamination from the inlet of the 1K pulse tube cryocooler.
5. Turn off the pulse tube compressor.
6. Pump out the helium buffer gas adsorbed in the charcoal sorb from the beam box. Keeps  $\sim 0.5$  Torr helium in the beam box during warm-up to avoid cold spots.
7. Turn on heaters for faster warm-up (optional).

## D.2 GOLD PLATED 40K SHIELDS

One feature of the CaF Gen2 beam box is using gold plated copper to replace the aluminium 40 K radiation shield instead of super-insulation (Aluminized Mylar). This improvement maintain the cleanliness of the beam box during scheduled maintenance, and ensure repeatable performance over the long service life of the beam box. The copper surface is first sanded to 1000 grit, then polished using metal polishing paste and thoroughly cleaned. The surface is then gold plated by an external company, and the surface is slightly polished again with the metal polishing paste. Finally, the shields are thoroughly cleaned again to high vacuum standard.

### D.3 PULSE TUBE LEAKS

We learned in a hard way that water condensed from air (basically distilled water) is pure enough, that once touch a metal surface, ions will preferentially dissolve into that, making it very corrosive to metals, even stainless steel. After finding out two pulse tube lines starts leaking, and the similar leak spot is located using a helium leak checker with sniffer probe, we found that the outside of a chilled water line is touching the helium lines, and condensed water might flow onto the helium lines causing corrosion. The leaky lines are removed from the system, vented and inspected using an endoscope to locate the leak spot inside the bellow. We than cut open one flexible line and find water corrosion stains on both the stainless steel braids and the bellow. This is an unfortunate case that the mechanical room where we install all our chillers and pulse tube compressors are not temperature or humidity controlled, and has complicate building pipes and HVAC systems installed on the ceiling. To quickly recover from the helium leak, we setup a helium trickle charge manifold, that maintains the amount of helium in the pulse tube system, by using a check valve and a pressure regulator with its setpoint slightly higher then the normal running pressure of the low pressure line. Our long-term solution is running the stainless steel helium lines through plastic tubing from the compressor the to lab. Since then, we have not seen helium leaks. It is always a good idea to log the pressure of the HP and LP pressure lines of the pulse tube compressor, as it provides precious debugging information when a leak occurs.

### D.4 HEATER AIDED WARM UP

Our first generation beam box relies on convective heating from the residual helium gas in the beam box to warm up, which usually takes tens of hours. It is fine if the

warm-up process happens over weekend, but becomes undesired for quick test of beam box ideas or emergency warm-up in a week day. In the CaF Gen2 beam box design, 10 cartridge heaters (HTR-50, LakeShore) rated at 50W power each, are installed at different sections of the beam box. Due to different thermal mass of the cold sections, we need to separately control the heating power delivered to each heater, in order to warm up the whole beam box to room temperature around the same time. The heaters in CaF Gen2 beam box is powered by a 600 W 48 V switching power supply through 10 individual DC solid state relays. The relays is then driven by 10 pulse width modulated (PWM) signals generated by a LabVIEW program to control the duty cycle of heaters.

One concern of the heater aided warm up is overheating the pulse tube cold stages. During the assembly of many cryogenic systems, low temperature solder are used. Overheating cold stages above room temperature is risky, and according to Cryomech, heating pulse tubes above 350 K will void the warranty. We protect the beam box through both software interlock and hardware interlock. The same LabVIEW program that generates the heater PWM signals will monitor all the cold stage temperatures and turn off all PWM signals if any temperature reading is out of range. The LakeShore 218S temperature monitor has an internal alarm function, which will latch relay outputs once the alarm condition is met. These normally closed relay outputs are then connected in series to control the 120 V power input to the heater power supply through a solid state relay.

# E

## Control System

One upgrade that we would like to have on Gen2 is the ability to realize large multi-dimensional parameter scans. This requires the sequence control software reporting the parameter set it is currently using to the data collection software. Other than that, the sequence control software should also let the data collection software know when a new data set is started and the old data set needs to be saved to disks. In our case, the sequence control software is Cicero Word Generator (Cicero), the data collection

software could be the custom LabVIEW program that record a voltage trace from a PMT preamplifier, or the custom PyQt based camera control program that acquires images.

#### E.1 SAVE SCANNING VARIABLES WITH CICERO

Cicero, in its original form, unfortunately can only communicate with GPIB devices and RS232 devices. It seems the only way would be modifying Cicero code to support sockets. However, here we choose to utilize the RS232 communication capability of Cicero to circumvent this issue. We rely on an open-source null modem emulator (comocom), which generates a pair of virtual COM ports. The two virtual ports in a COM is connected in a loop back style, where the input of A is connected to output of B, and input of B is connected to output of A. We let Cicero talking to one COM port, we can then write any script that connects to the other COM port and communicate with Cicero. The lists in Cicero are preset to be variables from “Variable\_0” to “Variable\_10”. These numbers are used to generate RS232 messages like

```
Variable_0=0.0\n
Variable_1=1.0\n
Variable_2=3.1415926\n
Variable_3=2.71818\n
...
Variable_10=42\n
```

These messages are then forwarded to various TCP/IP sockets through a program called “hub4com” in the package of comocom. “hub4com” acts as a TCP/IP server that our data collection software can connect to it. These messages are then parsed to control the

behavior of the data collection. We called the first variable “trigger variables”, where the data collection software should start saving the last data set to disk and starting a new acquisition once receives this variable. All the variable names and values should be stored in the data file together with the acquired images and voltage traces. These information would allow the data analysis program to sort the data into correct orders disregards the original order of parameter scanning. One advantage here is, we can also randomize the order of parameter scans, which proves to be beneficial when averaging out CBGB fluctuations and avoiding bias.

We usually choose to order instruments that have build-in Ethernet communication ports. However, sometimes the commands to control these instruments are too complicate for Cicero to generate, or the Ethernet port is simply not available on those instruments. To solve this problem, we write light-weight Python scripts to translate from Cicero scanning variables messages to commands for each instrument. Several examples including Siglent SDG2000X series arbitrary waveform generators, Siglent SPD1000X series linear power supply, Thorlabs Elliptec ELL14 motorized rotation mounts, Stanford Research Systems (SRS) SG392 vector signal generators.

## E.2 IMAGING SOFTWARE

The imaging software is completely rewritten in Python using PyQt as GUI framework. We own several Andor cameras around the lab, so this software only supports Andor SDK 2.



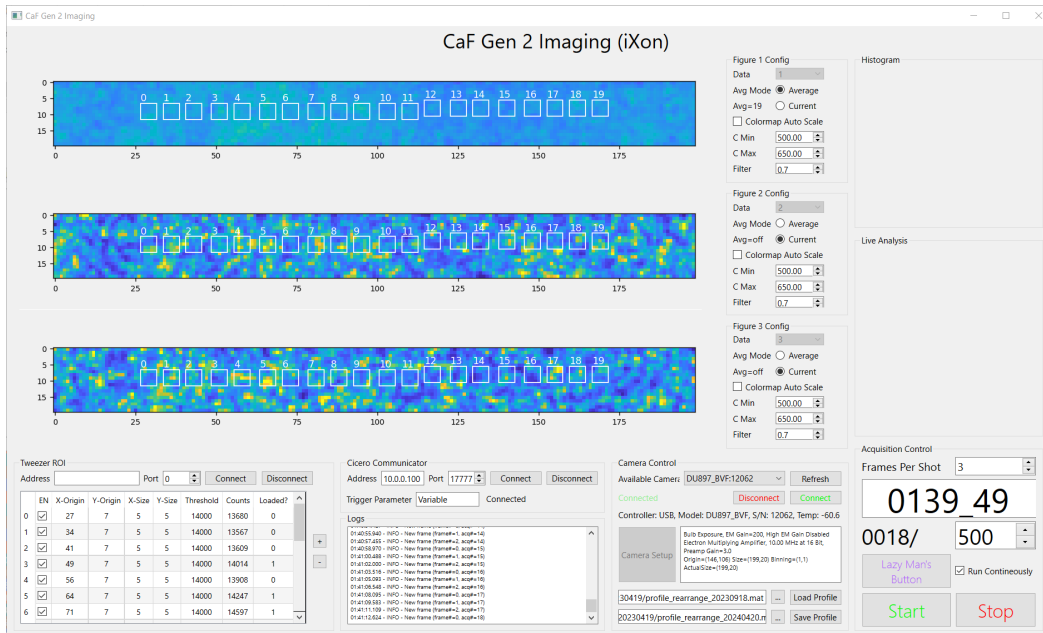


Figure E.1: Imaging software based on PyQt.

### E.3 SPECTRUM INSTRUMENTATION AWG CARD SEQUENCE GENERATOR

The Spectrum Instrumentation AWG cards are widely used on our experiment to synthesize various waveforms and pulse sequences. Generating milliseconds long waveforms at high sampling rate requires significant computation power. However, most of the time, only a small section of the waveform needs to be updated for a parameter scan and many sections of the waveforms are periodic signals. The AWG card we choose has a built-in sequence controller that can solve this problem. We wrote a GUI software based on PyQt to interface this capability. Our software allows dynamically loading a Python function which generates required waveform data using several parameters as input. This allows us to generate any kind of waveforms by writing simple Python scripts, without modifying the code for the main AWG control software. The same software can be adapted for many different applications in the experiment. For

example, both our microwave I/Q baseband generator and Raman beam pulse sequence generator are based on the same piece of code with little modification (Figure E.2).

The top left of the software panel shows the sequence that is ready to be uploaded to the AWG card. The middle left panel shows the trigger variable name that the controller will respond to when receiving a message through Ethernet. The bottom left panel displays the actions that the controller will perform when a variable name is received. A common usage is to modify a parameter of a sequence step, regenerate the waveform and update to the AWG card. The top right panels allow editing the detailed parameters and configurations of the selected sequence step. The bottom right panels allow editing of the frequency and amplitudes for multi-tone sweeps.

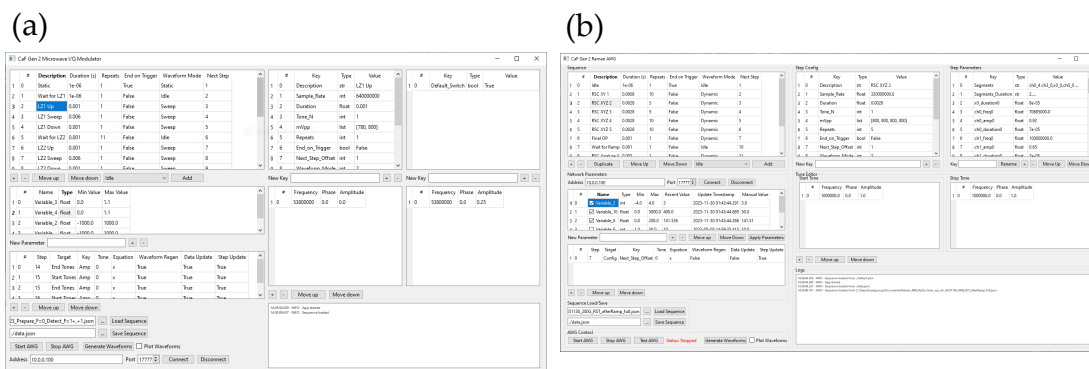


**Figure E.2:** (a) Microwave I/Q modulator software based on the Spectrum Instrumentation AWG card sequence generator code. (b) Raman beam pulse sequence generator based on the Spectrum Instrumentation AWG card sequence generator code.

#### E.4 TWEEZER AOD WAVEFORM GENERATOR

The multi-tone RF signal for tweezer AOD is generated by a 16-bit dual channel PCI-E AWG card (M4i-6631-x8, Spectrum Instrumentation GmbH). At the current stage of the

experiment, we would like to avoid generating and streaming the buffer to the AWG card, as it requires careful optimization of the code for maximum performance, and might leads to buffer underrun if other programs on the same computer interrupt the thread. Thus, the software is based on a similar AWG sequence generator platform discussed in the previous section (Figure E.3).

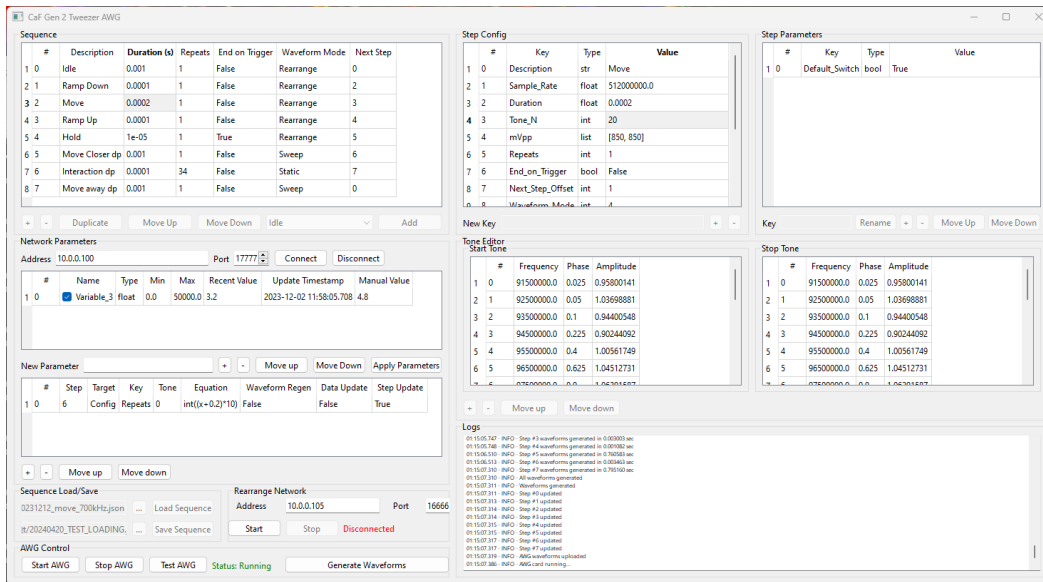


Figure E.3: 1-D Tweezer AWG controller

Due to the limitation of the AWG card, each segment in a sequence must have a length of multiples of 32. It is quite easy to see that it is quite hard to generate a frequency sweep which has the same start and stop phase, and almost impossible if the sweep is multi-tone. This issue is circumvented by calculate the phase shift between the stop and start, and then divided that phase shift by the number of samples in the segment, finally distribute that small phase shift onto each sample in the segment. The waveform used during rearranging are generated by summing in pre-computed single tweezer moving waveforms. This must be done in real time. For flexibility, we choose

to run it on CPU using numba package for efficient vectorized and JIT compiled code.

## E.5 LABVIEW CONTROL

The LabVIEW program is responsible for two tasks for the experiment. The first is monitoring the vacuum, gas flows, temperature of the apparatus. The second is capturing analog traces of photomultiplier tubes and photodiodes during the experimental runs, triggered by Cicero TTL signals.

National Instruments decided to completely cease support of LabVIEW NXG in July 2022, without providing any tool to convert current LabVIEW NXG codes back to standard LabVIEW codes. This unfortunate decision makes all the LabVIEW NXG code we wrote for CaF Gen2 useless for future experiments.

# F

## RF MOT Coil and Amplifier

### F.1 RESONANT TANK CIRCUIT AND IMPEDANCE MATCHING

The circuit diagram for one side of the coil is shown in Figure F.1.

L<sub>1</sub> and L<sub>2</sub> are two double-side coil plates. Each L<sub>x</sub> consists of the two coils on both sides of the plate connected in series. L<sub>1</sub> and L<sub>2</sub> are connected in series, with the two high voltage differential ends and the center tap routed to the high voltage electrical

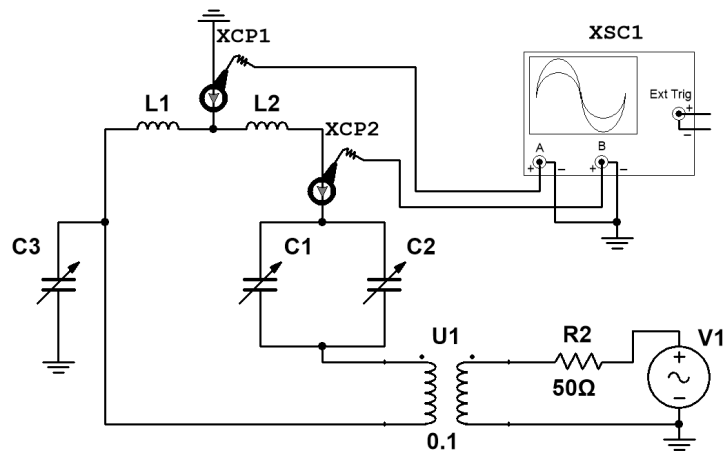


**Figure F.1:** Circuit diagram of the RF MOT coil tank circuit.

vacuum feedthroughs. The center tap is connected to the ground.

The two high voltage differential ends from L<sub>1</sub> and L<sub>2</sub> are connected to the tank circuit box through a homemade cable built from Litz wire (1162 strands 46AWG) to reduce the ohmic loss due to shallow skin depth at high frequency. Litz wire is insulated by a Teflon tubing, and then shielded by a copper braid, and further protected by heat shrink tubing. The tank circuit end is connectorized with a SHV-5 connector, where the Litz wire is soldered to the center pin and the copper braid is crimped to the case. Note that the other end of the copper braid is left floated (not connected to the MOT chamber), to avoid forming a shorted loop in the transformer formed by the area enclosed by the two cables. XCP<sub>2</sub> is a homemade current transformer that is used to monitor the current running through the MOT coils.

Two high voltage vacuum variable capacitors C<sub>1</sub> and C<sub>2</sub> forms a series resonant tank circuit with L<sub>1</sub> and L<sub>2</sub>. This tank circuit has a very low impedance near the LC resonance frequency. The transformer U<sub>1</sub> is used to impedance match the tank circuit to

the amplifier. It is made by winding magnet wire insulated by Teflon tubing on a stack of low loss toroid ferrite cores.

Ideally the circuit should be made as symmetric as possible to ensure balanced voltage on the coil (true differential driving). However, this condition cannot be obtained due to inevitable parasite capacitance and inductance. Since  $L_1$  and  $L_2$  are identical coils, imbalance voltage on the two ends of the coil will cause a non-zero current between the center tap and the ground, this current can be measured by the current transformer XCP1. If we can null the current reading on XCP1, then we know the current through  $L_1$  and  $L_2$  is equal, and the coils are driven in a balanced condition. The tuning is achieved by adding a balancing variable capacitor between either end of the coil ( $L_1$ , in this example diagram) and the ground. By tuning the capacitor, we can zero the current reading on XCP1. If addition of the capacitor makes the XCP1 current reading larger, the capacitor is connected at the wrong side. The balanced voltage on  $L_1$  and  $L_2$  are required to reduce electric field between the top and bottom coils, which could mix the opposite parity states of the  $\Lambda$ -doublet in CaF  $A$  state and cause a short RF MOT lifetime<sup>4</sup>.

The tank circuit box is shown in Figure F.2 (a).

## F.2 ISSUES WITH MOT COIL

After the baking the MOT chamber, we found that one coil is open-circuited after cooling down. It appeared that the electric connection was broken during the thermal cycling. Later, we determined that this is due to tolerance issues of the copper spacers between the two coil plates and loose screws due to thermal cycling. We fixed this problem by hand sanding the spacers to a tighter tolerance and using Belleville wash-

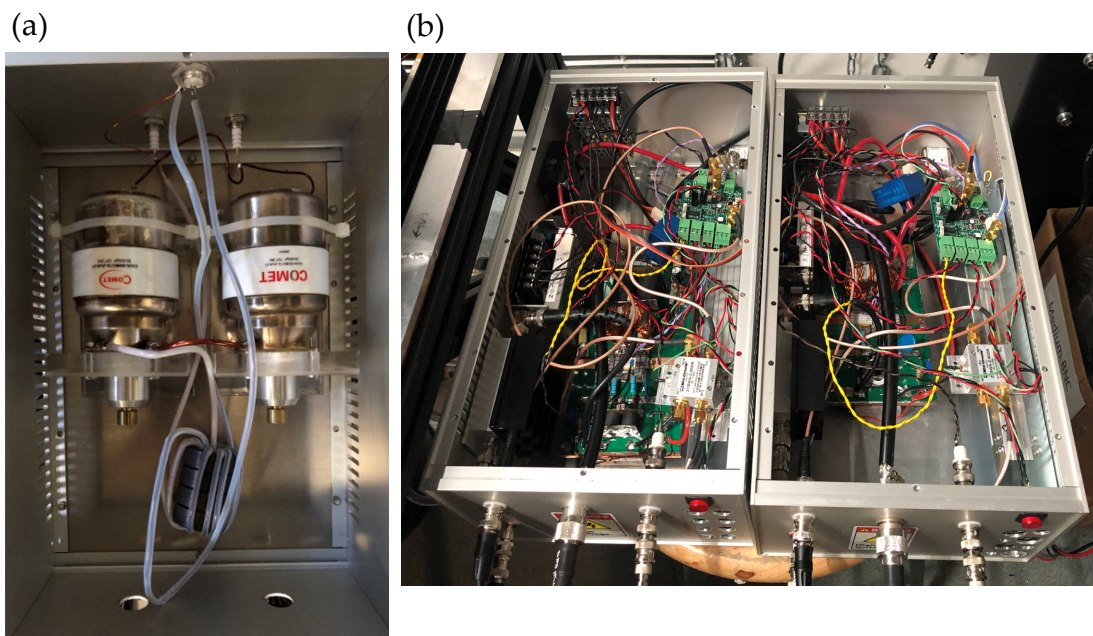


**Figure F.2:** (a) Tank circuit box used for each coil. Note the balancing variable capacitor is not shown in this photo. (b) 1kW RF amplifiers used for driving the RF MOT coils.



ers to apply clamping force.

We also observed arcing on the high voltage feedthroughs for the RF MOT coils. We confirmed that the arcing was happening outside of the vacuum by spraying neon gas around the feedthrough, where a change of arc color from purple to orange was observed, as shown in Figure F.3. The feedthroughs are rated for 3 kV, which should be enough. However, the voltage rating is only for DC, and it seems the safe voltage for the feedthroughs has to be downgraded for RF voltages. The solution to this issue is upgrading to a 5 kV rated feedthrough, and modifying the coil driving scheme to a fully balanced one. This modification of the circuit halves the voltage on each feedthrough while maintaining the same current through the coil.



**Figure F.3:** Arcing on the RF MOT coil electrical feedthrough.

### F.3 1kW RF AMPLIFIER

We build a homemade 1kW RF amplifier based on modification of a board from Ham radio amplifier using BLF188XR laterally-diffused metal-oxide semiconductor transistor (LDMOS). The LDMOS is mounted on a piece of copper heat spreader and cooled

by a water cooling block. The two transistors in the package of BLF188XR is connected to form a push-pull amplifier. The differential output of the amplifier is then converted to single-ended using a center tapped transformer, which also impedance matched the output to  $50 \Omega$ .

To protect the amplifier from overheating and back reflection, we implement full protection in the amplifier. Any triggered protection is latched and will quickly turn off the drain bias using a solid state relay and the RF input using a fast RF switch. The LDMOS overheat protection is achieved by monitor the temperature at the top surface of the LDMOS case. The back reflection monitor is a straight forward one. We simply use a high speed comparator to monitor the voltage of both drains of the LDMOS, and trigger protection if voltage peaks above 120 V. Since the maximum drain source voltage of BLF188XR is 135 V, this should prevent drain-source breakdown of the LDMOS.

There is one extra overheating protection for the in-vacuum RF MOT coil. We don't want to install a temperature sensor in the UHV section just for this purpose. Instead, we monitor the high frequency current flowing into the RF MOT coil through a current transformer. The current signal is squared using a high speed analog multiplier, essentially calculate the instantaneous heating power on the coil. This signal is finally converted to current and integrate on a capacitor with a discharge resistor in parallel, where the voltage on the capacitor is compared with a setpoint to trigger the protection. The idea here is the equation of charging a parallel RC circuit with current source is identical to heating an object that is conduction cooled by a thermal bath, we can use a simple circuit to estimate the temperature of the coil. This almost shares the same spirit of quantum simulation.

The amplifier is shown in Figure F.2 (b), where the main body of the amplifier is mounted on the bottom plate. A 48 V 1500 W switching DC power supply is mounted

on the right side, providing the drain bias for the LDMOS amplifier. The protection circuit and the RF switch used to quickly shut off RF input is mounted over the drain bias power supply. A 1 W RF preamp (and its 24 V power supply) and a DC solid state relay for quickly shutdown of the drain bias are mounted on the left side. The power supply for biasing the gate of the LDMOS amplifier is mounted on the back panel. A Hall current sensor (Blue block around thick gauge red wire) is used to monitor the drain current drawn by the amplifier and trigger protection when necessary.



# Magnetic Field Compensation

## G.1 MAGNETIC FIELD COMPENSATION COILS

### G.1.1 ROOM COILS

The room coils are build for compensating the magnetic field noise that is coming from far away in the building. This coil is created using a multi-core cable that runs along the edges of the room. To allow personnel moving across one edge of the room, the wire

is replaced by four thin copper foil, taped onto the floor, and protected by heavy-duty floor tape.

### G.1.2 TABLE COILS

The table coils are wound with 14AWG magnet wires on a frame made from aluminum U-shape tray (McMaster-Carr). These coils are driven by linear bench power supplies (Tenma) in constant current mode. To scan the current during optimization of sub-Doppler cooling, we temporarily connect the specific coil that we would like to scan to a programmable linear bench power supply and scan the current through Ethernet.

### G.1.3 GLASS CELL COILS

Due to the inhomogeneities of the magnetic field generated by the table coils, we cannot guarantee the magnetic field they generate is the same at MOT chamber center and glass center. These glass cell coils are used to properly offset the magnetic field in the glass cell. They are all driven by linear bench power supplies (Tenma).

## G.2 MAGNETIC FIELD COMPENSATION CONTROLLER

The magnetic field are measured by a flux-gate magnetic field sensor (Mag-13MS100, Bartington Instruments) and converted to an analog voltage signal. The magnetic compensation controller is realized in LabVIEW for flexibility. We use the 60 Hz zero-crossing signal to trigger the acquisition of a 18-bit analog input card (PXI-6289, National Instruments). The mean value of the digitized magnetic field signal per 60 Hz cycle is then used as the input for a digital PID controller. The PID controller output is scaled and converted to analog control signal by a 16-bit analog output card (PXI-6733,

National Instruments). This analog signal is finally fed into our homemade bipolar voltage controlled current source to drive the room coil and close the loop. By using a LabVIEW program as a controller, we can easily log the performance of the magnetic field compensation as well as the magnetic field fluctuation from the outside of the lab. We can also use fast Fourier transform (FFT) algorithm to inspect the magnetic field noise in the frequency domain.

This current source is based on four OPA549 high power operational amplifiers (op-amps). The outputs of the op-amps are connected in parallel through  $0.1\Omega$  load balancing resistors, where each op-amp are limited to a maximum 5 A output current by design. The output current is sampled by a low drift current sensing resistor and then amplified by a fixed gain instrumentation amplifier (AD8228, Analog Devices). The current sensing signal is then subtracted by an external analog set point signal to create an error signal. An analog PI controller is then used to close the feedback loop, where proportional and integral parameters can be tuned separately for balancing between speed and noise. All high power op-amps and high power resistors are mounted to a copper heat spreader with AlN ceramic insulating pads. The copper heat spreader is then attached to a aluminum heatsink or a water cooling block. To increase the efficiency of the current source and reduce heat load in the lab, while still maintain low noise performance, the power rail of the high power op-amps are driven by two 15 V 20 A low noise switching power supplies (PFS300A-15, Daitron).

The biasing and high magnetic field coils used in our experiment can saturate the flux-gate magnetic sensor during the experimental sequence. We have to hold the state of PID controller during sequence running. This makes the compensation a shot-to-shot one, rather than a real time one or 60 Hz cycle-to-cycle one. However, this could be sufficient for a relative slow magnetic field drift.

We hope that we can realize a 60 Hz cycle-to-cycle control of the magnetic field. It seems possible if a second magnetic field sensor can be placed in the center of the room, far away from the experiment, but still enclosed by the room magnetic coil. We tried this idea, magnetic field from the bias coil can be still seen on the flux gate, which will disturb the operation of PID.

We find that the magnetic field noise is greatly reduced between 2:00 am and 5:00 am. This is attribute to the MBTA red line train that goes around the campus, where the closest distance from the rail track to our lab is just under 240 m. We do see severe magnetic field drift before implementing this magnetic field compensation system.\* We are no longer bothered by this issue after having the compensation system running during the day.

---

\*Running the experiment after midnight is clearly A solution, but not an ideal one.



# Wavemeter and Lithium Laser Lock

## H.1 WAVEMETER AND GALVANOMETER SWITCHER

The software GUI provided by HighFinesse only shows up to 10 MHz resolution, but we find that the double precision float number read out from the dynamic-link library (DLL) of the wavemeter driver provides sensitivity down to 100 kHz level. The wavemeter comes with an 8-channel fiber switch option (early version), which does not provide



wide enough wavelength range and has a relative short lifetime. We opt to build our own galvanometer switcher based on a 2-D galvanometer scanner (PS1, Cambridge Technology). Total 16 channels are implemented in an 8 channels per row, 2 rows arrangement, where X axis galvanometer is used to switch between 8 channels in the same row and Y axis galvanometer is used to switch rows. The galvanometers require analog voltage input, which are provided by two 16-bit digital-to-analog converter controlled by an Arduino. The Arduino runs a custom program that decodes the 3-bit TTL signal from the wavemeter hardware to receive which channel of the 8 channels in a row the wavemeter CCD is currently exposing. The Arduino then generates the required analog voltage for moving galvanometers to the correct channel, and tells a custom Python program on the computer about which row the galvanometer Y axis is on. Using these information, the Python program can correctly sort the data from HighFinesse DLL into 16 channels.

Although a modern HighFinesse WS7-30 wavemeter is equipped with a atmosphere pressure sensor and temperature sensor, the relative old WS7 used in our experiment does not have these features, making it easier to be affected by the environment. We place the WS7 wavemeter in a sealed chamber built from a huge ISO-K 400 nipple. The sealed chamber is then placed in a temperature controlled room. This stabilize both the temperature and pressure of the wavemeter. The wavemeter and galvanometer scanner setup are shown in Figure H.1.

## H.2 LITHIUM LASER LOCK

To reach even better stability, a single frequency ECDL at 671 nm is locked to a Lithium-6 oven to provide a reference laser frequency for the wavemeter. The oven is loaded

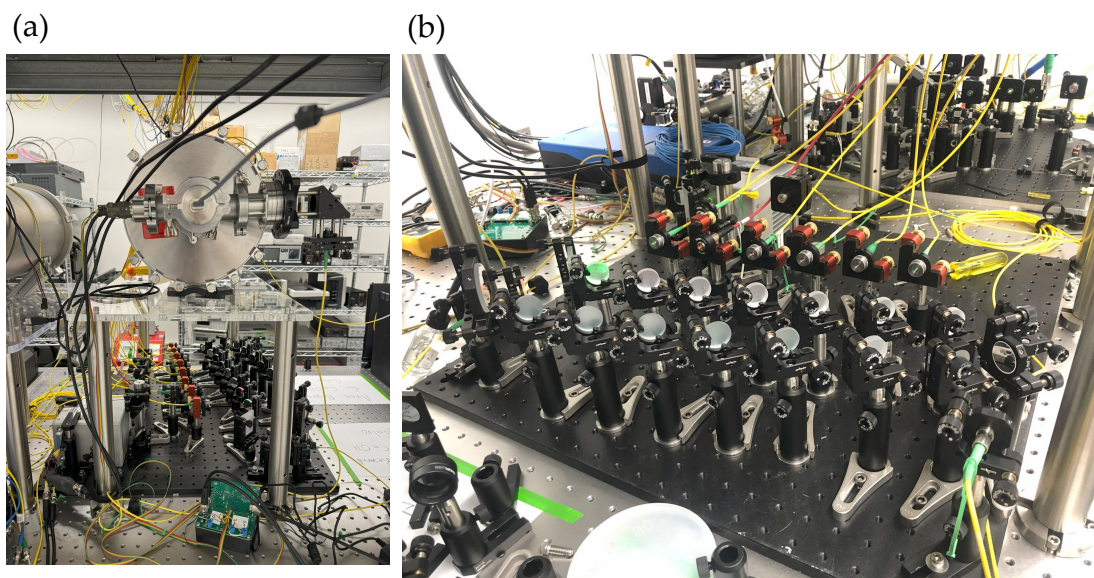


**Figure H.1:** (a) Wavemeter and galvanometer scanner setup. (b) A closer look at the 16-channel galvanometer switcher.

with enriched Lithium-6 and  $\sim 100$  mTorr of Argon buffer gas to prevent migration of Lithium onto the viewports. The lithium laser lock is realized using a modulation transfer spectroscopy (MTS) scheme for saturated absorption spectroscopy<sup>113,102,39,40</sup>. Unlike a frequency modulation spectroscopy scheme, where the frequency of the probe beam is modulated, in MTS, the frequency of the pump beam is modulated. This brings several advantage, one of which is, there is no residual amplitude modulation due to cross talk between frequency modulation and amplitude modulation. Thus, a very flat background can be obtained which provides a stable lock point. The whole lithium laser lock setup and its frequency noise read by the wavemeter are shown in Figure H.2.

With the lithium laser lock reference laser in place, we find that the wavemeter accuracy is improved to  $\sim 1$  MHz level, which is sufficient for maintaining a good molecular

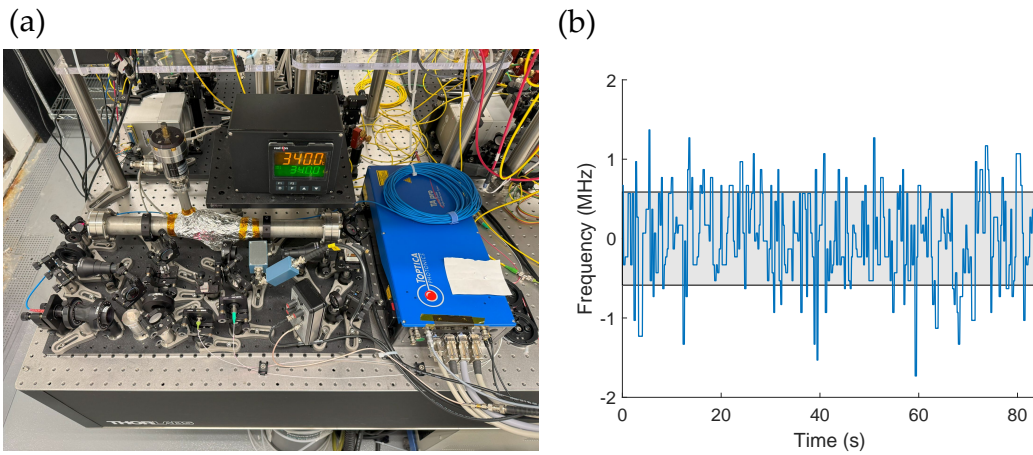


**Figure H.2:** (a) Lithium laser lock setup. (b) Lithium laser lock frequency noise read by wavemeter. Gray area indicates standard deviation of the noise.

MOT from day to day. The wavemeter readings are then sent through Ethernet to a computer running a custom LabVIEW program, where frequency readings are compared with desired laser frequency setpoints. The error signals are then generated and fed into a digital PID. The digital PID output is finally converted to analog signal by National Instruments (NI) analog output cards (PXI-6733), and delivered to frequency modulation inputs of corresponding lasers.

# I

## Collection of Opto-mechanical Ideas

### I.1 FIBER-OPTICS VACUUM FEEDTHROUGH

Our wavemeter requires a single mode fiber to reach the highest resolution and accuracy. To properly keep the wavemeter in a hermetically sealed, vacuum feedthroughs for its USB connection, input switcher TTL signal and single mode fiber input are required. It is not a easy job to find a single mode fiber vacuum feedthrough. We tried

to make our own fiber feedthrough by applying TorrSeal epoxy to fill the gap between optical fiber and a hole drilled on a KF vacuum blank. It turns out to be a terrible idea that the epoxy eventually cracks, probably due to mismatch of thermal expansion coefficient, and the chamber slowly leaks.

We then switched to a fiber-free space-fiber design that nicely put together with Thorlabs cage system, shown in Figure I.1. The laser from the optical fiber is first collimated by a fiber collimator, sent through a commercial vacuum viewport, and then coupled into another fiber inside the sealed vessel. A  $45^\circ$  cage system turning mirror and a cage system kinematic mount where the fiber collimator mounted on, are responsible for providing all the required degrees-of-freedom for alignment. The whole optical setup on the outside of the viewport is rigidly mounted on the perimeter of the 2.75-inch CF viewport using Thorlabs VFA275A adapter. The fiber collimator on the inside of the viewport is mounted onto the glass using UV cured epoxy (NOA61, Norland). By switching to all achromatic fiber collimators and endlessly single mode photonic crystal fibers, one can use this setup to cover a very broad wavelength.

## I.2 "EYE SAFE" OPTICAL ISOLATOR

For a single stage optical isolator, the polarization is rotated by  $45^\circ$ , where one of the polarizer must be rotated  $45^\circ$  relative to the table. The rejected beam from this polarizer poses an eye safety hazard unless being properly dumped. Dumping this beam sometimes becomes a tricky task, due to its high power nature and awkward angle. By inserting a half waveplate between the rotator and polarizer, all the rejected beams will leave the polarizers in parallel with the table surface. For high power laser applications, I recommend buying Faraday rotators, rather than isolators.



**Figure I.1:** Fiber-optics vacuum feedthrough

### I.3 COMPACT PROGRAMMABLE WAVEPLATE

In principle one can produce any polarization state (not including the random polarization component) starting from a linearly polarized laser. This usually requires one half waveplate and one quarter waveplate, with the capability to precisely control the rotation of both waveplates.

Here we propose such kind of device based on two resonant piezoelectric motorized rotation mounts (ELL14, Thorlabs Elliptec). These mounts are relatively cheap and has a built-in magnetic encoders that enable absolute closed loop positioning. By installing one half waveplate and one quarter waveplate on two stacked mounts, this assembly is used to optimize the optical pumping light polarization purity on our experiment through a fully automated parameter scan.

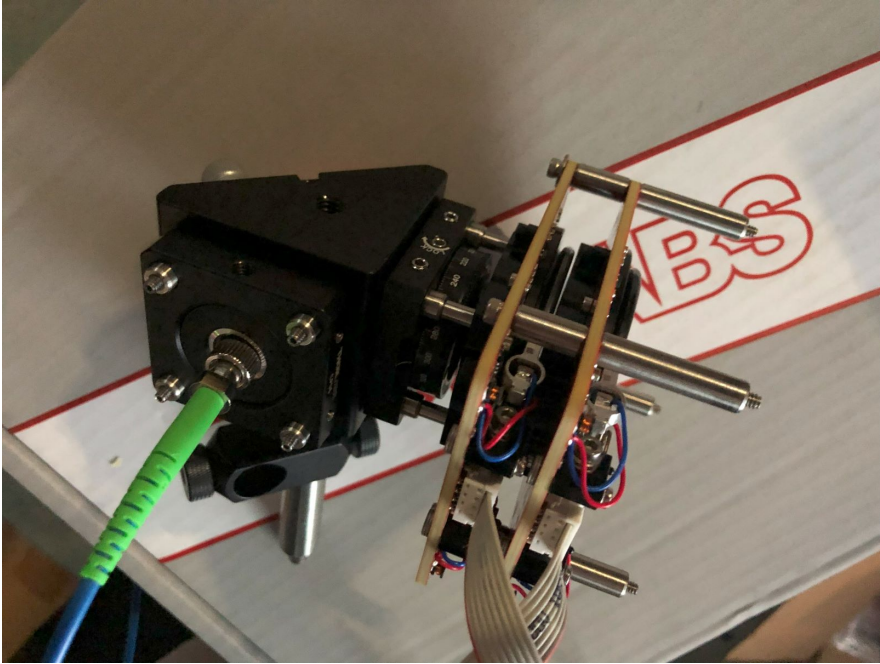


**Figure I.2:** Compact programmable waveplate.

#### I.4 MINILITE YAG BUTTON PUSHER

The Minilite YAG laser on our experiment has a built-in safety feature that it stops flashlamp simmer if there is no trigger arriving for a random amount of time. We were told by the vendor that this is a safety requirement for exporting the laser to European union countries. The vendor offers removing the feature for us, but requires us sending the laser back for this modification. Instead of halting the experiment for several months, we come up with a homemade button pusher. The button pusher is simply two solenoid linear actuators (from Amazon) that are controlled by an Arduino Micro board and a custom mount made of water-jet aluminum sheet metal. The whole setup is attached to the front panel of Minilite controller by four strong magnets. The Arduino controller monitors the TTL trigger from experimental sequence controller. If there is

no trigger arriving in 10 s, the two linear actuators will perform pre-programmed “reset” action by pressing “Stop” button then “Start” button. This action puts the laser back to flashlamp simmer mode and be ready for the incoming trigger pulse. With the help of this gadget, we are able to run the experiment remotely overnight.

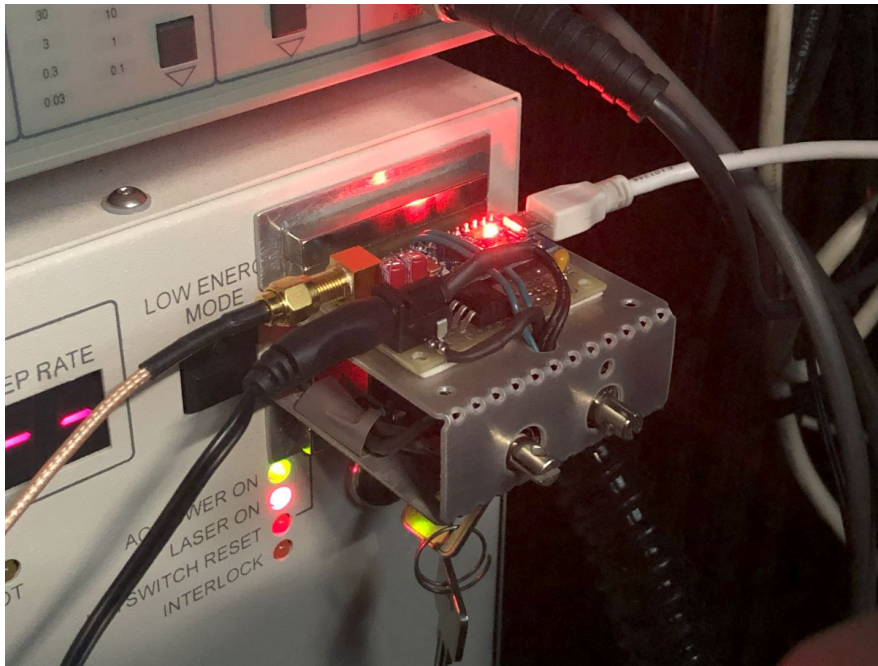


**Figure I.3:** Minilite button pusher.



# References

- [4] Anderegg, L., Augenbraun, B. L., Chae, E., Hemmerling, B., Hutzler, N. R., Ravi, A., Collopy, A., Ye, J., Ketterle, W., & Doyle, J. M. (2017). Radio frequency magneto-optical trapping of caF with high density. *Physical Review Letters*, 119(10), 103201.
- [5] Anderegg, L., Burchesky, S., Bao, Y., Yu, S. S., Karman, T., Chae, E., Ni, K.-K., Ketterle, W., & Doyle, J. M. (2021). Observation of microwave shielding of ultracold molecules. *Science*, 373(6556), 779–782.
- [6] Anderegg, L., Cheuk, L. W., Bao, Y., Burchesky, S., Ketterle, W., Ni, K.-K., & Doyle, J. M. (2019). An optical tweezer array of ultracold molecules. *Science*, 365(6458), 1156–1158.
- [7] Bao, H., Duan, J., Jin, S., Lu, X., Li, P., Qu, W., Wang, M., Novikova, I., Mikhailov, E. E., Zhao, K.-F., et al. (2020). Spin squeezing of 10<sup>11</sup> atoms by prediction and retrodiction measurements. *Nature*, 581(7807), 159–163.
- [8] Baranov, M. A. (2008). Theoretical progress in many-body physics with ultracold dipolar gases. *Physics Reports*, 464(3), 71–111.
- [9] Barredo, D., De Léséleuc, S., Lienhard, V., Lahaye, T., & Browaeys, A. (2016). An atom-by-atom assembler of defect-free arbitrary two-dimensional atomic arrays. *Science*, 354(6315), 1021–1023.
- [10] Barredo, D., Lienhard, V., De Leseleuc, S., Lahaye, T., & Browaeys, A. (2018). Synthetic three-dimensional atomic structures assembled atom by atom. *Nature*, 561(7721), 79–82.
- [11] Barry, J., McCarron, D., Norrgard, E., Steinecker, M., & DeMille, D. (2014). Magneto-optical trapping of a diatomic molecule. *Nature*, 512(7514), 286–289.
- [12] Barry, J. F. (2013). *Laser cooling and slowing of a diatomic molecule*. Yale University.
- [13] Bernien, H., Schwartz, S., Keesling, A., Levine, H., Omran, A., Pichler, H., Choi, S., Zibrov, A. S., Endres, M., Greiner, M., et al. (2017). Probing many-body dynamics on a 51-atom quantum simulator. *Nature*, 551(7682), 579–584.

- [14] Bilitewski, T. & Rey, A. M. (2023). Manipulating growth and propagation of correlations in dipolar multilayers: From pair production to bosonic kitaev models. *Physical Review Letters*, 131(5), 053001.
- [15] Bornet, G., Emperauger, G., Chen, C., Ye, B., Block, M., Bintz, M., Boyd, J. A., Barredo, D., Comparin, T., Mezzacapo, F., et al. (2023). Scalable spin squeezing in a dipolar rydberg atom array. *Nature*, 621(7980), 728–733.
- [16] Brown, J. M. & Carrington, A. (2003). *Rotational Spectroscopy of Diatomic Molecules*. Cambridge Molecular Science. Cambridge University Press.
- [17] Buhmann, S. Y., Tarbutt, M., Scheel, S., & Hinds, E. (2008). Surface-induced heating of cold polar molecules. *Physical Review A*, 78(5), 052901.
- [18] Burchesky, S. (2023). *Engineered Collisions, Molecular Qubits, and Laser Cooling of Asymmetric Top Molecules*. PhD thesis, Harvard University.
- [19] Burchesky, S., Anderegg, L., Bao, Y., Yu, S. S., Chae, E., Ketterle, W., Ni, K.-K., & Doyle, J. M. (2021). Rotational coherence times of polar molecules in optical tweezers. *Physical Review Letters*, 127(12), 123202.
- [20] Cairncross, W. B., Gresh, D. N., Grau, M., Cossel, K. C., Roussy, T. S., Ni, Y., Zhou, Y., Ye, J., & Cornell, E. A. (2017). Precision measurement of the electron's electric dipole moment using trapped molecular ions. *Physical review letters*, 119(15), 153001.
- [21] Cairncross, W. B., Zhang, J. T., Picard, L. R., Yu, Y., Wang, K., & Ni, K.-K. (2021). Assembly of a rovibrational ground state molecule in an optical tweezer. *Physical Review Letters*, 126(12), 123402.
- [22] Caldwell, L. & Tarbutt, M. (2020). Sideband cooling of molecules in optical traps. *Physical Review Research*, 2(1), 013251.
- [23] Campbell, W. C. (2008). *Magnetic Trapping of Imidogen Molecules*. PhD thesis.
- [24] Chae, E. (2021). Entanglement via rotational blockade of mgf molecules in a magic potential. *Physical Chemistry Chemical Physics*, 23(2), 1215–1220.
- [25] Charron, F., Guo, B., Zhang, K., Morbi, Z., & Bernath, P. (1995). High-resolution infrared emission spectrum of caf. *Journal of Molecular Spectroscopy*, 171(1), 160–168.
- [26] Cheuk, L. W., Anderegg, L., Augenbraun, B. L., Bao, Y., Burchesky, S., Ketterle, W., & Doyle, J. M. (2018).  $\lambda$ -enhanced imaging of molecules in an optical trap. *Physical Review Letters*, 121(8), 083201.

- [27] Childs, W., Goodman, G., & Goodman, L. (1981). Precise determination of the  $v$  and  $n$  dependence of the spin-rotation and hyperfine interactions in the  $\text{caf } x2\sigma12$  ground state. *Journal of Molecular Spectroscopy*, 86(2), 365–392.
- [28] Choi, J., Zhou, H., Knowles, H. S., Landig, R., Choi, S., & Lukin, M. D. (2020). Robust dynamic hamiltonian engineering of many-body spin systems. *Physical Review X*, 10(3), 031002.
- [29] Christakis, L., Rosenberg, J. S., Raj, R., Chi, S., Morningstar, A., Huse, D. A., Yan, Z. Z., & Bakr, W. S. (2022). Probing site-resolved correlations in a spin system of ultracold molecules. *arXiv preprint arXiv:2207.09328*.
- [30] Collaboration, A., Andreev, V., Ang, D., DeMille, D., Doyle, J., Gabrielse, G., Haefner, J., Hutzler, N., Lasner, Z., Meisenhelder, C., O’Leary, B., et al. (2018). Improved limit on the electric dipole moment of the electron. *Nature*, 562(7727), 355–360.
- [31] Collaboration, A., Baron, J., Campbell, W., DeMille, D., Doyle, J., Gabrielse, G., Gurevich, Y., Hess, P., Hutzler, N., Kirilov, E., et al. (2014). Order of magnitude smaller limit on the electric dipole moment of the electron. *Science*, 343(6168), 269–272.
- [32] Collopy, A. L., Ding, S., Wu, Y., Finneran, I. A., Anderegg, L., Augenbraun, B. L., Doyle, J. M., & Ye, J. (2018). 3d magneto-optical trap of yttrium monoxide. *Physical Review Letters*, 121(21), 213201.
- [33] de Léséleuc, S., Barredo, D., Lienhard, V., Browaeys, A., & Lahaye, T. (2017). Optical control of the resonant dipole-dipole interaction between rydberg atoms. *Physical Review Letters*, 119(5), 053202.
- [34] De Paz, A., Sharma, A., Chotia, A., Marechal, E., Huckans, J., Pedri, P., Santos, L., Gorceix, O., Vernac, L., & Laburthe-Tolra, B. (2013). Nonequilibrium quantum magnetism in a dipolar lattice gas. *Physical review letters*, 111(18), 185305.
- [35] DeMille, D. (2002). Quantum computation with trapped polar molecules. *Physical Review Letters*, 88(6), 067901.
- [36] Di Rosa, M. (2004). Laser-cooling molecules: Concept, candidates, and supporting hyperfine-resolved measurements of rotational lines in the  $ax(0,0)$  band of  $\text{cah}$ . *The European Physical Journal D-Atomic, Molecular, Optical and Plasma Physics*, 31, 395–402.
- [37] Du, J., Rong, X., Zhao, N., Wang, Y., Yang, J., & Liu, R. (2009). Preserving electron spin coherence in solids by optimal dynamical decoupling. *Nature*, 461(7268), 1265–1268.

- [38] Du, L., Barral, P., Cantara, M., de Hond, J., Lu, Y.-K., & Ketterle, W. (2023). Atomic physics on a 50 nm scale: Realization of a bilayer system of dipolar atoms. *arXiv preprint arXiv:2302.07209*.
- [39] Ducloy, M. & Bloch, D. (1981). Theory of degenerate four-wave mixing in resonant doppler-broadened systems-i. angular dependence of intensity and line-shape of phase-conjugate emission. *Journal de Physique*, 42(5), 711–721.
- [40] Ducloy, M. & Bloch, D. (1982). Theory of degenerate four-wave mixing in resonant doppler-broadened media-ii. doppler-free heterodyne spectroscopy via collinear four-wave mixing in two-and three-level systems. *Journal de Physique*, 43(1), 57–65.
- [41] Eckner, W. J., Darkwah Oppong, N., Cao, A., Young, A. W., Milner, W. R., Robinson, J. M., Ye, J., & Kaufman, A. M. (2023). Realizing spin squeezing with rydberg interactions in an optical clock. *Nature*, 621(7980), 734–739.
- [42] Endres, M., Bernien, H., Keesling, A., Levine, H., Anschuetz, E. R., Krajenbrink, A., Senko, C., Vuletic, V., Greiner, M., & Lukin, M. D. (2016). Atom-by-atom assembly of defect-free one-dimensional cold atom arrays. *Science*, 354(6315), 1024–1027.
- [43] Gadway, B. & Yan, B. (2016). Strongly interacting ultracold polar molecules. *Journal of Physics B: Atomic, Molecular and Optical Physics*, 49(15), 152002.
- [44] Gayer, O., Sacks, Z., Galun, E., & Arie, A. (2008). Temperature and wavelength dependent refractive index equations for mgo-doped congruent and stoichiometric linbo 3. *Applied Physics B*, 91, 343–348.
- [45] Gorshkov, A. V., Manmana, S. R., Chen, G., Ye, J., Demler, E., Lukin, M. D., & Rey, A. M. (2011). Tunable superfluidity and quantum magnetism with ultracold polar molecules. *Physical review letters*, 107(11), 115301.
- [46] Grant, M. & Boyd, S. (2008). Graph implementations for nonsmooth convex programs. In V. Blondel, S. Boyd, & H. Kimura (Eds.), *Recent Advances in Learning and Control*, Lecture Notes in Control and Information Sciences (pp. 95–110). Springer-Verlag Limited. [http://stanford.edu/~boyd/graph\\_dcp.html](http://stanford.edu/~boyd/graph_dcp.html).
- [47] Grant, M. & Boyd, S. (2014). CVX: Matlab software for disciplined convex programming, version 2.1. <http://cvxr.com/cvx>.
- [48] Gregory, P. D., Blackmore, J. A., Bromley, S. L., Hutson, J. M., & Cornish, S. L. (2021). Robust storage qubits in ultracold polar molecules. *Nature Physics*, 17(10), 1149–1153.

- [49] Gregory, P. D., Fernley, L. M., Tao, A. L., Bromley, S. L., Stepp, J., Zhang, Z., Kotochigova, S., Hazzard, K. R., & Cornish, S. L. (2024). Second-scale rotational coherence and dipolar interactions in a gas of ultracold polar molecules. *Nature Physics*, (pp. 1–7).
- [50] Greiner, M., Bloch, I., Hänsch, T. W., & Esslinger, T. (2001). Magnetic transport of trapped cold atoms over a large distance. *Physical Review A*, 63(3), 031401.
- [51] Gross, C., Gan, H., & Dieckmann, K. (2016). All-optical production and transport of a large li 6 quantum gas in a crossed optical dipole trap. *Physical Review A*, 93(5), 053424.
- [52] Gross, C., Zibold, T., Nicklas, E., Esteve, J., & Oberthaler, M. K. (2010). Nonlinear atom interferometer surpasses classical precision limit. *Nature*, 464(7292), 1165–1169.
- [53] Gullion, T., Baker, D. B., & Conradi, M. S. (1990). New, compensated carr-ourcell sequences. *Journal of Magnetic Resonance* (1969), 89(3), 479–484.
- [54] Guo, M., Zhu, B., Lu, B., Ye, X., Wang, F., Vexiau, R., Bouloufa-Maafa, N., Quémener, G., Dulieu, O., & Wang, D. (2016). Creation of an ultracold gas of ground-state dipolar  $^{23}\text{Na}^{87}\text{Rb}$  molecules. *Physical Review Letters*, 116(20), 205303.
- [55] Gustavson, T., Chikkatur, A., Leanhardt, A., Görlitz, A., Gupta, S., Pritchard, D., & Ketterle, W. (2001). Transport of bose-einstein condensates with optical tweezers. *Physical Review Letters*, 88(2), 020401.
- [56] Hallas, C., Li, G. K., Vilas, N. B., Robichaud, P., Anderegg, L., & Doyle, J. M. (2024). High compression blue-detuned magneto-optical trap of polyatomic molecules. *arXiv preprint arXiv:2404.03636*.
- [57] Hamann, S., Haycock, D., Klose, G., Pax, P., Deutsch, I., & Jessen, P. S. (1998). Resolved-sideband raman cooling to the ground state of an optical lattice. *Physical Review Letters*, 80(19), 4149.
- [58] Holland, C. M., Lu, Y., & Cheuk, L. W. (2022). On-demand entanglement of molecules in a reconfigurable optical tweezer array. *arXiv preprint arXiv:2210.06309*.
- [59] Holland, C. M., Lu, Y., & Cheuk, L. W. (2023). On-demand entanglement of molecules in a reconfigurable optical tweezer array. *Science*, 382(6675), 1143–1147.

- [60] Hu, M.-G., Liu, Y., Grimes, D. D., Lin, Y.-W., Gheorghe, A. H., Vexiau, R., Bouloufa-Maafa, N., Dulieu, O., Rosenband, T., & Ni, K.-K. (2019). Direct observation of bimolecular reactions of ultracold krb molecules. *Science*, 366(6469), 1111–1115.
- [61] Hu, M.-G., Liu, Y., Nichols, M. A., Zhu, L., Quéméner, G., Dulieu, O., & Ni, K.-K. (2021). Nuclear spin conservation enables state-to-state control of ultracold molecular reactions. *Nature Chemistry*, 13(5), 435–440.
- [62] Hummon, M. T., Yeo, M., Stuhl, B. K., Collopy, A. L., Xia, Y., & Ye, J. (2013). 2d magneto-optical trapping of diatomic molecules. *Physical review letters*, 110(14), 143001.
- [63] Hutzler, N. (2008). Charcoal as a helium cryopump.
- [64] Hutzler, N. R., Parsons, M. F., Gurevich, Y. V., Hess, P. W., Petrik, E., Spaun, B., Vutha, A. C., DeMille, D., Gabrielse, G., & Doyle, J. M. (2011). A cryogenic beam of refractory, chemically reactive molecules with expansion cooling. *Physical chemistry chemical physics*, 13(42), 18976–18985.
- [65] Iwai, D., Izawa, H., Kashima, K., Ueda, T., & Sato, K. (2019). Speeded-up focus control of electrically tunable lens by sparse optimization. *Scientific Reports*, 9(1), 12365.
- [66] Jepsen, P. N., Amato-Grill, J., Dimitrova, I., Ho, W. W., Demler, E., & Ketterle, W. (2020). Spin transport in a tunable heisenberg model realized with ultracold atoms. *Nature*, 588(7838), 403–407.
- [67] Karra, M., Sharma, K., Friedrich, B., Kais, S., & Herschbach, D. (2016). Prospects for quantum computing with an array of ultracold polar paramagnetic molecules. *The Journal of chemical physics*, 144(9), 094301.
- [68] Kaufman, A. M., Lester, B. J., & Regal, C. A. (2012). Cooling a single atom in an optical tweezer to its quantum ground state. *Physical Review X*, 2(4), 041014.
- [69] Keshet, A. & Ketterle, W. (2013). A distributed, graphical user interface based, computer control system for atomic physics experiments. *Review of Scientific Instruments*, 84(1).
- [70] Khriplovich, I. B. & Lamoreaux, S. K. (2012). *CP violation without strangeness: electric dipole moments of particles, atoms, and molecules*. Springer Science & Business Media.
- [71] Klostermann, T., Cabrera, C. R., von Raven, H., Wienand, J. F., Schweizer, C., Bloch, I., & Aidelsburger, M. (2022). Fast long-distance transport of cold cesium atoms. *Physical Review A*, 105(4), 043319.

- [72] Koller, M., Jung, F., Phrompao, J., Zeppenfeld, M., Rabey, I., & Rempe, G. (2022). Electric-field-controlled cold dipolar collisions between trapped ch 3 f molecules. *Physical Review Letters*, 128(20), 203401.
- [73] Kozyryev, I., Lasner, Z., & Doyle, J. M. (2021). Enhanced sensitivity to ultralight bosonic dark matter in the spectra of the linear radical sroh. *Physical Review A*, 103(4), 043313.
- [74] Léonard, J., Lee, M., Morales, A., Karg, T. M., Esslinger, T., & Donner, T. (2014). Optical transport and manipulation of an ultracold atomic cloud using focus-tunable lenses. *New Journal of Physics*, 16(9), 093028.
- [75] Leroux, I. D., Schleier-Smith, M. H., & Vuletić, V. (2010). Implementation of cavity squeezing of a collective atomic spin. *Physical Review Letters*, 104(7), 073602.
- [76] Lessard, P. A. (1989). Cryogenic adsorption of noncondensibles in the high-vacuum regime. *Journal of Vacuum Science & Technology A: Vacuum, Surfaces, and Films*, 7(3), 2373–2376.
- [77] Levine, H. J. (2021). *Quantum information processing and quantum simulation with programmable Rydberg atom arrays*. PhD thesis, Harvard University.
- [78] Lewandowski, H. J., Harber, D., Whitaker, D. L., & Cornell, E. A. (2003). Simplified system for creating a bose–einstein condensate. *Journal of Low Temperature Physics*, 132(5), 309–367.
- [79] Li, J.-R., Matsuda, K., Miller, C., Carroll, A. N., Tobias, W. G., Higgins, J. S., & Ye, J. (2022). Tunable itinerant spin dynamics with polar molecules. *arXiv preprint arXiv:2208.02216*.
- [80] Lin, J., He, J., Ye, X., & Wang, D. (2021). Anisotropic polarizability of ultracold ground-state  $^{23}\text{Na}^{87}\text{Rb}$  molecules. *Physical Review A*, 103(2), 023332.
- [81] Liu, L., Hood, J., Yu, Y., Zhang, J., Hutzler, N., Rosenband, T., & Ni, K.-K. (2018). Building one molecule from a reservoir of two atoms. *Science*, 360(6391), 900–903.
- [82] Matsuda, K., De Marco, L., Li, J.-R., Tobias, W. G., Valtolina, G., Quéméner, G., & Ye, J. (2020). Resonant collisional shielding of reactive molecules using electric fields. *Science*, 370(6522), 1324–1327.
- [83] Mayle, M., Ruzic, B. P., & Bohn, J. L. (2012). Statistical aspects of ultracold resonant scattering. *Physical Review A*, 85(6), 062712.
- [84] Micheli, A., Brennen, G., & Zoller, P. (2006). A toolbox for lattice-spin models with polar molecules. *Nature Physics*, 2(5), 341–347.

- [85] Middelmann, T., Falke, S., Lisdat, C., & Sterr, U. (2012). Long-range transport of ultracold atoms in a far-detuned one-dimensional optical lattice. *New Journal of Physics*, 14(7), 073020.
- [86] Minniberger, S., Diorico, F., Haslinger, S., Hufnagel, C., Novotny, C., Lippok, N., Majer, J., Koller, C., Schneider, S., & Schmiedmayer, J. (2014). Magnetic conveyor belt transport of ultracold atoms to a superconducting atomchip. *Applied Physics B*, 116(4), 1017–1021.
- [87] Molony, P. K., Gregory, P. D., Ji, Z., Lu, B., Köppinger, M. P., Le Sueur, C. R., Blackley, C. L., Hutson, J. M., & Cornish, S. L. (2014). Creation of ultracold  $^{87}\text{Rb}^{133}\text{Cs}$  molecules in the rovibrational ground state. *Physical Review Letters*, 113(25), 255301.
- [88] Monroe, C., Meekhof, D., King, B., Jefferts, S. R., Itano, W. M., Wineland, D. J., & Gould, P. (1995). Resolved-sideband raman cooling of a bound atom to the 3d zero-point energy. *Physical review letters*, 75(22), 4011.
- [89] Naides, M. A., Turner, R. W., Lai, R. A., DiSciaccia, J. M., & Lev, B. L. (2013). Trapping ultracold gases near cryogenic materials with rapid reconfigurability. *Applied Physics Letters*, 103(25), 251112.
- [90] Neyenhuis, B., Yan, B., Moses, S., Covey, J., Chotia, A., Petrov, A., Kotochigova, S., Ye, J., & Jin, D. (2012). Anisotropic polarizability of ultracold polar  $^{40}\text{K}^{87}\text{Rb}$  molecules. *Physical Review Letters*, 109(23), 230403.
- [91] Ni, K.-K., Ospelkaus, S., De Miranda, M., Pe'Er, A., Neyenhuis, B., Zirbel, J., Kotochigova, S., Julienne, P., Jin, D., & Ye, J. (2008). A high phase-space-density gas of polar molecules. *science*, 322(5899), 231–235.
- [92] Ni, K.-K., Ospelkaus, S., Wang, D., Quéméner, G., Neyenhuis, B., De Miranda, M., Bohn, J., Ye, J., & Jin, D. (2010). Dipolar collisions of polar molecules in the quantum regime. *Nature*, 464(7293), 1324–1328.
- [93] Ni, K.-K., Rosenband, T., & Grimes, D. D. (2018). Dipolar exchange quantum logic gate with polar molecules. *Chemical Science*, 9(33), 6830–6838.
- [94] Norrgard, E., McCarron, D., Steinecker, M., Tarbutt, M., & DeMille, D. (2016a). Submillikelvin dipolar molecules in a radio-frequency magneto-optical trap. *Physical Review Letters*, 116(6), 063004.
- [95] Norrgard, E. B., Sitaraman, N., Barry, J. F., McCarron, D. J., Steinecker, M. H., & DeMille, D. (2016b). In-vacuum scattered light reduction with black cupric oxide surfaces for sensitive fluorescence detection. *Review of Scientific Instruments*, 87(5).



- [96] Ospelkaus, S., Ni, K.-K., Wang, D., De Miranda, M., Neyenhuis, B., Quéméner, G., Julienne, P., Bohn, J., Jin, D., & Ye, J. (2010). Quantum-state controlled chemical reactions of ultracold potassium-rubidium molecules. *Science*, 327(5967), 853–857.
- [97] Park, J. W., Will, S. A., & Zwierlein, M. W. (2015). Ultracold dipolar gas of fermionic  $^{23}\text{Na}^{40}\text{K}$  molecules in their absolute ground state. *Physical Review Letters*, 114(20), 205302.
- [98] Park, J. W., Yan, Z. Z., Loh, H., Will, S. A., & Zwierlein, M. W. (2017). Second-scale nuclear spin coherence time of ultracold  $^{23}\text{Na}^{40}\text{K}$  molecules. *Science*, 357(6349), 372–375.
- [99] Perrin, H., Kuhn, A., Bouchoule, I., & Salomon, C. (1998). Sideband cooling of neutral atoms in a far-detuned optical lattice. *Europhysics Letters*, 42(4), 395.
- [100] Pezze, L., Smerzi, A., Oberthaler, M. K., Schmied, R., & Treutlein, P. (2018). Quantum metrology with nonclassical states of atomic ensembles. *Reviews of Modern Physics*, 90(3), 035005.
- [101] Prehn, A., Ibrügger, M., Glöckner, R., Rempe, G., & Zeppenfeld, M. (2016). Optoelectrical cooling of polar molecules to submillikelvin temperatures. *Physical review letters*, 116(6), 063005.
- [102] Raj, R., Bloch, D., Snyder, J., Camy, G., & Ducloy, M. (1980). High-frequency optically heterodyned saturation spectroscopy via resonant degenerate four-wave mixing. *Physical Review Letters*, 44(19), 1251.
- [103] Riedel, M. F., Böhi, P., Li, Y., Hänsch, T. W., Sinatra, A., & Treutlein, P. (2010). Atom-chip-based generation of entanglement for quantum metrology. *Nature*, 464(7292), 1170–1173.
- [104] Roussy, T. S., Caldwell, L., Wright, T., Cairncross, W. B., Shagam, Y., Ng, K. B., Schlossberger, N., Park, S. Y., Wang, A., Ye, J., et al. (2023). An improved bound on the electron’s electric dipole moment. *Science*, 381(6653), 46–50.
- [105] Rvachov, T. M., Son, H., Sommer, A. T., Ebadi, S., Park, J. J., Zwierlein, M. W., Ketterle, W., & Jamison, A. O. (2017). Long-lived ultracold molecules with electric and magnetic dipole moments. *Physical Review Letters*, 119(14), 143001.
- [106] Sackett, C. A., Kielpinski, D., King, B. E., Langer, C., Meyer, V., Myatt, C. J., Rowe, M., Turchette, Q., Itano, W. M., Wineland, D. J., et al. (2000). Experimental entanglement of four particles. *Nature*, 404(6775), 256–259.

- [107] Sawant, R., Blackmore, J. A., Gregory, P. D., Mur-Petit, J., Jaksch, D., Aldegunde, J., Hutson, J. M., Tarbutt, M., & Cornish, S. L. (2020). Ultracold polar molecules as qudits. *New Journal of Physics*, 22(1), 013027.
- [108] Schindewolf, A., Bause, R., Chen, X.-Y., Duda, M., Karman, T., Bloch, I., & Luo, X.-Y. (2022). Evaporation of microwave-shielded polar molecules to quantum degeneracy. *Nature*, 607(7920), 677–681.
- [109] Schmid, S., Thalhammer, G., Winkler, K., Lang, F., & Denschlag, J. H. (2006). Long distance transport of ultracold atoms using a 1d optical lattice. *New Journal of Physics*, 8(8), 159.
- [110] Seeßelberg, F., Luo, X.-Y., Li, M., Bause, R., Kotochigova, S., Bloch, I., & Gohle, C. (2018). Extending rotational coherence of interacting polar molecules in a spin-decoupled magic trap. *Physical Review Letters*, 121(25), 253401.
- [111] Sewell, R. J., Koschorreck, M., Napolitano, M., Dubost, B., Behbood, N., & Mitchell, M. W. (2012). Magnetic sensitivity beyond the projection noise limit by spin squeezing. *Physical review letters*, 109(25), 253605.
- [112] Shaw, J. & McCarron, D. (2020). Bright, continuous beams of cold free radicals. *Physical Review A*, 102(4), 041302.
- [113] Shirley, J. H. (1982). Modulation transfer processes in optical heterodyne saturation spectroscopy. *Optics Letters*, 7(11), 537–539.
- [114] Su, L., Douglas, A., Szurek, M., Groth, R., Ozturk, S. F., Krahn, A., Hébert, A. H., Phelps, G. A., Ebadi, S., Dickerson, S., et al. (2023). Dipolar quantum solids emerging in a hubbard quantum simulator. *Nature*, 622(7984), 724–729.
- [115] Takahashi, Y., Zhang, C., Jadbabaie, A., & Hutzler, N. R. (2023). Engineering field-insensitive molecular clock transitions for symmetry violation searches. *Physical Review Letters*, 131(18), 183003.
- [116] Takekoshi, T., Reichsöllner, L., Schindewolf, A., Hutson, J. M., Le Sueur, C. R., Dulieu, O., Ferlaino, F., Grimm, R., & Nägerl, H.-C. (2014). Ultracold dense samples of dipolar rbc molecules in the rovibrational and hyperfine ground state. *Physical review letters*, 113(20), 205301.
- [117] Thompson, J. D., Tiecke, T., Zibrov, A. S., Vuletić, V., & Lukin, M. D. (2013). Coherence and raman sideband cooling of a single atom in an optical tweezer. *Physical review letters*, 110(13), 133001.
- [118] Tobias, W. G., Matsuda, K., Li, J.-R., Miller, C., Carroll, A. N., Bilitewski, T., Rey, A. M., & Ye, J. (2022). Reactions between layer-resolved molecules mediated by dipolar spin exchange. *Science*, 375(6586), 1299–1303.

- [119] Truppe, S., Williams, H., Hambach, M., Caldwell, L., Fitch, N., Hinds, E., Sauer, B., & Tarbutt, M. (2017). Molecules cooled below the doppler limit. *Nature Physics*, 13(12), 1173–1176.
- [120] Tuchendler, C., Lance, A. M., Browaeys, A., Sortais, Y. R., & Grangier, P. (2008). Energy distribution and cooling of a single atom in an optical tweezer. *Physical Review A*, 78(3), 033425.
- [121] Turchette, Q., Wood, C., King, B., Myatt, C., Leibfried, D., Itano, W., Monroe, C., & Wineland, D. (1998). Deterministic entanglement of two trapped ions. *Physical Review Letters*, 81(17), 3631.
- [122] Unnikrishnan, G., Beulenkamp, C., Zhang, D., Zamarski, K. P., Landini, M., & Nägerl, H.-C. (2021). Long distance optical transport of ultracold atoms: a compact setup using a moiré lens. *Review of Scientific Instruments*, 92(6), 063205.
- [123] Vilas, N. B., Hallas, C., Anderegg, L., Robichaud, P., Winnicki, A., Mitra, D., & Doyle, J. M. (2022). Magneto-optical trapping and sub-doppler cooling of a polyatomic molecule. *Nature*, 606(7912), 70–74.
- [124] Vuletić, V., Chin, C., Kerman, A. J., & Chu, S. (1998). Degenerate raman sideband cooling of trapped cesium atoms at very high atomic densities. *Physical Review Letters*, 81(26), 5768.
- [125] Wall, M., Hazzard, K., & Rey, A. M. (2015). Quantum magnetism with ultracold molecules. In *From atomic to mesoscale: The Role of Quantum Coherence in Systems of Various Complexities* (pp. 3–37). World Scientific.
- [126] Wang, K., Williams, C. P., Picard, L. R., Yao, N. Y., & Ni, K.-K. (2022). Enriching the quantum toolbox of ultracold molecules with rydberg atoms. *PRX Quantum*, 3(3), 030339.
- [127] Williams, H., Caldwell, L., Fitch, N., Truppe, S., Rodewald, J., Hinds, E., Sauer, B., & Tarbutt, M. (2018). Magnetic trapping and coherent control of laser-cooled molecules. *Physical Review Letters*, 120(16), 163201.
- [128] Wineland, D. J., Monroe, C., Itano, W. M., Leibfried, D., King, B. E., & Meekhof, D. M. (1998). Experimental issues in coherent quantum-state manipulation of trapped atomic ions. *Journal of research of the National Institute of Standards and Technology*, 103(3), 259.
- [129] Wu, Y., Burau, J. J., Mehling, K., Ye, J., & Ding, S. (2021). High phase-space density of laser-cooled molecules in an optical lattice. *Physical Review Letters*, 127(26), 263201.

- [130] Yan, B., Moses, S. A., Gadway, B., Covey, J. P., Hazzard, K. R., Rey, A. M., Jin, D. S., & Ye, J. (2013). Observation of dipolar spin-exchange interactions with lattice-confined polar molecules. *Nature*, 501(7468), 521–525.
- [131] Yang, H., Cao, J., Su, Z., Rui, J., Zhao, B., & Pan, J.-W. (2022). Creation of an ultracold gas of triatomic molecules from an atom–diatomic molecule mixture. *Science*, 378(6623), 1009–1013.
- [132] Yelin, S., Kirby, K., & Côté, R. (2006). Schemes for robust quantum computation with polar molecules. *Physical Review A*, 74(5), 050301.
- [133] Yi, S. & You, L. (2000). Trapped atomic condensates with anisotropic interactions. *Physical Review A*, 61(4), 041604.
- [134] Yu, Y., Hutzler, N. R., Zhang, J. T., Liu, L. R., Hood, J. D., Rosenband, T., & Ni, K.-K. (2018). Motional-ground-state cooling outside the lamb-dicke regime. *Physical Review A*, 97(6), 063423.
- [135] Zeppenfeld, M., Englert, B. G., Glöckner, R., Prehn, A., Mielenz, M., Sommer, C., van Buuren, L. D., Motsch, M., & Rempe, G. (2012). Sisyphus cooling of electrically trapped polyatomic molecules. *Nature*, 491(7425), 570–573.
- [136] Zhang, C. & Tarbutt, M. (2022). Quantum computation in a hybrid array of molecules and rydberg atoms. *PRX Quantum*, 3(3), 030340.
- [137] Zhang, J. T., Picard, L. R., Cairncross, W. B., Wang, K., Yu, Y., Fang, F., & Ni, K.-K. (2022). An optical tweezer array of ground-state polar molecules. *Quantum Science and Technology*, 7(3), 035006.